Multiphysical behaviour of shales from Northern Switzerland

THÈSE N^{O} 7539 (2017)

PRÉSENTÉE LE 3 MARS 2017

À LA FACULTÉ DE L'ENVIRONNEMENT NATUREL, ARCHITECTURAL ET CONSTRUIT
LABORATOIRE DE MÉCANIQUE DES SOLS - CHAIRE GAZ NATUREL PETROSVIBRI
PROGRAMME DOCTORAL EN MÉCANIQUE

ÉCOLE POLYTECHNIQUE FÉDÉRALE DE LAUSANNE

POUR L'OBTENTION DU GRADE DE DOCTEUR ÈS SCIENCES

PAR

Valentina FAVERO

acceptée sur proposition du jury:

Prof. F. Gallaire, président du jury
Prof. L. Laloui, Dr A. Ferrari, directeurs de thèse
Dr P. Marschall, rapporteur
Dr R. Ewy, rapporteur
Prof. M. Violay, rapporteuse

ÉCOLE POLYTECHNIQUE
FÉDÉRALE DE LAUSANNE
Suisse
2017

Ai miei genitori Gianluigi e Fabiola

Alle mie sorelle Sara e Anna

Acknowledgments
Ringraziamenti

My first thanks go to my supervisor, Prof. Lyesse Laloui, who believed in me and gave me the possibility to start the PhD adventure. I would like to thank him also for the several professional opportunities he gave me, and for my involvement in projects and professional activities, which made me grow in my professional life. Special thanks go to my co-supervisor, Prof. Alessio Ferrari. I have no words to express my gratitude for his scientific support to my research, for being able to encourage and motivate me during my study, and for transforming into something fascinating every aspect of our research. I would like to thank him for his passion and dedication toward our profession, which are source of great inspiration.

I would like to acknowledge the financial support of Nagra, the Swiss National Cooperative for Radioactive Waste Disposal, who made this work possible. I would like to thank in particular Dr Paul Marschall and Dr Silvio Giger from Nagra, for their presence, support, and for the several scientific discussions, which allowed me to better develop my research. I would like to thank Dr Paul Marschall also for accepting to be part of my PhD jury and for the time he dedicated to revise my thesis manuscript. I would like to acknowledge all the members of my PhD jury, Prof. Marie Violay, Prof. François Gallaire, and in particular Dr Russell Ewy, who provided me with very useful comments and feedbacks during the revision of the thesis manuscript.

I would like to thank the wonderful LMS team. I would like to thank Patrick Dubey for his precious help in our soil mechanics laboratory, for his support in moments of discouragement, and for sharing with me the joy of successful tests. Special thanks go to Gilbert Gruaz for his presence and his wise words. I would like also to thank Swann, Bastien, Julien, Erwin, Benjamin and Mirco, for their precious help in the lab during installation and dismantling phases of my experiments. Great thanks go to Laurent Gastaldo, from LEMR, for his help, his advises and especially for his fantastic good humour. I would like to acknowledge Rosa Ana Turielle and Barbara Tinguely for being more than simple secretaries. I would like to thank them for their support, for their advices about life, and of course for their precious help in the administrative aspects of my work. Thanks also to Jessica and Michela for their great help.

My PhD research has developed through these almost five years also thanks to the precious presence of amazing colleagues. My gratitude goes first of all to Alice and Donatella, who welcomed me to Lausanne and helped me during my first days in this new country. Un grazie particolare ad Alice per aver condiviso con me la passione per la corsa e per i viaggi di lavoro. Thanks to Ali, for teaching me the tricks to successfully handle advanced laboratory devises and for helping me during my first days in the lab. Thanks to Thomas, my first officemate, for his calm and good humour. I would like to thank all my previous LMS colleagues, Fabrice, John, Suzanne, Mohammad, Abdusalam, Samila, Maria, Timur, Julia, Sergio, Roman, Victor and many others. I would like to thank Azad Koliji for his precious geomechanics lessons.

I would like to thank Francesco, who shared with me the path of the PhD Thesis. Special thanks go to my shales colleagues, Alberto and Eleonora. I would like to thank Alberto for our endless scientific discussions, for being always ready to listen, for having always the right words and for the contagious optimism. Thanks to Eleonora, my special officemate, for supporting me and for sharing with me the joy and pains of my last years of PhD.

I would like to deeply thank Anne-Catherine for reading with patience some of my thesis chapters, for listening to my presentation and for giving precious advices. I would like also to thank her for her ever-present smile and for her contagious peaceful and joyful personality. Special thanks go to Chao, for our numerous discussions about our researches, our cultures and about life. I would like to thank him for his help and advice about the world of modelling and about the art of making sides. I would like to thank all my current LMS colleagues, thanks to Alessandro for his joyful personality, thanks to Etienne for his cheerfulness, thanks to Dimitrios for his enterprising spirit, thanks to Samuel for his passion toward Swiss traditions, thanks to Melis, Matteo, Houda, Cristiano, Angelica, Gianluca, Jacopo, Hiram, Aldo and Barnaby. I would like also to thank the LEMR colleagues, Chiara, Mateo, Corentin and in particular Felipe.

Un grande grazie alla mia prima famiglia italiana a Losanna: Francesco, Massimo, Chloé, Simone, Patrizia, Anna, Pablo, Chiara, Andrea, Giulia e Martin. Grazie per avermi fatto sentire a casa fin dai primi giorni a Losanna. Un grazie particolare a Chiara per tutte le avventure vissute insieme. Un grazie speciale a Erika, Andrea e Jacopo per i pomeriggi lungo lago a cantare e suonare, e per le belle serate passate insieme di cui mantengo un caro ricordo. Special thanks go to my amigos salseros, Jose, Ali, Lara, Adrian, Nicolas, Heinz and Lucia, who made me find in Lausanne that rhythm that makes life more fun. In particular a big thank to Lucia, a lovely and crazy friend, who often reminds me that it is always worth to try to follow dreams.

Un immenso grazie va al GGAL, la mia seconda famiglia, il gruppo che mi ha permesso di conoscere delle persone meravigliose e di vivere momenti tanto preziosi. Troppe sarebbero le persone da ringraziare, vorrei limitarmi a nominare don Ottavio per la sua costante presenza e per le sue preziose riflessioni sulla vita. Grazie agli affezionati amici Aldo e Rima, Marina e Giovanni, Chiara e Federico, Francesco e Angelica, Roberto e Sara, per tutti i bei momenti vissuti insieme. Grazie a Sara C e a Sara S per la loro speciale amicizia e per esserci sempre e comunque.

Grazie a Elisa e Emanuele, per ricordarmi la bellezza delle cose semplici e delle tradizioni Venete. Grazie a Martina e Matteo, per tenere viva una amicizia decennale tanto preziosa. Grazie a Giorgia, Giulia e Flavio per aspettarmi sempre al mio rientro in patria. Vorrei ringraziare Teresa, Tonino, Angela e Gianluca per avermi accolto come una figlia e una sorella. Un grazie particolare ai miei zii torinesi Mimmo e Giuliana, per i bei fine settimana italiani e per l'affetto sempre dimostrato.

Il più grande grazie va alla mia famiglia, ai miei genitori Gianluigi e Fabiola per i loro sacrifici, per gli incoraggiamenti, e per avermi insegnato i valori che contano. Grazie alle mie sorelle, Sara e Anna, il mio tesoro più grande, che supera tempo e distanza. Infine voglio ringraziare Raffaele, la persona che rende speciale ogni mia giornata. Grazie per tutto il supporto durante l'ultimo periodo della tesi, grazie per le cene a tarda sera, per aver ascoltato la mia presentazione allo sfinimento, ma soprattutto grazie di essere l'amico, il compagno e l'amore più grande che potessi desiderare. Sono fortunata.

Table of Contents

Abstract

Shales are involved in energy-related applications such as the extraction of shale gas, the CO_2 storage and the nuclear waste disposal. In these contexts, fundamental issues come along with the multiphysical conditions in which shales are found, where mechanics, temperature, chemistry and unsaturated conditions play a relevant role. This thesis analyses, theoretically and experimentally, the multiphysical behaviour of Swiss shales: retention capacity, hydro-mechanical behaviour, thermo-mechanical response and chemo-mechanical processes are investigated.

The knowledge of shales retention capacity is relevant for energy-related applications. An advanced experimental methodology to analyse the retention behaviour of shales is presented. The existence of main wetting and drying paths is investigated, together with the hysteresis domain, the presence of scanning paths, the volume change induced by suction variations, and the dependency of the air entry value on the void ratio.

The generation of excess pore water pressure due to changes in stress is a concern during tunnel excavations and drilling operations in shales, therefore, the consolidation of shales must be analysed. This thesis describes an apparatus designed to perform high-pressure oedometric tests in multiphysical conditions, and an analytical model which allows to gather information on the coefficient of consolidation, stiffness, poroelastic properties, secondary compression and permeability as a function of the applied stress. Remoulded shales behaviour is compared to the intact shales response, in order to analyse the impact of diagenesis on the material behaviour. The results highlight greater stiffness, lower porosity, lower swelling sensitivity and less creep for the intact shale with respect to the remoulded one when the same vertical effective stress is applied: this response is considered to be the result of diagenesis rather than solely mechanical compaction.

The thermo-mechanical behaviour of Opalinus Clay is investigated at different stress conditions and overconsolidation ratio (OCR) values. Thermal expansion is found when heating is carried out at high OCR, while irreversible thermal compaction is observed when heat is applied at low OCR. Irreversible expansive strains can occur upon first heating at high OCR, while a reversible behaviour follows during subsequent thermal cycles. A decrease of the yield threshold with increasing temperature is observed. Compressibility and swelling indexes are not significantly influenced by thermal changes, whereas consolidation processes occur faster at high temperature.

The research on chemo-mechanical processes in Opalinus Clay highlights that the volume change of the material upon wetting is related to the osmotic suction of the pore fluid. Moreover, an increase in osmotic suction at constant stress leads to development of irreversible settlements, whose magnitude depends on the stress history. However, the compressibility and consolidation coefficient of Opalinus Clay are not significantly affected by osmotic suction. An elasto-plastic chemo-mechanical framework is formulated in order to model the chemo-mechanical behaviour of Opalinus Clay.

The strength and stiffness of Opalinus Clay are investigated through the performance of triaxial tests. The results allow to gain information on the anisotropic and stress-dependent behaviour of the material. Based on the experimental evidences, a constitutive framework is formulated. Transversely isotropic elasticity is considered in order to reproduce the anisotropic elastic response of the material. Moreover, the elastic parameters are defined in order to account for stress dependency. The possibility to consider anisotropic strength response is also included in the model. The constitutive approach includes the introduction of the disturbed state concept (DSC) in order to reproduce softening. The numerical simulations highlight the capability of the constitutive framework to take into account the main rheological features of Opalinus Clay.

Keywords: Shales, multiphysical behaviour, Opalinus Clay, nuclear waste storage, geo-energy, shales characterization, water retention behaviour, thermo-mechanical behaviour, chemo-mechanical processes, triaxial testing, anisotropy, constitutive framework.

Riassunto

Gli scisti sono coinvolti in applicazioni in ambito energetico come l'estrazione di gas, lo stoccaggio di CO_2 e lo smaltimento di scorie radioattive. In tale contesto, le condizioni multifisiche danno vita a rilevanti problematiche, in cui meccanica, temperatura, chimica e parziale saturazione giocano un ruolo fondamentale. La tesi analizza, dal punto di vista sperimentale e teorico, il comportamento multifisico di scisti svizzeri. Si indaga in particolare la capacità di ritenzione, il comportamento idro-meccanico, la risposta termo-meccanica e processi chemo-meccanici.

La capacità di ritenzione è di rilievo nelle applicazioni geo-energetiche. La tesi presenta un'avanzata metodologia sperimentale per analizzare il comportamento di ritenzione degli scisti. Si indagano i percorsi principali di imbibizione ed essiccamento, il dominio di isteresi, le scanning curves, la variazione di volume indotta da cambi di suzione e la dipendenza del valore di entrata d'aria dall'indice di porosità.

Le sovrapressioni generate da variazioni di tensione destano preoccupazione durante lo scavo di tunnel o in operazioni di perforazione in scisto, percui è importante analizzarne la consolidazione. La tesi descrive un apparato progettato per svolgere test edometrici ad alta pressione in condizioni multifisiche, e un modello analitico che permette di ottenere informazioni sul coefficiente di consolidazione, sulla rigidezza, sulle proprietà poroelastiche, sulla consolidazione secondaria e sulla permeabilità, in funzione della tensione. Il comportamento di scisti rimaneggiati è comparato a quello di scisti intatti, al fine di analizzare l'impatto della diagenesi. I risultati evidenziano maggior rigidezza, minor porosità, minor rigonfiamento e minor creep negli scisti intatti rispetto a quelli rimaneggiati, a parità di tensione efficace: si considera che tale risposta sia il risultato della diagenesi.

Il comportamento termo-meccanico dell'Opalinus Clay è studiato in questa tesi a diverse tensioni e a diversi gradi di sovraconsolidazione (OCR). Si osserva espansione termica in fase di riscaldamento ad alti valori di OCR, e compattazione termica irreversibile in fase di riscaldamento a bassi valori di OCR. Deformazioni di espansione irreversibili sono osservate durante il primo ciclo termico ad alti valori di OCR, mentre il comportamento è reversibile durante i successivi cicli termici. L'aumento di temperatura induce una diminuzione della soglia di snervamento. Gli indici di compressibilità e di rigonfiamento non sono influenzati in modo significativo da variazioni termiche, mentre la consolidazione è piu rapida ad alta temperatura.

La ricerca sui processi chemo-meccanici evidenzia che la variazione di volume degli scisti durante l'imbibizione è legata alla suzione osmotica del fluido. Inoltre, un aumento della suzione osmotica a tensione constante induce lo sviluppo di cedimenti irreversibili, la cui entità dipende dalla storia di carico. Tuttavia, la compressibilità e il coefficiente di consolidazione dell'Opalinus Clay non sono influenzati in modo significativo dalla suzione osmotica. Un modello elasto-plastico chemo-meccanico è formulato, al fine di riprodurre il comportamento osservato.

La resistenza e la rigidezza dell'Opalinus Clay sono studiate attraverso lo svolgimento di test triassiali. I risultati permettono di ottenere informazioni sul comportamento anisotropo e dipendente dalla tensione efficace. Un modello costitutivo è formulato sulla base delle evidenze sperimentali. L'elasticità trasversalmente isotropa è considerata al fine di riprodurre la risposta del materiale. Inoltre, i parametri elastici sono definiti in funzione dalla tensione efficace. La possibilità di considerare anisotropia in termini di resitenza al taglio è inclusa nel modello. L'approccio costitutivo include l'introduzione del concetto di stato disturbato (DSC) per riprodurre il softening. Le simulazioni numeriche evidenziano la capacità del modello di riprodurre la principali caratteristiche reologiche dell'Opalinus Clay.

Parole chiave: Scisti, comportamento multifisico, Opalinus Clay, stoccaggio di scorie nucleari, geo-energia, comportamento di ritenzione, comportamento termo-meccanico, processi chemo-meccanici test triassiali, anisotropia, modello constitutivo.

List of symbols

	Greek symbols	
α	Biot coefficient	-
α_c	Radial thermal expansion coefficient of the oedometric cell	$°C^{-1}$
α_i	Internal variable	-
α_l	Linear thermal expansion coefficient	$°C^{-1}$
$\alpha_{measured}$	Measured thermal expansion coefficient	$°C^{-1}$
α_{oed}	Biot coefficient in oedometric conditions	-
α_s	Thermal expansion coefficient of the solid constituents	$°C^{-1}$
β	Plastic stiffness index	-
β_f	Fluid compressibility	Pa^{-1}
β_π	Osmotic stiffness modulus	Pa
$\beta_{\pi 0}$	Material parameter for evolution of the osmotic stiffness modulus	Pa
γ_π	Parameter describing the evolution of the vertical effective yield stress with osmotic suction	-
γ_T	Parameter describing the evolution of the vertical effective yield stress with temperature	-
γ_w	Specific weight of water	N/m^3
δ	Settlement	m
δ_{ij}	Kronecker delta	-
ε	Volumetric strain	-
ε_a	Axial strain	-
ε_r	Radial strain	-
ε_z	Vertical strain	-
ε_{ij}	Strain tensor	-
ε_{ij}^e	Elastic strain tensor	-
ε_{ij}^p	Plastic strain tensor	-
ε_{dev}^p	Deviatoric plastic strains	-
ε_v^p	Volumetric plastic strains	-
$\varepsilon_v^{p,m}$	Mechanical volumetric plastic strains	-
$\varepsilon_v^{p,\pi}$	Osmotic volumetric plastic strains	-
η	Angle of rotation about the y-axis	°
θ	Angle between the z- axis and the bedding planes	°

θ	Fluid content	-
θ_{nw}	Contact angle of non-wetting fluid	°
θ_w	Contact angle of wetting fluid	°
θ'	Angle between the loading direction and the bedding planes	°
$\theta'_{c\min}$	Angle between the loading direction and the anisotropic plane at which c' has the minimum value	°
$\theta'_{\phi\min}$	Angle between the loading direction and the anisotropic plane at which $\tan\phi'$ has the minimum value	°
λ	Fitting parameter for Van Genuchten's model	-
λ_d	Coefficient related to the specimen drainage conditions	-
λ_{iso}^{p}	Mechanical isotropic plastic multiplier	-
λ_{dev}^{p}	Mechanical deviatoric plastic multiplier	-
λ_{π}^{p}	Osmotic plastic multiplier	-
ν	Poisson's ratio	-
ν_{xy} or ν_1	Poisson's ratio parallel to the bedding planes	-
ν_{zx} or ν_2	Poisson's ratio perpendicular to the bedding planes	-
π	Osmotic suction	Pa
π_{c0}	Initial yield osmotic suction	Pa
π_h	Osmotic pressure head	m
π_0	Reference osmotic suction	Pa
ρ	Bulk density	g/m^3
ρ'	Primary consolidation settlement	m
ρ''	Secondary compression settlement	m
ρ_0	Settlement due to the deformation of the testing apparatus	m
ρ_b	Settlement of the testing device at time $t = t_b$	m
ρ_{bottom}	Displacement of the cell components below the specimen	m
ρ_c	Settlement of the testing device at time $t = t_c$	m
ρ_f	Fluid density	g/m^3
$\rho_{measured}$	Measured displacement by the LVDT	m
ρ_{plates}	Displacement of the porous plates	m
ρ_s	Solid particles density	g/m^3
ρ_{sp}	Displacement of the specimen	m
ρ_{top}	Displacement of the cell components above the specimen	m
ρ_{tot}	Total measured settlement	m
ρ_w	Water density	g/m^3
σ'_a	Axial effective stress	Pa
σ'_c	Vertical effective yield stress	Pa
σ'_{c0}	Reference vertical effective yield stress	Pa

σ_{ij}^{ob}	Observed stress tensor	Pa
σ_{ij}^{i}	Stress tensor for the intact part	Pa
σ_{ij}^{d}	Stress tensor for the fully adjusted part	Pa
σ_{kk}	Trace of the isotropic stress tensor	Pa
σ'_{kl}	Effective stress tensor	Pa
σ_{nw}	Surface tension of non-wetting fluid	N/m
σ'_r	Radial effective stress	Pa
σ_w	Surface tension of wetting fluid	N/m
σ_z	Vertical total stress	Pa
σ'_z *or* σ'_v	Vertical effective stress	Pa
σ_{zb}	Vertical total stress at time $t = t_b$	Pa
σ_{zc}	Vertical total stress at time $t = t_c$	Pa
τ	Shear stress	Pa
τ	Tortuosity	-
ϕ'_1	Friction angle	°
ϕ'_1	Effective friction angle	°
ϕ'_2	Effective friction angle	°
ϕ'_a	Model parameter	°
ϕ'_b	Model parameter	°
χ	Constrictivity	-
ψ	Total suction	Pa
ψ_e	Air entry value	Pa
ψ_{ref}	Fitting parameter for evolution law of void ratio with total suction	Pa
ω	Osmotic membrane efficiency	-

Roman symbols

A	Material parameter for evolution of the osmotic stiffness modulus	Pa
A_d	Model parameter for definition of the disturbance function	-
a	Material parameter for evolution of the bounding surface	-
a	Intercept of the strength envelope with the q- axis	Pa
B	Skempton pore water pressure coefficient	-
$B_{corrected}$	Corrected Skempton pore water pressure coefficient	-
B_{obs}	Measured Skempton pore water pressure coefficient	-
C	Oedometric pore water pressure coefficient	-
C_α	Secondary compression coefficient	-

C_c	Compression index	-
C_s	Swelling index	-
$C_{c,*}$	Intrinsic compression index	-
$C_{s,*}$	Intrinsic swelling index	-
c	Concentration of the pore fluid	M = mol/L
c'	Cohesion	Pa
c_{pq}	Cohesive component in p'-q plane	Pa
c'_a	Model parameter	Pa
c'_b	Model parameter	Pa
c_v	Coefficient of consolidation	m^2/s
D	Diffusion coefficient	m^2/s
D	Disturbance function	-
D_0	Fick's diffusion coefficient	m^2/s
D_e	Effective diffusion coefficient	m^2/s
D or D_{ijkl}	Stiffness matrix	Pa
D_u	Model parameter for definition of the disturbance function	-
d	Diameter	m
E_{oed}	Oedometric modulus	Pa
E_x or E_1	Young's modulus parallel to the bedding planes	Pa
E_z or E_2	Young's modulus perpendicular to the bedding planes	Pa
$E_{1\,ref}$	Reference Young's modulus parallel to the bedding planes	Pa
$E_{2\,ref}$	Reference Young's modulus perpendicular to the bedding planes	Pa
e	Void ratio	-
e_0	Reference void ratio	-
e_i	Initial void ratio	-
f_{iso}	Isotropic yield limit	-
f_{MC}	Mohr-Coulomb failure surface	-
$G_{2\,ref}$	Reference shear modulus	Pa
G_2	Shear modulus	Pa
G_s	Specific gravity of solids	-
g	Specific gravity	m/s^2
H	Drainage or diffusion path length	m
H_{oed}	Poroelastic constitutive constant	Pa
h	Total head	m
J_{2D}	Second invariant of the deviatoric stress tensor	Pa
K	Bulk modulus	Pa
K	Rotation matrix	-
K_0	Lateral stress ratio for one-dimensional compression	-
K_f	Bulk modulus of the pore fluid	Pa

K_{ref}	Fitting parameter for evolution law of void ratio with total suction	Pa
K_s	Bulk modulus of the solid phase	Pa
k_z	Coefficient of permeability in vertical direction	m/s
k	Coefficient of permeability	m/s
M	Mass of the material	g
M	Slope of the strength envelope	-
M_1	Slope of the failure surface	-
M_2	Slope of the failure surface	-
M_e	Entering fluid mass	g
M_{pow}	Mass of the shale powder	g
M_{res}	Fluid mass within the reservoir	g
M_s	Mass of the solids	g
M_w	Mass of water	g
m	Fitting parameter for evolution law of void ratio with total suction	-
m_π	Osmotic coefficient of volume change	Pa^{-1}
m_v	Coefficient of volume change	Pa^{-1}
m_ϕ	Model parameter	-
n	Porosity	-
n^d	Model parameter for definition of the disturbance function	-
n_{el}	Elastic exponent	-
n_{VG}	Fitting parameter for Van Genuchten's model	-
P	Pressure	Pa
P_f	Fluid pressure	Pa
P_{VG}	Fitting parameter for Van Genuchten's model	Pa
PI	Plasticity index	-
p	Mean stress	Pa
p'	Mean effective stress	Pa
p'_c	Mean effective yield stress	Pa
p'_{c0}	Reference mean effective yield stress	Pa
p'_{ref}	Reference mean effective stress	Pa
p'_{tr}	Threshold mean effective stress	Pa
q	Deviatoric stress	Pa
R	Universal gas constant	J / (K mol)
R_{oed}	Poroelastic constitutive constant	Pa
RH	Relative humidity	-
r_{dev}	Bounding surface deviatoric radius	-
r_{dev}^{el}	Initial value of the deviatoric radius	-
$r_{dev\,S}$	Value of r_{dev} for S- samples	-
$r_{dev\,S}^{el}$	Value of r_{dev}^{el} for S- samples	-

S_{ij}	Deviatoric stress tensor	Pa
S_r	Degree of saturation	-
SP	Swelling pressure	Pa
s	Matric suction	Pa
T	Temperature	°C
T_0	Reference temperature	°C
T	Time factor	-
T_{95}	Time factor at a degree of consolidation of 95%	-
T_b	Time factor at time $t = t_b$	-
T_c	Time factor at time $t = t_c$	-
t	Time	s
t_{95}	Time at a degree of consolidation of 95%	s
t_{100}	Time at the end of the primary consolidation	s
t_b	Time value describing evolution of the load over time	s
t_c	Time value describing evolution of the load over time	s
u	Pore water pressure	Pa
u_e	Excess pore water pressure	Pa
u_{ss}	Steady-state pore water pressure	Pa
V	Total volume	m^3
V_0 or V_i	Initial volume	m^3
V_L	Dead volume	m^3
V_{res}	Volume of the reservoir	m^3
V_s	Volume of the solid particles	m^3
V_v	Volume of voids	m^3
V_w	Volume of water	m^3
v	Number of constituent ions	-
v_c	Velocity of the ions	m/s
v_f	Fluid velocity	m/s
v_{rf}	Relative Fluid velocity	m/s
w	Water content	-
w_{fp}	Water content measured on filter paper	-
w_L	Liquid limit	-
w_P	Plastic limit	-
w_{pow}	Water content of the shale powder	-
Z	Model parameter for definition of the disturbance function	-
Z_S	Model parameter for definition of the disturbance function	-
z	Elevation head	m

Introduction

1. General background

The involvement of shales in energy-related fields such as the extraction of shale gas and shales oil, the deep geothermal energy recovery, the storage of CO_2 and the nuclear waste geological disposal, has raised a new and growing interest in the geomechanical behaviour of this geomaterial. Shales play different roles in the engineering applications mentioned above:

- Host formation for deep geological disposal of radioactive waste;
- Cap rock for CO_2 storage into deep aquifers;
- Reservoir formation for unconventional oil and gas extraction;
- Heat source for deep geothermal energy recovery.

In these contexts, fundamental issues come along with the complex multiphysical conditions in which the shale formation is found, where mechanics, temperature, chemistry and unsaturated conditions play a significant role. The involvement of shale formations in such advanced energy-related technologies is due not only to their large worldwide presence, but also to their peculiar features. In fact, shales are characterized by an intermediate behaviour between that of a soil and of a rock, unifying in a single geomaterial some relevant features of clayey soils (low porosity and permeability, swelling potential, retention properties) and of rocks (high strength and stiffness). These properties are fundamental for the good performance of the shale formation in all the mentioned energy-related applications:

- The low porosity (5-20%) and low permeability (1nD-1μD) ensure a good barrier function in the context of nuclear waste disposal and CO_2 storage;
- The good water retention properties provide the ability to trap gas and oil in the context of the unconventional recovery of shale gas and shale oil, to avoid the radionuclide migration in the context of nuclear waste disposal, and to prevent any leakage in the CO2 geological storage;
- The swelling potential ensures self-sealing capabilities in case of fractures creation;
- The high strength and stiffness allow the safe construction of underground structures.

However, shales properties can vary significantly from one formation to another. This fact is due to their very heterogeneous composition, to the fact that shale formations are found from shallow to great depths, and to the fact that they may or may not have experienced diagenetic processes, natural weathering or complex burial histories. Therefore, a shallow shale formation characterized by high clay content and having experienced little or no diagenesis would be classified as a soil-like geomaterial, while a very deep formation characterized by a high degree of cementation and no weathering would be better classified as a rock-like geomaterial (Underwood, 1967).

Consequently, any shale material which is to be involved in a new engineering application should be carefully studied in order to evaluate its performance in the expected multiphysical conditions, and to understand its behaviour during the different phases of the exploitation of the shale formation.

2. Context and objectives of the Thesis

The research conducted in this Thesis was financed by the National Cooperative for the Disposal of Radioactive Waste (Nagra), which is the Swiss organization for deep geological disposal of radioactive waste. This introductive section proposes a brief historical background and presents the motivation and objective of this PhD Thesis.

As of today nuclear power accounts for the 40% of the total production of electricity in Switzerland, while the remaining 60% derives from hydroelectric power (Zuidema, 2015). Five nuclear power plants are currently operating in Switzerland; however the position of the country regarding the nuclear energy production is marked by debates and uncertainties, which date back to the 1990, when a ten-year moratorium on the construction of new nuclear power plants in Switzerland was imposed. Subsequently, the Swiss government decided to continue relying on nuclear energy with the planned substitution of existing nuclear installations when exhausted, and with the construction of new ones, as officially stated by the Swiss government in February 2007. After the disaster of Fukushima in 2011, a review of the Swiss long-term energy strategy was initiated, and three options regarding the destiny of the nuclear energy in Switzerland were elaborated by the Swiss governments with the clear intention to go toward the end of this energy source. Such three options were stated as follows: (1) early closure of the nuclear power plants only if required by safety issues and subsequent construction of new nuclear power plants; (2) closure of the nuclear power plants at the end of their lifetime with no replacement; (3) early closure of the nuclear power plants with no new general authorization for new nuclear power plants. Option 2 constituted the official position of the Swiss Federal Council on 25 May 2011, which decided the progressive closure of the five existing nuclear power plants at the end of their operative life between 2019 and 2034. The decision was approved by the Parliament in June 2011. After the decision of the Swiss Federal Council, regulations concerning the management of the nuclear wastes were urgently needed, and a series of practical difficulties were encountered: no permanent nuclear waste geological repository was available, while only a number of secured temporary storage sites existed where a limited amount of wastes could have been stored. In fact, Nagra has estimated that the total volume of waste that would be produced by the five Swiss nuclear power plants and from medicine, industry and research would be approximate 100,000 cubic metres, which corresponds to the volume of the part of the main hall of Zürich railway station[1]. As a consequence, a series of operational stages were initiated in order to identify the geological areas in Switzerland where permanent repositories could be hosted and the most suitable sites for the deep geological storage of all categories of radioactive waste:

- High-level waste (HLW): fission products and spent fuel rods (SF) that are used to supply energy in nuclear power plants, it constitutes about the 3% of the total waste volume;
- Low- and Intermediate-level waste (L/ILW): wastes from medicine, industry and research, as well as reprocessed spent fuel elements (structural components); it constitutes about the 96% of the total waste volume.

[1] www.nagra.ch

The construction of two different repositories is therefore required: a high-level waste repository (HLW repository) for spent fuel (SF), vitrified high level waste (HLW) and long-lived intermediate-level waste (ILW); and a repository for low and intermediate-level waste (L/ILW repository). The procedure and criteria for the identification of the geological areas and of the most suitable sites has been specified by the Federal Government in the framework of the "Sectorial Plan for Deep Geological Repositories (SGT)"[2], and it is implemented by the work of the National Cooperative for the Disposal of Radioactive Waste (Nagra). In 2011 the first stage of the SGT concerning the identification of the most suitable regions for nuclear waste disposal was completed. Nagra identified six candidate siting regions for the L/ILW repository and three candidate siting regions for the HLW repository in November 2008; the Federal Council approved all the potential siting regions on the 30th November 2011, thus concluding the first stage of the site selection process and initiating the second stage. The selected potential regions are shown in Figure 1.

The second stage of the process is now underway, with the aim of reducing the number of the potential geological siting regions to at least two for each repository type, by comparing the regions with one another. The decisive criteria are long-term safety and engineering feasibility. Based on this comparative assessment, Nagra proposed that the regions Zürich Nordost (ZNO) and Jura Ost (JO) undergo further investigations in the third stage of the site selection process, and that the region Nördlich Lägern be placed in reserve. Following an open consultation phase, the decision of the Federal Council on the proposed geological siting regions is expected in 2018.

In the selected siting regions, the geological formation considered for the construction of the repository for nuclear waste disposal is the Opalinus Clay formation. Consequently, major interest was raised toward the study of the behaviour of this shale, as well as on the adjacent shale layers (i.e. Brown Dogger shale), when subjected to thermo-hydro-chemo-mechanical loads. In fact, complex phenomena involving mechanic, hydraulic, thermal and chemical issues shall be expected in the context of the nuclear waste disposal: mechanical issues are foreseen during the construction of the repository and the emplacement of the waste; hydraulic issues are expected mainly due to desaturation during repository construction and resaturation after closure of the repository; chemical loads may occur due to changes in the salinity of the pore fluid caused by the corrosion of the steel canister, by contamination from other fluid sources, or by significant variations in depth during the long-term storage. Finally thermal loads are expected during the emplacement of the heat emitting nuclear waste and after closure of the repository. The PhD work is developed in this context, with the aim of analysing, both from an experimental and constitutive point of view, the multiphysical behaviour of the shales involved in the geological disposal of radioactive waste in Switzerland.

[2] BFE (2008): Sachplan geologische Tiefenlager. Konzeptteil. Swiss Federal Office of Energy SFOE, Bern, Switzerland.

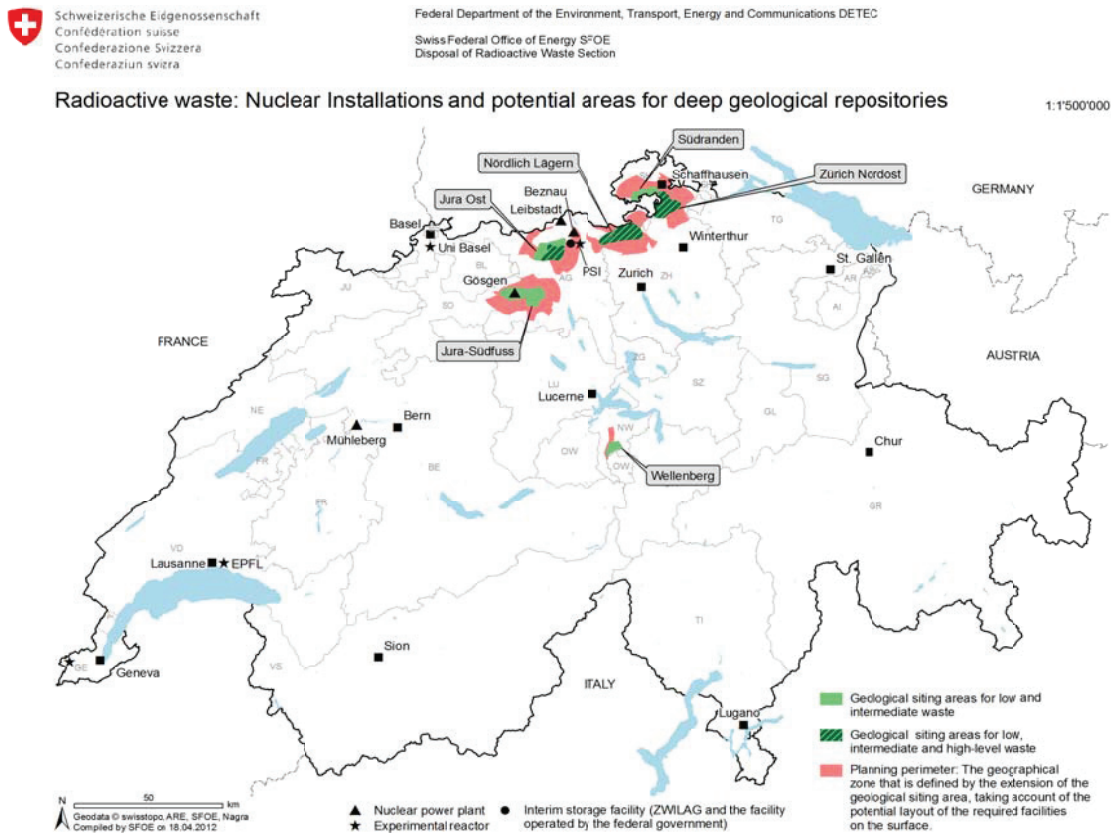

Figure 1: Nuclear installations and potential areas for deep geological repositories (IAEA, 2012).

3. Structure of the Thesis

As introduced in the previous section, the Thesis is devoted to the experimental study and constitutive analysis of the multiphysical behaviour of shales from Northern Switzerland, in the multiphysical context constituted by the emplacement of radioactive waste into a geological formation. Therefore this Thesis contributes to a better understanding and characterization of the behaviour of shales, extending the knowledge on their multiphysical response and elaborating constitutive laws to reproduce and predict their behaviour. The chapters of the Thesis are organized as follows:

Chapter 1 provides an overview of the tested shales, describing their origins, their locations and their characterization: the results of the geotechnical characterization of all the tested cores are presented. This chapter is often recalled throughout the Thesis, since the geologic history of the shales, their index properties, the dominant entrance pore size, and the mineralogical composition are fundamental aspects to be considered in the analysis of their multiphysical behaviour.

Chapter 2 is dedicated to the analysis of the water retention behaviour of selected cores from the studied shales. The goal is to provide a robust and complete experimental framework to investigate shale retention properties together with a detailed analysis of the results.

Chapter 3 addresses the one-dimensional compression and consolidation behaviour of Swiss shales both at natural and remoulded states. A comprehensive methodology, including experimental and analytical procedures to investigate the behaviour of shales during oedometric compression and consolidation is developed and presented. The chapter reports the analysis of results obtained on Opalinus Clay and Brown Dogger shales, in order to demonstrate the performance of the presented methodology. Further insights into the swelling behaviour of Opalinus Clay and on the permeability-void ratio relationship of the tested shales are also presented and discussed in this chapter.

Chapter 4 focuses on the thermo-mechanical volume change behaviour of Opalinus Clay, which is investigated in relation to different stress conditions and overconsolidation ratio (OCR) values. The impact of temperature on some hydro-mechanical properties of this material is also evaluated in the chapter. The results of a focused experimental campaign consisting in high-temperature/high-pressure oedometric tests are presented and analysed.

Chapter 5 investigates coupled chemo-mechanical processes in Opalinus Clay shale. It provides an insight into the chemo-osmotic effects on the volume change behaviour of Opalinus Clay shale and analyses the chemo-osmotic consolidation behaviour. The effect of the chemical loading on the mechanical properties and on the pore network evolution is also addressed. Based on the identified physical mechanisms, the research of this chapter addresses the development of a theoretical framework for reproducing and predicting the chemo-mechanical behaviour of shales.

Chapter 6 is dedicated to the analysis of the stiffness and strength behaviour of Opalinus Clay, taking into account the anisotropic features of this shale. To this purpose a series of triaxial tests have been carried out where different loading orientations with respect to the plane of anisotropy are considered.

Chapter 7 is dedicated to the formulation of a constitutive framework, which is developed in order to take into account the observed behavioural features of Opalinus Clay. The triaxial tests results presented in Chapter 6 are back-analysed in order to demonstrate the performance of the proposed framework.

The major outcomes of the seven chapters are summarized in the conclusions of the Thesis, where the possible further developments and future perspectives are also proposed.

4. References

Underwood, L.B. Classification and identification of shales. Journal of Soil Mechanics & Foundations Div (1967) 93: 97-116.

Zuidema, P. The Swiss waste management program. Progress in Nuclear Energy (2015) 84: 68-73.

IAEA (2012). Annual Report of the International Atomic Energy Agency.

Chapter 1
Tested Shales: Overview and Geotechnical Characterization

1.1. Foreword

Shales are among the most complex geomaterials in the Earth: their geologic history, their stratified structure and their intrinsic anisotropic behaviour are among the main factors that are responsible for this complexity. Shales are of sedimentary origin: they are formed through sediment deposition and diagenesis. These depositional and diagenetic processes produce the peculiar structure of shales, which is characterized by particles orientation, presence of depositional planes (called bedding planes), and fissile behaviour. The first part of this chapter provides an overview of the tested shales while the second part is devoted to the geotechnical characterization of the materials. This chapter will be often recalled through the thesis, since the geologic history of the tested shales, their index properties and mineralogical composition are fundamental aspects in the definition of their thermo-hydro-chemo-mechanical behaviour. The shale cores are defined here by specific names, each of the following chapters of the thesis will refer to the names of the involved shale cores as defined in this first chapter. A summary of all the tests carried out in this thesis and the shale cores used in each test is provided in Appendix A.

1.2. Overview of the tested shales

The shales studied in this thesis are presented in this section, which reports information regarding the geographic sites where the cores were retrieved, the research context in which they were obtained and the main characteristics of the formation in-situ such as depth and orientation of the bedding planes. The shales considered in this study come from two different sites: the Mont Terri Underground Rock Laboratory (URL) in north-western Switzerland and the Schlattingen site in the Swiss Molasse basin, close to the Schaffhausen area. The clay content of the material varies between 23% and 68%, while the void ratio varies between 0.10 and 0.23: such variations are mainly related to the geologic history of the material as well as to the mineralogical composition. The material presents anisotropic and fissile behaviour, which is typical of shales. The following sections provide a description of the shale formations considered at the two sites.

1.2.1. The Mont Terri Underground Rock Laboratory

The Mont Terri rock laboratory is an underground laboratory entirely constructed inside a shale formation called Opalinus Clay at about 300 m below ground (Figure 1-1). It is composed by about 600 m of galleries and niches where boreholes are drilled in order to carry out in-situ experiments and to provide cores for laboratory testing. The interest in the behaviour of Opalinus Clay is justified by the fact that this material is one of the shale formations considered, and the currently selected one, as host geomaterial for the construction of a deep geological repository for radioactive waste disposal in Switzerland.

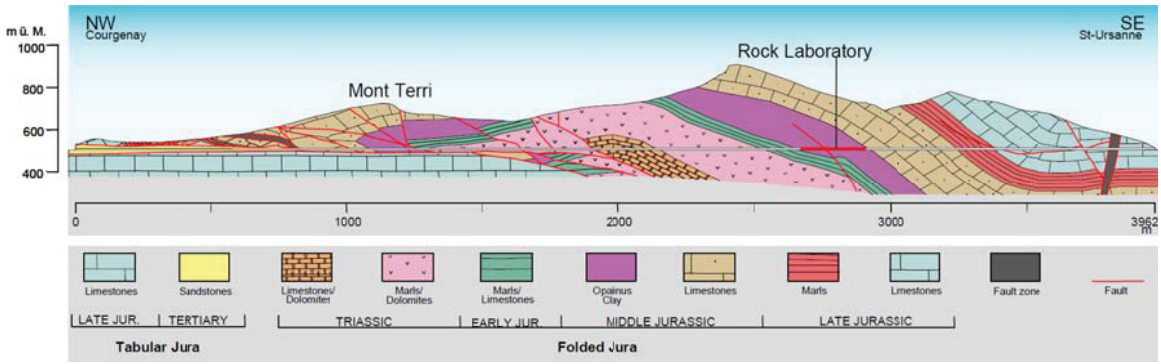

Figure 1-1: Location of the Mont Terri URL (Freivogel and Huggenberger, 2003).

The geological repository for spent fuel and high-level nuclear waste (HLW) would consist of two or three engineered barriers and one geological barrier: the high level radioactive waste (except for the spent fuel) is initially vitrified, thus the glass matrix constitutes a first engineered barrier; the system is then inserted into thick-walled metal containers, which form a second engineered barrier; finally the canister is placed on bentonite blocks and the tunnel is backfilled with bentonite granulate (third engineered barrier). Together with the overlying formations, Opalinus Clay constitutes the geological barrier (Figure 1-2). The repository for low- and intermediate-level waste (L-ILW) is also formed by three engineered barriers and one geological barrier following the same principle of the HLW repository; however, a special cementitious mortar is used as backfill material rather than bentonite.

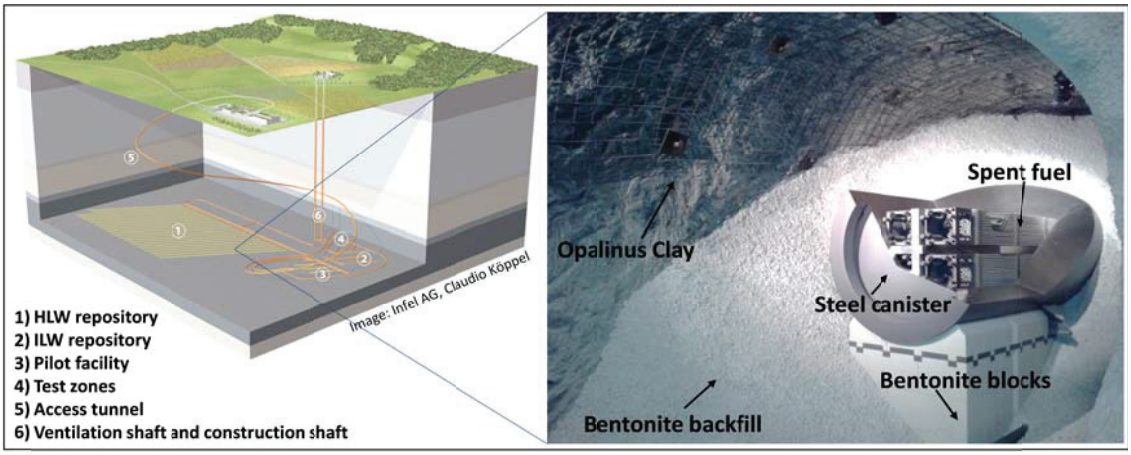

Figure 1-2: Deep geological repository concept for high level waste disposal in Switzerland.

Opalinus Clay is an argillaceous geomaterial classified as shale, which was formed approximately 174-170 million years ago in a marine environment, and which was subjected to burial, uplift and erosion processes (Gradstein et al., 2012; Nagra, 2014a). Opalinus Clay is thus a marine sediment, which consists of fine mud particles (Thury, 2002) and which was deposited uniformly over large areas of Northern Switzerland covering the Jura mountains, as well as the Swiss-German foreland basin from Lake Geneva to Lake Constance. The name “Opalinus” is due to the great presence of fossil shells of “Leioceras opalinum” ammonites which are named in this way because of their

shimmering (opalescent) lustre. Compared to other Mesozoic sediments in the area, Opalinus Clay is described as a homogeneous formation with only small vertical and lateral lithological variability. At a meter-scale some coarsening upward cycles with characteristic changes in grain size from clay to silt/sand particles are observed (Nagra, 2002; Nagra, 2014b). At Mont Terri, the formation presents three different facies (Bläsi et al., 1991) which result from different sedimentary environments:

- The shaly facies;
- The sandy facies;
- The carbonate-rich facies.

The shaly facies consists in dark grey silty calcareous shales and argillaceous marls (Figure 1-3a). It presents about 5-15% of quartz, 55-60% of silicates and 25-30% of carbonates together with other diagenetic minerals (such as pyrite and siderite). The sandy facies is composed of silty to sandy marls with sandstones lenses cemented with carbonate. The average composition consists in 25-30% of quartz, 10% of silicates, 55-60% of carbonate and other diagenetic minerals (Figure 1-3b). Finally the carbonate-rich facies is constituted of grey sandy and argillaceous limestones, intercalated with marly sandstones. It contains about 20-25% of quartz, 10-15% of silicates, 60% of carbonate and other diagenetic minerals (Bossart and Thury, 2008).

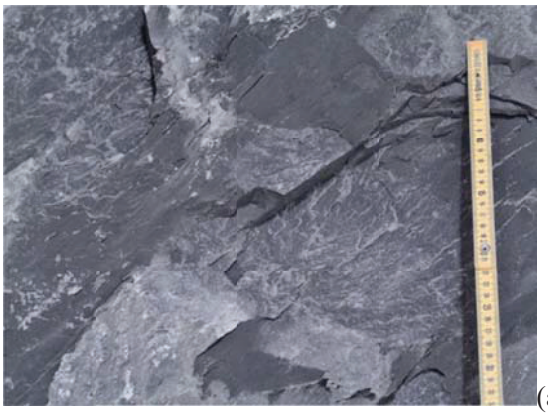
(a)

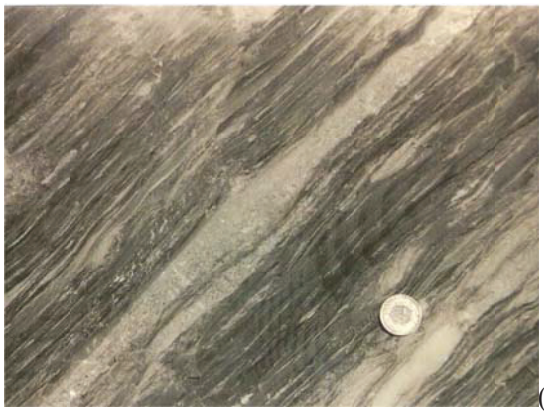
(b)

Figure 1-3: Opalinus Clay shaly facies (a); Opalinus Clay sandy facies (b) (Bossart and Thury, 2008).

The spatial disposition of the different facies is illustrated in Figure 1-4: the Opalinus Clay shaly facies represents the deeper part of the formation and it is overlaid by a 10-15 m thick carbonate-rich Opalinus Clay stratum. The sandy facies is located in the upper part of the formation and it is interstratified with the shaly facies. The entire Opalinus Clay formation is about 160 m thick and it dips towards the south-east with an angle of around 45 degrees. This inclination corresponds to the orientation of the bedding planes. A 1–3 m thick tectonic fault zone is also present in the centre of the formation and it is called “main fault”.

The Opalinus Clay formation in Mont Terri is nowadays found at about 300 m depth, however in the past it reached a depth of about 1200-1300 m; it is located in the Folded Jura, a zone where the Jura

fold-and-trust belt was subjected to intense deformation during the late Miocene (about 5-11 million year ago) (Giger et al., 2015). Nowadays, the Opalinus Clay formation is found in overconsolidated conditions. In this thesis, the Opalinus Clay cores retrieved from the Mont Terri URL are referred as OPA-shallow in order to distinguish them from the Opalinus Clay cores retrieved from greater depths and called OPA-deep. Four OPA-shallow cores from the shaly facies have been considered in order to carry out the experimental work reported in the thesis: the cores are named BHG-D1, BOP-A5, BFE-B and BDR-B7, and they have been retrieved from different niches and galleries of the underground laboratory. Figure 1-5 reports the names of the different niches and galleries which constitute the underground rock laboratory, while Figure 1-6 depicts a 3D reconstruction of the Mont Terri URL together with the exact location from where the studied shale cores were obtained. The laboratory is accessed through the security gallery of the Mont Terri tunnel of the A16 motorway, which passes through the Jura Mountains.

Core BHG-D1 was retrieved from the Gallery 98; here Opalinus Clay cores were extracted in order to carry out in-situ experiments on “gas transport in Opalinus Clay”. This experimental campaign was entitled HG-D and belongs to the Phase 15 of the Mont Terri Project. The “Mont Terri Project” identifies the ensemble of all the experimental phases – 22 as of today - carried out in the Mont Terri URL since 1996. The BHG-D1 core was delivered at the Laboratory for Soil Mechanics (LMS) at EPFL inside a black PVC tube, the core was retrieved at a distance of 3.0 m from the tunnel wall.

Core BOP-A5 was retrieved in the context of the in-situ and laboratory experiments entitled OP-A on the “osmotic effects in Opalinus Clay” which belong to the Phase 16 of the Mont Terri Project. It was retrieved from borehole BOP-A5, in the niche DR-A located in gallery 08. The borehole BOP-A5 reached a distance of 4.3 m from the tunnel wall. The core delivered at EPFL was stored in aluminium bags.

Several BFE-B cores were retrieved in the context of the “THM Full scale emplacement demonstration” experiment, which started in 2011 in the FE gallery. This 1:1 scale experiment has the aim of simulating both the heat generated by the decay of the radioactive waste and the weight of the waste container, through the emplacement of a heating element. The investigation will last several years to observe the long term behaviour of the backfill material and of the Opalinus Clay under the influence of temperature and saturation of the bentonite barrier. The results are expected to provide significant information on the feasibility of the nuclear waste repository. Six BFE-B cores were delivered at the Laboratory for Soil Mechanics at EPFL inside black PVC tubes filled with resin, and two of them (named BFE-B019 and BFE-B022) have been considered in this study.

Core BDR-B7 is the last core delivered at EPFL, it was retrieved in the context of the DR-B experimental campaign, which belongs to the phase 16 of the Mont Terri project, and which has the aim of investigating the long term diffusion processes in Opalinus Clay. Borehole BDR-B7 was drilled perpendicular to bedding in gallery 08 between niche DR-A and MB. The tested samples were cored from a distance of about 18 m from the tunnel wall. As in the previous case, the core was delivered at EPFL inside black PVC tubes filled with resin.

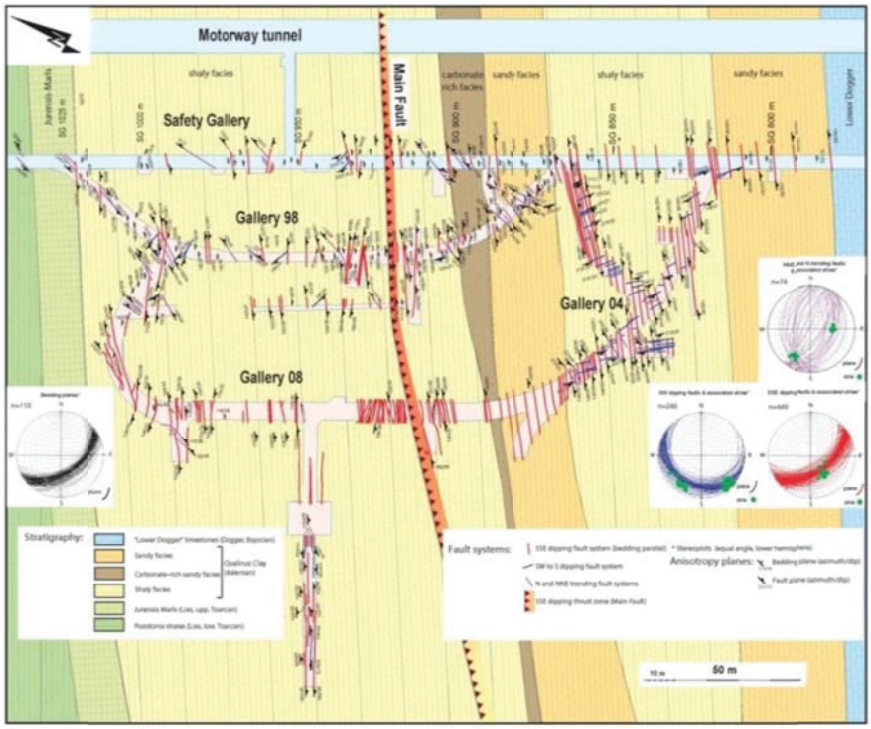

Figure 1-4: Structural map of Opalinus Clay at Mont Terri (Office fédérale de topographie Swisstopo).

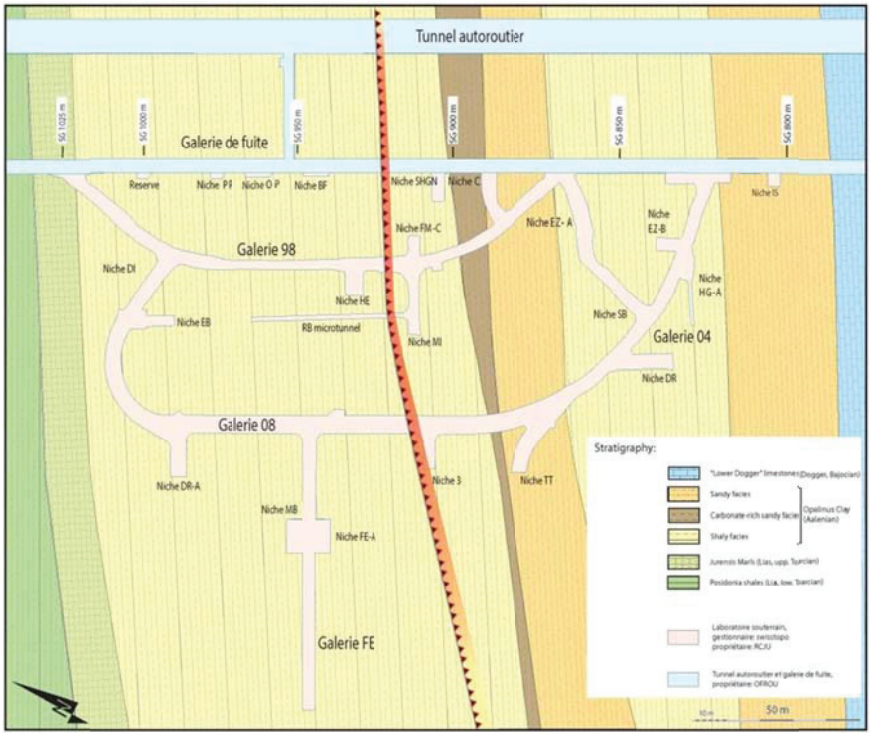

Figure 1-5: Geological map of the Opalinus Clay at Mont Terri with specification of the different Niche (Office fédérale de topographie Swisstopo).

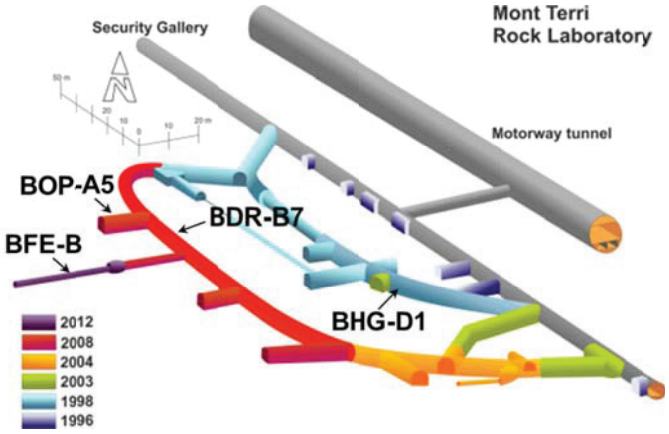

Figure 1-6: 3D reconstruction of Mont Terri URL and location of Opalinus Clay cores (modified from[1]).

When shale cores have to be retrieved for laboratory testing, it is important to take into account the possible impact of desaturation due to excavation and ventilation at the tunnels walls. Specific investigations have been carried out on OPA-shallow samples coming from the FE gallery in order to analyse the impact of ventilation on the water content of the material in relation to the distance from the tunnel wall (Ferrari and Dubey, 2013). The results highlight that the material experiences desaturation due to ventilation up to a distance of about 40 cm from the tunnel wall (Figure 1-7). Therefore, it is important to underline the fact that all the cores considered in this study have been retrieved at a distance from the tunnel wall greater than 40 cm.

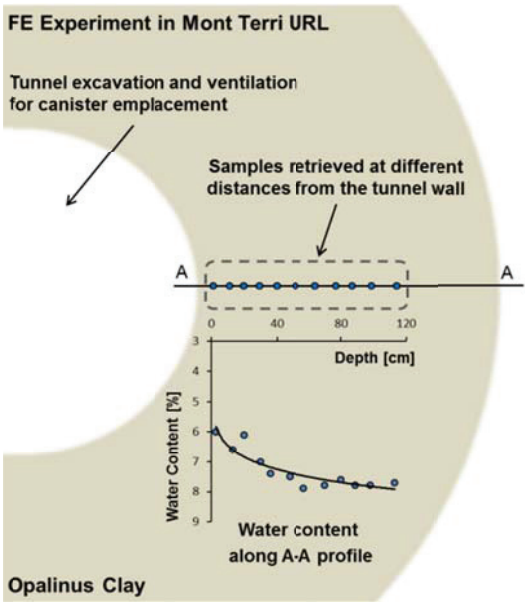

Figure 1-7: Impact of excavation and ventilation of the tunnel on the water content of the material (Ferrari and Dubey, 2013).

[1] www.mont-terri.ch

When accurate experimental investigations are sought, it is important to take into account possible shale-fluid interaction phenomena. The use of a pore fluid reproducing the in-situ pore water composition is strictly necessary to obtain sounded experimental evidences. The in-situ pore water chemical composition at the Mont Terri site has been analysed (Pearson, 1998) with the aim of producing a synthetic water having the same chemical composition. The chemical composition of the artificial pore fluid used in the laboratory experiments is reported in Table 1-1.

Table 1-1: Composition of the artificial pore water for the Mont Terri site (Pearson, 1998).

Salt	Grams anhydrous salt per litre of pure water
KCl	0.109
MgCl2	1.704
CaCl2	1.754
SrCl2	0.074
NaBr	3.035
Na2SO4	2.088
NaHCO3	0.048

1.2.2. The Schlattingen Site

The deep shale cores considered in this PhD thesis have been retrieved at the Schlattingen site, in the Swiss Molasse Basin (Figure 1-8). A deep geothermal well named SLA-1 was drilled 1508 m below ground with the purpose of carrying out investigation on the geothermal energy production for an economical and CO_2-emission-free operation of greenhouses. The drilling of borehole SLA-1 was accompanied by an extensive site characterization program, including lithostratigraphic and structural mapping of the cores and water sampling. The stratigraphic profile of the borehole is shown in Figure 1-9.

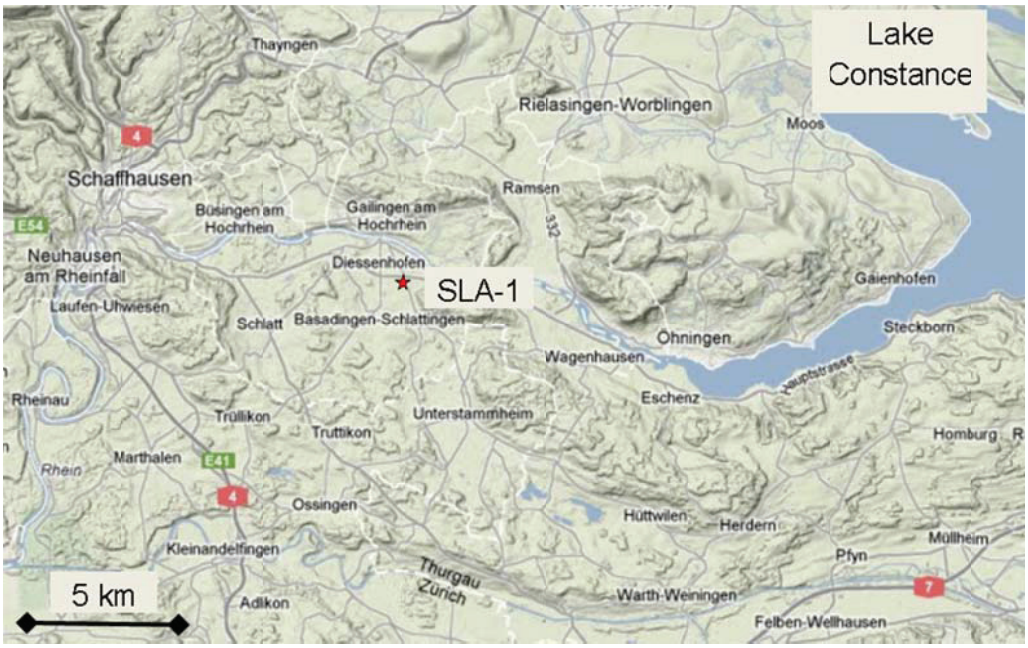

Figure 1-8: Topographic map of the location of the geothermal well in Schlattingen (Ferrari et al., 2013).

A total of eleven cores were retrieved from the Schlattingen site using air as cutting fluid, and they are considered for geomechanical characterization. Five cores were retrieved from the Opalinus Clay formation at a depth between 837.44 m and 891.25 m, while six cores were obtained from the overlaying "Brown Dogger" formation at a depth between 766.70 m and 807.44 m. The Opalinus Clay formation in Schlattingen is located in the Tabular Jura, a zone which underwent less deformation during late Miocene with respect to the Folded Jura. The maximum depth experienced by the Opalinus Clay formation is about 1700 m. The "Brown Dogger" formation consists in clay to argillaceous marls and calcareous marls; it was deposited about 175-160 million years ago.

All the cores were stored in PVC tubes filled with a layer of resin and constrained with metal frames immediately after the coring. Each core was given a name corresponding to a well-defined depth. The complete list of cores with the corresponding depth and lithology is reported in Table 1-2. In an analogous way with respect to the Mont Terri pore water, the in-situ pore water composition has been

analysed also in this site (Traber, 2011), with the aim of producing a synthetic water having the same chemical composition. The chemical composition of this artificial pore fluid used in the laboratory experiments is reported in Table 1-3.

Table 1-2: Shale cores retrieved from the Schlattingen site.

Name	Depth [m]	Lithology
BD-6	766.67 - 767.00	Clay to Argillaceous Marl
BD-16	769.55 - 769.85	Clay to Argillaceous Marl
BD-18	774.95 - 775.16	Clay to Argillaceous Marl
BD-12	778.30 - 778.52	Argillaceous Marl
BD-7	781.18 - 781.48	Calcareous Marl
BD-30	807.14 - 807.44	Calcareous Marl
OPA-3	837.44 - 837.66	Clay to Argillaceous Marlstone
OPA-2	837.98 - 838.25	Claystone
OPA-20	854.60 - 854.82	Claystone
OPA-6	882.20 - 882.50	Claystone with fine-sandy layers (ca. 1 mm)
OPA-18	891.00 - 891.25	Claystone with sandy layers

Table 1-3: Composition of the artificial pore water for the Schlattingen site (Traber, 2011).

Cationic component	$mmol/kg_{H2O}$	Mg/kg_{H2O}	Anionic component	$mmol/kg_{H2O}$	Mg/kg_{H2O}
Na	163.8	3765.7	Cl	169.0	5672.5
K	2.551	99.75	SO_4	24.00	2305.5
Ca	11.91	477.4	HCO_3	0.5431	33.14
Mg	9.166	222.8			

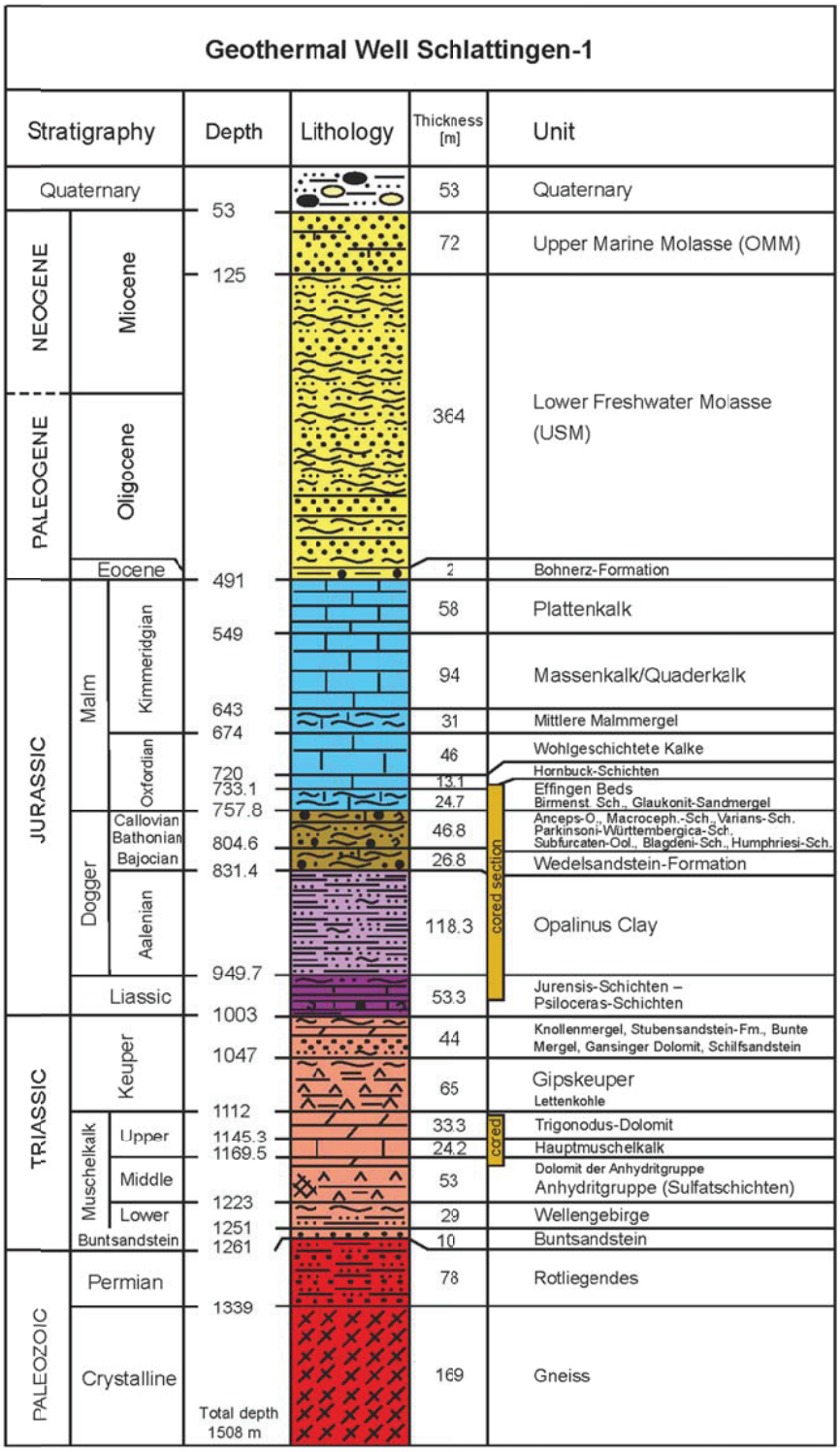

Figure 1-9: Stratigraphy of the geothermal well SLA -1 in the Schlattingen site (Albert et al., 2012).

1.3. Geotechnical characterization

This section presents a comprehensive description of the methodologies and of the results concerning the geotechnical characterization of the tested shales. Due to the lack of standard procedures for shales, several efforts were put into the elaboration of suitable protocols for the geotechnical characterization. The workflow includes the determination of index properties, the classification of the material based on the determination of the Atterberg limits, the grains size distribution and the pore size distribution. Selected core samples were subjected to the different phases of the workflow: Table 1-4 reports the complete list of the tested cores and of the selected tests carried out on them.

Table 1-4: Selected tests carried out on the cores in the context of the geotechnical characterization.

Cores	*Index properties*	*Atterberg limits*	*Grain size distribution*	*MIP tests*
Opalinus Clay – shallow				
BHG-D1	x	x	x	x
BOP-A5	x			
BFE-B cores	x			
BDR-B7	x			
Opalinus Clay - deep				
OPA-3	x	x	x	x
OPA-2	x	x	x	
OPA-20	x	x	x	
OPA-6	x	x	x	
OPA-18	x	x	x	
Brown Dogger				
BD-6	x	x	x	x
BD-16	x	x	x	x
BD-18	x	x	x	
BD-12	x	x	x	
BD-7	x	x	x	x
BD-30	x	x	x	x

The mineralogical composition of three cores belonging to OPA-shallow, of all the cores belonging to OPA-deep and of the BD shale cores was determined by XRD analysis at the Institute of Geological Science at the University of Bern (Ferrari et al., 2013). The available information on the mineralogical composition of the shales is reported in section 1.3.4.

1.3.1. Index properties

This section reports the determination of the index properties of the tested cores, which include:

- Solid particles density (ρ_s);
- Bulk density (ρ);
- Water content (w);
- Void ratio (e);
- Degree of saturation (S_r);
- Atterberg limits (w_L, w_P) and plasticity index (PI).

The determination of the Atterberg limits and of the plasticity index allows to classify the material through the use of the plasticity chart, as well as to quantify the activity of the shales. The detailed procedures for the determination of the index properties are described in the following sections. The resulting index properties are summarized in Table 1-5 for the shale cores retrieved at the Mont Terri site, while Table 1-6 reports the results for the shale cores retrieved at the Schlattingen site.

Table 1-5: Index Properties of the cores from the Mont Terri site.

Core	*Bedding orientation*	ρ_s (Mg/m^3)	ρ (Mg/m^3)	w (%)	e (-)	S_r (%)	w_L (%)	w_P (%)	PI (%)
BHG-D1	S	2.75	2.46	6.9	0.21	90	38	23	15
BOP-A5	S	2.76	2.46	7.5	0.21	99	-	-	-
BFE-B019	P	2.73	2.44	7.4	0.20	96	-	-	-
BFE-B022	P	2.78	2.44	7.7	0.23	94	-	-	-
BDR-B7	S	2.72	2.42	7.6	0.21	99	-	-	-

Table 1-6: Index Properties of the cores from the Schlattingen site.

Core	*Depth* (m)	ρ_s (Mg/m^3)	ρ (Mg/m^3)	w (%)	e (-)	S_r (%)	w_L (%)	w_P (%)	PI (%)
Opalinus Clay - deep									
OPA-3	837.44 - 837.66	2.74	2.49	4.3	0.15	80	39	22	17
OPA-2	837.98 - 838.25	2.71	2.49	4.9	0.14	94	36	25	11
OPA-20	854.60 - 854.82	2.72	2.55	3.6	0.11	93	31	22	9
OPA-6	882.20 - 882.50	2.71	2.56	3.3	0.10	94	29	19	10
OPA-18	891.00 - 891.25	2.70	2.54	3.6	0.10	96	33	19	13
Brown Dogger									
BD-6	766.67 - 767.00	2.75	2.56	2.7	0.10	72	25	22	3
BD-16	769.55 - 769.85	2.76	2.56	2.7	0.11	69	25	18	7
BD-18	774.95 - 775.16	2.74	2.55	3.2	0.11	81	25	19	6
BD-12	778.30 - 778.52	2.72	2.55	3.5	0.10	92	29	23	6
BD-7	781.18 - 781.48	2.70	2.52	4.4	0.12	100	33	21	12
BD-30	807.14 - 807.44	2.75	2.56	2.9	0.11	76	27	10	17

The orientation of the bedding with respect to the coring direction is specified for the OPA-shallow cores (Mont Terri), while no specification is required for the OPA-deep cores (Schlattingen) as they are all cored perpendicular to the bedding direction. The following nomenclature is used: "S-sample" identifies the material cored perpendicular to the bedding direction, while "P-sample" corresponds to the material cored parallel to the bedding direction (Figure 1-10).

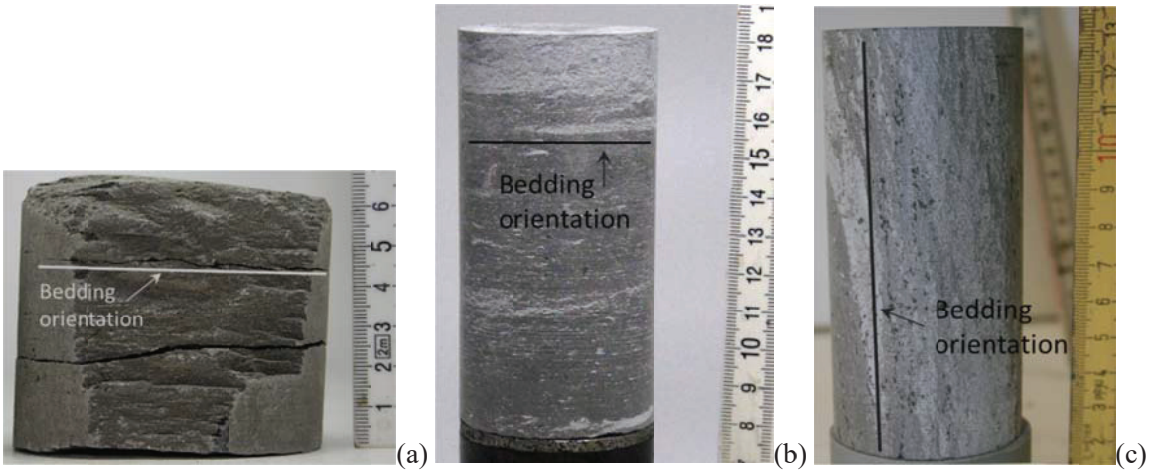

(a) (b) (c)

Figure 1-10: S-sample (BOP-A5) (a); S-sample (BDR-B7) (b); P-sample (BFE-B022) (c).

1.3.1.1. Solid particles density

The solid particles density (ρ_s) is defined as the ratio of the solid phase mass (M_s) to the volume of the solid phase (V_s). In order to determine the solid particles density, the material was preliminary crushed and passed through an ASTM No. 35 sieve (with aperture diameter d = 500 μm). The solid particles density of the deep shales coming from the Schlattingen site was first determined; the Swiss Norm 670335a was followed: it consists in the application of the Pycnometer method on the material preliminary oven-dried at 105 °C. The subsequent determination of the solid particles density of Opalinus Clay cores retrieved from the Mont Terri URL was carried out according to the ASTM D854-10 (Standard Test Methods for Specific Gravity of Soil Solids by Water Pycnometer). The American Standards suggest to oven-dry the material after the Pycnometer test, in order to determine the water content. The procedure suggested by the Swiss norm induces a slight underestimation (2%) of the particle density, with respect to the procedure suggested in the ASTM standards. Overall, the obtained results are considered to be comparable.

1.3.1.2. Bulk density

The bulk density (ρ) is defined as the ratio of the mass of the material (M) to its total volume (V); it was determined according to the water displacement principle and the SN 670335a.

$$\rho = \frac{M}{V} \tag{1.1}$$

The measurements were carried out on shales slices cut from the delivered cores and having a thickness of 3 - 5 cm. The slices were immersed in a melted paraffin bath in order to apply two wax coats; the weight of the slices before and after the application of the wax coats was measured. The waxed specimens were then immersed in the water displacement apparatus and their volume was obtained by measuring the weight of the overflowed water, taking into account the volume of the applied paraffin whose density is known.

1.3.1.3. Water content

The water content (w) is defined as the ratio of the mass of water (M_w) to the mass of the solid phase (M_s):

$$w = \frac{M_w}{M_s} \tag{1.2}$$

The water content was determined by oven-drying the material at 105 °C for 24 hours according to the SN 670340b. Drying the material for longer time does not affect the result as shown in Figure 1-11: the measured mass of an OPA-shallow sample does not change significantly after 24 hours or 48 hours in the oven.

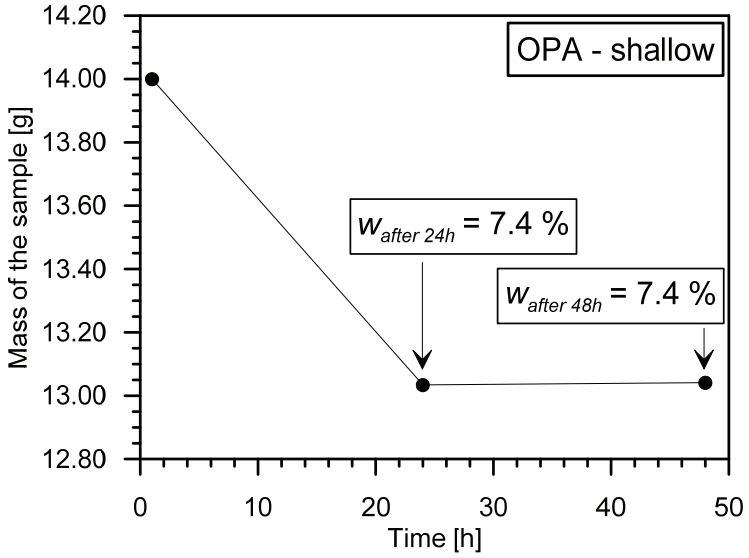

Figure 1-11: Mass variation of an OPA-shallow sample after 24 hours and 48 hours of oven-drying.

1.3.1.4. Void ratio

The void ratio (e) is defined as the ratio of the volume of voids to the volume of the solid phase. The void ratio was computed according to the following relationship:

$$e = \rho_s \frac{(1+w)}{\rho} \tag{1.3}$$

1.3.1.5. Degree of saturation

The degree of saturation (S_r) is defined as the ratio of the volume of water to the volume of voids. The degree of saturation was computed according to the following relationship:

$$S_r = \frac{\rho_s w}{\rho_w e} \tag{1.4}$$

where ρ_w is the density of water at a temperature of 23 °C.

1.3.1.6. Atterberg limits

The determination of the liquid and plastic limits and the subsequent computation of the plasticity index allow the classification of the material according to the SN 670008a and to the ASTM D2487-11, where the information regarding the liquid limit and the plasticity index is inserted in the plasticity chart (Figure 1-12). The A-line represents the empirical boundary between inorganic clays (CL-CH), which are found above the A-line, and plastic organic soils (OL-OH) which are located below such line. Inorganic silts (ML-MH) are found below the A-line, however, in case the liquid limit is lower than 30%, low plasticity inorganic silts (ML) may also be found above the A-line. The studied shales are classified according to the SN 670004-2a, they are observed to fall very close to the A-line. Opalinus Clay is mainly classified as medium plasticity lean clay with a tendency toward the range of low plasticity silty clays with sand for the OPA-deep. The OPA-deep cores displaying greater plasticity are OPA-3 and OPA-2, which present significantly less quartz and greater clay content according to the mineralogical composition (section 1.3.4); OPA-6 is the core presenting less plasticity. Brown Dogger appears to have lower plasticity with respect to Opalinus Clay, in agreement with the lower clay content highlighted in the mineralogical analysis (section 1.3.4). Brown Dogger is classified mainly as clayey silt with sand, with a tendency toward lean clays and silty clays regions for the deeper cores (BD-7 and BD-30, respectively), which are at the border with the Opalinus Clay formation, while the shallower core (BD-6) seems to fall in the category of silt.

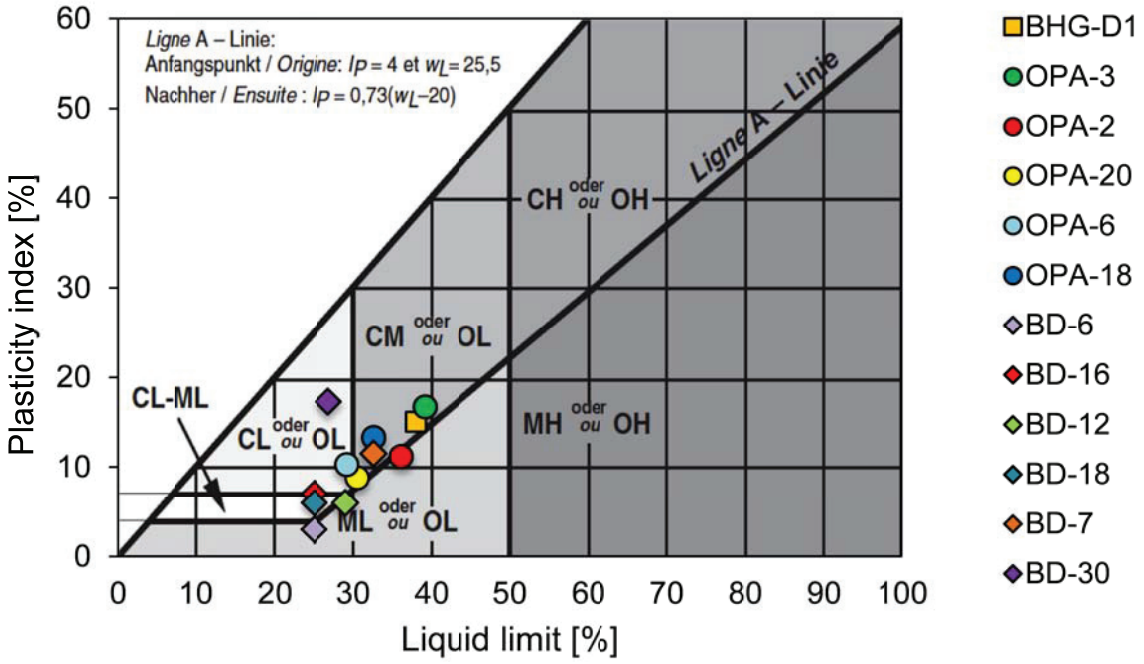

Figure 1-12: Plasticity chart.

Soil classification implies the sorting of different materials into groups which exhibit similar behaviour; such procedure is empirical and developed through experience (Lambe and Whitman, 1979). It is useful in order to guide the elaboration of testing programs, since relations between the position on the plasticity chart and some physical properties have been raised by the experience (Casagrande, 1948). Even though soil classification by the determination of the Atterberg limits has proved to be a useful tool for engineers, since it provides guidance, it involves the disturbance of the material, erasing the contribution of fabric and bonds between particles. Fabric and bonds may play a significant role in determining the behaviour of the material at the natural state (Lambe and Whitman, 1979); this concept will be further analysed in Chapter 3 of this thesis.

Moreover, Atterberg limits are useful for the determination of the Activity of the material, which is a quantity defined by Skempton (1953) as follows:

$$Activity = \frac{Plasticity\ Index}{\%\ by\ weight\ finer\ than\ 2\ \mu m} \tag{1.5}$$

The concept of activity is based on the idea that the decrease in particle size corresponds to an increase in surface area per mass; therefore, the amount of attracted water is related to the amount of clay size fraction present in the material. The greater the activity, the more important the influence of the clay size fraction on the material properties and the more susceptible the value of such properties to changes in pore fluid composition. In order to compute the activity of the studied shales, the determination of the clay size fraction is necessary (see section 1.3.2).

The results in terms of activity are reported in Figure 1-13 for the studied shales and compared to other materials having different clay size fractions and plasticity index.

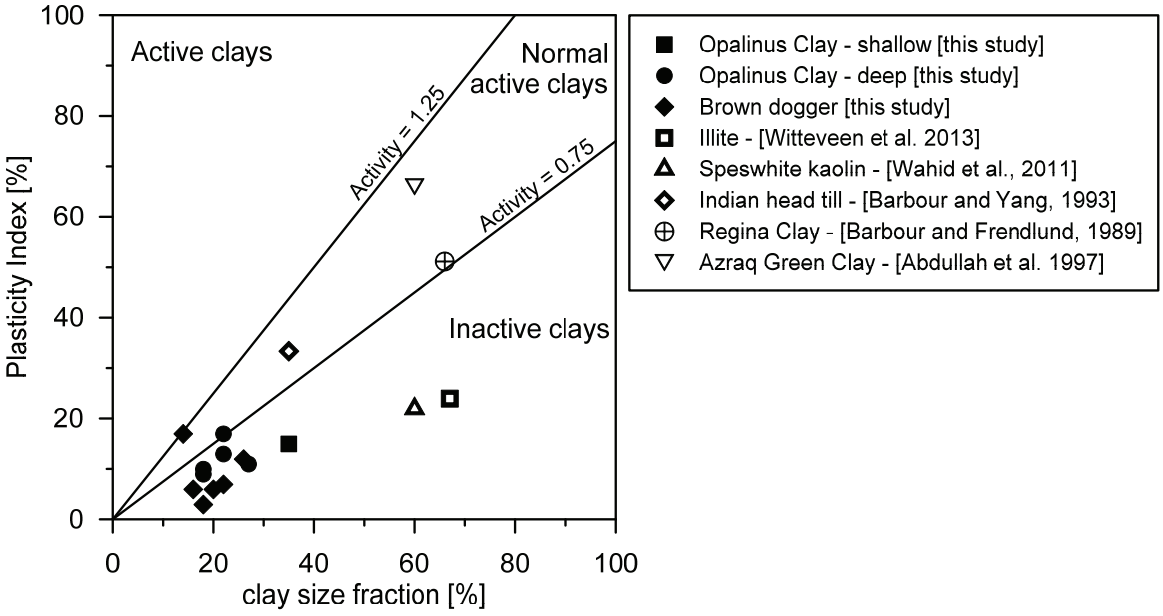

Figure 1-13: Relationship between plasticity index and clay size fraction.

The investigated shales manifest mainly activity lower than 0.75 falling in the category of inactive materials. The result is in good agreement with the mineralogical composition of the material reported in Bossart (2012) which shows that majority of the clay minerals consist in non-active clays such as kaolinite (activity between 0.33 and 0.46 (Skempton, 1953)). The low activity of the material provides a first indication of the fact that variation in pore fluid composition may have a relatively moderate impact on the hydro-mechanical properties of the material. However, since this statement derives from empirical knowledge and is based on the analysis of highly disturbed material, further insight will be carried out to quantify the impact of pore fluid composition on hydro-mechanical properties of the shales (Chapter 5 of this thesis).

1.3.2. Grain size distribution

The grain size distribution describes the distribution of the particles dimensions in a geomaterial; it consists in plotting the percentage finer by weight with respect to the diameter. When the size of a soil particle has to be described it is possible to cite either the dimension or, in alternative, a name which describe a certain size range and which has arbitrary assigned to it (Lambe and Whitman, 1979). The particles having a diameter between 2 mm and 60 μm are defined as sand, the particles having a diameter between 60 μm and 2 μm are defined as silt, while particles having a diameter smaller than 2 μm are defined as clay. However this type of nomenclature may raise confusion; it is considered more appropriate to use "sand sized particle", "silt sized particle" or "clay sized particle" rather than "sand", "silt" or "clay" to denote a certain particle dimension, since "sand", "silt" and "clay" should be merely used to denote soils having the corresponding physical characteristics (Casagrande, 1948).

In the context of the thesis the determination of the grain size distribution of the tested shales was relevant for different reasons. The grains size distribution provides a first indication of the differences between units coming from the same geological site (Opalinus Clay and Brown Dogger from the Schlattingen site) in terms of particles size. The evaluation of the colloidal activity of the material (section 1.3.1.6) requires the determination of the percentage by weight of the particles finer than 2 μm. Finally the determination of the grain size distribution of the Opalinus Clay coming from Mont Terri is particularly useful to compare and distinguish the different facies of the material which are characterized by significantly different compositions and particle sizes as discussed is section 1.2.1.

The grain size distribution was obtained by sedimentation analysis following the SN 670816. In order to carry out the sedimentation analysis, the material was initially crushed by means of a grinder and the fraction passing a 0.5 mm sieve (ASTM 35) was selected (Figure 1-14). The crushed material was placed in distilled water along with a dispersing agent (Tetrasodium pyrophosphate $Na_4P_2O_7$) and shaken overnight for 12 hours (Ferrari and Laloui, 2013). The effect of a longer shaking time has been taken into consideration and it has shown negligible effects on the final results (Figure 1-15).

Figure 1-14: Crushing of the material for the determination of the grain size distribution.

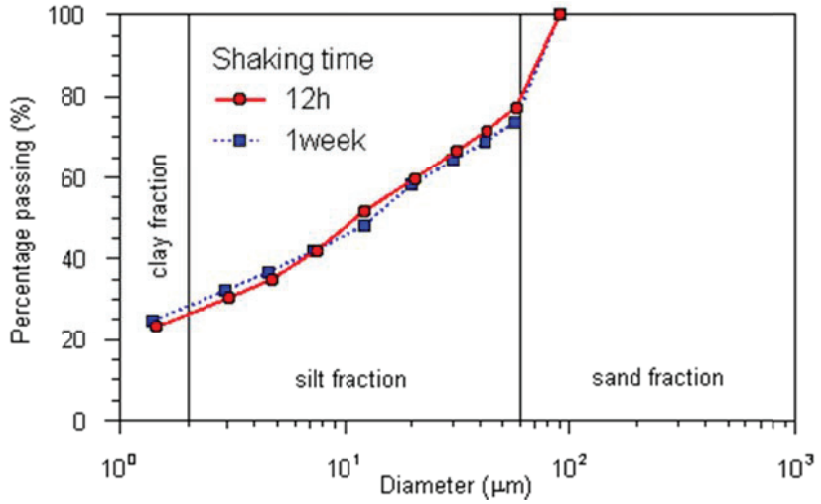

Figure 1-15: Evaluation of the impact of different shaking time on the grain size distribution.

The grain size distributions are reported in Figure 1-16 for all the tested shales. The figure shows that the obtained curves are situated on the left of the maximum dimension of the selected material; this observation confirms that the material does not present particles with a diameter larger than the maximum dimension of the crushed blocks, therefore it validates the procedure selected for the preparation of the sedimentation analysis.

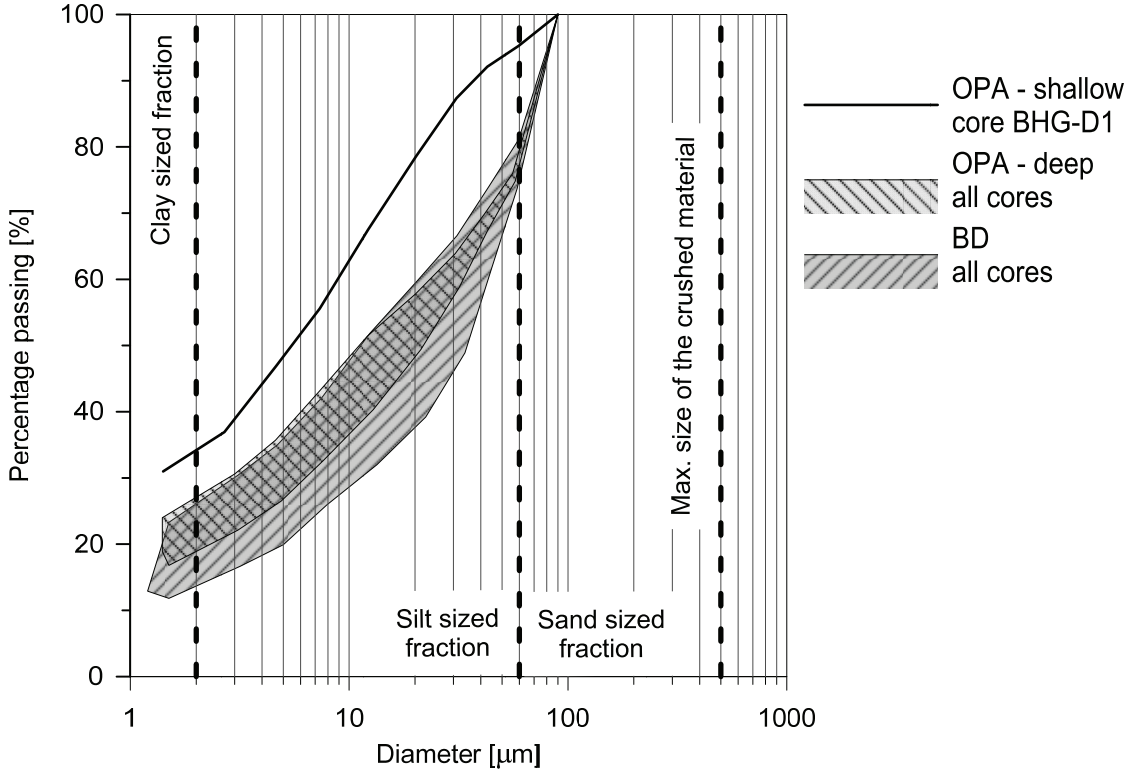

Figure 1-16: Grain size distributions of the tested shales.

The Opalinus Clay found at shallower depth presents a greater fraction of fine with respect to the same formation found at greater depth. This is probably due to the lower amount of quartz present in the OPA-shallow shaly facies cores with respect to the OPA-deep. However, the different grain size distribution may also reveal information on the geomechanical behaviour of the material: higher grain sizes might suggest a higher presence of true cohesive bonding, less plasticity and consequently a greater strength and stiffness of the material. The analysis of the grain size distribution is thus fundamental to obtain an initial possible estimation of the different expected properties of the tested cores. As to the deeper shales, the results highlight that the Brown Dogger has, on average, a lower fraction of fine particles compared to the Opalinus Clay.

1.3.3. Pore size distribution

Mercury Intrusion Porosimetry (MIP) tests were carried out in order to determine the Pore Size Distribution (PSD) for selected cores of the tested shales. The MIP technique consists in forcing the penetration of mercury inside a specimen and measuring the intruded volume of mercury as a function of the applied pressure. The applied pressure is inversely proportional to the size of the pores that are filled progressively by the mercury. Washburn equation relates the applied pressure (P) to the equivalent diameter (d, assuming a circular shape for the pores) of the intruded porosity:

$$d = -\frac{4\sigma_{nw}\cos\theta_{nw}}{P} \tag{1.6}$$

where σ_{nw} is the surface tension equal to 0.486 N/m at 23 °C, and θ_{nw} is the contact angle of the mercury equal to 142° (values between 139° and 147° are usually assumed for clayey materials; (Diamond, 1970)). Samples were cut from the original cores by means of a saw; dimensions of about 8 mm in width and 18 mm in height were selected in order to allow the specimens to easily fit inside the dilatometer. The tests were conducted on freeze-dried specimens by sublimation inside a vacuum chamber at 0.06 mbar and -50 °C for 24 hours. The freeze-drying technique allows to limit as much as possible the disturbance of the microstructure due to the removal of water from the specimen. MIP tests were performed in a Thermo Electron Corporations Porosimeter that attains a maximum intrusion pressure of 400 MPa (the corresponding minimum entrance pore size diameter is about 4 nm). After the maximum pressure was reached, the pressure was progressively reduced and the extruded mercury volume was registered. Apparent pore sizes were determined by applying corrections for compressibility changes of the various components of the equipment.

The pore size density function (PSD) is the derivative of the cumulated intruded void ratio with respect to the logarithmic of the entrance pore diameter:

$$PSD = \frac{\Delta e_{HG}}{\Delta \log d} \tag{1.7}$$

where d is the entrance pore size and e_{HG} represents the void ratio intruded at each increment of the mercury pressure. The cores selected for the pore size distribution analysis are reported in Table 1-7.

Table 1-7: Shale cores selected for MIP tests.

Shale	Cores
Opalinus Clay - shallow	BHG-D1
Opalinus Clay - deep	OPA-3
Brown Dogger	BD-6, BD-16, BD-7, BD-30

The results of the MIP tests for all the considered cores are depicted in Figure 1-17 in terms of pore size density function versus the equivalent entrance pore diameter. Unimodal PSD functions are found for all the tested shales. The entrance pore mode is at approximately 20 nm for the OPA-shallow while it is found at 8 nm for the OPA-deep. The entrance pore size for the BD specimens is in the range between 14 and 30 nm. The greater entrance pore mode observed for the OPA-shallow with respect to OPA-deep is in line with the significantly greater porosity of the former with respect to the latter. The lower entrance pore diameter for OPA-deep with respect to BD, in spite of the higher porosity, can be justified by considering the lower quartz content registered for the former (section 1.3.4); this reduced quartz content may imply a reduced amount of larger pores formed at the contact between the clay particles and the coarser grains (Keller et al., 2013). The results in terms of entrance pore diameter at the peak of the PSD function are reported in Table 1-8.

The shape of the PSD functions of the tested shales reveals significant information: the PSD functions are relatively flat on the right side of the curve, suggesting that the non-detected porosity (pores larger than the maximum pore size measured in an MIP test) is negligible.

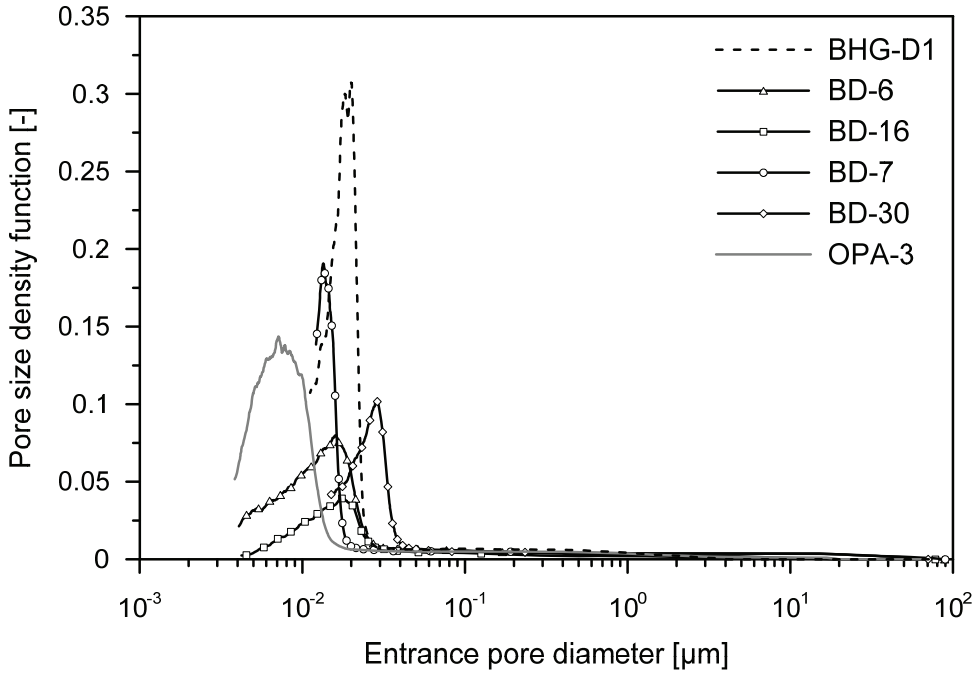

Figure 1-17: Pore size density functions of the tested shales.

Besides the possibility of having the so called non-detected porosity, the MIP technique presents also other limitations that have to be taken into account when interpreting the results. The tested materials may have pores that are accessible only through smaller ones (constricted porosity), therefore they are not detected until the smaller pores are penetrated; if the extruded mercury volume is lower with respect to the intruded mercury volume when the initial pressure is restored, it means that some mercury has been permanently entrapped in the constricted porosity. The maximum pressure applicable by the apparatus limits the capacity to enter the smallest pores of the material (non-intruded porosity). This observation justifies the fact that, when a specimen is intruded by mercury, the maximum intruded void ratio (ratio of the volume of the cumulative intruded mercury to the volume of the solid phase) usually does not coincide with the expected void ratio of the material.

According to the previous observations, additional information may be derived trough the examination of the intruded and extruded porosity. The results in terms of maximum cumulative intruded void ratio and constricted void ratio are reported in Table 1-8 for all the tested cores. The comparison between the maximum cumulative intruded void ratio values and the void ratio computed on the original cores (Table 1-5 and Table 1-6) shows that not the overall porosity is intruded and therefore investigated with the MIP test; this limit can be related to the smallest pores that require higher pressures to be intruded.

The constricted void ratio (intruded minus extruded void ratio) for the OPA-shallow specimen is the 49% of the maximum intruded void ratio; the constricted void ratio of the BD specimens result in the range of 39% - 47% of the maximum intruded void ratio, while it reaches the value of 54% of the maximum intruded void ratio for the OPA-deep specimen. The values of constricted porosity are significant for all the tested shales, suggesting that not all the intruded pores present the observed pore size while the measured values of the dominant pore size represent rather an entrance pore size, which defines the size of the pores controlling the pore network connectivity. For this reason, the word “entrance pore diameter” rather than “pore diameter” is used in Figure 1-17 and in Table 1-8.

Table 1-8: Results of MIP tests in terms of dominant entrance pore diameter and constricted porosity.

Core	*Dominant entrance pore diameter* (nm)	*Max. intruded void ratio* (-)	*Max. intruded porosity* (%)	*Constricted void ratio* (-)	*Constricted porosity* (%)
BHG-D1	20	0.13	12	0.06	6
OPA-3	8	0.09	8	0.05	5
BD-6	16	0.07	7	0.03	3
BD-16	18	0.04	4	0.02	1.5
BD-7	14	0.10	9	0.04	4
BD-30	30	0.07	7	0.03	3

1.3.4. Mineralogical composition

The mineralogical composition of three cores belonging to the OPA-shallow shaly facies has been communicated personally from Nagra. The mineralogical composition of the OPA-deep and the BD shales was determined separately for all the tested cores at the Institute of Geological Science at the University of Bern. All the results have been obtained by XRD analysis and they are reported in Table 1-9. The mineralogical analysis provides relevant information to be taken into account when evaluating the hydro-mechanical properties of the tested materials. The results suggest that Opalinus Clay has a greater amount of clay with respect to Brown Dogger. The Opalinus Clay cores retrieved at the Schlattingen site present different characteristics: the shallower ones (OPA-3 and OPA-2) have considerably lower quartz content and significantly greater clay content with respect to the deeper cores (OPA-20, OPA-6 and OPA-18). The results are in line with the two different densities measured on the cores, where the most superficial cores have a higher void ratio with respect to the deepest ones. In fact, the interconnected porosity of Opalinus Clay is mainly observed at the level of the clay matrix, while non-clayey components are mainly non-porous (Houben et al., 2013). As to the Brown Dogger, differences are recognised in BD-7 and BD-18 cores with respect to all the other BD cores. BD-7 and BD-18 present significantly less calcite and much more clay with respect to the other BD cores. The deeper BD core (BD-30) presents much more quartz with respect to the shallower cores in line with the greater entrance pore size measured for this core, since the presence of quartz grains enhances the formation of greater pores at the boundaries with the clay matrix (Keller et al., 2013).

Table 1-9: Mineralogy of the cores (*Nagra personal communication; **Ferrari et al., 2013).

Core	Depth m	Quartz (wt.%)	Feldspar (wt.%)	Calcite (wt.%)	Dolomite (wt.%)	Siderite (wt.%)	Pyrite (wt.%)	Clay (wt.%)
OPA-shallow*								
BDR-B7	~300	10	2	16	1.3	1.3	10	66
BFE-B019	~300	9	3	14	1.4	1.4	9	67
BFE-B022	~300	9	2	17	1.4	1.4	9	66
OPA-deep**								
OPA-3	837.6	17	2	16	<1	1	0.7	63
OPA-2	838.1	17	2	11	<1	<1	1.9	68
OPA-20	854.7	32	4	14	2.1	2.1	0.7	44
OPA-6	882.4	25	2	21	<1	<1	0.4	50
OPA-18	891.1	28	3	15	1.9	1.9	0.9	50
BD**								
BD-6	766.8	21	2	51	0	<1	0.9	25
BD-16	769.7	15	3	53	2.8	<1	1.1	25
BD-18	775.1	20	3	26	1.5	<1	2.1	47
BD-12	778.4	11	2	55	2.6	<1	0.9	28
BD-7	781.3	18	3	29	4.4	<1	1.7	43
BD-30	807.3	32	4	38	1.3	<1	1.1	23

1.4. Concluding remarks

The chapter provided a comprehensive description of the shale formations considered in this study. Details about the different sites and the main characteristics of the formations in-situ were reported in the first part of the chapter, together with a detailed description of the shale cores retrieved in each site and of the research context in which each core was obtained. The workflow for the geotechnical characterization of the shale cores was described in depth in the second part of the chapter, together with a detailed analysis of the results.

A total of 16 cores were considered in this study, five of them were retrieved in the Mont Terri site and belong to the Opalinus Clay (OPA-shallow) formation; the remaining eleven cores were retrieved in the Schlattingen site: five of them belong to the Opalinus Clay (OPA-deep) formation while the remaining six were retrieved from the overlaying Brown Dogger (BD) formation. The cores were subjected to the workflow for their geotechnical characterization: the results presented in this chapter will be often recalled through the thesis, since the index properties and mineralogy of the tested materials play a fundamental role in determining their hydro-mechanical properties.

1.5. References

Albert, W., Bläsi, H., Madritsch, H., Vogt, T. and Weber, H. Geologie, Stratigraphie, Strukturgeologie, bohrlochgeophysikalisches Logging und Wasserproben der Geothermiebohrung Schlattingen SLA-1 (Rohdaten). Nagra Project Report NPB (2012): 12-16.

Bläsi, H., Peters, T. and Mazurek, M. (1991). Der Opalinus-Ton des Mt. Terri (Kanton Jura): Lithologie, Mineralogie und physico-chemische Gesteinsparameter. Unpubl, Nagra Internal Report, Wettingen.

Bossart, P. (2012). Characteristics of the Opalinus Clay at Mont Terri. http://www.mont-terri.ch/internet/mont-terri/de/home/geology/key_characteristics.html.

Bossart, P. and Thury, M. (2008). Mont Terri Rock Laboratory Project, Programme 1996 to 2007 and Results. Reports of the Swiss Geological Survey

Casagrande, A. Classification and identification of soils. Transactions of the American Society of Civil Engineers (1948) 113(1): 901-930.

Diamond, S. Pore size distributions in clays. Clays and Clay Minerals (1970) 18(1): 7-23.

Ferrari, A. and Dubey, P. (2013). FE-B experiment: identification of initial hydraulic properties of Opalinus Clay for gallery near-filed instrumentation during ventilation phase of Gallery FE. Technical Note TN2013_37.

Ferrari, A., Favero, V., Manca, D. and Laloui, L. Geotechnical characterization of core samples from the geothermal well Schlattingen SLA-1. Nagra Arb. Ber. NAB (2013): 12-50.

Ferrari, A. and Laloui, L. (2013). Advances in the testing of the hydro-mechanical behaviour of shales. In: Multiphysical Testing of Soils and Shales, Springer**:** 57-68.

Freivogel, M. and Huggenberger, P. Modellierung bilanzierter Profile im Gebiet Mont Terri–La Croix (Kanton Jura). Mont Terri Project–Geology, paleohydrogeology and stress field of the Mont Terri region. Federal Office for Water and Geology Rep (2003) 4: 7-44.

Giger, S., Marschall, P., Lanyon, G. and Martin, C.D. Transferring the Geomechanical Behaviour of Opalinus Clay Observed in Lab Tests and Mont Terri URL to Assess Engineering Feasibility at Potential Repository Sites. 49th US Rock Mechanics/Geomechanics Symposium, American Rock Mechanics Association, (2015).

Gradstein, F.M., Ogg, J.G., Schmitz, M. and Ogg, G. The Geologic Time Scale 2012 2-Volume Set, elsevier, (2012).

Houben, M., Desbois, G. and Urai, J. Pore morphology and distribution in the Shaly facies of Opalinus Clay (Mont Terri, Switzerland): insights from representative 2D BIB–SEM investigations on mm to nm scale. Applied Clay Science (2013) 71: 82-97.

Keller, L.M., Schuetz, P., Erni, R., Rossell, M.D., Lucas, F., Gasser, P. and Holzer, L. Characterization of multi-scale microstructural features in Opalinus Clay. Microporous and mesoporous materials (2013) 170: 83-94.

Lambe, T.W. and Whitman, R.V. Soil Mechanics, Wiley and Sons, (1979).

Nagra (2014a). Sicherheitstechnischer Bericht zu SGT-Etappe 2: Sicherheitstechnischer Vergleich und Vorschlag der in Etappe 3 weiter zu untersuchenden geologischen Standortgebiete. Nagra Technischer Bericht. NTB 14-01. Nagra, Wettingen. .

Nagra (2002). Projekt Opalinuston: Synthese der geowissenschaftlichen Untersuchungsergebnisse. Entsorgungsnachweis für abgebrannte Brennelemente, verglaste hochaktive sowie langlebige mittelaktive Abfälle. Nagra Technischer Bericht. NTB 02-03. Nagra, Wettingen.

Nagra (2014b). SGT Etappe 2: Vorschlag weiter zu untersuchender geologischer Standortgebiete mit zugehörigen Standortarealen für die Oberflächenanlage. Geologische Grundlagen. Nagra Technischer Bericht. NTB 14-02. Nagra, Wettingen. .

Pearson, F. (1998). Opalinus clay experimental water: A1 Type, Version 980318. PSI Internal report TM-44-98-07. V. P. Paul Scherrer Institut, Switzerland.

Skempton, A. The colloidal activity of clays. Selected Papers on Soil Mechanics (1953): 106-118.

Thury, M. The characteristics of the Opalinus Clay investigated in the Mont Terri underground rock laboratory in Switzerland. Comptes Rendus Physique (2002) 3(7): 923-933.

Traber, D. Recipe and preparation of a simplified artificial pore water for Opalinus Clay and “Brown Dogger. (personal communication / internal memo) (2011).

Chapter 2
Experimental Analysis of the Water Retention Behaviour of Shales

2.1. Foreword

This chapter is dedicated to the analysis of the water retention behaviour of selected cores from the studied shales. It aims at providing a robust and complete experimental framework to investigate shale retention properties together with a detailed analysis of the results. The chapter is based on the paper entitled "Experimental analysis of the water retention behaviour of shales" (Ferrari, Favero, Marschall and Laloui, 2014), which is published in the International Journal of Rock Mechanics and Mining Science. The content of the paper is reported here and adjusted in order to be consistent with the rest of the Thesis. Complementary data, which were obtained during the PhD research but not included in the published paper, are reported in the last section of this chapter. The sections of the paper to which these complementary data belong to, are annotated with a footnote which indicates the available additional information reported at the end of the chapter.

2.2. Background

In the context of the engineering activities involving shales, such as the extraction of shale gas and shale oil, the geological storage of nuclear waste and the CO_2 sequestration, a deep understanding of shale retention behaviour is of primary significance. Water retention mechanisms play a major role in fluid trapping due to the capillary forces in the two-phase flows in shale gas reservoirs as well as in the desaturation and resaturation of shale formations, during and after ventilation respectively, as in the case of deep geological repositories. Wetting and drying episodes also have significant impacts on shale volumetric behaviour: swelling/shrinkage of shales may be caused by suction or by variations in the degree of saturation; additionally, significant swelling pressures may develop when volumetric expansion upon wetting is prevented.

In general, the water retention behaviour of geomaterials is expressed as a relationship between the pore water potential (suction) and the amount of water stored in the material (degree of saturation); the water retention curve represents this relationship. Suction is often used as the variable that expresses pore liquid potential. Matric suction (s) is the component of the potential that accounts for the effects related to the presence of the matrix (capillarity, osmotic mechanism and electrostatic forces) (Tarantino, 2010). Osmotic, or solute, suction (π) expresses the component of the potential associated with the solute concentration in the aqueous solution that constitutes the pore liquid. Total suction (ψ) is the sum of these two components and is directly related to the relative humidity and temperature established in the pore gaseous phase. The amount of water is quantified by the gravimetric water content (the ratio of the weight of the water to the weight of the solid phase, w) or the degree of saturation (the ratio of the water volume to the pore volume, S_r).

The main features of the water retention behaviour are found in the existence of a main wetting path (starting from dry conditions) and a main drying path (starting from saturated conditions), which, for a given density, embrace all the possible hydraulic states of the material. Any hydraulic path that moves from a main drying curve to a main wetting curve (or vice versa) takes place inside this hysteresis domain and is defined as a scanning curve (Figure 2-1).

The determination of water retention curves is becoming a well-established practice for the characterisation of unsaturated soils. For clayey materials, the characteristics that are usually quantified are the air entry value (value of suction at which the material starts to desaturate in a main drying episode) and its dependency on the void ratio (Romero and Vaunat, 2000), the residual degree of saturation and the hysteresis upon wetting and drying cycling (Airò Farulla et al., 2010) (Figure 2-1). For compacted clays, attention has also been paid to the effects of the evolution of the microstructure on retention behaviour (Vanapalli et al., 1999; Romero et al., 2011). Numerical models have been developed to reproduce the retention behaviour that accounts for these highlighted features (Wheeler et al., 2003; Nuth and Laloui, 2008; Romero et al., 2011; Salager et al., 2013).

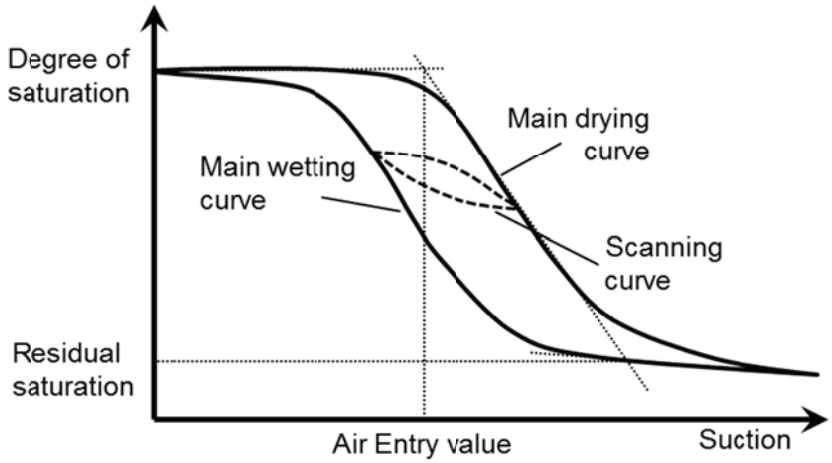

Figure 2-1: Retention curve.

In spite of this information on unsaturated soil retention behaviour, knowledge on shale retention behaviour is still limited. Indeed, the strength and stiffness of shales are significantly influenced by the degree of saturation or, alternatively, by the suction, as highlighted by Valès et al. (2004) for the case of Tournemire shale (France). Ramos da Silva et al. (2008) reported a reduction in the UCS for Beringen shale (Belgium) to a fifth of the original value when the suction was decreased from 50 to 10 MPa.

Despite this recognised impact, few experimental studies have been conducted to evaluate shale water retention properties in a comprehensive way. The limitation of the acquired information is even more evident when compared to the available experimental evidence on the retention behaviour of low-porosity compacted clays (Romero et al., 1999; Airò Farulla et al., 2010) and natural clays (Pham et al., 2007; Lima et al., 2012; Laloui et al., 2013; Wan et al., 2013). Schmitt et al. (1994) presented data on the retention behaviour of Tournemire shale (France), which was obtained from porosimetry tests along with data on two different sandstones highlighting the higher suction range that is needed for the shale in order to observe appreciable variations in the degree of saturation. Ramos da Silva et al. (2008) investigated the water retention curve for Beringen shale along drying paths and compared it to the curve for Lixhe chalk, asserting that suction of a magnitude greater by two orders was needed

for the shale to dry the materials at a 90% degree of saturation. Information on the water retention behaviour of the Opalinus Clay shale (Switzerland) has been also provided. Muñoz (2007) presented data on the evolution of the water content and the degree of saturation with total suction. Zhang et al. (2007) compared the water retention curves of Opalinus Clay shale in free and constrained volume conditions and discovered that there is a significant increase in the water amount that can be stored in the material when it is allowed to swell during the wetting phase. Villar and Romero (2012) determined the retention curve for Opalinus Clay shale in terms of matric and total suction for free and confined volume conditions; they reported air entry values in the range of 9-21 MPa for free volume conditions and 15-35 MPa for confined conditions. Romero et al. (2012) reported values of the air entry value of Opalinus Clay shale at different depths to be equal to 13 and 18 MPa, as obtained from mercury intrusion porosimetry. From the analysis of the available data, it appears that no investigation has been conducted to compose a comprehensive picture, containing all relevant features, of the shale retention behaviour. In particular, to the authors' knowledge, the retention behaviour along scanning paths has not been experimentally investigated. This chapter aims to provide a robust and complete experimental framework to analyse shale retention properties, highlighting and quantifying all the features of the retention behaviour, such as the air entry value and its dependency on the void ratio, the hysteresis phenomena and the volumetric response to suction changes.

Total suction has been selected for this study as the suction component for describing shale retention behaviour. This choice is justified, considering that shales have high air entry pressures (several MPa) and that a wide range of suction values needs to be taken into consideration to observe significant changes in the degree of saturation. Indeed, typical values of dominant pore sizes for shales are in the range of nanometers or dozens of nanometers (e.g., 20 nm for the Pierre shale - Josh et al. (2012)). The Young-Laplace equation would allow to compute that matric suction values in the order of dozens of MPa (approximately 7 MPa for a pore radius of 20 nm) would be required in order to remove the water from pores with characteristic size in this range. On the other hand, most techniques for controlling and measuring matric suction are limited to a maximum suction of 1.5 MPa (Murray and Sivakumar, 2010). However, it is a common practice in petroleum engineering to gather information on the relationship between matric suction and degree of saturation by the analysis of porosimetry tests (Josh et al., 2012). In order to compare results in terms of matric and total suction, the osmotic component must be assessed; this aspect has been poorly addressed for shales. Laloui et al. (2013) reported values of 12.13 MPa and 17.3 MPa for the matric and total suction, respectively, for a sandy facies Opalinus Clay shale at a 74% degree of saturation. When comparing the water retention curves in terms of total and matric suction for Opalinus clay shales, Villar and Romero (2012) pointed out that no clear difference is observed between the two curves; however, the scattering of the data did not seem to allow for a precise assessment of the osmotic component.

In the following section, the developed experimental protocol is described first. Selected results on shales from the northern region of Switzerland are subsequently presented and analysed in light of the proposed experimental methodology. Additional data are reported in the last section of the chapter. Complementary information is gained from the analysis of the porosimetry tests. The assessment of

the osmotic suction component is performed by independently measuring the total and the matric suction; these measurements are used to explain the difference between the water retention curve that was obtained using the porosimetry technique and the methodology that is proposed in this chapter.

2.3. An experimental technique to investigate the water retention behaviour of shales

The developed experimental technique for determining shale retention behaviour is based on the direct control of the water content and the subsequent measurement of the total suction. Different hydraulic paths are considered in order to analyse the response of the material to wetting and drying episodes. The following sections provide details on the specimen preparation, water content control, suction measurement and volume change detection.

2.3.1. Specimen preparation and water content control

The material is obtained from a shale core: slices of approximately 7 – 8 mm in height are cut with a diamond saw without using water, and they are immediately divided into smaller specimens with lateral sizes of approximately 20 mm. Three specimens are immediately tested to obtain the initial condition in terms of water content, void ratio and total suction, using the procedure detailed in the next sections. The initial measured void ratio is compared with the void ratio of the core in order to assess the quality of the obtained specimens. The main wetting and drying paths are sought first; to this aim the material is initially brought to a dry state or to a "zero-matric-suction" state, respectively. The dry state is obtained by placing the specimens in desiccators that contain silica gel and leaving them to dry for approximately three weeks (applied total suction of approximately 300 MPa) until no significant change in their weight can be detected. The "zero-matric-suction" condition is achieved by placing the specimens in a sealed-glass jar, within which a relative humidity of 100% is imposed; the specimens are wrapped in filter paper and rest on porous stones immersed in water, resulting in a direct contact of the specimens with the fluid; synthetic water (corresponding to the in-situ water composition) may be used for this initial wetting stage in order to preserve the initial osmotic suction of the material. The specimen is therefore in direct contact with the considered fluid (see Figure 5-1). The weight of the specimens is monitored using a precision balance (0.001 g), and the process is stopped once no further evolution is observed (usually in three weeks).

Once equilibration is achieved, the main wetting and drying paths can be determined. To obtain the main drying path, the equalized specimens are air-dried in a controlled way under laboratory-controlled conditions (T = 23 °C, RH ≈ 45%, equivalent total suction of about 110 MPa) or placed in a desiccator with silica gel for the driest states. During the drying, the weight of the specimens is monitored using a precision balance (0.001 g), and the process is halted once the target water content is reached; the specimens are then packed hermetically for three days to allow for internal redistribution of the water content. Preliminary testing showed that three days of curing time were sufficient for having a repeatable measurement of the total suction on the prepared specimens.

The procedure to obtain the main wetting path consists on the addition of a target amount of water, either by the gaseous phase (distilled water) or by pouring small droplets of water (distilled or synthetic water) on the surface of the specimen with a small syringe. In this work the gaseous phase (the relative humidity) is considered to increase the water content in the high suction range, while direct contact of small droplets of synthetic water is used to increase the water content in the low suction range, in order to ensure that the osmotic suction component is preserved and that no additional swelling is induced in the material due to decrease in osmotic suction (see Chapter 5). The internal redistribution of the water content is allowed for three days by keeping the specimens in hermetically closed containers.

When the retention properties are sought in terms of degree of saturation, the measurement of the volume change upon water content evolution is required. This determination allows for the quantification of shale swelling/shrinkage behaviour related to suction variation under unstressed conditions. In this case, the specimen volume is measured just after the measurement of the total suction with a destructive technique. When the retention behaviour is sought only in terms of water content or a limited amount of core material is available, a different procedure is considered. This latter technique consists of a progressive drying or wetting of the same shale specimen; the water content control is performed following the procedure that was previously described. Because no volume measurement is conducted, the specimen can be equalized to a new target water content after the total suction for the previous step has been measured. In general, three specimens are submitted to the same hydraulic path, allowing for a more representative analysis.

2.3.2. Suction measurement

The total suction readings are taken on the equalized specimens by means of a dew-point chilled-mirror psychrometer (Decagon, WP4C) (Leong et al., 2003; Cardoso et al., 2007) (Leong et al., 2003; Cardoso et al., 2007). A schematic representation of the device is shown in Figure 2-2. A mirror is placed inside a sealed chamber, and its temperature is precisely controlled by a thermoelectric (Peltier) cooler. The relative humidity is imposed by the shale specimen inside the sealed chamber where a fan is placed so that the environment reaches equilibrium. The temperature on the mirror is progressively lowered, and a photoelectric cell captures the exact moment when condensation occurs in the mirror. The corresponding temperature of the specimen is measured using an infrared thermometer. The relative humidity, which is the ratio of the vapour pressure at the specimen temperature to the saturated vapour pressure of water at the same temperature, is obtained from the difference between the dew point temperature on the mirror and the temperature of the specimen. Once the relative humidity is measured by the device, the total suction is obtained using the psychrometric law (Fredlund and Rahardjo, 1993), which relates the relative humidity (RH) and the absolute temperature (T) to the total suction:

$$\psi = -\frac{\rho_w RT}{M_w}\ln\left(\mathrm{RH}\right) \tag{2.1}$$

where R is the universal gas constant and ρ_w and M_w are the density and the molecular mass of water, respectively.

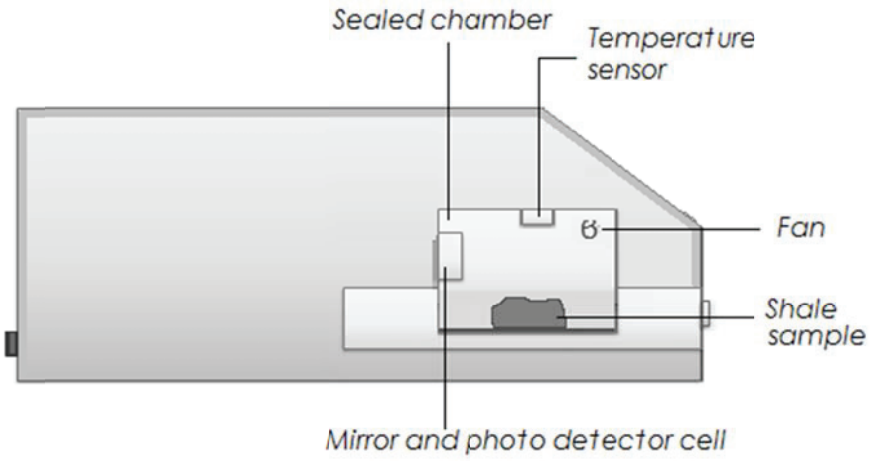

Figure 2-2: Outline of the WP4C (Decagon, 2010) chilled-mirror dew-point psychrometer with a shale fragment positioned inside the measuring chamber (after Leong et al. 2003).

The chilled-mirror dew point psychrometer is commonly used for suction measurement in natural and compacted soils (Decagon, 2010). The accuracy of the device as specified by the manufacturer is ±0.05 MPa for total suction from 0 to 5 MPa and ±1% for total suction in the range of 5 – 300 MPa. The manufacturer recommends that the specimen covers the entire surface of the sample holder. Due to the high suction values expected for shales and the fact that the shale specimens do not fill the entire sample holder, further analysis and calibrations have been conducted to assess the applicability of the device for analysing the water retention behaviour using shale fragments. Figure 2-3 gives the total suction values read by the device for salt solutions at different temperatures of known water potential in the range of 4 – 393 MPa. An average accuracy of 3% can be derived, except for the highest applied suction, and it is considered to be satisfactory for the purposes of this study.

The effects of the dimension of the specimen with respect to the size of the sample holder are analysed in Figure 2-4. Tests were conducted at 25 °C by partially filling the sample holder with saturated NaCl and KCl solutions (reference total suction of 39.2 MPa for the NaCl and 23.8 MPa for the KCl). Figure 2-4 shows a negligible influence of the percentage of the covered surface and height on the measurements because a maximum error of only 1.1% is observed for the suction readings. With this investigation, the suitability of this device for the total suction reading of shale fragments was confirmed.

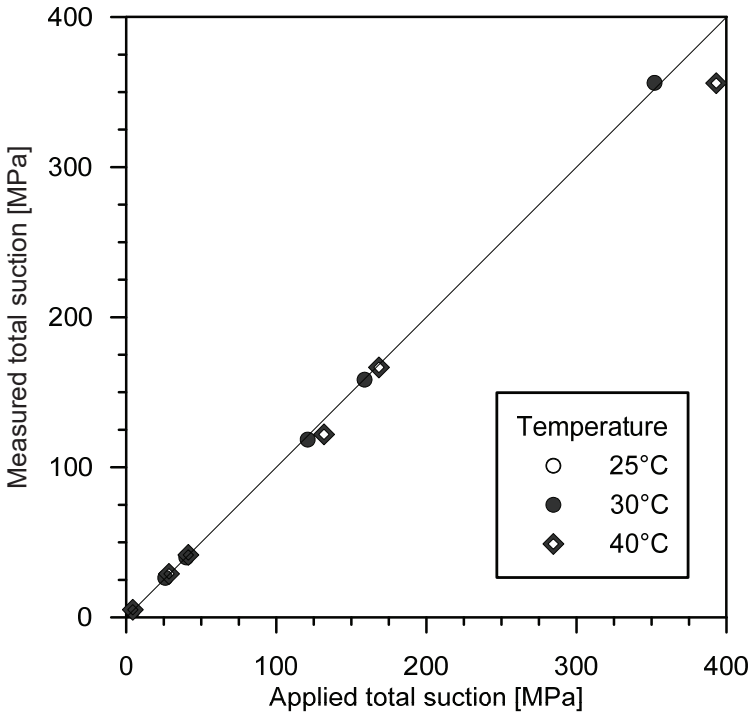

Figure 2-3: Evaluation of the accuracy of the psychrometer in the range of measured suction when testing shale samples.

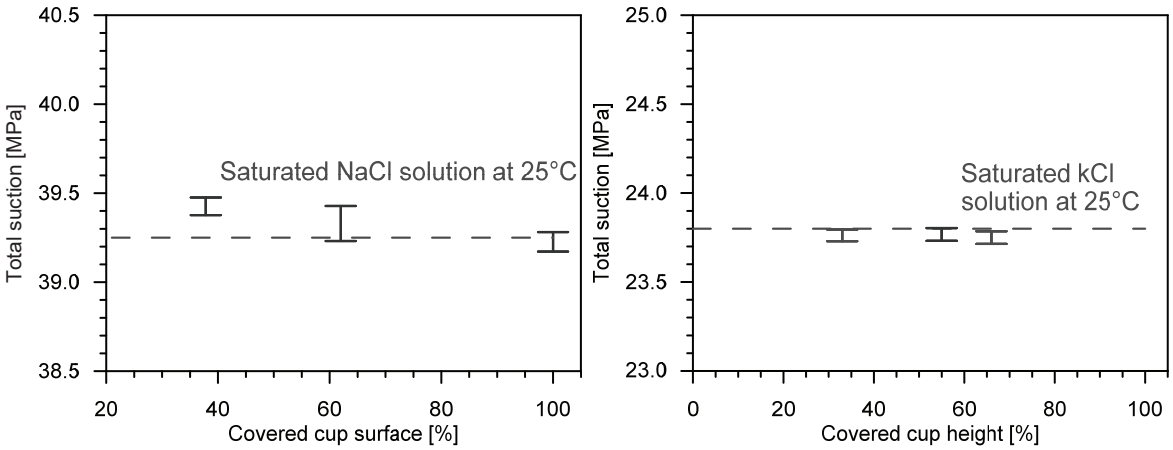

Figure 2-4: Assessment of the errors in psychrometric readings associated with a partial filling of the sample holder by the shale fragment.

2.3.3. Assessment of volume change behaviour

The method adopted for the volume measurement is based on a fluid displacement technique using a pycnometer filled with kerdane. Kerdane was selected for its immiscibility with water and its ability to invade the air-filled pore spaces of the surface without affecting the soil structure (Péron et al., 2006). The analysis of the accuracy of this method, together with the precision in the estimation of the weight, allows for an estimation of the degree of saturation to be made with an accuracy of 4%. The method used for volume determination is a destructive technique; a complete assessment of the retention behaviour in terms of main wetting and drying paths, requires a large number of specimens to be prepared and tested (typically about 50 specimens). Other non-destructive techniques could be considered for this analysis (e.g., non-contact techniques such as laser scanning and micro computed tomography, or the use of wax for hydrostatic weighting as performed by Wan et al. (2013)); however, in the experience gained through this work, difficulties in handling the shale specimens, especially at high water contents, make the applicability of these techniques inadvisable for the tested materials.

Complementary free swelling tests are also performed, for which the material is wetted in oedometric conditions, starting from its initial state, and the volume change is assessed through the continuous measurement of the heave of the specimen.

2.4. Experimental results

The experimental analysis of the water retention behaviour has been carried out on selected shale cores: the BHG-D1 core from the OPA-shallow formation, the BD-6 core from the BD formation and the OPA-3 and OPA-18 cores from the OPA-deep shale formation. OPA-3 and OPA-18 are distinguished in the following and they are called OPA-deep´ and OPA-deep´´, respectively. This clear distinction is due to the fact that the two cores are characterized by significantly different densities as highlighted in section 1.3.1: OPA-3 is the shallower core, it is characterized by lower density and higher void ratio with respect to the OPA-18 core. Due to the relevance of the impact of porosity on retention features, the distinction between the mentioned OPA-deep cores is strictly needed.

Synthetic pore waters were used in the experiments with the aim of recreating the in-situ pore water compositions. The osmotic suction of the synthetic waters presented in section 1.2 was measured by the dew-point psychrometer and resulted in values of 1.2 MPa for the Mont Terri synthetic water (OPA-shallow) and 0.98 MPa for the Schlattingen synthetic water (BD and OPA-deep).

2.4.1. Main drying and wetting paths

The results obtained in the determination of the main wetting and drying paths for the OPA-shallow are shown in Figure 2-5.

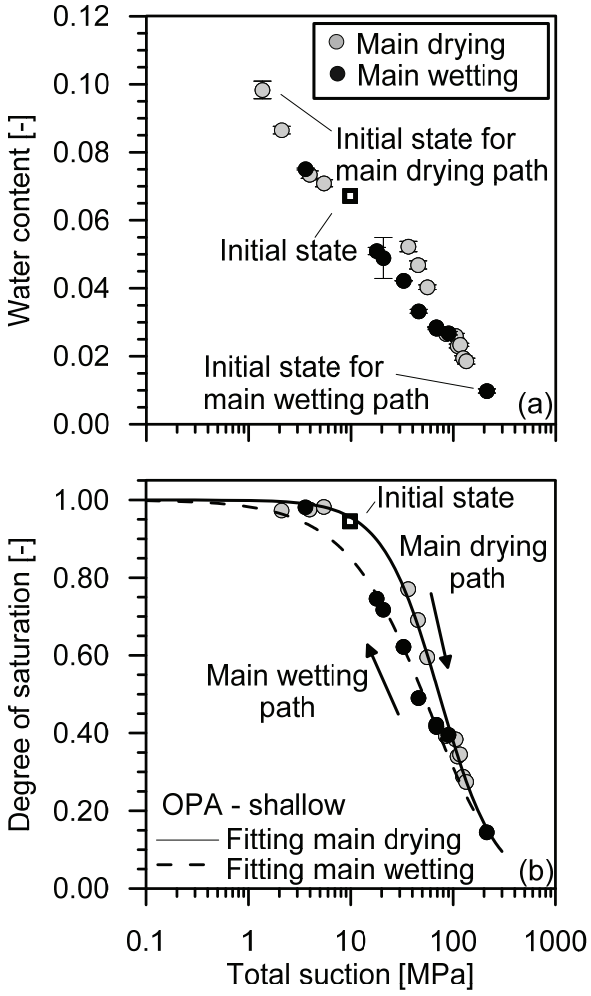

Figure 2-5: Water retention behaviour of the OPA-shallow shale in terms of water content (a) and degree of saturation (b) as a function of the total suction.

The evolution of the water content with the total suction is shown in Figure 2-5a; each point represents an average value of three specimens, which were brought to the same target water content value; their standard deviation is also represented. The initial condition corresponds to a water content of 6.7%. For the specimens equalized to the "zero matric suction" state, the measured total suction was 1.4 MPa, which is in good agreement with the osmotic suction of the synthetic water used for this initial wetting. Starting from this state, the points obtained by the controlled drying procedure describe a progressive increase in total suction along with a reduction in water content; the driest state obtained with this procedure corresponds to a water content of 1.9% and a measured total suction of

134 MPa. This drying path tends to the residual condition that was achieved in the desiccator (w = 1.0%, suction = 213 MPa), when the initial state for the main wetting path was sought. For all the tested specimens, volume measurements were obtained at the end of the equalization stage. The obtained results are depicted in Figure 2-8 in terms of void ratio versus total suction. Significant swelling/shrinkage behaviour was observed with suction variation. The void ratios obtained for the lowest measured suction are in very good agreement with the results of a free swelling test carried out with the same synthetic water used for determining the water retention curves. The void ratio reduction upon drying allows for the identification of the shrinkage limit. The suction value at which no significant volume reduction is observed (here defined when $\Delta e/\Delta\psi < 0.1$ %) is approximately 10 MPa; the corresponding shrinkage limit can be seen in Figure 2-5a on the drying path and was found to be 6.4%. The void ratio evolution with suction was fitted with the following incremental expression:

$$\dot{e} = -\frac{\dot{\Psi}}{K_{ref}}\left(\frac{\Psi_{ref}}{\Psi}\right)^{m}\left(1+e_0\right) \tag{2.2}$$

where K_{ref}, ψ_{ref} and m are the fitting parameters and e_0 is a reference void ratio. The values of the parameters obtained by the least square method are reported in Table 2-1. The retention curves in terms of the degree of saturation were obtained by combining the volume evolution and the water content along the wetting and drying paths. The results have been fitted with a Van Genuchten's type (Van Genuchten, 1980) expression:

$$S_r = \left(1+\left(\frac{\Psi}{P_{VG}}\right)^{n_{VG}}\right)^{(-\lambda)} \tag{2.3}$$

where P_{VG}, n_{VG} and λ are the fitting parameters; the fitting values obtained by the least square method are reported in Table 2-1.

Table 2-1: Fitting parameters for volumetric behaviour and water retention behaviour.

Shale	K_{ref} (MPa)	ψ_{ref} (MPa)	m (-)	e_0 (-)	n_{VG} (-)		P_{VG} (MPa)		λ (-)	
					wetting	drying	wetting	drying	wetting	drying
OPA-shallow	14.66	1.62	2.63	0.31	0.98	1.53	110.1	78.2	1.80	1.08
BD	29.00	1.03	1.50	0.20	1.31	1.85	126.2	130.0	2.82	2.10
OPA-deep´	45.00	0.98	1.30	0.22	1.16	2.05	30.0	49.0	0.63	0.42

The initial state for the OPA-shallow corresponds to a degree of saturation of 95%; this value seems to confirm the fact that the material is reported to be saturated or close to saturation in situ. In addition, the initial state is found to be located along the main drying path as a consequence of the coring process and the exposure to the atmosphere before preservation. The main drying path allows for the identification of the maximum total suction value that the material can sustain without

significant changes in the degree of saturation (air entry value, ψ_e). For the OPA-shallow, this value is about 11 MPa (taken as the total suction corresponding to 95% of the degree of saturation), and the corresponding void ratio is 0.19. The main drying and wetting curves embrace the hysteresis domain of the material, which is significant for total suction values lower than 100 MPa (Figure 2-5b).

Figure 2-6 and Figure 2-7 depict the results concerning the wetting and drying paths for the BD and OPA-deep core samples, respectively. The water content evolution with total suction is shown in Figure 2-6a and Figure 2-7a; the initial states correspond to a water content of 3.2% for both the BD and OPA-deep´ shale samples. For the BD and OPA-deep´ specimens that were equalized to the "zero matric suction" state, the measured total suction was 1.2 MPa, which is in good agreement with the osmotic suction of the synthetic water.

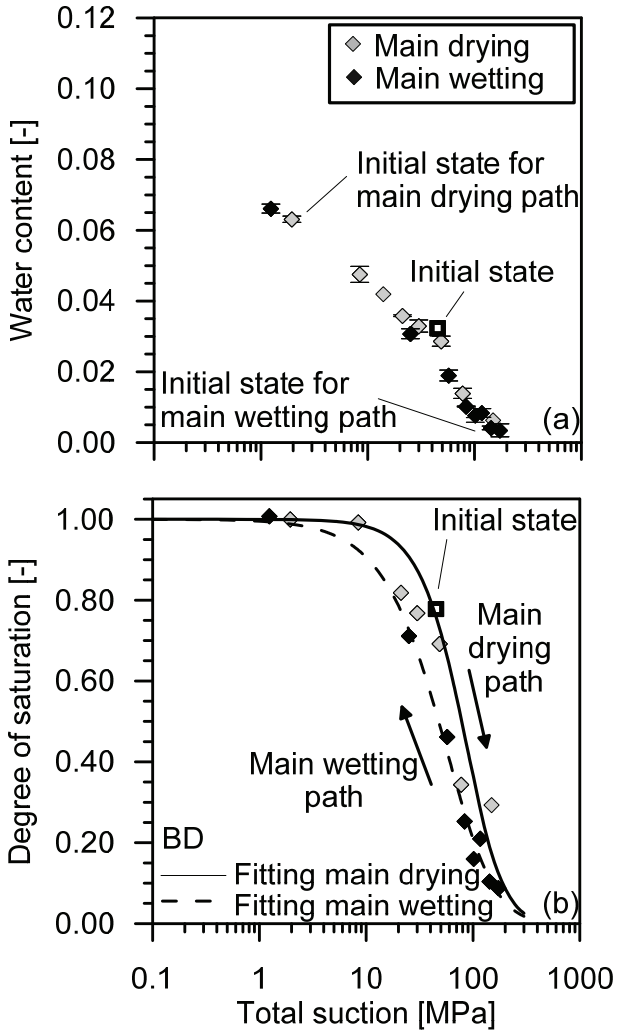

Figure 2-6: Water retention behaviour of the BD shale in terms of water content (a) and degree of saturation (b) as a function of the total suction.

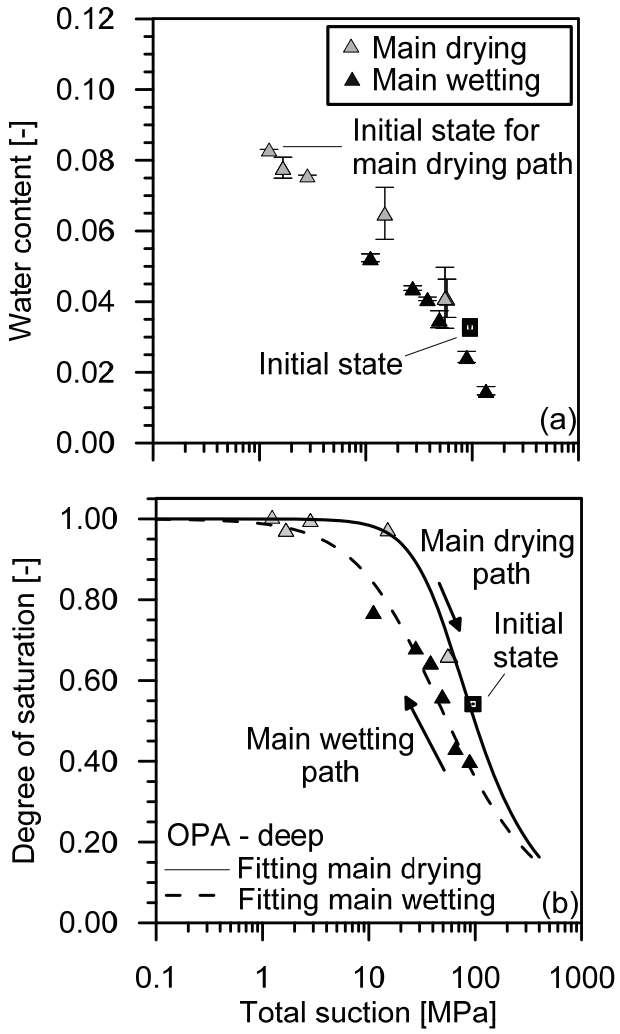

Figure 2-7: Water retention behaviour of the OPA-deep´ shale in terms of water content (a) and degree of saturation (b) as a function of the total suction.

The volume evolution for the two shales is reported in Figure 2-8. Again, a good agreement is found with the result of a free swelling test carried out on a BD sample using the same synthetic water. The observed shrinkage limits were found to be approximately 4.1% and 6.4% for the BD and for the OPA-deep´, respectively, which correspond to a total suction of approximately 14 MPa for both shales. The void ratio evolutions were fitted with Equation (2.2), and their fitting parameters are reported in Table 2-1. Due to the limited quantity of available material for OPA-deep´´, a systematic analysis of the void ratio evolution with total suction was not possible. The results collected on this material are also shown in Figure 2-8 along with the results of a free swelling test. The collected points align well with the trend registered for the BD shale; in this sense, a unique trend is used to describe the swelling/shrinkage behaviour for these two shales.

The analysis of the volumetric response to suction changes allows for the quantification of swelling potential for the tested shales. The measured volumetric deformations associated with the complete wetting of the material, starting from the driest condition, were 12.3%, 11.4% and 8.6%, for OPA-shallow, BD and OPA-deep, respectively. The highest swelling potential was observed for OPA-shallow; this behaviour can be explained by the slightly higher clay content of this shale compared to the deep shales; in addition, greater depth and diagenetic processes, which result in a higher degree of cementation, might be responsible for the lower swelling potential of the deepest shales. The retention curves in terms of degree of saturation are reported in Figure 2-6b and Figure 2-7b for BD and OPA-deep´, respectively. The initial conditions correspond to a degree of saturation of 80% for BD and 54% for OPA-deep´. The registered low initial degree of saturation for OPA-deep´ is attributed to a non-perfect preservation of the core used in the investigation.

A general comparison of the retention behaviour of the tested shales reveals that very limited changes in the gravimetric water content are required for the deeper shales to undergo complete cycles of wetting and drying. [1]

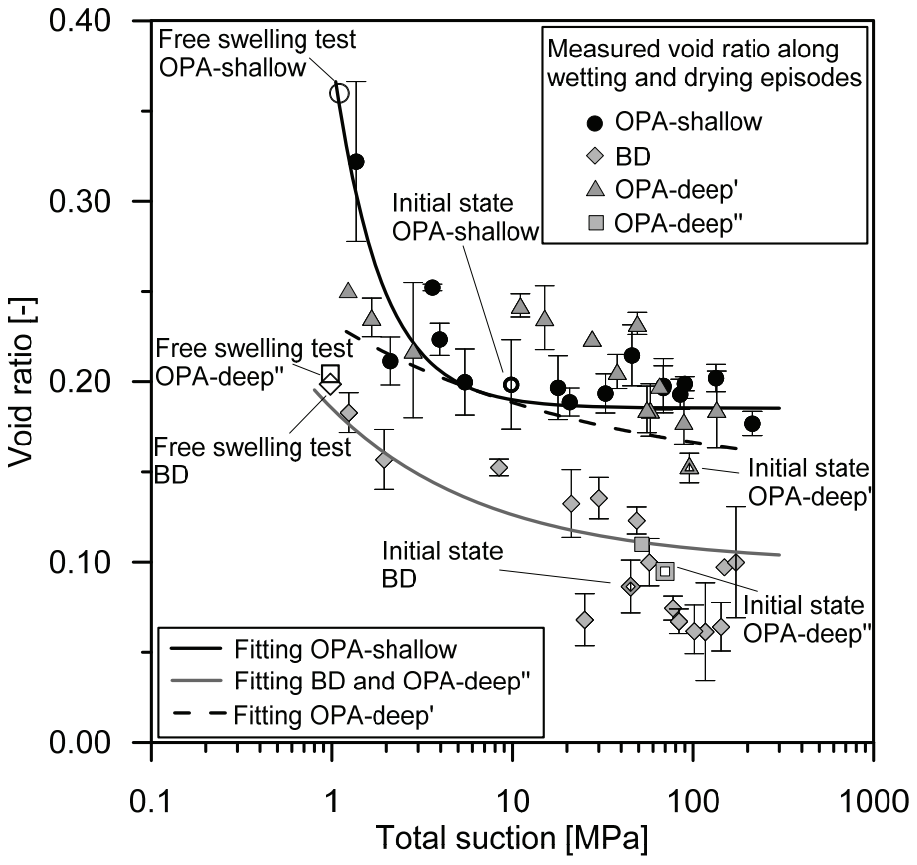

Figure 2-8: Void ratio evolution as a function of the total suction for the various shale samples.

[1] Additional results on a BD shale sample, which are related to this section, are reported in section 2.5.

2.4.2. Assessment of the scanning behaviour

In order to gain additional information on the retention behaviour with cyclic variations of water content, a wetting path was initiated for OPA-deep´´, starting directly from the initial state. The results are presented in Figure 2-9.[2]

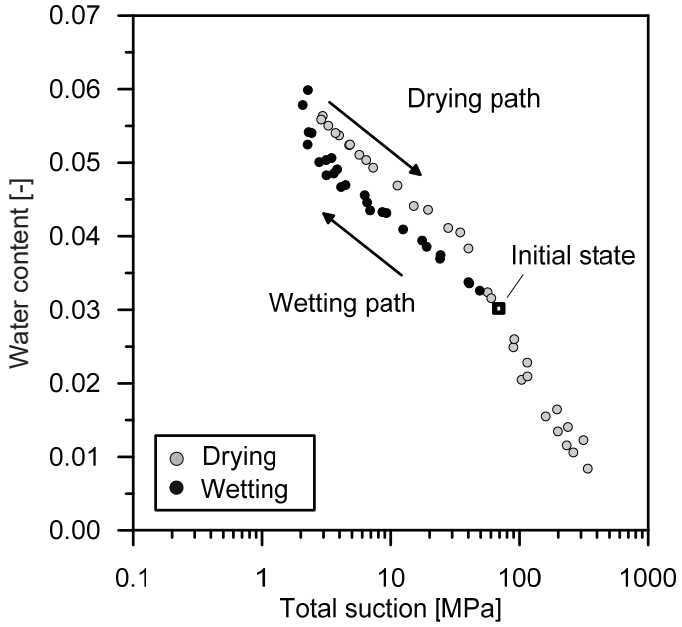

Figure 2-9: Retention behaviour of the OPA- deep´´ core sample.

Three specimens were used, and they were progressively wetted following the procedure detailed in section 2.3.1 until the material stopped showing a further tendency to absorb water. The corresponding total suction at this stage was approximately 2 MPa. The drying path was then initiated and carried out until a suction of 340 MPa was reached.

The obtained results are presented in Figure 2-10 in terms of degree of saturation versus total suction; the curve depicted in Figure 2-8 for OPA-deep´´ was used in order to compute the evolution of the void ratio with total suction. In Figure 2-10, the reference main wetting and drying curves for the OPA-deep are also represented. The initial wetting from the initial state (path A-B) takes place inside the hysteresis domain, and a scanning curve is clearly observed. As the hydraulic path encounters the main wetting curve, it follows this trend until saturation is reached (point C). Starting from this state, the hydraulic path follows the main drying path until the residual degree of saturation is reached (path C-D). The observed behaviour shows clearly that attention must be paid when wetting the shale, starting from its "as-extracted" state; in other words, the registered water contents may not be referred to a main wetting path, and this could have significant consequences when hydraulic properties, such as relative permeability, are sought.

[2] Additional results on OPA-deep and BD specimens, tested according to the procedure described in this section, are presented in section 2.5.

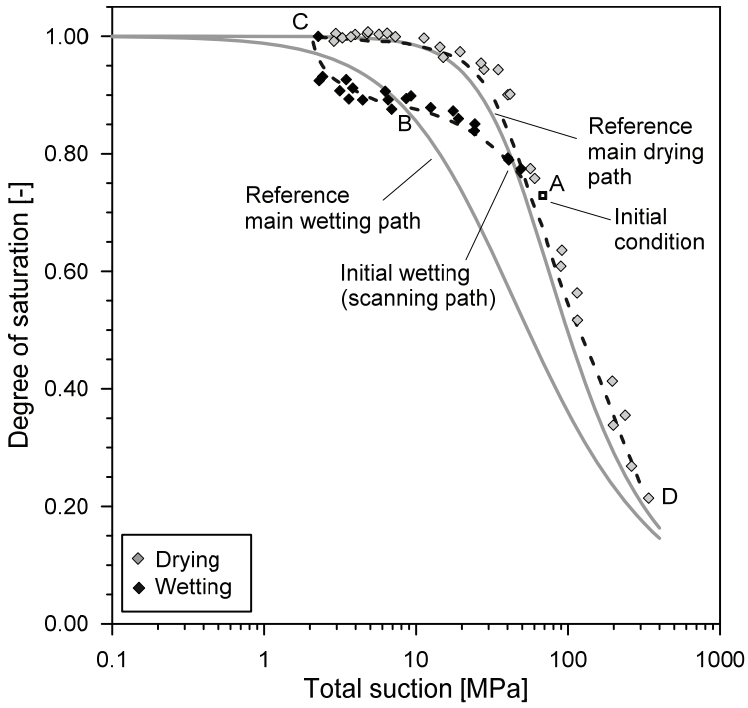

Figure 2-10: Retention behaviour of an Opalinus Clay sample (OPA- deep´´) during wetting and drying cycling.

2.4.3. The air entry value

The collected results on the retention properties of the tested shales provide information on the effects of the void ratio on the air entry value. Figure 2-11 depicts the total suction and the void ratio at which the shales started to desaturate along the main drying paths. The results are supplemented with other available data from the literature for the Opalinus Clay. A unique exponential evolution function is proposed, and it captures the observed trend well ($R^2 = 0.78$):

$$\Psi_e\left[MPa\right] = 69.39 \cdot \exp\left(-9.82 \cdot e\right) \tag{2.4}$$

Using Equation (2.1) and (2.4), the relative humidity values at which the shales start to desaturate can be calculated as a function of the void ratio. In Figure 2-12, the minimum relative humidity to which the shales should be exposed in order to prevent desaturation is shown for a reference temperature of 22 °C. This analysis may have an important application in the context of tunnel excavations in shale formations when the material is exposed to atmospheric conditions (ventilation phase in nuclear waste disposal). By combining the information with the cracking upon drying behaviour (Péron et al., 2009), it is possible to establish a threshold for relative humidity as a function of the void ratio and depth in order to minimize the possibility of the creation of a tunnel excavation damage zone.

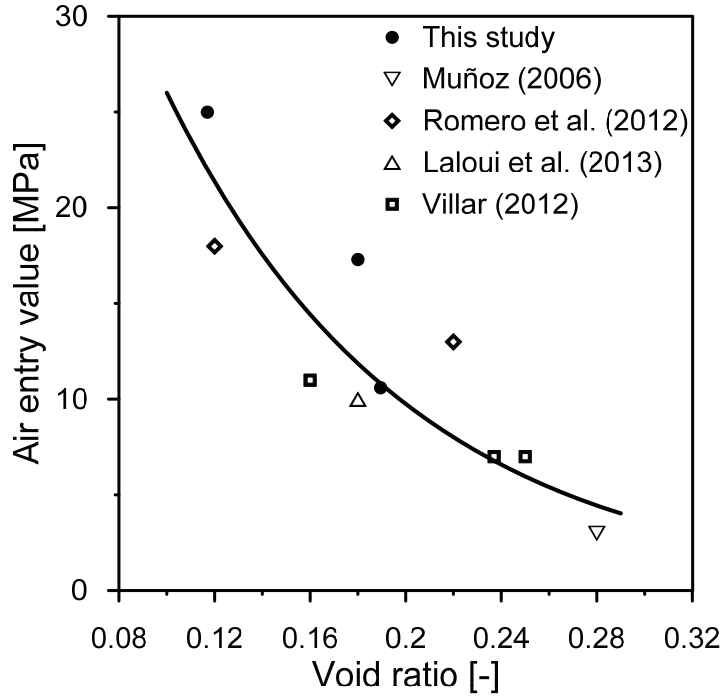

Figure 2-11: Air entry values as a function of the void ratio for Opalinus Clay Shale.

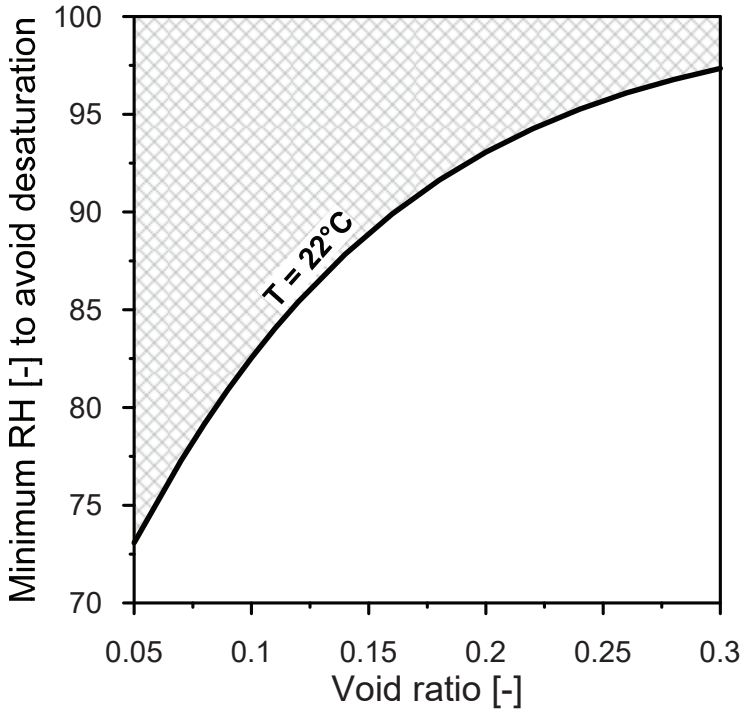

Figure 2-12: Relative humidity at the air entry value as a function of the void ratio at 22 °C.

2.4.4. The osmotic suction component

Total suction has been selected in this study to describe the retention behaviour of shales. In order to highlight the role of osmotic suction in the retention behaviour, complementary information has been collected by independent measurements of the total and matric suction for two of the tested shales (OPA-shallow and OPA-deep´´). The suction was measured using contact (matric suction) and non-contact (total suction) filter paper. Ad-hoc calibration curves were determined on initially oven-dried Schleicher and Schuell No. 589 filter paper. The initial oven-dried condition ensured that there was an adequate transfer of water from the specimen to the paper during the measurement. The calibration curves were obtained by applying matric suction by means of the axis translation technique and total suction by the vapour equilibrium technique to the filter paper. An equalization time of two weeks was selected for both the calibration and the measurements. The obtained calibration curves are:

$$s(MPa) = 15.972 \cdot w_{fp}^{-3.002} \tag{2.5}$$

$$\psi(MPa) = 59.076 \cdot w_{fp}^{-2.865} \tag{2.6}$$

where w_{fp} is the water content measured on the filter paper. The measured total and matric suctions and computed osmotic suctions are reported in Table 2-2. The retention curves in terms of matric suction (capillary forces) for the two considered shales were obtained from the MIP results using the following expression, which relates the pressure of the mercury intrusion P and the matric suction for the same pore diameter:

$$s = -\frac{\sigma_w \cos\theta_w}{\sigma_{Hg} \cos\theta_{nw}} P = 0.196P \tag{2.7}$$

where σ_w and σ_{Hg} are the water and mercury surface tension values (equal to 0.072 N/m and 0.486 N/m, respectively), θ_w is the contact angle of the air-water interface (0°), and θ_{nw} is the non-wetting contact angle between the mercury and the soil grain (taken as equal to 140°). The obtained results are depicted in Figure 2-13 along with the results of the osmotic suction determination. It can be seen that the osmotic suction component explains the distance between the two curves well. The impact of clay-related suction effects, which are taken into account by the filter paper technique but not from the MIP technique, may manifest at suction values higher than those considered. A slight difference between the results from MIP tests and the filter paper technique could therefore manifest in the high suction range. This type of analysis can serve as a link between the common practice in petroleum engineering of obtaining information on the capillary pressure of shales from the MIP results (Josh et al., 2012) and the proposed methodology, which uses the total suction component.

Table 2-2: Results of total, matric and osmotic suction from the filter paper technique.

	OPA-shallow	OPA-deep´´
Shale water content	0.068	0.029
Total suction (MPa)	13.3	76.4
Matric suction (MPa)	1.0	34.4
Osmotic suction (MPa)	12.3	42.0

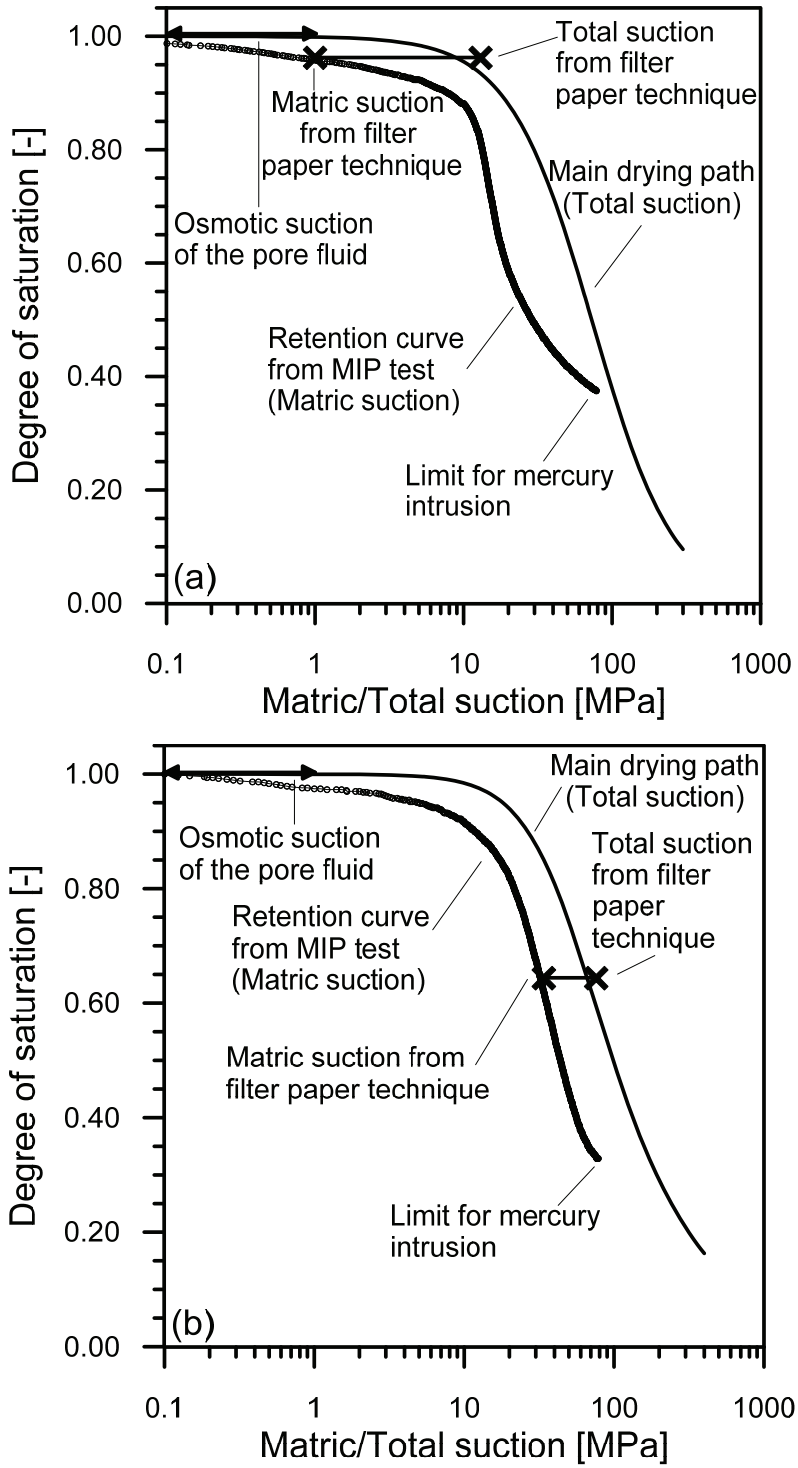

Figure 2-13: Comparison of the retention curves in terms of matric and total suction and assessment of the role of the osmotic suction for Opalinus Clay at different depths: (a) OPA-shallow, (b) OPA-deep.

2.5. Complementary data

This section provides complementary information concerning the water retention behaviour of OPA-deep and BD cores upon main wetting paths and upon wetting-drying cycles. Two cores belonging to the OPA-deep formation (OPA-6 and OPA-20) and three cores belonging to the BD formation (BD-7, BD-18 and BD-30) were included in the analysis. OPA-6 and OPA-20 have density and void ratio values that are comparable with those of the OPA-18 core (Table 1-6), therefore they can be also named as OPA-deep´´.

The void ratio evolution with total suction along a main wetting path was measured for one of these five additional cores (BD-18), following the procedure detailed in section 2.3.3. The results are reported in Figure 2-14: they are in good agreement with the trend identified from the analysis of the volumetric behaviour of the BD-6 core (Figure 2-8). Concerning the remaining four cores, as in the case of OPA-18, the limited quantity of available material did not allow the systematic analysis of the void ratio evolution with total suction; the available information on these additional cores is reported in Figure 2-14. The result of a free-swelling test carried out on a BD-18 sample is also depicted in Figure 2-14, together with its initial state. All the presented results are in good agreement with the trend measured on BD-6 shale core and already adopted for describing the void ratio variation with total suction for OPA-18. Therefore, the same unique trend is used to describe the swelling/shrinkage behaviour as a function of total suction for these five additional shale samples.

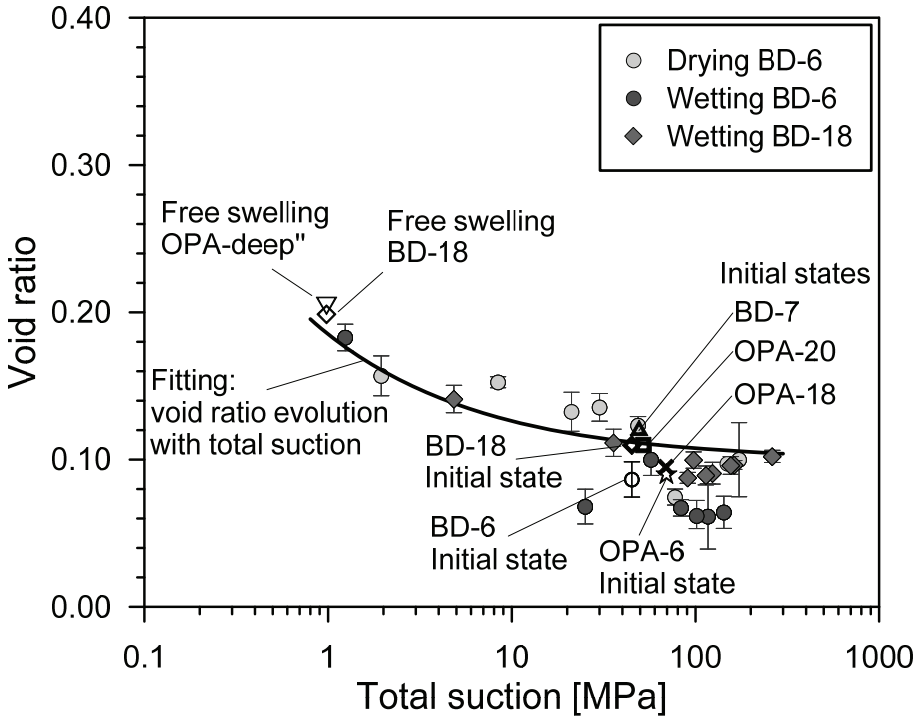

Figure 2-14: Void ratio evolution as a function of the total suction for the BD and OPA-deep´´ cores.

The procedure described in section 2.4.2 is applied here in order to further investigate the retention behaviour of the tested shales. The wetting path was applied first for all the tested specimens; three specimens for each shale core were subjected to the same hydraulic path, in order to obtain a more representative analysis. The OPA-deep´´ and BD-7 specimens were wetted starting from their "as extracted" state, as depicted in Figure 2-15 and Figure 2-17, respectively. The BD-18 and the BD-30 specimens were wetted starting from a dry state: the initial water content and total suction for the BD-18 specimens were equal to 0.3% and 262 MPa respectively, while the initial water content and total suction for the BD-30 specimens were equal to 0.7% and 135 MPa respectively (Figure 2-17).

The results on OPA-6 and OPA-20 are discussed first. The retention behaviour of the two cores in terms of water content versus total suction is presented in Figure 2-15. OPA-20 presents greater gravimetric water content values with respect to OPA-6, which are required in order to undergo a complete cycle of wetting and drying. In both cases, a hysteretical behaviour is clearly observed where the rewetting path is located below the drying path.

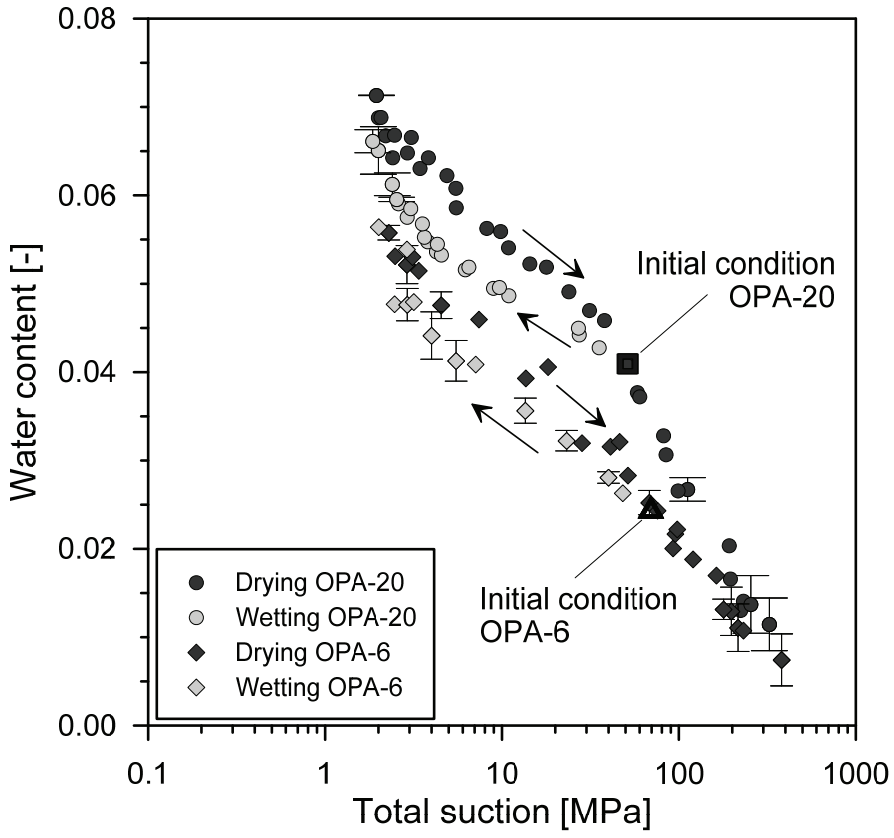

Figure 2-15: Retention behaviour of OPA-6 and OPA-20 shale samples upon a wetting-drying cycle in terms of water content versus total suction.

Combining the information on the water content and on the void ratio evolution with total suction, the retention behaviour in terms of degree of saturation can be represented: Figure 2-16 reports the results

in terms of degree of saturation together with the reference main drying and main wetting paths determined for the OPA-deep (section 2.4.1). The initial state is found along the main drying path for both the tested samples indicating that the material experienced some drying during the coring process. The initial rewetting from the main drying branch defines a scanning path which takes place inside the hysteresis domain. The hydraulic path follows then the trend of the main wetting branch until saturation is reached. The subsequent drying follows the main drying branch. The air entry values for both the tested OPA-deep samples are found at about 19 MPa, in good agreement with the trend identified in Figure 2-11, taking into account the adopted void ratio evolution with suction for these shales.

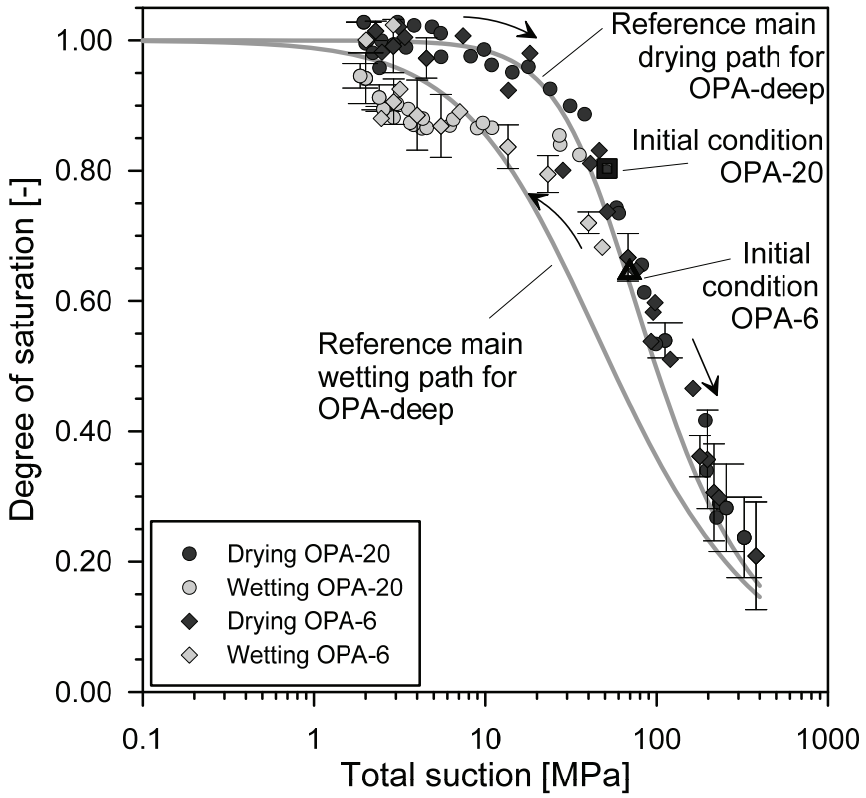

Figure 2-16: Retention behaviour of OPA-6 and OPA-20 shale samples upon a wetting-drying cycle in terms of degree of saturation versus total suction.

The results of the retention behaviour of BD-7, BD-18 and BD-30 cores are reported in Figure 2-17 in terms of water content versus total suction. BD-7 presents slightly higher gravimetric water content variations with respect to BD-6 (Figure 2-6) in order to obtain a wetting-drying cycle. The main wetting paths obtained from BD-18 and BD-30 specimens, are located below the main drying path, highlighting the hysteretic properties of the material. In particular BD-30 presents lower water content values for the same total suction with respect to BD-18.

The results in terms of degree of saturation versus total suction are reported in Figure 2-18. The results for the main drying and main wetting branches are fitted with a Van Genuchten's type (Van Genuchten, 1980) expression using the parameters reported in Table 2-3. As to the main wetting paths, different parameters were necessary in order to fit the results obtained from BD-18 and BD-30 specimens, since the two cores display different retention characteristics: BD-30 manifests lower retention properties with respect to BD-18. This observation is justified by the different mineralogical composition of the two cores (Table 1-9): the BD-30 core presents a significantly higher amount of quartz with respect to the BD-18 core; the presence of quartz enhance the formation of bigger pores at the contact boundaries between non-clayey grains and clay matrix (Keller et al., 2013), decreasing the retention properties of the material. The results of the MIP tests are in good agreement with this observation since a greater dominant entrance pore size is obtained on the BD-30 core with respect to the other BD shale cores (Figure 1-17). On the other hand, the mineralogical compositions of the BD-18 and BD-7 cores are well comparable and they both present considerably higher clay content with respect to the other tested BD shale cores. Their greater clay content is found to affect their retention properties: in fact, when the main drying curve of BD-7 is compared to the one of BD-6 (Figure 2-6), a greater air entry value for BD-7 is highlighted with respect to BD-6. The observed behaviour is also in agreement with the MIP tests results, where a slightly lower dominant entrance pore size is found for the BD-7 core with respect to BD-6 core (Figure 1-17). The initial condition for the BD-7 specimens is again found on the main drying path, while the initial rewetting phase highlights the hysteretic features of the tested material.

Table 2-3: Fitting parameters for main drying and main wetting paths of BD shale samples.

Core	n_{VG} **(-)**	P_{VG} **(MPa)**	**λ (-)**	n_{VG} **(-)**	P_{VG} **(MPa)**	**λ (-)**
	Main wetting			Main drying		
BD-7	-	-	-	1.73	200	2.29
BD-18	1.09	200	2.77	-	-	-
BD-30	0.90	125	2.75	-	-	-

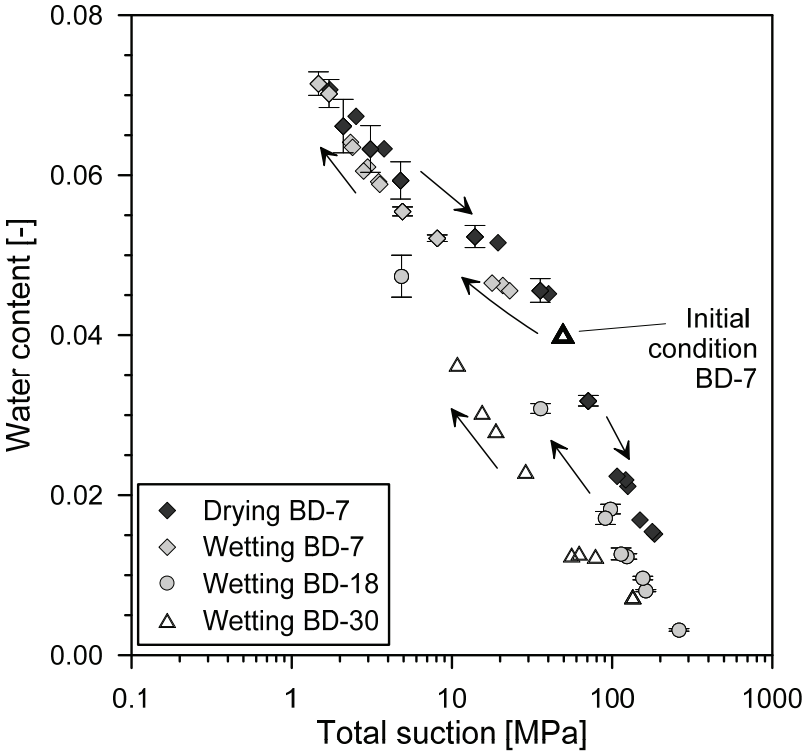

Figure 2-17: Retention behaviour of BD shale samples in terms of water content versus total suction.

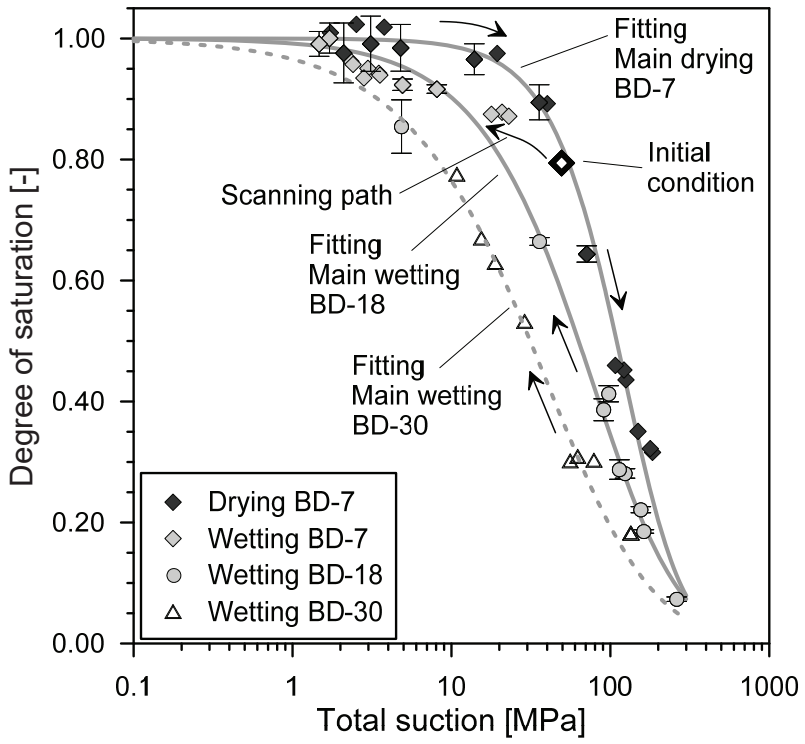

Figure 2-18: Retention behaviour of BD samples in terms of degree of saturation versus total suction.

2.6. Summary and conclusions

In spite of the relevance of shales to emerging energy-related geomechanical applications for which variations in the degree of saturation are expected, the characterization of shale retention properties has received limited attention. This chapter presented the results of an experimental analysis that was designed and carried out in order to gain insight on shales retention behaviour. Testing materials with very low porosity and pore size constituted a great challenge in this investigation. An advanced testing methodology was designed, which involves direct control of the shales water content and the subsequent measurement of the total suction and void ratio.

The proposed technique has been shown to be capable of capturing the important features of retention behaviour, such as the hysteresis domain and the existence of scanning paths when the shale is initially rewetted from its after-extraction state. The assessment of the volume change due to suction variation has allowed to express the retention behaviour in terms of degree of saturation, to capture the air entry value along the main drying paths, and to highlight the significant changes in porosity undergone by the shales along wetting and drying hydraulic paths.

Results from samples of different shale types, such as Opalinus Clay and Brown Dogger, have been presented. Testing different shale types allowed for the possibility to capture the important features of their retention behaviour such as the dependency of the air entry value on the void ratio and the impact of mineralogy and dominant entrance pore size on the retention properties. This fact is highlighted in Figure 2-18: the BD-30 core present a higher quartz content and a greater dominant entrance pore size, its retention capacity appears to be lower with respect to the other tested cores. The obtained results from the tested shale samples are believed to be of great importance, considering that these materials are host rock candidates for a deep geological repository of high-level nuclear waste. Thus, retention capacity will be a fundamental component of the ventilation (drying) and resaturation (wetting) phase of the repository.

2.7. References

Airò Farulla, C., Battiato, A. and Ferrari, A. The void ratio dependency of the retention behaviour for a compacted clay. Unsaturated Soils, Unsaturated Soils, (2010). 417-422.

Cardoso, R., Romero, E., Lima, A. and Ferrari, A. (2007). A comparative study of soil suction measurement using two different high-range psychrometers. Experimental unsaturated soil mechanics, Springer**:** 79-93.

Decagon. WP4C Dewpoint Potentiameter - Operator's Manual Decagon Devices (2010).

Ferrari, A., Favero, V., Marschall, P. and Laloui, L. Experimental analysis of the water retention behaviour of shales. International Journal of Rock Mechanics and Mining Sciences (2014) 72: 61-70.

Fredlund, D.G. and Rahardjo, H. Soil mechanics for unsaturated soils, John Wiley & Sons, (1993).

Josh, M., Esteban, L., Delle Piane, C., Sarout, J., Dewhurst, D. and Clennell, M. Laboratory characterisation of shale properties. Journal of Petroleum Science and Engineering (2012) 88: 107-124.

Keller, L.M., Schuetz, P., Erni, R., Rossell, M.D., Lucas, F., Gasser, P. and Holzer, L. Characterization of multi-scale microstructural features in Opalinus Clay. Microporous and mesoporous materials (2013) 170: 83-94.

Laloui, L., Salager, S. and Rizzi, M. Retention behaviour of natural clayey materials at different temperatures. Acta Geotechnica (2013) 8(5): 537-546.

Leong, E.-C., Tripathy, S. and Rahardjo, H. Total suction measurement of unsaturated soils with a device using the chilled-mirror dew-point technique. Geotechnique (2003) 53(2): 173-182.

Lima, A., Romero, E., Piña, Y., Gens, A. and Li, X. (2012). Water retention properties of two deep belgian clay formations. Unsaturated Soils: Research and Applications, Springer**:** 179-184.

Muñoz, J.J. Thermo-hydro-mechanical analysis of soft rock. Application to a large scale heating test and large scale ventilation test, Universitat Politècnica de Catalunya, (2007).

Murray, E.J. and Sivakumar, V. Unsaturated soils: a fundamental interpretation of soil behaviour, John Wiley & Sons, (2010).

Nuth, M. and Laloui, L. Advances in modelling hysteretic water retention curve in deformable soils. Computers and Geotechnics (2008) 35(6): 835-844.

Péron, H., Hueckel, T., Laloui, L. and Hu, L. Fundamentals of desiccation cracking of fine-grained soils: experimental characterisation and mechanisms identification. Canadian geotechnical journal (2009) 46(10): 1177-1201.

Péron, H., Laloui, L. and Hueckel, T. An improved volume measurement for determining soil water retention curves. (2006).

Pham, Q., Vales, F., Malinsky, L., Minh, D.N. and Gharbi, H. Effects of desaturation–resaturation on mudstone. Physics and Chemistry of the Earth, Parts A/B/C (2007) 32(8): 646-655.

Ramos da Silva, M., Schroeder, C. and Verbrugge, J.-C. Unsaturated rock mechanics applied to a low-porosity shale. Engineering Geology (2008) 97(1): 42-52.

Romero, E., Della Vecchia, G. and Jommi, C. An insight into the water retention properties of compacted clayey soils. Geotechnique (2011) 61(4): 313-328.

Romero, E., Gens, A. and Lloret, A. Water permeability, water retention and microstructure of unsaturated compacted Boom clay. Engineering Geology (1999) 54(1): 117-127.

Romero, E., Senger, R. and Marschall, P. Air Injection Laboratory Experiments on Opalinus Clay. Experimental techniques, Results and Analyses. 3rd EAGE Shale Workshop-Shale Physics and Shale Chemistry, (2012).

Romero, E. and Vaunat, J. Retention curves of deformable clays. Experimental evidence and theoretical approaches in unsaturated soils (2000): 91-106.

Salager, S., Nuth, M., Ferrari, A. and Laloui, L. Investigation into water retention behaviour of deformable soils. Canadian geotechnical journal (2013) 50(2): 200-208.

Schmitt, L., Forsans, T. and Santarelli, F. Shale testing and capillary phenomena. International journal of rock mechanics and mining sciences & geomechanics abstracts, Elsevier, (1994). 411-427.

Tarantino, A. (2010). Basic concepts in the mechanics and hydraulics of unsaturated geomaterials. Mechanics of Unsaturated Geomaterials. L. Laloui, ISTE - John Wiley & Sons**:** 3-28.

Valès, F., Minh, D.N., Gharbi, H. and Rejeb, A. Experimental study of the influence of the degree of saturation on physical and mechanical properties in Tournemire shale (France). Applied Clay Science (2004) 26(1): 197-207.

Van Genuchten, M.T. A closed-form equation for predicting the hydraulic conductivity of unsaturated soils. Soil science society of America journal (1980) 44(5): 892-898.

Vanapalli, S., Fredlund, D. and Pufahl, D. The influence of soil structure and stress history on the soil-water characteristics of a compacted till. (1999).

Villar, M. and Romero, F. Oplainus Clay 2–phase flow parameters. FORGE Report (2012) D5: 14-37.

Wan, M., Delage, P., Tang, A.M. and Talandier, J. Water retention properties of the Callovo-Oxfordian claystone. International Journal of Rock Mechanics and Mining Sciences (2013) 64: 96-104.

Wheeler, S., Sharma, R. and Buisson, M. Coupling of hydraulic hysteresis and stress–strain behaviour in unsaturated soils. Geotechnique (2003) 53(1): 41-54.

Zhang, C.-L., Rothfuchs, T., Su, K. and Hoteit, N. Experimental study of the thermo-hydro-mechanical behaviour of indurated clays. Physics and Chemistry of the Earth, Parts A/B/C (2007) 32(8): 957-965.

Chapter 3
One-Dimensional Compression and Consolidation of Natural and Remoulded Shales

3.1. Foreword

This chapter is dedicated to the analysis of the one-dimensional compression and consolidation of shales both at the natural and remoulded states. Section 3.2 presents a comprehensive methodology to analyse the behaviour of shales during oedometric compression and consolidation. It reports the analysis of results obtained on Opalinus Clay shales, in order to demonstrate the performance of the presented methodology. Section 3.2 is based on the paper entitled "One-dimensional compression and consolidation of shales" (Ferrari, Favero and Laloui, 2016) , which is published in the International Journal of Rock Mechanics and Mining Science. Section 3.3 goes deeper in the analysis of the hydro-mechanical behaviour of natural and remoulded shales: additional results on remoulded Opalinus Clay are presented, and the role of diagenesis and depth, and their impact on the response of the material are investigated. Section 3.3 is based on the paper entitled "On the hydro-mechanical behaviour of remoulded and natural Opalinus Clay shale" (Favero, Ferrari and Laloui, 2016), which is published in the Engineering Geology Journal.

Finally, additional results and analyses on the one-dimensional compression and consolidation of deep Swiss shales, obtained during the PhD research but not included in the above-mentioned papers are reported in section 3.4. In the same section, further insights into the swelling behaviour of Opalinus Clay and on the permeability-void ratio relationship of the tested shales are presented and discussed.

3.2. One-dimensional compression and consolidation of shales

One of the main concerns related to tunnel excavations, drilling operations and wellbore stability in shales is the generation of excess pore water pressure due to changes in mechanical stress, and the consolidation of shales is a fundamental process that must be considered. Creep phenomena must also be taken into account when the long-term behaviour of the shale formation is relevant. Compaction and consolidation processes are well-understood for soils, but additional factors must be considered in the analysis of hydro-mechanical couplings in shales; the poroelastic features may no longer be negligible, and testing at high mechanical stresses becomes critical for studying the behaviour of the material under in situ stress conditions and to observe the transition from pre- to post-yield compaction behaviour.

This section presents a comprehensive methodology for analysing the compression and consolidation behaviour of shales, in which all aspects noted above are addressed.

3.2.1. Background

The relevance of shales in many geo-energy related fields has led to the need for a profound understanding of their hydro-mechanical behaviour. Variations in stress levels and the consequent changes in porosity affect the stiffness and permeability of the material, which are fundamental parameters in the assessment of the performance of a shale formation as reservoir rock for shale gas extraction, cap rock for CO_2 storage, or host rock for nuclear waste disposal. As proof of the relevance of this topic to engineering practice, the quantification of the volumetric behaviour of

shales under mechanical loading has received significant attention in recent decades. Mesri et al. (1978) studied the compression behaviour of four shales from the USA (Duck Creek shale, Crab Orchard shale, Cucaracha shale and Bearpaw shale) under oedometric and isotropic conditions, highlighting the increase in the swelling index as a function of the overconsolidation ratio of the material. Picarelli (1991) presented the results of one-dimensional tests on Leviano clay shale in which a number of loading-unloading cycles were performed, evidencing the increase in the swelling index with the yield stress; similar results were also reported by Aversa et al. (1993) for the Bisaccia clay shale. Savage and Braddock (1991) studied the isotropic consolidation processes of the Pierre shale. Wong (1998) reported the oedometric compression curves of La Biche shale. Mohajerani et al. (2011) reported data concerning the oedometric response of COx argillite. Gutierrez et al. (2015) focused on the consolidation of the Mancos shale.

Changes in stress in clayey materials generate excess pore water pressures to be dissipated over time, causing a delay in reaching the final strain state of the material. Therefore, it is important to be able to analyse and predict this time-dependent consolidation process. Creep phenomena are also involved when the long-term behaviour of such a system is considered, and the clear distinction of the primary consolidation processes, which are related to the dissipation of excess pore water pressures, from the secondary consolidation phenomena (creep) is of critical importance. Despite the significance of the consolidation process in shale applications, very few studies have discussed the time-dependent settlement behaviour of shales and argillites (Savage and Braddock, 1991; Mohajerani et al., 2011; Gutierrez et al., 2015). Indeed, although the compaction and consolidation processes induced by the application of loads have been well understood for soils since the pioneering work of Terzaghi (1923), important issues remain unresolved in the analysis of the hydro-mechanical behaviour of shales. Additional factors related to the hydro-mechanical couplings in shales, such as the pore pressure coefficients and poroelastic properties (Biot, 1941; Skempton, 1954) as well as their dependency on the stress level (Detournay and Cheng, 1993), must be included in analyses of settlement evolution (Savage and Braddock, 1991; Mohajerani et al., 2011; Gutierrez et al., 2015) and in assessments of the porosity changes induced by loading.

A proper analysis of consolidation behaviour is also needed when additional information is to be inferred from the settlement evolution, such as the strain rate to be adopted in triaxial testing or the permeability for a given loading step.

Moreover, compared with conventional soil testing, shale testing requires addressing additional issues. Because of their stress history and diagenesis, shales exhibit high yield stresses (frequently greater than 10 MPa); in addition, shale formations are typically located at great depths. As a consequence, the mechanical testing of shales requires the ability to work in high-stress conditions. Testing under high confining stresses may be necessary to observe the transition from pre- to post-yield compaction behaviour as well as to assess the poroelastic properties of the material under in situ stress conditions. However, the instantaneous application of high vertical stresses in the laboratory is rarely feasible. Indeed, the time dependence of the loading must be considered when analysing the settlement evolution (Gibson, 1958; Olson, 1977; Conte and Troncone, 2006; Hsu and Lu, 2006; Hanna et al., 2011; Lovisa et al., 2012).

Considering all the concerns discussed above, this chapter introduces a comprehensive methodology for analysing the compression and consolidation behaviour of shales. The developed methodology allows oedometric tests to be performed on shales under a wide range of vertical effective stresses and allows the displacement evolution over time to be analysed through a meticulous analytical procedure. For this purpose, an apparatus was designed to perform high-pressure oedometric tests by applying a maximum vertical total stress of 100 MPa and simultaneously controlling the pore water pressure of the specimen. The proposed analytical method combines (i) a modified form of the classical Biot theory (Biot, 1941) to account for the behaviour of shales under oedometric conditions and (ii) an extended one-dimensional consolidation theory to consider the poroelastic behaviour of shales and time-dependent loading conditions. The proposed analytical method allows information to be gathered on the coefficient of consolidation, stiffness, poroelastic properties, secondary compression and permeability of the tested material as a function of the applied stress.

The experimental device and procedures adopted in this work are described in the following section. Subsequently, the analytical method developed for the analysis of the consolidation of shales under non-instantaneous loading is presented. The application of the presented methodology is demonstrated through a series of tests performed on Opalinus Clay shale.

3.2.2. Experimental apparatus and techniques

The experimental component of the developed methodology for analysing shale compression and consolidation behaviour is based on the use of an ad hoc oedometric set-up designed to perform loading-unloading cycles at high stress levels. The following sections provide details on the apparatus, the specimen preparation and the experimental procedures used in the tests.

3.2.2.1. The high-pressure oedometric cell

The developed experimental apparatus is depicted in Figure 3-1. It consists of an oedometric cell inserted into a rigid stainless steel frame, two pressure/volume (PV) controllers and a system of LVDTs. The cell is made of stainless steel and consists of an oedometric ring of 12.5 mm in height and 35 mm in internal diameter inserted into a high-rigidity cylindrical vessel to minimize expansion in the radial direction. The bases of the specimen in the oedometric ring are in contact with metallic plates equipped with a drainage system. This latter is composed of a system of vertical holes of 0.5 mm in diameter, which are connected to a spiral path to remove the air from the bases before any pore water pressure is applied. Pre-compressed filter paper disks are placed between the specimen and the plates. The pore water pressures at the bottom and top bases are controlled by means of a PV controller, which also allows the pore water volume exchanges to be measured. The upper base of the specimen is in contact with a fixed piston constrained by the high-rigidity frame. The vertical displacements are measured by the three LVDTs (with a resolution of 1 μm), which measure the relative displacement of the cell with respect to the piston. Because of the high range of vertical stress that can be applied by the apparatus, the deformation of the system could be significant and requires a proper evaluation. In fact, because of the high stiffness of shales, the displacement of the system

could seriously compromise the evaluation of the real volume change of the specimen. Therefore, the system displacement must be quantified and corrected for each loading step. A calibration with a dummy metallic sample revealed that the typical unwanted displacement in this system ranges from 20 to 180 μm for vertical total stresses from 1 to 100 MPa. As detailed in the following sections, the analytical solution derived for the analysis of the settlement versus time curves is capable of automatically accounting for the deformation of the device.

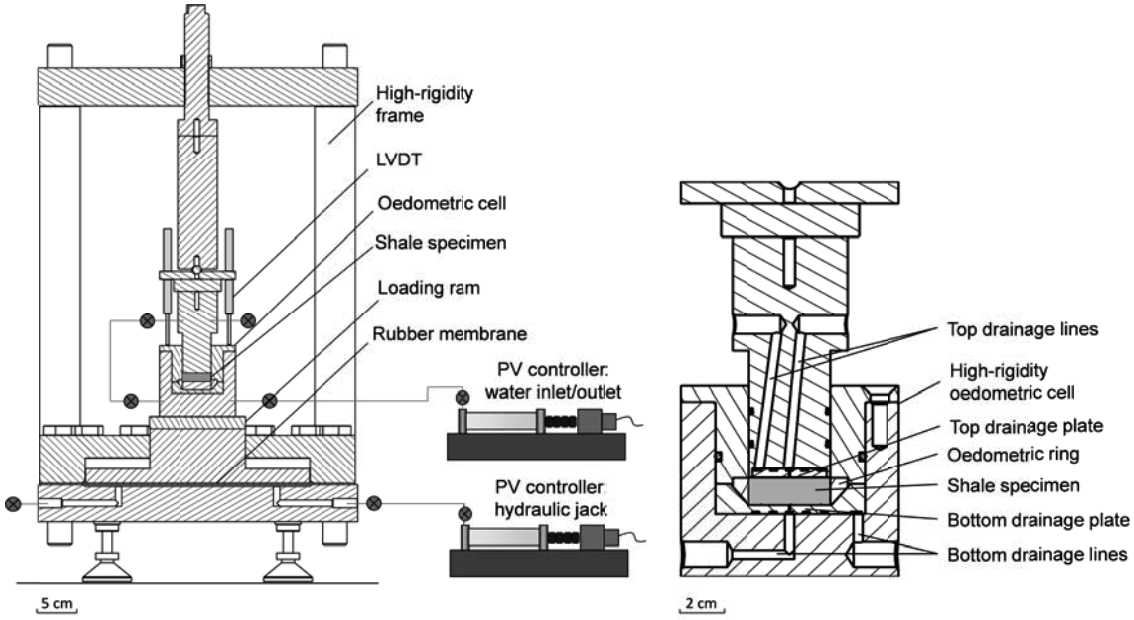

Figure 3-1: Overview of the high-pressure oedometric setup.

The vertical load is applied by a hydraulic jack connected to a PV controller. The vertical stress acting on the specimen is obtained by amplifying the pressure imposed by the controller by means of the ratio of the area of the specimen to the area of the hydraulic jack. The relationship between the pressure specified by the controller and the vertical stress on the specimen was assessed via calibration. For the lowest values of controller pressure, the cell was filled with water and the incremental increase in the water pressure was measured as a function of the pressure applied by the controller. For high stress values, a load cell was placed in contact with the load piston (Salager et al., 2010) and the friction developed in the system was quantified.

The instantaneous application of high confining stresses when testing geomaterials is not feasibly achievable. In the loading system used here, water must be pressurized and displaced from the controller to the hydraulic jack; the rate of water transfer depends not only on the performance of the PV controller but also on the compressibility values of the tested material and the apparatus. As a consequence, a significant proportion of the consolidation can develop before the target vertical stress is reached. Thus, any analysis of the settlement versus time curves must consider the time dependence of the loading conditions. Figure 3-2 presents a typical curve shape for the evolution of the applied

vertical total stress (σ_z) once the target pressure is set in the PV controller. A stepwise expression is used to describe this evolution in terms of four parameters, t_b, t_c, σ_{zb} and σ_{zc}:

$$\sigma_z(t) = \frac{\sigma_{zb}}{t_b} t,\ 0 \le t \le t_b \tag{3.1}$$

$$\sigma_z(t) = \sigma_{zb} + \left(\frac{\sigma_{zc} - \sigma_{zb}}{t_c - t_b} \right)(t - t_b),\ t_b \le t \le t_c \tag{3.2}$$

$$\sigma_z(t) = \sigma_{zc},\ t \ge t_c \tag{3.3}$$

For the purpose of developing the analytical solution presented in this work, it is convenient to write the expression for the derivative of σ_z versus time, as follows:

$$\frac{d\sigma_z}{dt} = \frac{\sigma_{zb}}{t_b},\ 0 \le t \le t_b \tag{3.4}$$

$$\frac{d\sigma_z}{dt} = \left(\frac{\sigma_{zc} - \sigma_{zb}}{t_c - t_b} \right),\ t_b \le t \le t_c \tag{3.5}$$

$$\frac{d\sigma_z}{dt} = 0,\ t \ge t_c \tag{3.6}$$

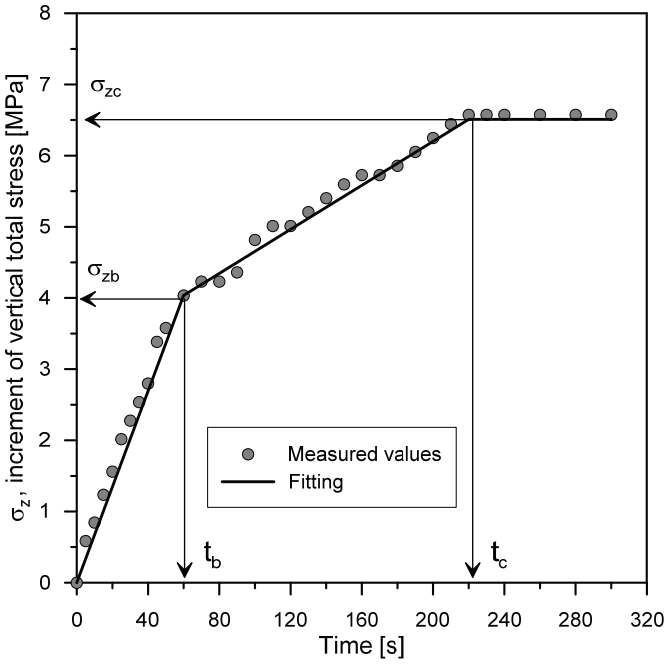

Figure 3-2: Typical increase in the vertical total stress as a function of time; t = 0 is the time at which the target pressure is set on the PV controller.

3.2.2.2. Specimen preparation procedure

Because of the swelling/shrinkage behaviour of shales induced by changes in water content (as highlighted in Chapter 2), one of the main concerns during specimen preparation is the need to preserve the initial water content; this need implies that no water should be used during the cutting phase. In addition, when oedometric conditions are sought, perfect contact between the specimen and the internal surface of the oedometric ring must be achieved. To satisfy these requirements, an ad hoc procedure was developed and systematically applied to produce the specimens for the oedometric tests from cores of the shales to be tested. The procedure began with the initial cutting of a slice of material with a thickness of approximately 20 mm from the original core, without removing the original packaging (Figure 3-3a-b). The diameter of the slice was progressively reduced to yield a disk with a diameter slightly larger than that of the final confining ring; in this phase, a lathe was used, which was operated in a room with a controlled temperature and relative humidity (T = 23 °C, RH ≈ 45%). The lathe also allowed regular and parallel top and bottom faces to be obtained (Figure 3-3c-d). The final re-coring of the specimen was performed by pushing the oedometric ring into the prepared specimen using a hydraulic press (Figure 3-3e).

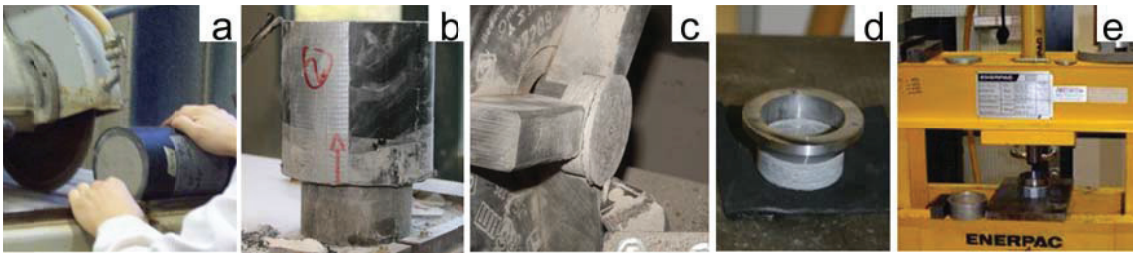

Figure 3-3: Specimen preparation procedure for oedometric testing of natural shales.

3.2.2.3. Experimental procedure

The general experimental procedure for the performance of high-pressure oedometric tests on shale samples under saturated and isothermal conditions (the temperature of the laboratory was controlled at 23±1°C). is described in this section. After the initial conditions of the specimen (size, weight and water content) were determined and the oedometric cell was assembled, the procedure for saturating the specimen was begun. Saturation was performed by applying a pore water pressure at the bottom base. The flushing of the specimen was initially performed from the bottom only to avoid the trapping of air, while the top of the specimen was maintained at zero pore water pressure. During this phase, the volume expansion of the specimen was limited by increasing the vertical stress as soon as a tendency to swell was registered by the LVDT system. The vertical stress required to prevent volumetric expansion provides direct information regarding the swelling pressure of the specimen. Once the rate of swelling pressure development stabilized, a pore water pressure was imposed at both the bottom and top bases of the specimen. In general, several days were required for the completion of the saturation phase (i.e. constant swelling pressure was observed and no more water flowing into the cell was recorded). Afterwards, the mechanical loading-unloading cycles were performed in steps.

In each loading step, the excess pore water pressure was allowed to completely dissipate (drained conditions). The settlement evolution over time was recorded by the LVDT system while the pressure in the controller connected to the hydraulic jack was held constant.

3.2.3. Theory of the one-dimensional consolidation of shales

This section presents a framework for analysing the compressibility and consolidation process of a shale specimen subjected to loading under oedometric conditions; the framework is formulated to account for the poroelastic behaviour of the material and for the time-dependent loading conditions used in the experiments.

3.2.3.1. Poroelastic behaviour under oedometric conditions

Poroelastic constitutive equations provide a coupled hydro-mechanical description of the volumetric response of porous materials subjected to a particular change in the total stress tensor and pore water pressure (Detournay and Cheng, 1993). Under oedometric conditions, radial deformations are prevented such that the vertical strain equals the volumetric strain; in other words, the vertical strain is sufficient to describe the volumetric response upon loading. The vertical total stress is the only stress component that is controlled, and in general, no information is available on the radial stress; this lack of information implies that a complete assessment of the changes in the total stress tensor is not possible. Even in the simplest case of isotropic poroelastic materials, for which the volumetric response is affected only by changes in mean stress and pore water pressure, information on the radial stress would be required to compute the mean total stress. As a first attempt, a value of the lateral stress ratio could be assumed; then, the radial stress, and consequently the mean stress, could be computed. However, the lateral stress ratio is dependent on the stress path (Mesri and Hayat, 1993), and its behaviour has not been extensively quantified for shales. Moreover, in shales, the hypothesis of isotropy is generally invalid; therefore, the poroelastic constitutive equations should consider the anisotropic features of the material, and a large number of constitutive constants should be introduced into the analysis (Coussy, 1991). A proper quantification of these constants would be difficult to perform using only the information provided by an oedometric test. To overcome these limitations (the unknown radial stress and the relevant number of constitutive constants for the anisotropic case), an ad hoc poroelastic formulation is presented in this work for the analysis of the one-dimensional consolidation of shales. The use of moduli and coefficients specifically relevant to oedometric conditions allows the unknown radial stress to be overcome and the number of constitutive constants to be reduced. However, the moduli and coefficients determined through this analysis are specific to a particular loading direction and to the particular case in which lateral deformations are prevented.

In the following, the basic constitutive equations for a poroelastic material are derived for oedometric conditions; they apply to oedometric tests in which the loads and the unloads are carried out in steps, and time is allowed for the dissipation of the excess pore water pressures generated in each loading/unloading step. The response of the material in terms of settlement versus time for each load increment is analysed independently from the other steps; in this sense the moduli adopted in the

following are to be intended as tangent moduli. The analysis is presented for a load applied in the vertical direction, z. The vertical total stress (σ_z) and pore water pressure (u) are considered to be positive when compressive; the vertical strain (ε_z) and volumetric strain (ε) are considered to be positive for volume reduction. As mentioned, under oedometric conditions, the variation in the vertical strain is equal to the variation in the volumetric strain ($\varepsilon_z = \varepsilon$). The fluid content ($\theta$) is defined as the ratio of the volume of water (V_w) to the initial total volume (V_0):

$$\theta = \frac{V_w}{V_0} \tag{3.7}$$

The volumetric relations for a linear poroelastic material (Detournay and Cheng, 1993) can be adapted to the oedometric case as follows:

$$\delta\varepsilon = \frac{\delta\sigma_z}{E_{oed}} - \frac{\delta u}{H_{oed}} \tag{3.8}$$

$$\delta\theta = -\left(\frac{\delta\sigma_z}{H_{oed}} - \frac{\delta u}{R_{oed}} \right) \tag{3.9}$$

where E_{oed} is the oedometric modulus, which expresses the ratio of the increment of the applied total vertical stress to the corresponding increment of volumetric strain when the pore water pressure returns to its initial value ($\delta u = 0$) and H_{oed} and R_{oed} are poroelastic constitutive constants that are formally equivalent to the constants introduced by Biot (1941), adapted here to the oedometric case. The use of the same constant H_{oed} in both Eq. (3.8) and Eq. (3.9) implies the assumption of reversibility of the deformation process. As commonly done in geomechanics, this assumption is considered valid during the single loading steps. A new set of constitutive equations equivalent to the previous set can be obtained by replacing H_{oed} and R_{oed} with two alternative poroelastic coefficients. In this manner, the behaviour upon loading in undrained and drained conditions can be considered separately. In undrained (or short-term) conditions, there is no variation in the fluid content, and pore water pressure builds up as a result of the loading; Eq. (3.9) yields:

$$\delta u = \frac{R_{oed}}{H_{oed}} \delta\sigma_z = C\delta\sigma_z \tag{3.10}$$

where C is the coefficient defining the ratio of the increment in the pore water pressure to the increment in the vertical total stress under one-dimensional and undrained conditions (Lambe and Whitman, 1979):

$$C = \left. \frac{\delta u}{\delta\sigma_z} \right|_{\varepsilon_r = 0} \tag{3.11}$$

where ε_r is the radial strain. In drained (long-term) conditions, the excess pore water pressure generated by the loading dissipates ($\delta u = 0$); combining Eq. (3.8) and Eq. (3.9) yields

$$\delta\theta = -\frac{E_{oed}}{H_{oed}}\delta\varepsilon = -\alpha_{oed}\delta\varepsilon \tag{3.12}$$

where α_{oed} is the Biot coefficient, here defined for the oedometric case as the ratio of the variation in the fluid content to the volumetric deformation when the development of radial strain is prevented:

$$\alpha_{oed} = \left.\frac{\delta\theta}{\delta\varepsilon}\right|_{\varepsilon_r=0} = \left.\frac{\delta V_w}{\delta V}\right|_{\varepsilon_r=0} \tag{3.13}$$

Considering the poroelastic coefficients C and α_{oed}, a new set of volumetric relations can be written that is equivalent to Eq. (3.8) and Eq. (3.9):

$$\delta\varepsilon = \frac{1}{E_{oed}}(\delta\sigma_z - \alpha_{oed}\delta u) \tag{3.14}$$

$$\delta\theta = -\frac{\alpha_{oed}}{E_{oed}}\left(\delta\sigma_z - \frac{\delta u}{C}\right) \tag{3.15}$$

3.2.3.2. The consolidation equation

Along with the poroelastic volumetric response, the consolidation behaviour is governed by the continuity equation for the pore fluid. Under the assumption of an incompressible fluid phase and a homogeneous permeability, the continuity equation in the z direction is written as follows:

$$k_z\frac{\partial^2 h}{\partial z^2} = \frac{\partial\theta}{\partial t} \tag{3.16}$$

where k_z is the coefficient of permeability in the vertical direction and h is the total head. The total head can be expressed as (Lambe and Whitman, 1979)

$$h = z + (u_e + u_{ss})/\gamma_w \tag{3.17}$$

where z is the elevation head, u_e is the excess pore water pressure generated by the loading that is dissipated during the consolidation process, u_{ss} is the steady-state pore water pressure at the end of the consolidation process, and γ_w is the specific weight of water. Because the pore water pressure varies linearly with the elevation in the final steady-state conditions, the left-hand side of Eq. (3.16) becomes

$$k_z \frac{\partial^2 h}{\partial z^2} = \frac{k_z}{\gamma_w} \frac{\partial^2 u_e}{\partial z^2} \tag{3.18}$$

The variations in fluid content, vertical total stress and pore water pressure can be approximated in terms of their derivatives:

$$\delta\theta = \frac{\partial \theta}{\partial t}\delta t\ ,\ \delta\sigma_z = \frac{\partial \sigma_z}{\partial t}\delta t\ ,\ \delta u = \delta u_e = \frac{\partial u_e}{\partial t}\delta t \tag{3.19}$$

where, by definition, the steady-state component of the pore water pressure (i.e. the back pressure applied in the performed tests) has disappeared from the last equation. By substituting Eq. (3.19) into Eq. (3.15), the variation in the fluid content over time can be written as

$$\frac{\partial \theta}{\partial t} = -\frac{\alpha_{oed}}{E_{oed}}\left(\frac{\partial \sigma_z}{\partial t} - \frac{1}{C}\frac{\partial u_e}{\partial t}\right) \tag{3.20}$$

Finally, by considering Eq. (3.18) and Eq. (3.20), Eq. (3.16) can be written as

$$\frac{k_z E_{oed} C}{\alpha_{oed}\gamma_w}\frac{\partial^2 u_e}{\partial z^2} = \frac{\partial u_e}{\partial t} - C\frac{\partial \sigma_z}{\partial t} \tag{3.21}$$

By introducing the coefficient of consolidation c_v, considered constant during each loading step, and defined as

$$c_v = \frac{k_z E_{oed} C}{\alpha_{oed}\gamma_w} \tag{3.22}$$

Eq. (3.21) can be written as follows:

$$c_v \frac{\partial^2 u_e}{\partial z^2} = \frac{\partial u_e}{\partial t} - C\frac{\partial \sigma_z}{\partial t} \tag{3.23}$$

Eq. (3.23) is the consolidation equation that describes the one-dimensional consolidation process in shales. It is an extended form of the classical Terzaghi consolidation equation that accounts for the poroelastic behaviour of shales and for a time-dependent loading. The poroelastic behaviour of shales is considered through the constitutive parameters C and α_{oed}, which contribute to the definition of the coefficient of consolidation. Even if the poroelastic coefficients as well as the coefficient of consolidation are considered constant during the analysis of a loading step, they vary for the different loading steps. The parameter C also influences the effect of the time-dependent loading on the consolidation process: a higher value of C corresponds to a higher excess pore water pressure, generated by the increment in total stress, which must be dissipated. The coefficient of consolidation expressed in Eq. 3.22 describes a 1D consolidation problem which occurs in oedometric conditions; Wang (2000) proposes an expression for the coefficient of consolidation which can be considered

equivalent to Eq. 3.22 but not specific to the oedometric case. Therefore the radial stress conditions cannot be neglected in the analysis proposed by this author. An analytical solution to Eq. (3.23) is provided in the following section.

3.2.3.3. Analytical solution to the consolidation equation under time-dependent loading

In the analytical method developed for analysing the poroelastic and consolidation behaviour of shales, it is considered that the total measured settlement of a specimen (ρ_{tot}) can be expressed in terms of three different components:

$$\rho_{tot}(t) = \rho_0(t) + \rho'(t) + \rho''(t) \tag{3.24}$$

where ρ_0 is the component of the registered settlement related to the deformation of the device, ρ' is the component of the settlement due to the primary consolidation of the specimen under the applied load, and ρ'' is the component of the settlement due to secondary compression (creep). Expressions for these three different components of the measured settlement are provided in the following sections.

3.2.3.3.1. Settlement due to the deformation of the testing device

As the vertical load is applied over time, the device settlement also develops over time; consequently, it can be expressed as follows:

$$\rho_0(t) = \frac{\rho_b}{t_b} t,\ 0 \le t \le t_b \tag{3.25}$$

$$\rho_0(t) = \rho_b + \left(\frac{\rho_c - \rho_b}{t_c - t_b} \right)(t - t_b),\ t_b \le t \le t_c \tag{3.26}$$

$$\rho_0(t) = \rho_c,\ t \ge t_c \tag{3.27}$$

where ρ_b is the settlement at time t_b and ρ_c is the settlement at time t_c , corresponding to the final constant value of the deformation of the device.

3.2.3.3.2. Primary consolidation settlement

Primary consolidation is related to the evolution of the excess pore water pressure in time and space. The general solution to the one-dimensional consolidation equation for a time-dependent loading was presented by Olson (1977). The Olson solution is adapted here to the case of a poroelastic geomaterial, whose consolidation behaviour is described by the consolidation equation given in Eq. (3.23), subjected to a time-dependent load as described in Eq.(3.1), (3.2), (3.3) and in Figure 3-2. Unlike the original Olson solution, the equations used in this work consider that the initial excess

pore water pressure is not equal to the increment in the vertical stress through the use of the coefficient *C* (Eq.(3.11)).

To describe the primary consolidation process, the time factors T, T_b and T_c are defined as follows:

$$T = \frac{c_v t}{H^2} \quad T_b = \frac{c_v t_b}{H^2} \quad T_c = \frac{c_v t_c}{H^2} \tag{3.28}$$

where *H* is the drainage path length (half of the specimen height in the oedometric set-up) and t_b and t_c are the values of time used to described the evolution of the load over time (Eq.(3.1), (3.2), (3.3)). Three different equations for the evolution of the excess pore water pressure are obtained:

$$u_e = \sum_{m=0}^{\infty} \frac{2C\sigma_{zb}}{M^3 T_b}\left(\sin\frac{Mz}{H}\right)\left(1-e^{-M^2 T}\right) \quad for\ 0 \le t \le t_b \tag{3.29}$$

$$\begin{aligned} u_e &= \sum_{m=0}^{\infty} \frac{2C\sigma_{zb}}{M^3 T_b}\left(\sin\frac{Mz}{H}\right)\left(e^{M^2 T_b}-1\right)e^{-M^2 T} \\ &+\sum_{m=0}^{\infty} \frac{2C\left(\sigma_{zc}-\sigma_{zb}\right)}{M^3\left(T_c-T_b\right)}\left(\sin\frac{Mz}{H}\right)\left(1-e^{-M^2(T-T_b)}\right) \quad for\ t_b \le t \le t_c \end{aligned} \tag{3.30}$$

$$\begin{aligned} u_e &= \sum_{m=0}^{\infty} \frac{2C\sigma_{zb}}{M^3 T_b}\left(\sin\frac{Mz}{H}\right)\left(e^{M^2 T_b}-1\right)e^{-M^2 T} + \\ &+\sum_{m=0}^{\infty} \frac{2C\left(\sigma_{zc}-\sigma_{zb}\right)}{M^3\left(T_c-T_b\right)}\left(\sin\frac{Mz}{H}\right)\left(e^{-M^2(T-T_c)}-e^{-M^2(T-T_b)}\right) for\ t > t_c \end{aligned} \tag{3.31}$$

where $M = 0.5\pi(2m+1)$, with m being an integer.

Considering Eq. (3.14), the primary consolidation settlement is computed as follows:

$$\rho'(t) = \int_0^{2H} \frac{\delta\sigma_z(t) - \alpha_{oed}\delta u(t,z)}{E_{oed}} dz \tag{3.32}$$

Inserting Eq. (3.1), (3.2), (3.3) and Eq. (3.29), (3.30) and (3.31) into Eq. (3.32) yields the following equations for the time-dependent settlement curves for primary consolidation:

For $0 \le t \le t_b$

$$\rho'(t) = \frac{2H}{E_{oed}}\left(\frac{\sigma_{zb}}{t_b}t - \alpha_{oed}\sum_{m=0}^{\infty}\frac{2C\sigma_{zb}}{M^4 T_b}\left(1-e^{-M^2 T}\right)\right) \tag{3.33}$$

For $t_b \le t \le t_c$

$$\rho'(t)=\frac{2H}{E_{oed}}\left\{\sigma_{zb}+\left(\frac{\sigma_{zc}-\sigma_{zb}}{t_c-t_b}\right)(t-t_b)-\alpha_{oed}\sum_{m=0}^{\infty}\frac{2}{\mathrm{M}^4}\cdot\left[\begin{array}{l}\dfrac{C\sigma_{zb}\left(e^{\mathrm{M}^2\mathrm{T_b}}-1\right)e^{-\mathrm{M}^2\mathrm{T}}}{\mathrm{T_b}}\\ +\dfrac{C\left(\sigma_{zc}-\sigma_{zb}\right)}{\left(\mathrm{T_c}-\mathrm{T}_b\right)}\left(1-e^{-\mathrm{M}^2(\mathrm{T}-\mathrm{T_b})}\right)\end{array}\right]\right\} \quad (3.34)$$

For $t>t_c$

$$\rho'(t)=\frac{2H}{E_{oed}}\left\{\sigma_{zc}-\alpha_{oed}\sum_{m=0}^{\infty}\frac{2}{\mathrm{M}^4}\left[\begin{array}{l}\dfrac{C\sigma_{zb}\left(e^{\mathrm{M}^2\mathrm{T_b}}-1\right)e^{-\mathrm{M}^2\mathrm{T}}}{\mathrm{T_b}}\\ +\left(\dfrac{C\sigma_{zc}-C\sigma_{zb}}{\mathrm{T_c}-\mathrm{T_b}}\right)\left(e^{-\mathrm{M}^2(\mathrm{T}-\mathrm{T_c})}-e^{-\mathrm{M}^2(\mathrm{T}-\mathrm{T_b})}\right)\end{array}\right]\right\} \quad (3.35)$$

3.2.3.3.3. Secondary compression settlement

The secondary compression settlement is computed through the coefficient of secondary compression C_α, considering that this settlement develops only after the shale reaches a degree of consolidation of 95%. The following expressions are consequently derived:

$$\rho''(t)=0,\ t<t_{95} \quad (3.36)$$

$$\rho''(t)=2HC_\alpha\left(logt-logt_{95}\right),\ t\geq t_{95} \quad (3.37)$$

With

$$t_{95}=\frac{\mathrm{T_{95}}H^2}{c_v};\quad \mathrm{T_{95}}=1.12 \quad (3.38)$$

3.2.3.3.4. Best fitting

The settlement versus time curves obtained in each loading step of the oedometric tests were analysed using the proposed model. The curve fitting was performed based on the principle of the least-squares method, by minimizing the sum of the squared differences between the computed and measured settlements for the different time steps. Chan (2003) discussed the determination of the coefficient of consolidation using the least-squares method in the analysis of settlement curves for soils. The formulation presented in this work allows information on the poroelastic parameters to be gathered, as well. The parameters used in the optimization process are E_{oed}, c_v, C, α_{oed} and C_α as well as the components of the settlement induced by the deformation of the apparatus at loading times t_b and t_c (ρ_b and ρ_c). The optimization process is guided by certain restrictions on some of the parameters and by preliminary estimations. A preliminary estimation of the value of ρ_c can be obtained from the

calibration of the oedometric cell. C_α and ρ'' can be estimated directly from the final part of the settlement versus time curve represented in the semi-logarithmic plane. The settlement ρ' can be estimated by subtracting the predicted ρ_c and ρ'' from the final recorded settlement; consequently, E_{oed} can be estimated as the ratio of the increment in the vertical effective stress to the deformation related to the primary consolidation. As shown in a later section, by virtue of these constraints, the search for the absolute minimum of the sum of the squared errors can be achieved in a satisfactory manner.

3.2.3.4. Assessment of the void ratio, porosity, permeability and bulk modulus of the solid phase

Once the optimization is concluded for each loading step, based on the definitions of the coefficient of consolidation c_v (Eq. (3.22)) and the Biot coefficient α_{oed} (Eq. (3.13)), it is possible to derive additional fundamental information regarding the hydro-mechanical behaviour of the tested shales, such as the variations in void ratio, the coefficient of permeability and the bulk modulus of the solid phase.

3.2.3.4.1. Void ratio and porosity variations

Under the assumption of full saturation of the shale specimen, the variation in the fluid volume is equal to the variation in the volume of voids (V_v):

$$\delta V_w = \delta V_v \tag{3.39}$$

From Eq. (3.13), the change in the void volume can be expressed as

$$\delta V_v = \alpha_{oed} \delta V \tag{3.40}$$

Then, the change in the solid volume can be computed as follows:

$$\delta V_s = (1 - \alpha_{oed}) \delta V \tag{3.41}$$

The change in the void ratio related to the primary consolidation is

$$\delta e = \frac{V_v + \delta V_v}{V_s + \delta V_s} - \frac{V_v}{V_s} \tag{3.42}$$

Similarly, the change in porosity can be expressed as

$$\delta n = \frac{V_v + \delta V_v}{V + \delta V} - \frac{V_v}{V} \tag{3.43}$$

3.2.3.4.2. Coefficient of permeability

The coefficient of permeability can be estimated based on the definition of the coefficient of consolidation (Head, 1984). From Eq. (3.22), the coefficient of permeability can be computed as follows:

$$k = \frac{c_v \alpha_{oed} \gamma_w}{CE_{oed}} \tag{3.44}$$

Eq. (3.44) highlights that an assessment of the poroelastic parameters is required for the calculation of the coefficient of permeability.

3.2.3.4.3. Estimation of the bulk modulus of the solid phase

The micromechanical interpretation of the Biot coefficient allows information to be gathered on the bulk modulus of the solid phase (Detournay and Cheng, 1993). Cheng (1997) discussed the form of the Biot coefficient for anisotropic materials and its relation to the bulk modulus of the solid phase (K_s), which was assumed to be isotropic. In general, shales are observed to be transversely isotropic. Consequently, the Biot coefficient α_{oed} for oedometric conditions can be related to the Young's moduli and Poisson ratios in the direction perpendicular to the bedding (E_z and ν_{zx}) and in the direction parallel to the bedding (E_x and ν_{xy}) (see Appendix B for details):

$$\alpha_{oed} = 1 - \frac{E_{oed}}{3K_s}\left[1 + \frac{2\nu_{zx}E_x}{E_z(1-\nu_{xy})}\right] \tag{3.45}$$

In the case of isotropy, Eq. (3.45) reduces to the well-known form of the Biot coefficient:

$$\alpha = 1 - \frac{K}{K_s} \tag{3.46}$$

where K is the bulk modulus. For a precise derivation of K_s from the Biot coefficient α_{oed} in the case of a transversely isotropic geomaterial, the elastic properties introduced in Eq. (3.45) are required, whereas in the simpler case of isotropy, only one elastic modulus (the bulk modulus K) is needed. As a first attempt to estimate K_s from the results of the oedometric tests, Eq. (3.46) was considered, where the bulk stiffness modulus K was computed from the oedometric modulus (obtained through the analysis of the oedometric tests) and from an assumed value of the Poisson's ratio. The approximation of α_{oed} by the more general parameter α is justified by the fact that anisotropic values of the poroelastic parameters have been rarely investigated or used because of the difficulties encountered in measuring them (Gutierrez et al., 2015).

3.2.4. Compression and consolidation behaviour of Opalinus Clay shale

The methodology described in the previous sections is applied here in order to investigate the compression and consolidation behaviour of Opalinus Clay. Two OPA-shallow cores (BOP-A5 and BHG-D1) and two OPA-deep cores (OPA-18 and OPA-20) were considered in the analysis. Additional results on OPA-deep and BD shale cores are reported in the last section of this chapter. All the experiments were carried out using synthetic water reproducing the in-situ pore water composition at Mont Terri (Pearson, 1998) and at the Schlattingen site (Mäder, 2011).

3.2.4.1. Volume change and primary consolidation

The results of the first oedometric test (Test 1) performed on a specimen of Opalinus Clay from Mont Terri (BOP-A5 core) are depicted in Figure 3-4 in the form of the recorded and modelled settlement versus time curves for all of the applied loading-unloading steps.

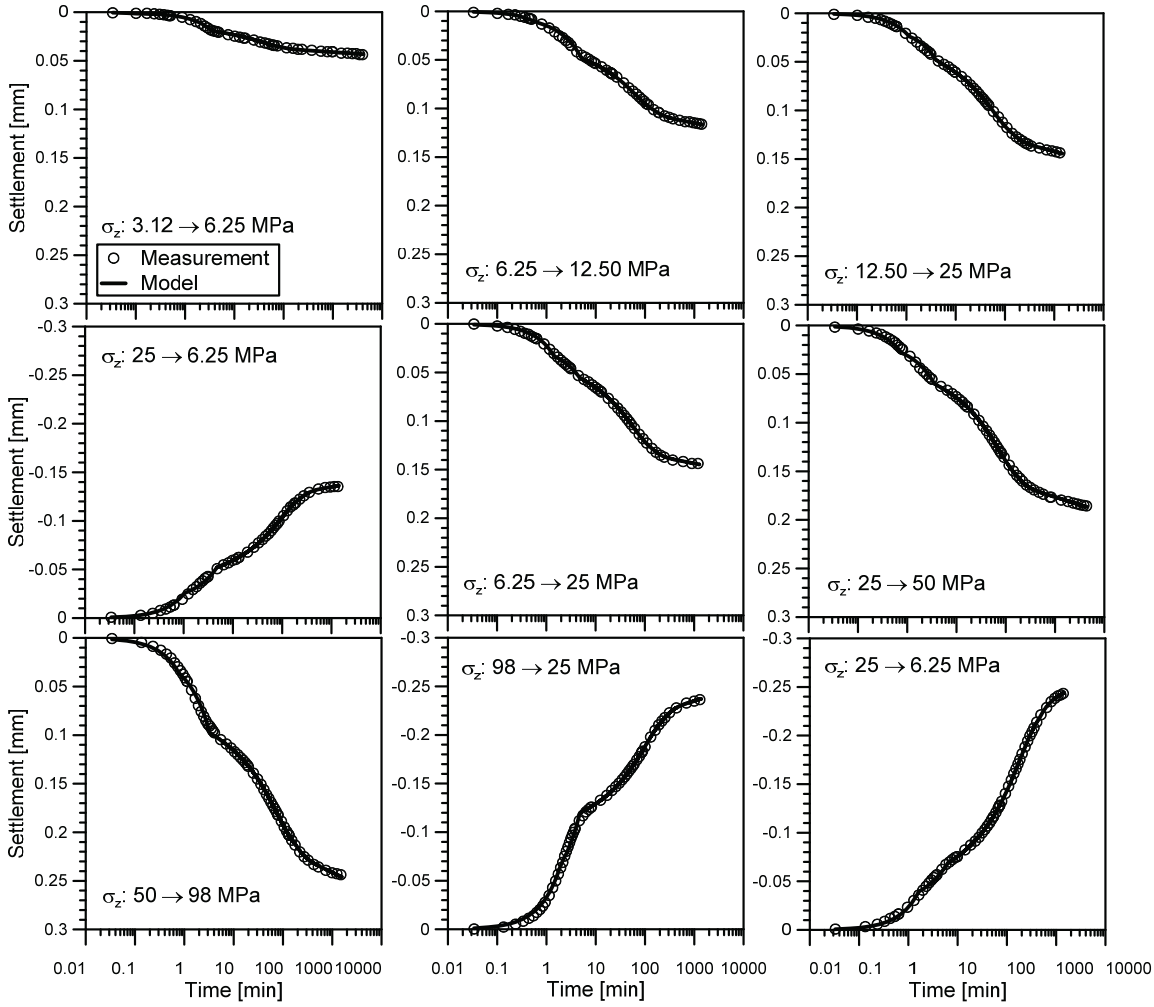

Figure 3-4: Settlement vs time curves - comparison between the experimental data and the model for all load increment steps of an oedometric test on Opalinus Clay Shale (OPA-shallow, Test 1).

The proposed analytical solution is observed to demonstrate an excellent ability to reproduce the settlement evolution over time. In general, the optimization process in the search for the fitting parameters does not present particular difficulties. As an example, Figure 3-5 depicts the contours for the sum of the squared errors for the case of the loading step from 12.5 to 25 MPa in the planes of the parameters C and α, and of the parameters c_v and C_α: the absolute minimum for the optimization process is well defined.

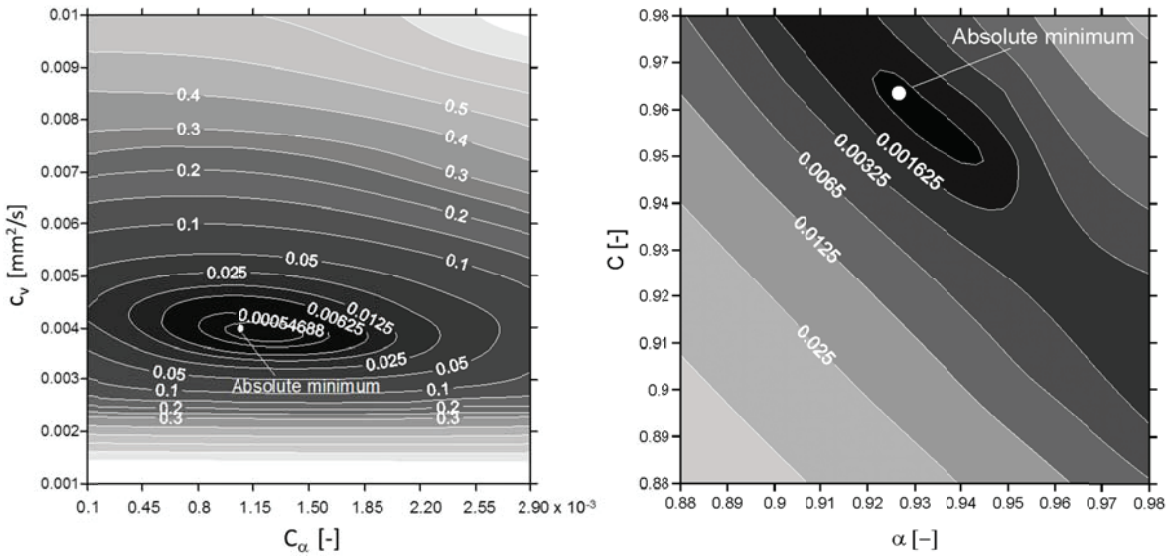

Figure 3-5: Example of the sum-of-squared-errors contours in the optimization procedure for one loading step of the first test on an Opalinus Clay Shale specimen (incrementing σ_z from 12.5 to 25 MPa).

Once each loading step has been analysed, the change in void ratio related to the consolidation process can be obtained (Eq.(3.42)). The end-of-primary oedometric curves obtained for the specimens of the Opalinus Clay from Mont Terri are depicted in Figure 3-6. The initial void ratios were similar for both prepared specimens (0.218 and 0.216). The swelling pressures developed during the saturation phase were 3.1 MPa and 3.7 MPa for the first (BOP-A5 core) and second tests (BHG-D1 core), respectively. The higher value observed in the second test can be primarily attributed to better control of the constant-volume condition during the wetting of the specimen; the void ratio at the end of saturation almost did not change for the second specimen, whereas a slight increase in the void ratio (from 0.218 to 0.222) was recorded in the first test. Beginning with the saturation phase, the plots in Figure 3-6 depict the volumetric response of the OPA-shallow specimens along the applied loading-unloading stress paths. A pre-yield to post-yield transition is observable for both specimens, with vertical yield stresses obtained with the Casagrande's graphical method equal to approximately 12.5 and 13 MPa for the first and second tests, respectively. The graphical method of Casagrande (1936) is selected for the estimation of the yield stress, because it takes into account an important aspect that is common to natural soils and shales, that is the effect of sampling disturbance. Sampling disturbance increases the compressibility of the soil upon reloading, and causes the occurrence of plasticity before the yield threshold is encountered (Fredlund and Rahardjo, 1993). In fact a sharp

transition between elastic and plastic behaviour is rarely encounter when dealing with natural soils and shales. The energy based method proposed by Wood (1990), has been also considered to estimate the yield stress. The method is based on the computation of the work required to deform a specimen, and the yield is identified when a sharp increase in the energy is recorded as a function of the applied stress. The method provides estimates of the yield stress that are quite in agreement with the results of the Casagrande method (15 MPa for OPA-shallow and 20 MPa for OPA-deep).

The computed values of the compression index (C_c) and swelling index (C_s) are also reported in Figure 3-6. The compression index is nearly identical for both tests, confirming that the compression line for the shallow Opalinus Clay was well characterized by the performed tests. An increase in the swelling index is observed with an increase in the maximum stress level reached during the loading history: greater swelling occurs upon mechanical stress release when greater vertical stresses are reached. This observed behaviour is commonly associated with the mechanical degradation of the material when subjected to high stresses and to various loading and unloading cycles (Alonso and Alcoverro, 2002; Mohajerani et al., 2011).

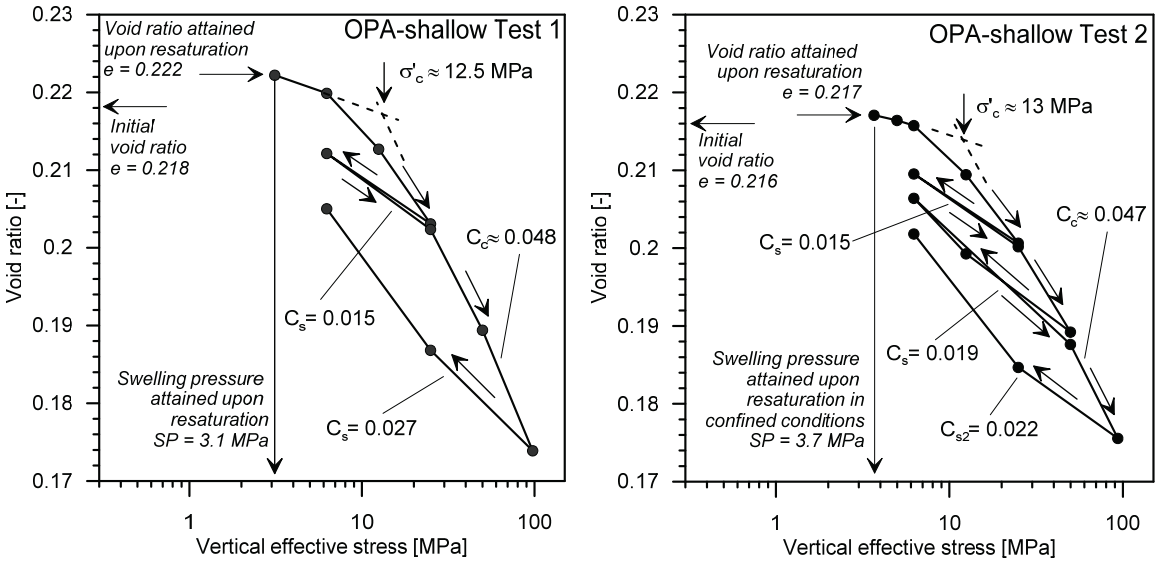

Figure 3-6: End-of-primary oedometric curves for the two tested OPA-shallow cores.

The computed values of the oedometric modulus are depicted in Figure 3-7 as a function of the vertical effective stress at the beginning of the loading/unloading steps. An initial decrease in the oedometric modulus is observed for both tests. This higher initial stiffness could be partially attributed to imperfect saturation of the specimens after the re-saturation phase, as well as to a transition from a pre-yield phase to a post-yield phase.

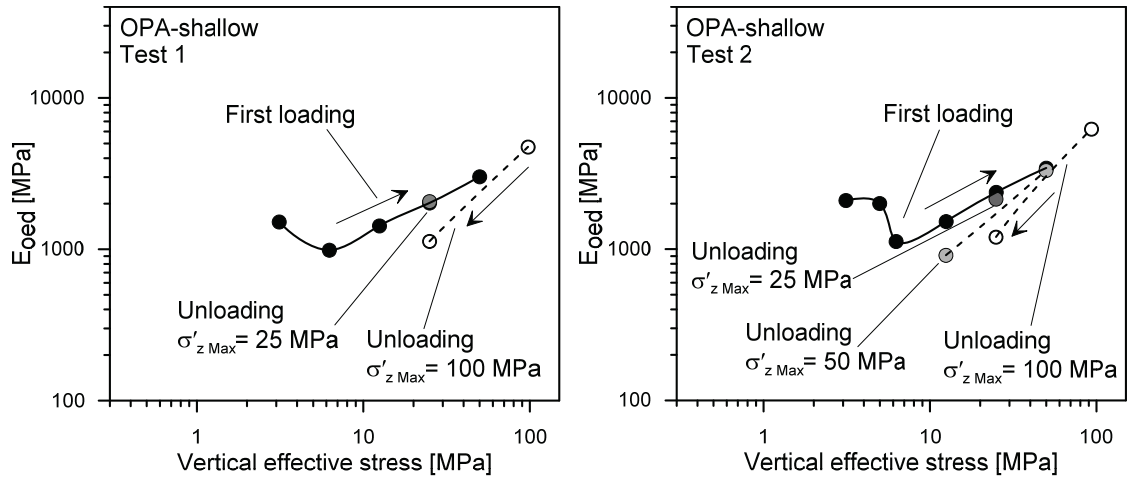

Figure 3-7: Oedometric modulus as a function of the vertical effective stress at the beginning of the loading/unloading steps for the OPA-shallow cores.

After this initial decrease, an increase in the oedometric modulus with increasing vertical effective stress is evident, showing that as expected, the material becomes stiffer with increasing stress. The oedometric moduli measured during the unloading phases are also reported; in accordance with the trend reported for the swelling index, a reduction in the stiffness for the same vertical effective stress is observed in cases in which a higher vertical stress was previously reached. Figure 3-8 presents the values of the coefficient of consolidation as a function of the vertical effective stress. For both tests, the variation in this coefficient with the vertical effective stress for the OPA-shallow specimens shows a trend similar to that typically observed for soils (Lambe and Whitman 1979): during the first loading phase, it is observed to decrease as the vertical effective stress approaches the yield stress, whereas afterwards, it remains approximately constant in the post-yield region; during unloading, the coefficient decreases as the vertical effective stress is released.

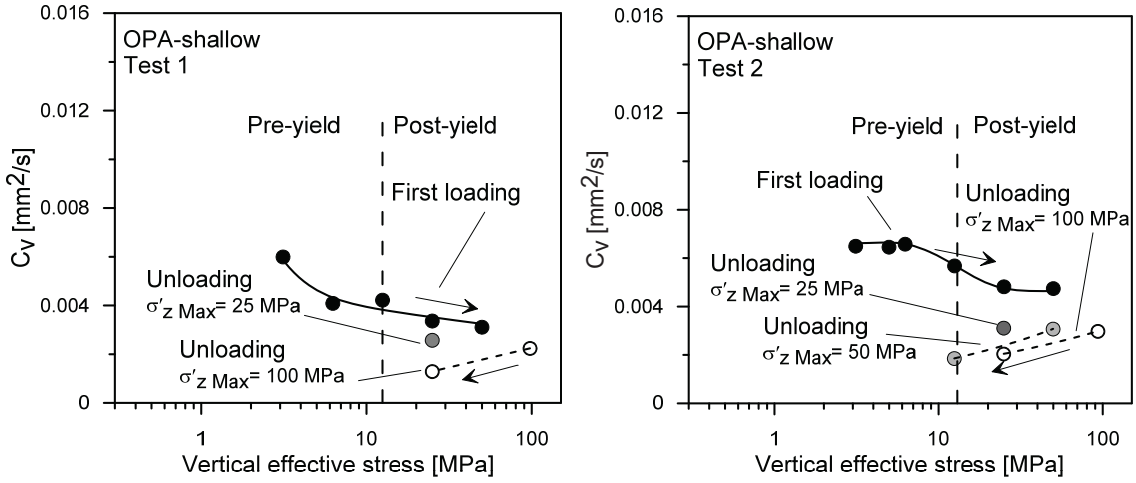

Figure 3-8: Coefficient of consolidation as a function of the vertical effective stress at the beginning of the loading/unloading steps for the OPA-shallow cores.

The end-of-primary oedometric curves obtained for the OPA-deep specimens from Schlattingen are depicted in Figure 3-9. The attained values of the swelling pressure were found to be 0.65 MPa and 0.69 MPa for Test 1(OPA-18) and Test 2 (OPA-20), respectively, for void ratio increments from 0.112 to 0.115 in Test 1 and from 0.108 to 0.113 in Test 2. The vertical yield stresses observed for the OPA-deep specimens are between 22 MPa and 26 MPa, with the lowest value having been recorded for the specimen that had the higher void ratio after saturation. These high yield stress values highlight the need to test materials under high vertical stresses to be able to reproduce the transition from the pre- to the post-yield state. The swelling and compression indices are also reported in Figure 3-9. A progressive increase in the swelling index with increasing maximum vertical stress is also observed for the OPA-deep specimens.

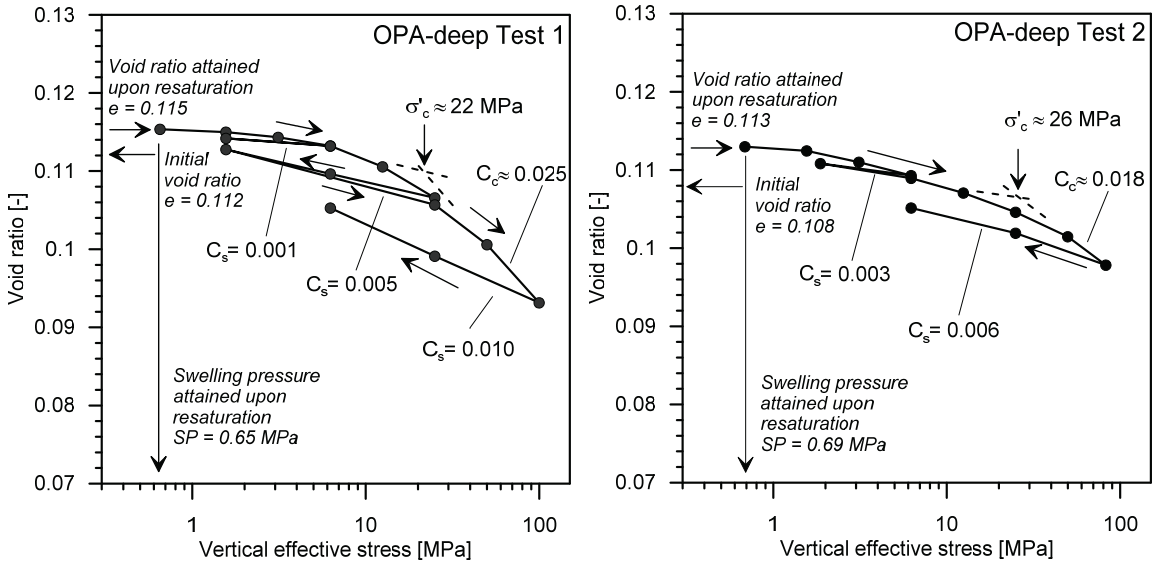

Figure 3-9: End-of-primary oedometric curves for the two tested OPA-deep cores.

The compression indexes suggested that the OPA-deep samples are less compressible than the OPA-shallow samples. The values of the oedometric modulus (E_{oed}) as a function of the vertical effective stress for the OPA-deep samples are depicted in Figure 3-10. As observed for the OPA-shallow cores, the oedometric moduli of the OPA-deep samples measured during the unloading phases at the same vertical effective stress appear to be lower when a greater vertical stress was previously reached.

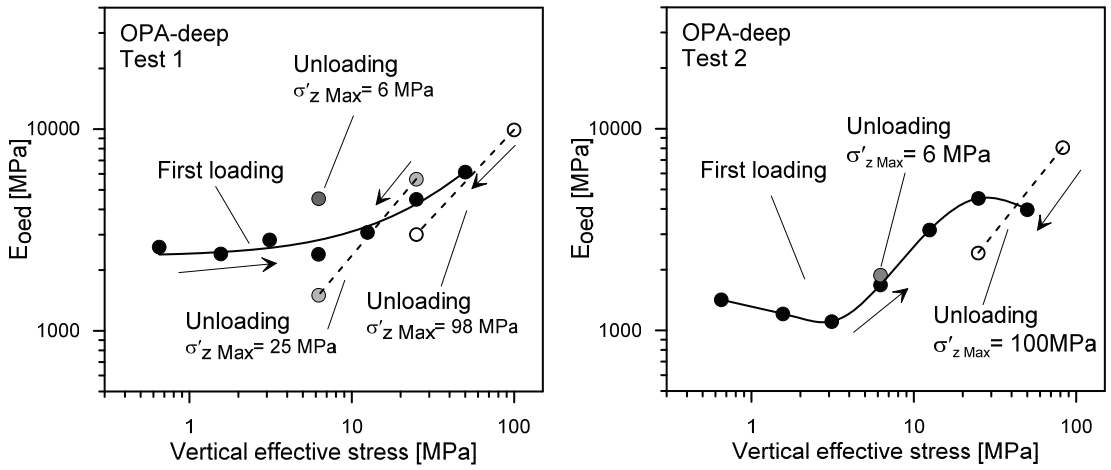

Figure 3-10: Oedometric modulus as a function of the vertical effective stress for the OPA-deep cores.

The coefficients of consolidation (c_v) of the OPA-deep cores as a function of the applied vertical effective stress are depicted in Figure 3-11. As observed for the shallow cores, a reduction in the consolidation coefficient with increasing vertical effective stress is evident in the pre-yield phase, whereas the coefficient remains approximately constant in the post-yield phase. As observed for the OPA-shallow specimens, for unloading phases performed at different maximum vertical stress levels, the coefficient of consolidation is lower at the same vertical effective stress for cases in which a higher vertical stress was previously reached.

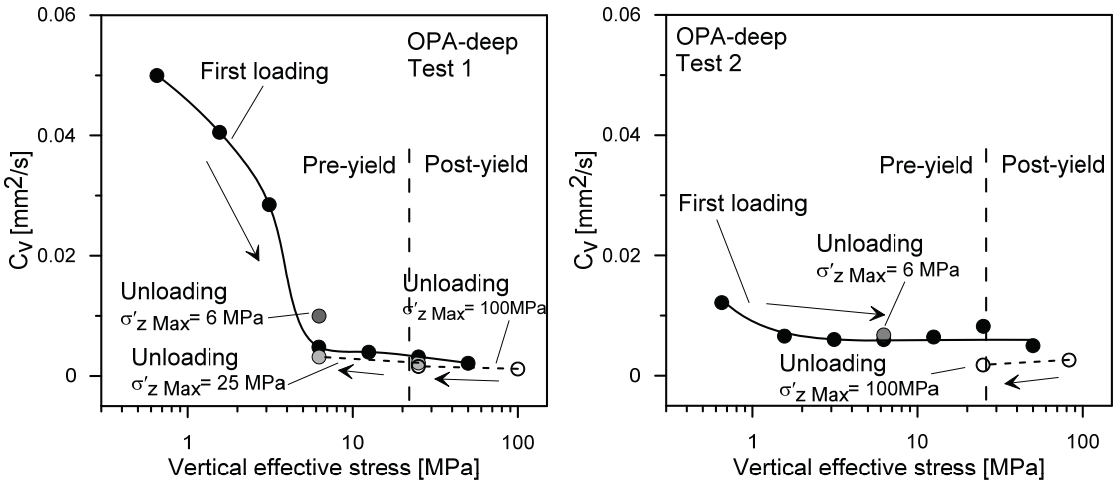

Figure 3-11: Coefficient of consolidation as a function of the vertical effective stress for OPA-deep cores.

3.2.4.2. Secondary compression

The values of the secondary compression coefficient (C_α) obtained in the analysis of the time-dependent settlement curves for the main loading path, are reported in Figure 3-12 for both considered depths.

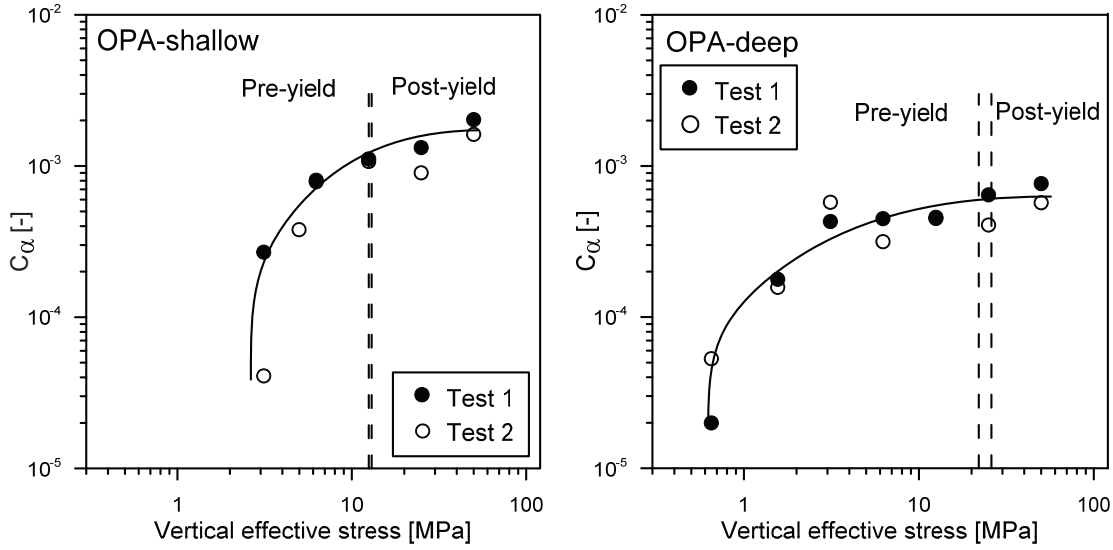

Figure 3-12: Secondary compression coefficients of Opalinus Clay samples from two different depths as a function of the vertical effective stress.

The ranges of the vertical effective yield stresses observed for the two tested specimens are also reported. The secondary compression coefficient is observed to depend on the stress: the coefficient generally increases with increasing vertical effective stress in the pre-yield phase for both the OPA-shallow and OPA-deep samples, whereas it remains approximately constant in the post-yield phase. Such behaviour is in good agreement with the trend commonly observed for soils (Lambe and Whitman, 1979). The observed trend reveals that creep effects must be carefully considered when working at great depths or high stresses. In general, higher values of the secondary compression coefficient are observed for the OPA-shallow specimens than for the OPA-deep specimens.

3.2.4.3. Poromechanical behaviour

The values of the Biot coefficient obtained from the analysis of both OPA-shallow and OPA-deep are reported in Figure 3-13 (for both tests 1 and 2) as a function of the vertical effective stress at the beginning of the loading step for the main loading path. For OPA-shallow, an initial increase in the Biot coefficient is followed by a decrease as the vertical effective stress increases. The initial increase in this coefficient well reflects the initial decrease in the oedometric modulus observed for OPA-shallow. In fact, the Biot coefficient is related to the stiffness of the material: a lower stiffness translates into a greater Biot coefficient (Eq. (3.45)). It should be recalled that the Biot coefficient and the oedometric modulus were determined independently in this study; however, the evolutions of these quantities with the vertical effective stress exhibit very good agreement. The reduction in the

Biot coefficient with increasing vertical effective stress is observed for both OPA-shallow and OPA-deep, and this trend agrees well with the increase in the oedometric modulus.

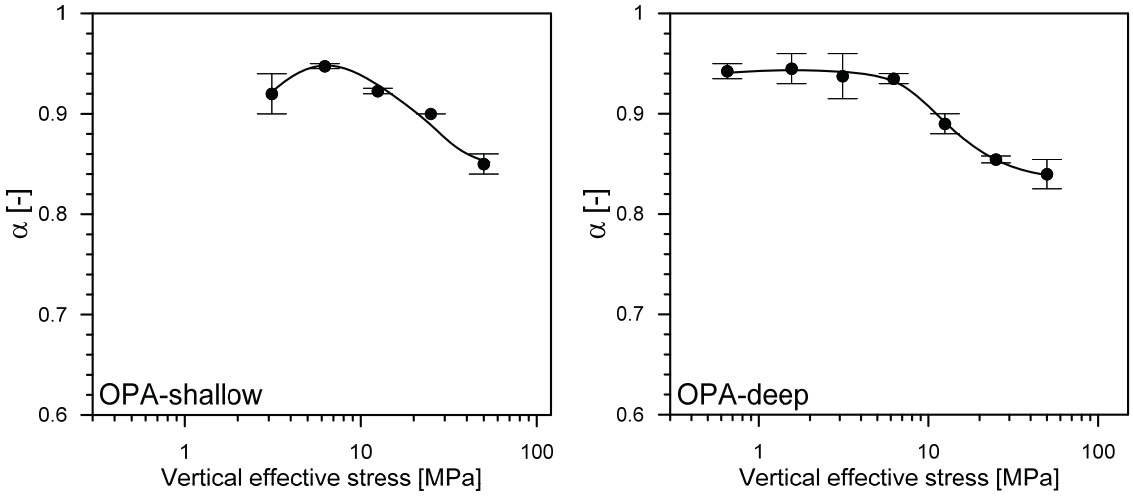

Figure 3-13: Values of the poroelastic parameter α for Opalinus Clay samples from two different depths as a function of the vertical effective stress derived from the analysis of the settlement versus time curves.

As described in section 3.2.3.4.3, the values obtained for the Biot coefficient were used to infer information about the value of the bulk modulus of the solid phase K_s: a Poisson ratio of 0.3 was assumed for OPA-shallow (Bock, 2009), and a Poisson ratio of 0.25 was assumed for OPA-deep (Jahns, 2013). A variation of the value of the Poisson's Ratio of 10% induces a variation of the estimated K_s of about 6%. The K_s values obtained in this study are reported in Figure 3-14. The obtained values of K_s are also compared with the values estimated by considering the mineralogical compositions of the tested materials (Table 1-9) and the compressibility of their solid constituents (Bass, 1995; Vanorio et al., 2003) (Table 3-1). Different approaches for the computation of K_s have been proposed in the past, beginning with Voigt (1928) and Reuss (1929), who estimated the upper and lower bounds, and followed by Hill (1952) and Shukla and Padial (1973), who proposed different averaging methods for the estimation of K_s. The K_s values obtained in this study appear to be approximately constant with the vertical effective stress and are in good agreement with the values that can be computed from the mineralogical compositions using the various available approaches (Figure 3-14).

Table 3-1: Compressibility values of the mineralogical constituents of the tested shales (*Bass 1995, **Vanorio et al. 2003).

	*Quartz (GPa^{-1})	*Feldspar (GPa^{-1})	*Calcite (GPa^{-1})	*Dolomite (GPa^{-1})	*Siderite (GPa^{-1})	*Pyrite (GPa^{-1})	**Clay (GPa^{-1})
Compressibility	0.027	0.020	0.014	0.011	0.008	0.007	0.125

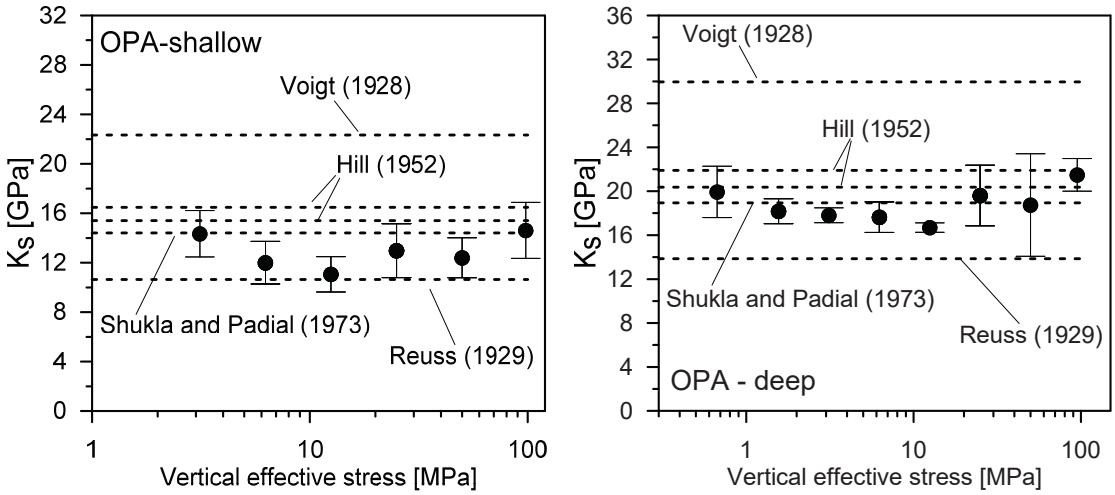

Figure 3-14: Bulk moduli of the solid phase of Opalinus Clay samples from two different depths as a function of the vertical effective stress - values obtained in this study and those inferred from the mineralogical compositions of the materials.

Figure 3-15 reports the values of the pore pressure coefficient *C* as a function of the vertical effective stress at the beginning of the loading step for the main loading path (for both tests 1 and 2). The obtained values are observed to decrease as the maximum vertical stress increases. This is a common trend that is often observed in stiff geomaterials in which the poroelastic properties play a significant role (Cook, 1999; Gutierrez et al., 2015): *C* values lower than one mean that under undrained compression, part of the load is carried by the solid constituents rather than by the pore water alone. A slight initial increase in *C* is evident for OPA-deep; this may be attributable to the presence of air in the pores of the specimen at the beginning of the test (Cook, 1999).

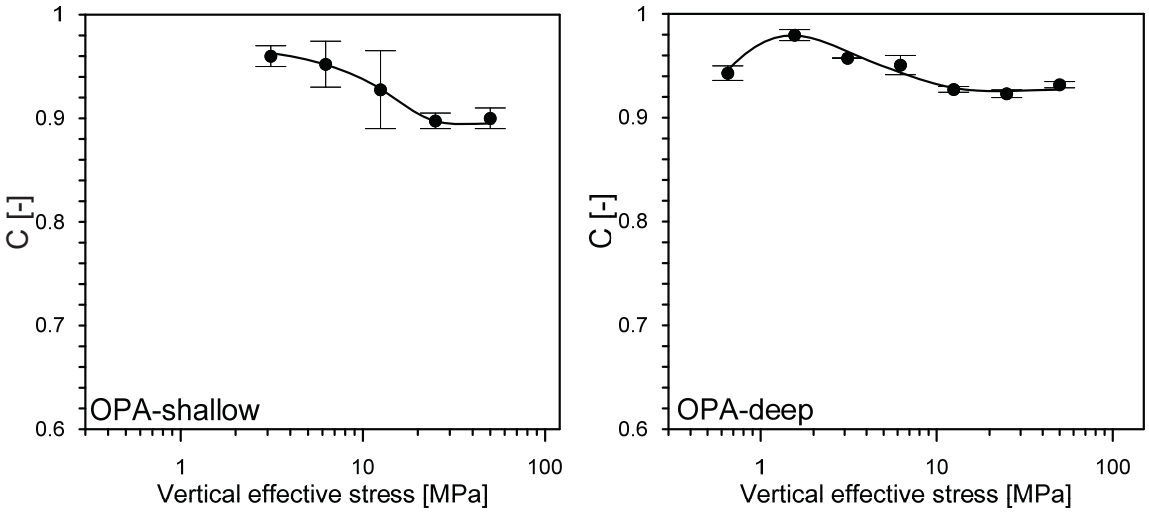

Figure 3-15: Values of the poroelastic parameter *C* for Opalinus Clay samples from two different depths as a function of the vertical effective stress derived from the analysis of the settlement versus time curves.

3.2.4.4. Coefficient of permeability

Consolidation tests are often conducted to determine the permeability of a soft sediment and its dependence on the stress (Gutierrez et al. 2014); several extensions of this procedure to stiff and very-low-porosity geo-materials, such as argillites and shales, can be found in the literature (Savage and Braddock 1991, Mohajerani et al. 2011, Gutierrez et al. 2014). In fact, a correct evaluation of the coefficient of permeability requires knowledge of the poroelastic properties of the material because they are relevant to the hydro-mechanical behaviour of stiff geomaterials. Consequently, a rigorous mean of including the poroelastic features in the analysis is strongly needed.

In this work, the expression used for the coefficient of permeability (Eq. (3.44)) was derived from the consolidation equation for a poroelastic geomaterial, and all parameters that appear in the expression were obtained by fitting the experimental results. To validate the presented procedure, the values of the coefficient of permeability for OPA-deep in the post-yield phase are presented as a function of the void ratio. A comparison of the obtained results with direct measurements from constant-head permeability tests conducted on a core sample of the same material (Romero et al., 2013) reveals good agreement (Figure 3-16), especially when the possible heterogeneity of the different tested cores is considered.

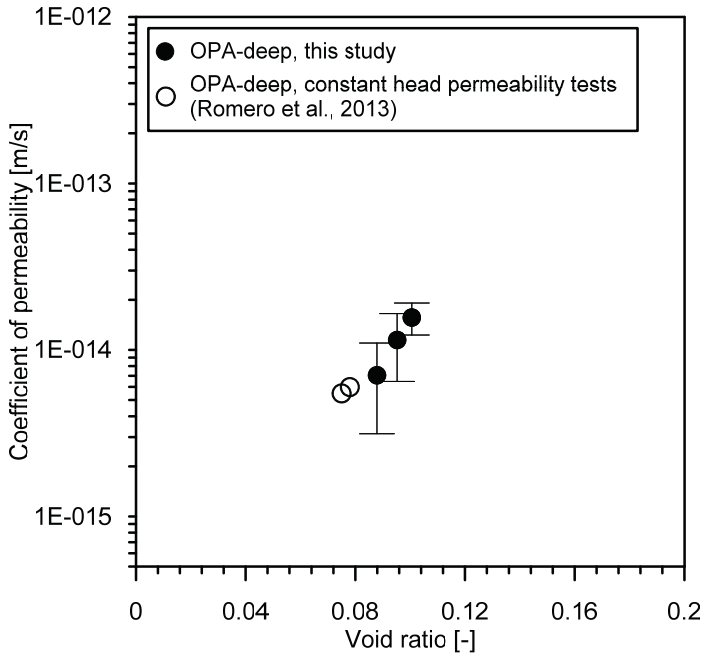

Figure 3-16: The coefficient of permeability of OPA-deep as a function of the void ratio, as obtained from the analysis of the settlement versus time curves and compared to results from the literature.

3.3. Hydro-mechanical behaviour of remoulded and natural shales: insight on the impact of diagenesis

This section presents an experimental campaign aimed at (i) characterizing the role of diagenesis and depth for Opalinus Clay shale and their impact on the hydro-mechanical behaviour of the material and (ii) understanding how representative the behaviour of the remoulded material is with respect to that of the natural shale. In fact, due to the great depths and the consequent difficulties in retrieving intact samples, remoulded shale specimens are often adopted for hydro-mechanical testing. Remoulded and intact shales may substantially differ in their hydro-mechanical behaviour due to the particular structure of the natural material, which is the result of diagenesis and burial history.

3.3.1. Background

Due to the great depths encountered in several engineering applications involving shales (shale gas exploitation, CO2 sequestration and nuclear waste geological disposal) and due to the difficulties in retrieving intact and undisturbed samples, remoulded shale specimens may be adopted for hydro-mechanical testing (Mesri et al., 1978; Flemings and Betts, 2014). The mechanical behaviour of natural sedimentary soils appears to be significantly different from the behaviour of the same materials at their remoulded state due to the effect of the structure developed during their burial history (Burland, 1990; Leroueil and Vaughan, 1990; Schmertmann, 1991; Cotecchia and Chandler, 1997; Cotecchia and Chandler, 2000; Hong et al., 2012; Zeng et al., 2015). Shales are sedimentary geomaterials that have been consolidated and strengthened during their geologic history; the high contact stresses between the particles and the consequent recrystallization are responsible for the formation of strong diagenetic bonds (Bjerrum, 1967; Leroueil and Vaughan, 1990). Such mineralogical and chemical processes impact the geomechanical properties of shales to a considerable degree (Bjørlykke and Høeg, 1997), causing a significant decrease in porosity and enhancing the brittleness and strength. The phenomena associated with burial and diagenesis may thus be fundamental in determining the hydro-mechanical behaviour of shales.

Opalinus Clay is classified as overconsolidated shale, and it has experienced a complex geologic history. It was formed approximately 174-170 million years ago in a marine environment, and it was subjected to burial, uplift and erosion processes (Gradstein et al., 2012; Nagra, 2014a). Compared to other Mesozoic sediments in the area, Opalinus Clay is described as a homogeneous formation with only small vertical and lateral lithological variability. At a meter-scale some coarsening upward cycles with characteristic changes in grain size from clay to silt/sand particles are observed. At the decimeter to millimeter-scale the preferred alignment of platy clay particles is responsible for a distinct fabric (referred to as “bedding”) (Nagra, 2002; Nagra, 2014b). The considered shale formation is found at different depths in the sites that have been selected for the investigation of the feasibility of nuclear waste repositories: from approximately 300 m bg. to approximately 900 m bg. (Nagra, 2014a). The different positions and depths of the formation imply that different stress conditions and different diagenetic processes may have been experienced by the material during burial. As a consequence, the mechanical properties of Opalinus Clay found at shallow depths may

not be equal to the ones of the same material found at greater depths. In the long term perspective of nuclear waste geological disposal, further chemical and mineralogical changes are also likely to occur. The investigation reported in this section aims at deriving information on the effects of burial and diagenesis on Opalinus Clay shale. To fulfil this objective, the intrinsic properties of the material, i.e., those properties that are independent from its natural state (Burland, 1990) have to be studied. The intrinsic behaviour of the material can be analysed when the effect of diagenesis on the shale structure is removed thanks to the process of remoulding. However, such a process may induce significant deviations from the hydro-mechanical response of the natural material. The second objective of this work is to investigate the degree of representativeness of hydro-mechanical tests results obtained on remoulded Opalinus Clay shale specimens with respect to the behaviour of intact specimens, and thus to understand to which extent the response of the remoulded material can help in understanding the behaviour of the intact one.

The volume change behaviour of argillaceous sediments during sedimentation, burial and diagenesis has received significant attention in the geotechnical literature (Hedberg, 1936; Gibson, 1958; Skempton, 1969; Jones and Addis, 1984; Addis and Jones, 1985; Jones and Addis, 1985; Burland, 1990; Dewhurst et al., 1998; Djéran-Maigre et al., 1998; Nygård et al., 2004). The testing of clays at the remoulded state is quite a common practise in the geotechnical community, and several studies have been conducted to compare the compaction behaviour of undisturbed specimens to that of remoulded specimens (Burland, 1990; Leroueil and Vaughan, 1990; Cotecchia and Chandler, 1997; Cotecchia and Chandler, 2000; Hong, 2006; Chandler, 2010; Hong et al., 2012). On the other hand, very few investigations have been carried out on the behaviour of remoulded argillites and shales. William (2005) studied the compression behaviour of remoulded specimens of Bringelly shale and compared the results with those obtained on the intact material. The investigation highlighted the relatively minor influence of diagenesis: when the remoulded material is compressed to the same density as the intact shale, the difference in stiffness between the natural and remoulded specimens is sufficiently small to indicate that very little cementation is present (William and Airey, 2009). Different results were obtained by Nygård et al. (2004), who investigated the impact of diagenesis on the compaction behaviour of Kimmeridge clay and Kimmeridge Clay shale. The comparison between the remoulded and intact hydro-mechanical response of the material allowed the authors to draw the conclusion that diagenesis has a significant impact, since mechanical compaction alone could not explain the much lower porosity, compressibility and permeability of the natural shale with respect to the remoulded and uncemented material. Flemings and Betts (2014) investigated the compaction and permeability evolution of remoulded specimens from Plio-Pleistocene aged mudrocks and found good agreement between the measurements on remoulded and intact materials, drawing the conclusion that very little diagenesis or other ageing processes occurred in the studied mudrocks. These previous studies on shales highlight that the impact of diagenesis on the hydro-mechanical behaviour is very much dependent on the specific geologic history of the considered formation. Considerations on the fact that diagenetic phenomena may not be negligible for Opalinus Clay shale have been formulated by Corkum and Martin (2007): they estimated the normal consolidated porosity of Opalinus Clay from the sedimentation compression curves for normal consolidated argillaceous sediments obtained

by Skempton (1969) and found a value of approximately 25%. Since the in situ porosity of Opalinus Clay at a depth of 300 m bg. is approximately 18% (Bossart, 2012), the observation led the authors to the conclusion that gravity-induced mechanical compaction is not the only process involved in the porosity reduction and that diagenesis also has a significant contribution in determining the final porosity of Opalinus Clay shale. However, a focused experimental campaign devoted to study the diagenetic effects and the role of depth on the hydro-mechanical behaviour of Opalinus Clay shale has not been so far conducted, and thus it is strongly needed. The experimental campaign presented in this section consists in a series of low and high-pressure oedometric tests, carried out in order to study the remoulded behaviour of Opalinus Clay shale specimens retrieved both from the Mont Terri and the Schlattingen sites. The comparison between the behaviour of the remoulded and of the intact shales provides significant evidences on the roles of depth, diagenesis and structural disturbance and quantifies their impact on the hydro-mechanical response of Opalinus Clay.

3.3.2. Material and methods

Both OPA-shallow and OPA-deep cores were involved in this study; in particular the results considered in this section for the intact material are the ones presented in section 3.2 for BOP-A5 (Test 1 on OPA-shallow) and for OPA-18 (Test 1 on OPA-deep). As described in the first chapter of this thesis, the OPA-shallow from the Mont Terri URL is located at a depth of approximately 300 m, but the maximum depth reached during its burial history was approximately 1200 m (Bossart, 2012). The Opalinus Clay formation at the Schlattingen site (OPA-deep) is found at a depth of approximately 830 m until a depth of approximately 950 m, while the maximum burial depth was approximately 1700 m (SHARC, 2014).

A first indication of the effects of diagenesis can usually be found in the mineralogical composition of the materials. In fact, diagenetic processes mainly manifest as three phenomena (Ali et al., 2010): (i) recrystallization, where particles may change their shape and size without changing composition; (ii) precipitation, where the particles become cemented due to the precipitation of new minerals from the pore fluid in the existing pores; and (iii) replacement, where particles change their chemical composition. The first two processes mainly involve quartz and carbonate grains; carbonate cementation may enhance the brittleness even at very shallow depths (Bjørlykke and Høeg, 1997). As for replacement, this process manifests mainly through the transformation of calcite into dolomite (dolomitization). As a consequence, one should expect significant amount of quartz, calcite and dolomite in sediments once they are subjected to diagenesis. The meaning of such mineralogical indicators for Opalinus Clay and their impact on the hydro-mechanical properties of the material are still open questions and thus require investigation.

Standard (max vertical stress: 1 MPa) and high-pressure (max vertical stress: 100 MPa) oedometric cells have been used in this study. The oedometric ring for standard testing is 60 mm in diameter and 15 mm in height, while the oedometric ring for high-pressure testing is 35 mm in diameter and 12.5 mm in height. The testing campaign consists of five oedometric tests which are conducted to study the remoulded behaviour of OPA-shallow and OPA-deep in both the low-pressure range and the high-

pressure range. In addition three constant head permeability tests were carried out on a remoulded OPA-shallow specimen after oedometric compression at different void ratio values. The detailed description of all the tests is reported in Table 3-2.

Table 3-2: Summary of the performed oedometric tests.

Material	*Oedometric tests*
Remoulded OPA-shallow	One test in the conventional oedometric cell: one loading-unloading cycle, max vertical effective stress applied equal to 1 MPa One test in the high-pressure oedometric cell: one loading-unloading cycle, max vertical effective stress applied equal to 100 MPa One test in the high-pressure oedometric cell with three constant-head permeability tests at vertical effective stresses equal to 1.4 MPa, 3.3 MPa and 13 MPa
Remoulded OPA-deep	One test in the conventional oedometric cell: one loading-unloading cycle, max vertical effective stress applied equal to 1 MPa One test in the high-pressure oedometric cell: one loading-unloading cycle, max vertical effective stress applied equal to 100 MPa

An ad hoc procedure has been developed to prepare remoulded shale specimens, since no international standards are available and no protocols have been so far developed and systematically applied for their preparation. Burland (1990) suggested that a remoulded soil is a soil that has been thoroughly mixed with water at a water content between the liquid limit (w_L) and $1.5w_L$, without air drying or oven drying, and then consolidated in one-dimensional conditions to obtain a reconstituted specimen. In this study, the intact shale is crushed by means of a grinder, and the fraction passing a 0.5 mm sieve is selected. The crushed material is placed in a closed environment to avoid air drying, while a small portion is used to measure the water content by oven-drying at 105°C. Once the water content is known, the amount of water (M_w) to be added for a certain mass of shale can be calculated as follows:

$$M_w = (w_L - w_{pow})\frac{M_{pow}}{1 + w_{pow}} \tag{3.47}$$

where w_L is the liquid limit and w_{pow} and M_{pow} are the initial water content and wet mass of the shale powder, respectively. Synthetic waters are used in this study with the aim of reproducing the composition of the in situ water for both the Mont Terri site (Pearson, 1998) and the Schlattingen site (Mäder, 2011). An amount of water slightly greater than M_w is systematically added to ensure a water content higher than the liquid limit because a certain degree of evaporation may take place during the subsequent equilibration phase. Once the slurry is prepared, it is stored in a closed environment for 24 hours to attain the equalization of the water content. After equalization, the resulting water content is measured on a small portion of the prepared slurry, while the remaining material is used for the

specimen preparation for oedometric testing. The slurry is placed in the oedometric ring with the aid of a metallic spatula, and small portions of material are progressively disposed to avoid air trapping as much as possible; the upper and lower bases are finally smoothed. The water contents of the final slurry were equal to 45% and 31% for the OPA-shallow and OPA-deep, respectively, both approximately 1.1-1.2 times the corresponding liquid limits (Table 1-5 and Table 1-6).

3.3.3. Results and discussion

In this section, the hydro-mechanical behaviour of remoulded Opalinus Clay specimens is compared to the behaviour of the intact specimens. The tests are run by incremental loading at both low and high pressures. Time-settlement curves are analysed to distinguish the end-of-primary consolidation settlement from the settlement due to secondary consolidation.

3.3.3.1. Oedometric compression and porosity reduction mechanisms

The oedometric curves for the shales tested at the natural state were presented in Figure 3-6 and in Figure 3-9. The in-situ vertical total stress at the Mont Terri URL is estimated to be between 6.5 MPa and 8 MPa, while the pore water pressure is approximately 2 MPa (Martin and Lanyon, 2003). The in situ vertical effective stress is thus approximately 4.5-6 MPa: for this effective stress range, void ratio values of about 0.21-0.22 is read on the oedometric curves presented in Figure 3-6, in good agreement with the porosity value reported in Bossart (2012), 18%, which corresponds to a void ratio of 0.22. No information is available on the in situ vertical effective stress of the OPA-deep, but the density and depth allow estimating a vertical total stress of approximately 22 MPa.

In Figure 3-17, the results of tests on the remoulded shales, in terms of the void ratio (computed at the end-of-primary consolidation) versus the vertical effective stress, are presented and compared to the results on the intact shales (for the intact shales, for a clearer exposition, only first loading and final unloading for BOP-A5 and OPA-18 cores are represented). The compression curves derived from low-pressure and high-pressure testing on remoulded specimens appear to be in good agreement, especially for the OPA-deep shale. A slight discrepancy between the compression curves from low-pressure testing and high-pressure testing is observed for the remoulded OPA-shallow: this may be due to small variations in water content because the two specimens were not made at the same time, even though they were obtained from the same remoulded shale material. In fact, small variations in water content have been observed to affect the initial compressibility of remoulded clays up to pressures of approximately 1.6 MPa (Hong et al., 2010; Zeng et al., 2015).

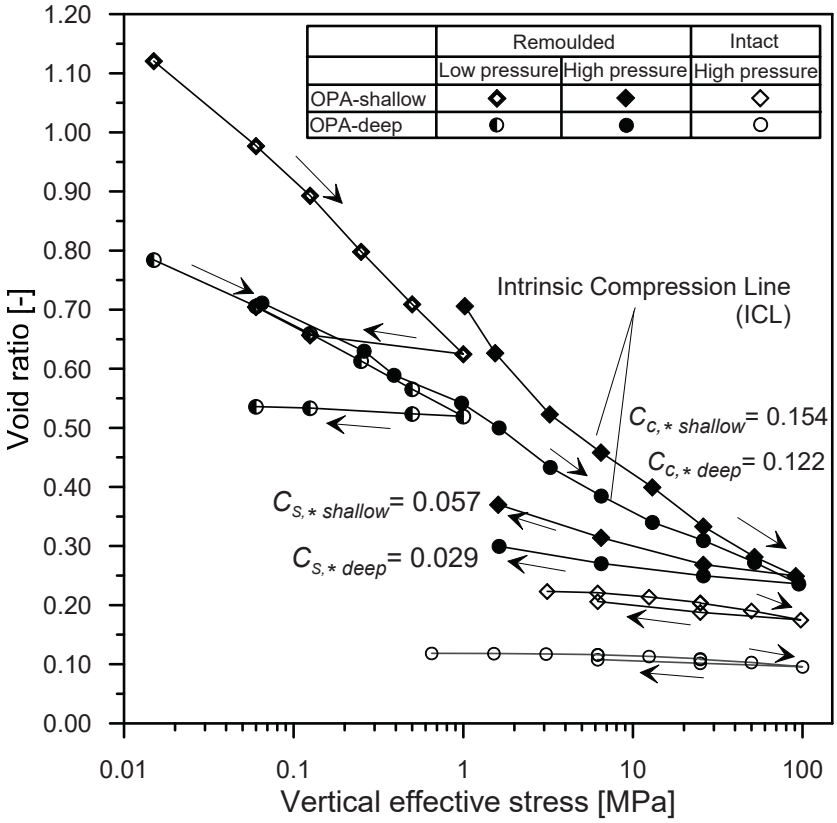

Figure 3-17: Oedometric test results on remoulded and intact Opalinus Clay shale.

The compression line of a remoulded material is called the intrinsic compression line (ICL) (Burland, 1990). The ICLs of the remoulded OPA-shallow and OPA-deep specimens do not coincide for the lower pressure range: this is clearly a consequence of the fact that the specimens have been prepared at different water contents. In fact, as mentioned before, it has been observed that even the same clay, remoulded at different water contents, presents diverging compression curves at low pressures and that the ICL is usually well-defined only at high pressures (Burland, 1990; Hong et al., 2010; Zeng et al., 2015). The mineralogical composition is slightly different for the two considered materials: this fact may induce some variation in the compressibility of the two remoulded specimens. However, the compression curves clearly manifest a tendency to converge for the highest vertical stress levels: this is in line with the observations of Skempton (1969), who observed the converging pattern of the compression curves of various normal consolidated clays. Burland (1990) observed that the ICL has often a shape slightly concave upward when represented in the traditional semi-logarithmic plot of Figure 3-17. This phenomenon is also observable in Figure 3-17, even though not very pronounced, for the compression curves of the two remoulded shale specimens.

When the compression behaviour of a remoulded clay is compared to that of the same clay in the natural state, the compression lines display a tendency to become parallel at high vertical stresses as a result of fabric orientation (Burland, 1990). William and Airey (2009), in their studies on Bringelly

shale, report a change in the slope of the ICL at high vertical stresses toward the compressibility of the intact material, as the void ratio of the remoulded material approaches the void ratio of the intact one. A tendency toward a reduction in compressibility at high vertical stresses is also detected for the studied remoulded Opalinus Clay (Figure 3-17); however the stiffness of the natural material is still considerably higher in the range of vertical effective stress considered. At the maximum effective stress level, the void ratio of the remoulded material is still far from that of the intact shale leading to the conclusion that the porosity of the natural Opalinus Clay shale is related not only to the mechanical compaction and fabric configuration but also to diagenesis.

The mechanism of porosity reduction can be schematized as shown in Figure 3-18: when remoulded Opalinus Clay is compacted at the in-situ vertical effective stress at Mont Terri and at the Schlattingen site, the initial void ratio e_0 reduces to a value that is much greater with respect to the void ratio values observed in-situ equal to e_1 and e_2 for the OPA-shallow and OPA-deep, respectively. This observation shows that factors other than the increase of the vertical effective stress are responsible for this porosity reduction and that the variation of the void ratio is likely to be related also to diagenetic phenomena. Diagenetic processes have also manifested between the OPA-shallow and OPA-deep; in fact, when the OPA-shallow is brought to a vertical stress close to the one estimated for the Schlattingen site, the void ratio is still considerably greater with respect to the value e_2 observed for the OPA-deep. The values e_3, e_4 and e_5 represent the void ratio achieved when the remoulded material, the intact OPA-shallow and the intact OPA-deep, respectively, are compressed at 100 MPa of vertical effective stress: the observed results (Figure 3-17) confirm that mechanical compaction at this high stress is not enough to attain the same void ratio for the three materials. Therefore, the observed lower porosity values of the intact materials with respect to the remoulded one (e_4 and e_5 versus e_3 in Figure 3-18) are to be related to diagenetic effects. The impact of creep deformations has been evaluated, based on the secondary compression response of the material (discussed in Figure 3-23) and on the burial history of the shale, which started about 174 million years ago: the variation in porosity that would be observed in 174 million years for a material which has a secondary compression coefficient of 0.003 is lower with respect to the observed porosity loss. Therefore creep alone could not explain the observed reduction in porosity, and diagenesis is considered to have a fundamental impact in the mechanism of porosity reduction. Further evidences related to the swelling sensitivity and compressibility of the natural and remoulded shales (which are discussed in the coming paragraphs) support this observation.

The intrinsic compression index $C_{c,*}$ expresses the compressibility of the remoulded material. In this work, this index is defined between 25 MPa and 100 MPa to allow a meaningful comparison with the compression index (C_c) of the natural material. The intrinsic compression indexes for the OPA-shallow and OPA-deep ($C_{c,*shallow}$ and $C_{c,*deep}$) have values of 0.154 and 0.122, respectively. The comparison between compression indexes of the studied materials at their remoulded and intact states provides information about the lower compressibility of the natural material, which is likely to be the result of diagenesis. The intrinsic swelling indexes for OPA-shallow and OPA-deep ($C_{s,*shallow}$ and $C_{s,*deep}$) are also reported in Figure 3-17 for the final unloading phase and present values of 0.057 and

0.029, respectively: the slightly greater swelling tendency of remoulded OPA-shallow with respect to remoulded OPA-deep may be due to the greater clay content. A lower swelling sensitivity is observed for the natural shale compared to its remoulded state, as the presence of cementation and diagenetic bonds inhibits the rebound upon mechanical unloading and reduces the magnitude of the swelling (Mesri et al., 1978).

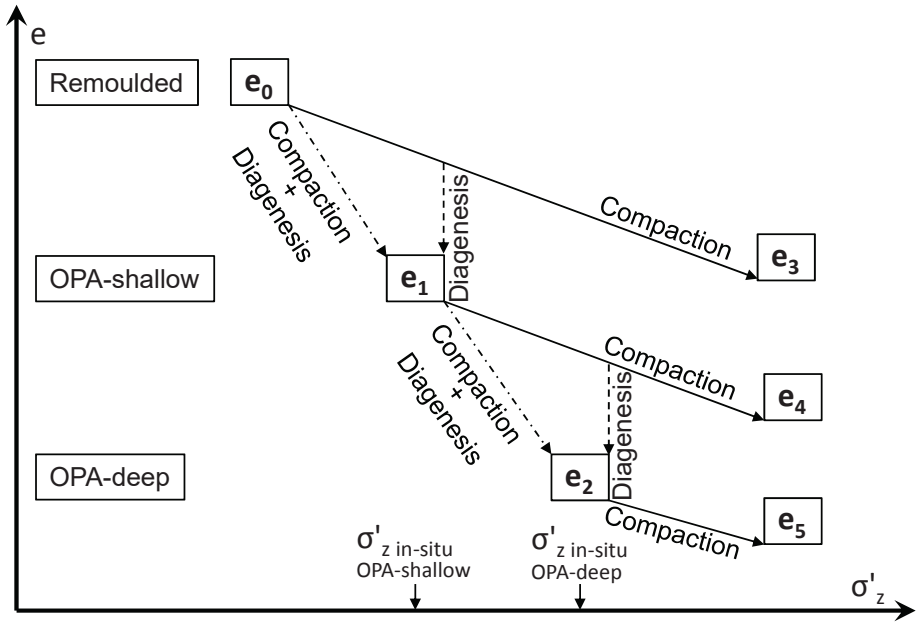

Figure 3-18: Mechanism of porosity reduction due to mechanical compaction and diagenesis.

The oedometric modulus (E_{oed}) of the considered samples is presented in Figure 3-19a for the main loading path as a function of the vertical effective stress at the beginning of the loading steps, while in Figure 3-19b, it is represented as a function of the final void ratio at the end of each loading step: lower values of oedometric modulus for the same vertical effective stress are observed for the remoulded material compared to the intact one, highlighting the enhanced stiffness of the intact material (Figure 3-19a). The remoulded OPA-shallow and OPA-deep show very similar values of oedometric modulus, especially in the high-pressure range, in good agreement with the tendency displayed by the ICLs, which seem to align at high vertical stresses. The enhanced stiffness of the natural material with respect to the remoulded one, for the same vertical effective stress, seems to be due to the reduction in porosity caused by diagenetic processes. In fact, all the specimens display a stress dependent oedometric modulus but this relationship is specific for each single specimen; on the other hand, when void ratio is considered, a fairly unique relationship between oedometric modulus and void ratio is found (Figure 3-19b). The results highlight that both mechanical loading and diagenetic processes have a great relevance in determining the stiffness of the material due to the impact of both phenomena on the porosity of the material.

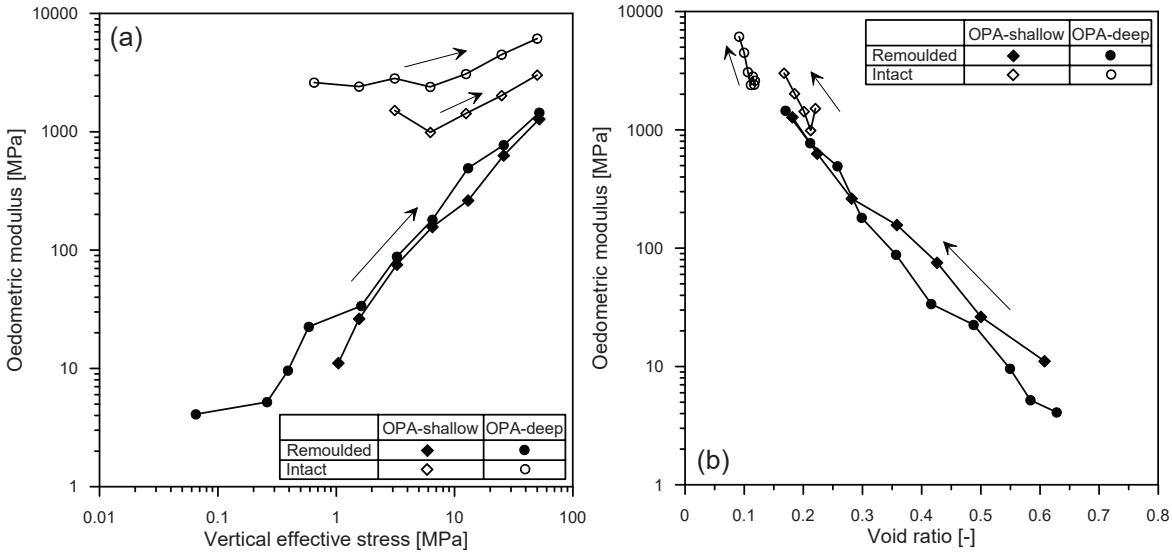

Figure 3-19: Oedometric modulus as a function of the vertical effective stress (a) and void ratio (b).

3.3.3.2. Permeability

The coefficient of permeability, computed from the results of the oedometric tests, is presented in Figure 3-20 as a function of the final void ratio (computed at the end of each loading step). In general, the mechanical compaction and the consequent reduction of porosity have a strong impact on the permeability of Opalinus Clay in both the remoulded and intact states, as the permeability decreases significantly with the decreasing porosity during mechanical compaction.

In order to validate the permeability values obtained in this study by back analysis of the oedometric test results, constant head permeability tests were carried out on a remoulded OPA-shallow specimen that was compressed to different void ratio values. The tests were conducted in the high-pressure oedometer cell to reproduce the same stress path as experienced in the previous oedometric compression test on the same material. The compression line for this last remoulded OPA-shallow specimen is reported in Figure 3-21 and compared with the previous oedometric test on remoulded OPA-shallow. Very good agreement is obtained for the two tests, confirming the fact that the intrinsic compression line (ICL) is well defined at high pressure. At each oedometric compression step, a constant head permeability test was carried out: the independent control of the pore water pressure at the top and bottom bases of the specimen in the high-pressure oedometer cell allowed applying a differential pore water pressure while maintaining oedometric conditions. The coefficient of permeability has been measured at three different values of void ratio, and the results are reported in Figure 3-20 and Figure 3-21: very good agreement with the permeability values obtained from the consolidation tests analysis is highlighted. The results of the constant head permeability tests on the intact OPA-deep, reported by Romero et al. (2013), are also presented in Figure 3-20. The good accordance between the constant head permeability test results and the values of the coefficient of permeability computed from the results of the oedometric testing campaign on both remoulded and

natural shales provides confidence in the derivation of this significant information through the performance of consolidation tests.

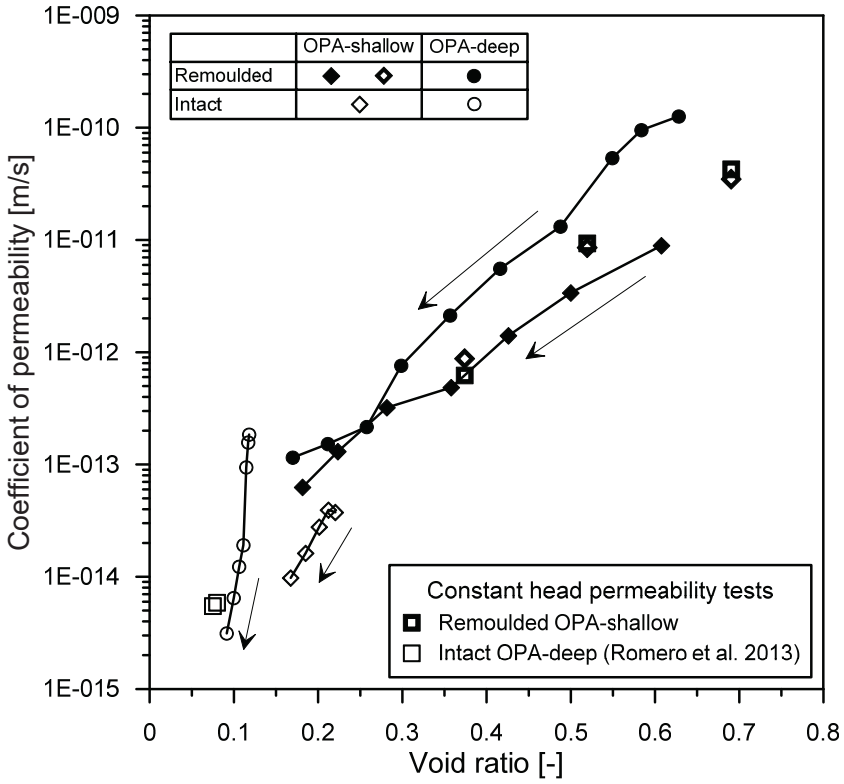

Figure 3-20: Coefficient of permeability as a function of the void ratio from consolidation tests and from constant head permeability tests.

The decrease in porosity due to diagenesis has already been discussed: diagenetic processes, which lead to the formation of the natural Opalinus Clay shale, are responsible for a marked reduction in porosity (Figure 3-17). However, considerations on the effect of diagenesis on the transport properties are not straightforward because diagenesis does not seem to have a strong impact on permeability reduction, yet a decrease in porosity is observed. As a consequence, further considerations about the structure and connectivity of the pore network are needed. To better explain the transport processes, it is fundamental to understand which porosity is involved in the diagenesis and which pores dictate the transport properties of the material. Microstructural observations reveal that the interconnected porosity is found mainly in the clay matrix (Houben et al., 2013). Houben et al. (2013) defined three types of pores for Opalinus Clay: (i) elongated pores between clay stacks oriented in a similar manner, (ii) crescent-shaped pores in saddles of folded clay stacks and (iii) large pores surrounding non-clayey grains. Keller et al. (2013) also observed the presence of an enhanced porosity formed between clay stacks and non-clayey grains due to geometric incompatibilities along such boundaries, which may be classified as type (iii). This enhanced porosity is likely to be part of the pore network (Keller et al., 2013), acting also as storage pores with greater dimensions than other pores. The pore network structure may be simplified by the conceptual model proposed in Figure 3-22, which has

been inspired by microstructural observations and the considerations of Houben et al. (2013) and Keller et al. (2013). The larger storage pores are likely to be part of the porosity network, constituting a bridge between pores in the clay matrix; however, the transport properties are mainly dictated by the smaller connecting pores, with pore throats smaller than 10 nm (Houben et al., 2013). In this sense, a reduction in the dimension of these larger pores would not affect the flow properties in a considerable way. In fact, the flow velocity is likely to slow down when the fluid enters such larger pores around non-clayey grains, thus enhancing further precipitation and cementation. The results of these processes would be a reduction in the porosity and storage capacity, while the permeability and flow properties would not be as affected as the porosity.

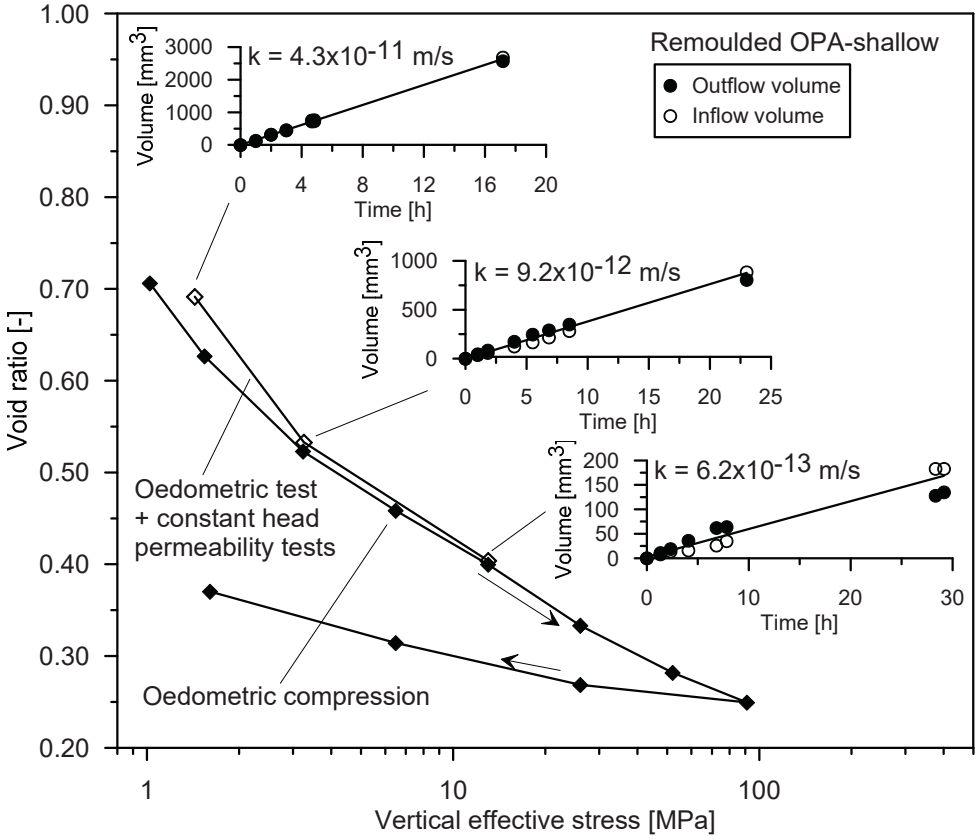

Figure 3-21: Oedometric curve on a reconstituted OPA-shallow specimen: comparison with a previous oedometric test on reconstituted OPA-shallow and determination of the coefficient of permeability by constant head permeability tests.

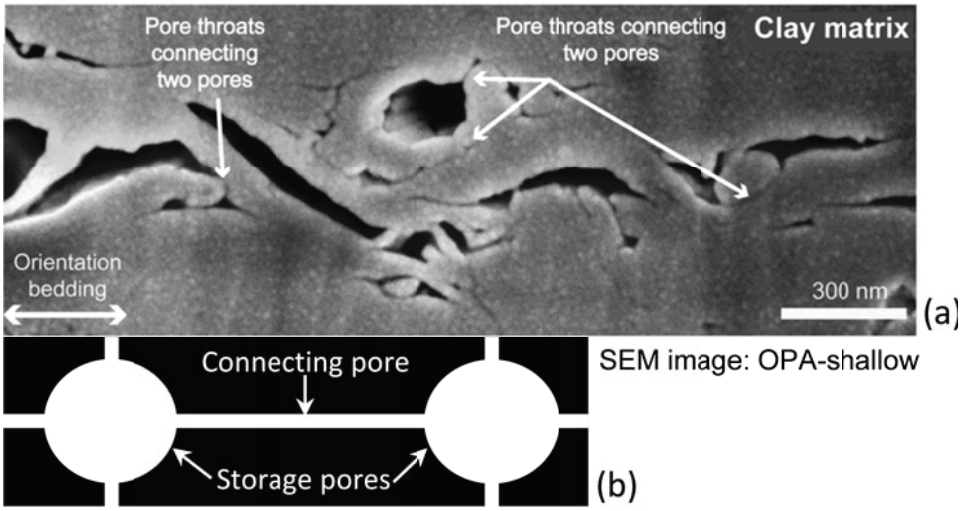

Figure 3-22: Pore network structure for Opalinus Clay: (a) SEM image of the OPA-shallow (from Houben et al. (2013));(b) conceptual model of the pore network structure (after Asef and Farrokhrouz (2013)).

3.3.3.3. Secondary compression effects

The secondary compression coefficient (C_α) provides an indication of the significance of creep effects for shales. The results for the C_α of the remoulded and intact Opalinus Clay are reported in Figure 3-23 for the main loading path as a function of the vertical effective stress at the beginning of the loading steps.

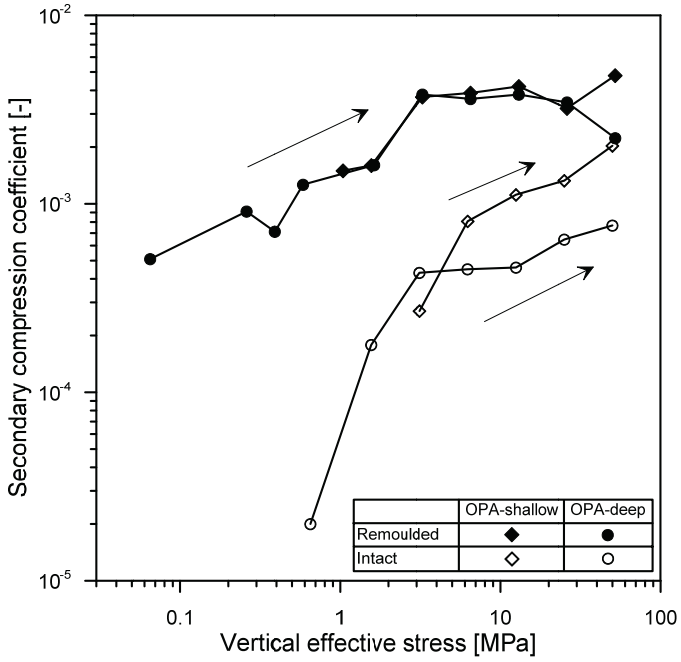

Figure 3-23: Secondary compression coefficient (C_α) as a function of the vertical effective stress.

The secondary compression coefficient appears in general to be stress-dependent, with increasing values as the vertical effective stress increases in the low stress range, while fairly constant values are found in the high stress range; this behaviour is typical for geomaterials (Lambe and Whitman, 1979). The natural shales present values of C_α lower than 0.002, while the remoulded material reveals greater secondary consolidation effects with respect to the intact shales for the same vertical effective stress. Figure 3-23 shows that, for the same vertical effective stress, creep phenomena are mitigated by diagenetic processes, while the disturbance of the material and the destruction of diagenetic bonds may enhance the creep behaviour when the same stress conditions are considered.

3.4. Further insights on the hydro mechanical-behaviour of shales

The third part of this chapter is dedicated (i) to the analysis of additional high-pressure oedometric tests results obtained on shale cores retrieved at the Schlattingen site (section 1.2.2), (ii) to further insights into the swelling behaviour of Opalinus Clay, and (iii) to the investigation of the permeability-void ratio relationship for the tested shales.

Section 3.4.1 and 3.4.2 presents the results obtained on two OPA-deep cores (OPA-2 and OPA-6) and on four BD cores (BD-6, BD-16, BD-12 and BD-7), respectively (the shale cores have been described in detail in section 1.3). All the cores are tested in the direction perpendicular to the bedding planes, while the OPA-6 core has been tested also in the direction parallel to the bedding planes. The results are analysed and conclusions are drawn on the impact of mineralogical variability, anisotropy and loading history on the hydro-mechanical response of the shales.

In section 3.4.3 an insight is conducted into the swelling behaviour of Opalinus Clay, based on the material response observed during the initial resaturation phases of several high-pressure oedometric tests. The impact of boundary conditions, initial void ratio and mineralogical composition on the swelling behaviour is highlighted.

Results and analyses on the permeability-porosity relationship of the studied shales are presented in section 3.4.4. The permeability- void ratio relationship is analysed taking into account the mechanical loading history of the material as well as the pore network microstructure.

3.4.1. One-dimensional compression behaviour of OPA-deep shale cores

The end-of-primary oedometric curves of OPA-2 and OPA-6 specimens (tested perpendicular to the bedding planes) are reported in Figure 3-24a and b, respectively.

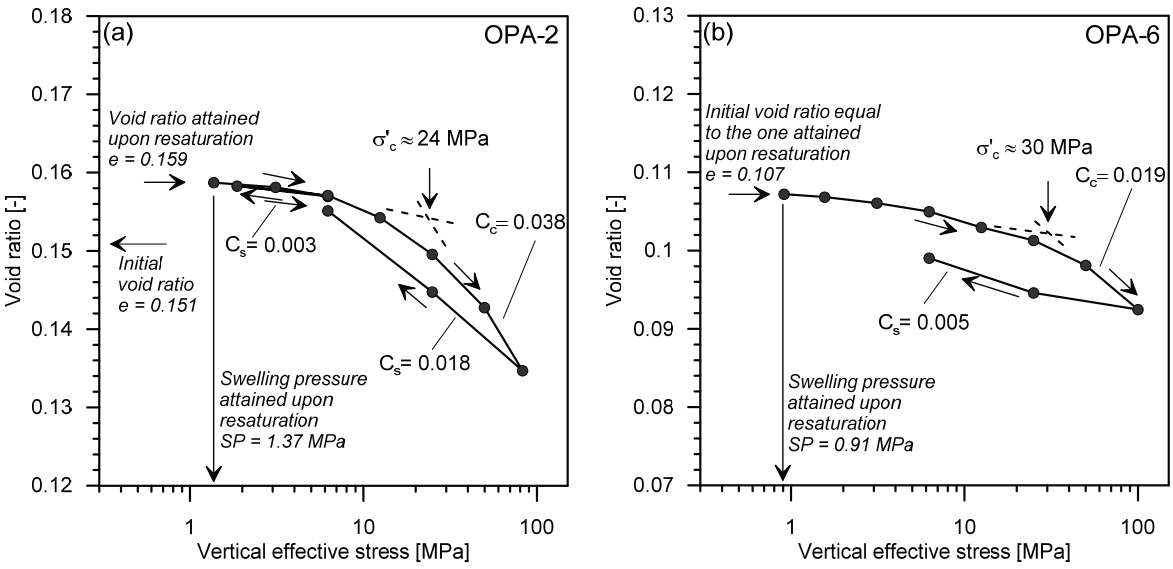

Figure 3-24: End-of-primary oedometric curves of OPA-2 and OPA-6 cores (perpendicular to bedding).

A pre-yield to post-yield transition is clearly observed for OPA-2 specimen: an initial elastic reloading phase is followed by an elasto-plastic compression phase; a vertical effective yield stress equal to approximately 24 MPa is found. All vertical effective yield stresses are computed here according to Casagrande (1936) method. The pre-yield to post-yield transition is less marked but still observable for the OPA-6 specimen, where a vertical yield stress equal to about 30 MPa is obtained using Casagrande (1936) method. OPA-2 core is characterized by a significantly greater void ratio with respect to the other tested OPA-deep cores. As observed in section 1.3.4, this is due to the different mineralogical composition of the material with a much greater clay content and considerably lower quartz content with respect to the other OPA-deep cores. Moreover, the tested OPA-2 specimen presents a greater compression index (C_c = 0.038) and swelling indexes (C_s = 0.003 at 6 MPa and 0.018 at 100 MPa) with respect to the other tested OPA-deep cores, revealing greater elastic and elasto-plastic compressibility.

The analysis of the one-dimensional compression behaviour of OPA-6, which has been tested both perpendicular (Figure 3-24b) and parallel (Figure 3-25) to the bedding planes, reveals the limited impact of anisotropy on the hydro-mechanical response, since very similar compression and swelling indexes are found, as well as about the same vertical effective yield threshold. The OPA-6 specimen tested perpendicular to the bedding planes presents a slightly lower swelling pressure with respect to the OPA-6 specimen tested parallel to the bedding planes. This may be due to some internal swelling into open fissures (having the same orientation of the bedding planes), which reduces the magnitude of the vertical swelling pressure development when the material is tested perpendicular to them, even though total volume and thus total void ratio remains constant (Mesri et al., 1994).

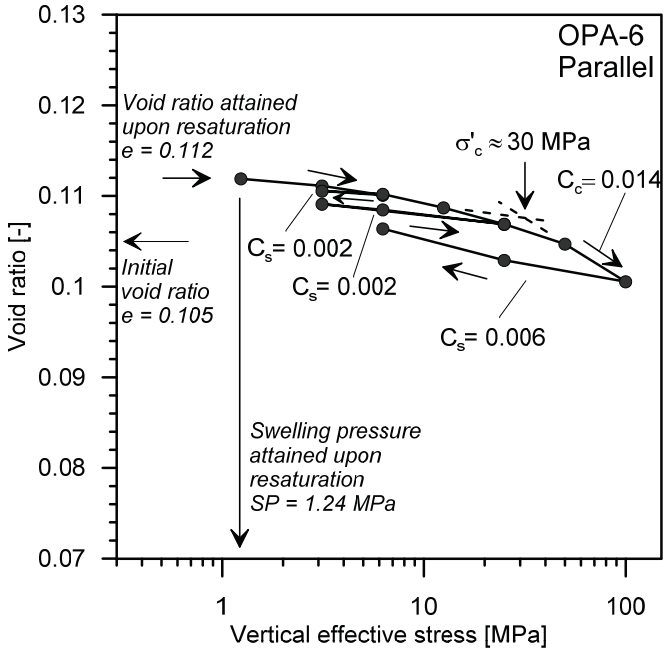

Figure 3-25: End-of-primary oedometric curve of OPA-6 core (parallel to bedding).

The results of the analysis in terms of oedometric modulus (E_{oed}) and coefficient of consolidation (c_v) versus vertical effective stress applied at the beginning of each loading step are reported in Figure

3-26. For the sake of clarity, only the first loading is represented, while the behaviour of the material during unloading-reloading phases has been analysed in section 3.2.4.1.

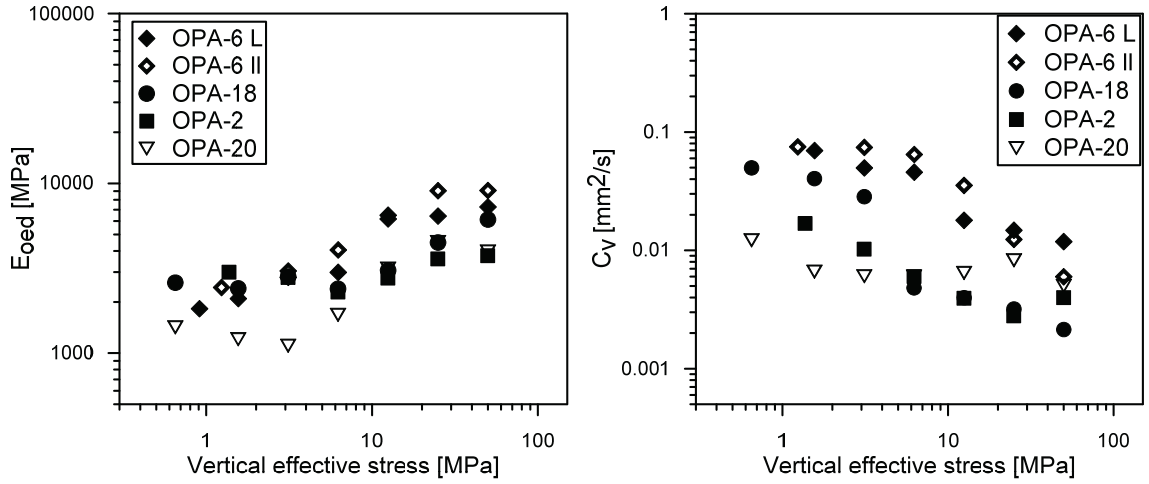

Figure 3-26: Oedometric modulus and coefficient of consolidation as a function of the vertical effective stress for OPA-deep cores.

As observed in section 3.2.4.1, the oedometric modulus increases with increasing stress (Figure 3-26a) while the coefficient of consolidation presents a decrease (Figure 3-26b), in line with the typical behaviour of soils (Lambe and Whitman, 1979). The results present a noticeable variability among the different cores. In particular the OPA-6 core has slightly greater stiffness and presents higher values of the coefficient of consolidation with respect to the other tested OPA-deep cores. This fact can be justified by the presence of fine sandy layers in OPA-6 (Ferrari et al., 2013). No relevant impact of anisotropy on the hydro-mechanical response is highlighted. The values of the secondary compression coefficient as a function of the vertical effective stress are reported in Figure 3-27.

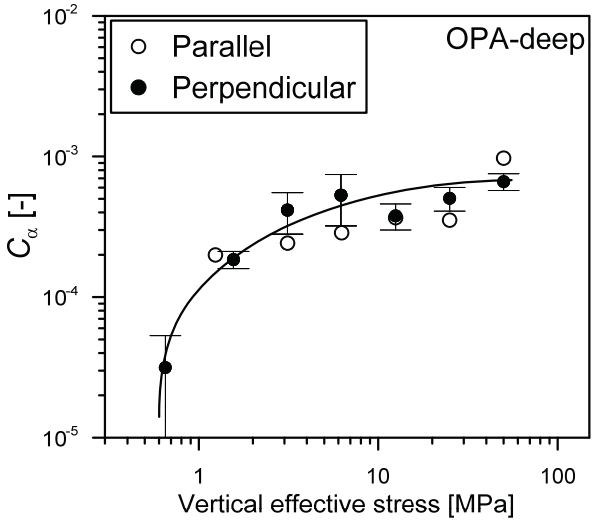

Figure 3-27: Secondary compression coefficient as a function of vertical effective stress for OPA-deep.

The coefficient generally increases with increasing vertical effective stress in the pre-yield phase, whereas it remains approximately constant in the post-yield phase, presenting values lower than 10^{-3}. The poroelastic coefficients α and C are reported in Figure 3-28 as a function of the vertical effective stress. The obtained values are observed to decrease as the maximum vertical effective stress increases. This is a common trend that is often observed in stiff geomaterials in which the poroelastic properties play a significant role (Cook, 1999; Gutierrez et al., 2015). No relevant impact of the anisotropy on the secondary consolidation behaviour and on the poroelastic parameters is observed.

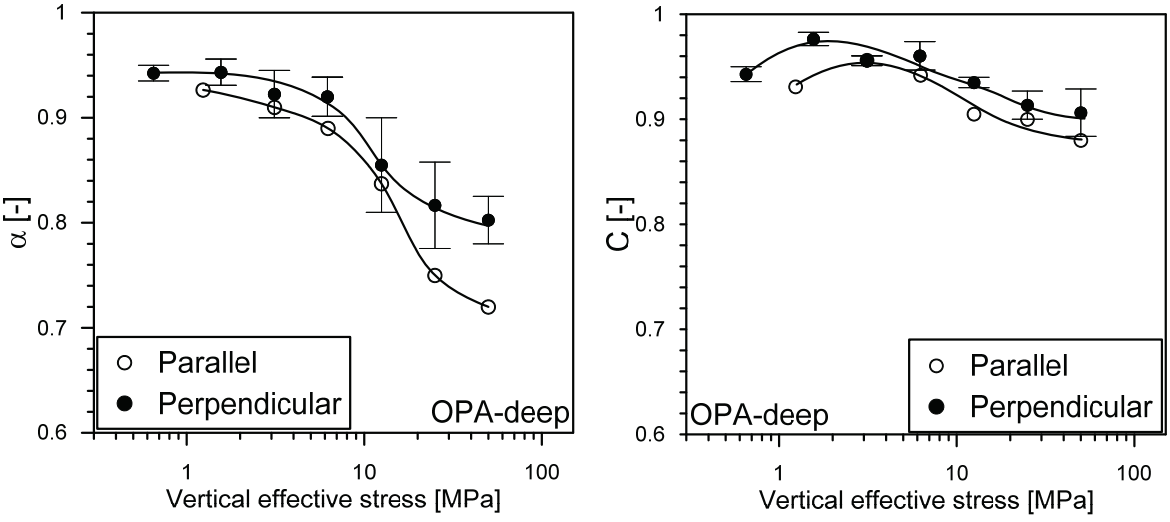

Figure 3-28: Poroelastic coefficients α and C as a function of the vertical effective stress for OPA-deep cores.

3.4.2. One-dimensional compression behaviour of BD shale cores

The end-of-primary oedometric curves obtained on BD specimens are reported in Figure 3-29. A pre-yield to post-yield transition is observed for all the specimens, where an initial elastic reloading phase is followed by an elasto-plastic compression phase with vertical yield stresses observed between 16 MPa and 21 MPa. The values of the swelling pressure attained during resaturation are between 0.26 and 1.11 MPa, for void ratio variations between 0 and 1%, highlighting a lower swelling tendency of BD with respect to OPA-deep. The greater swelling pressure manifested by the BD-7 core with respect to the other BD cores is justified by the considerably greater clay content (43%) and lower calcite content (29%) with respect to the other tested BD cores (25-28% clay content and 51-55% calcite content). The swelling and compression indexes are also reported in Figure 3-29: the compression index suggests that the BD samples are, in general, less compressible than the OPA-deep samples.

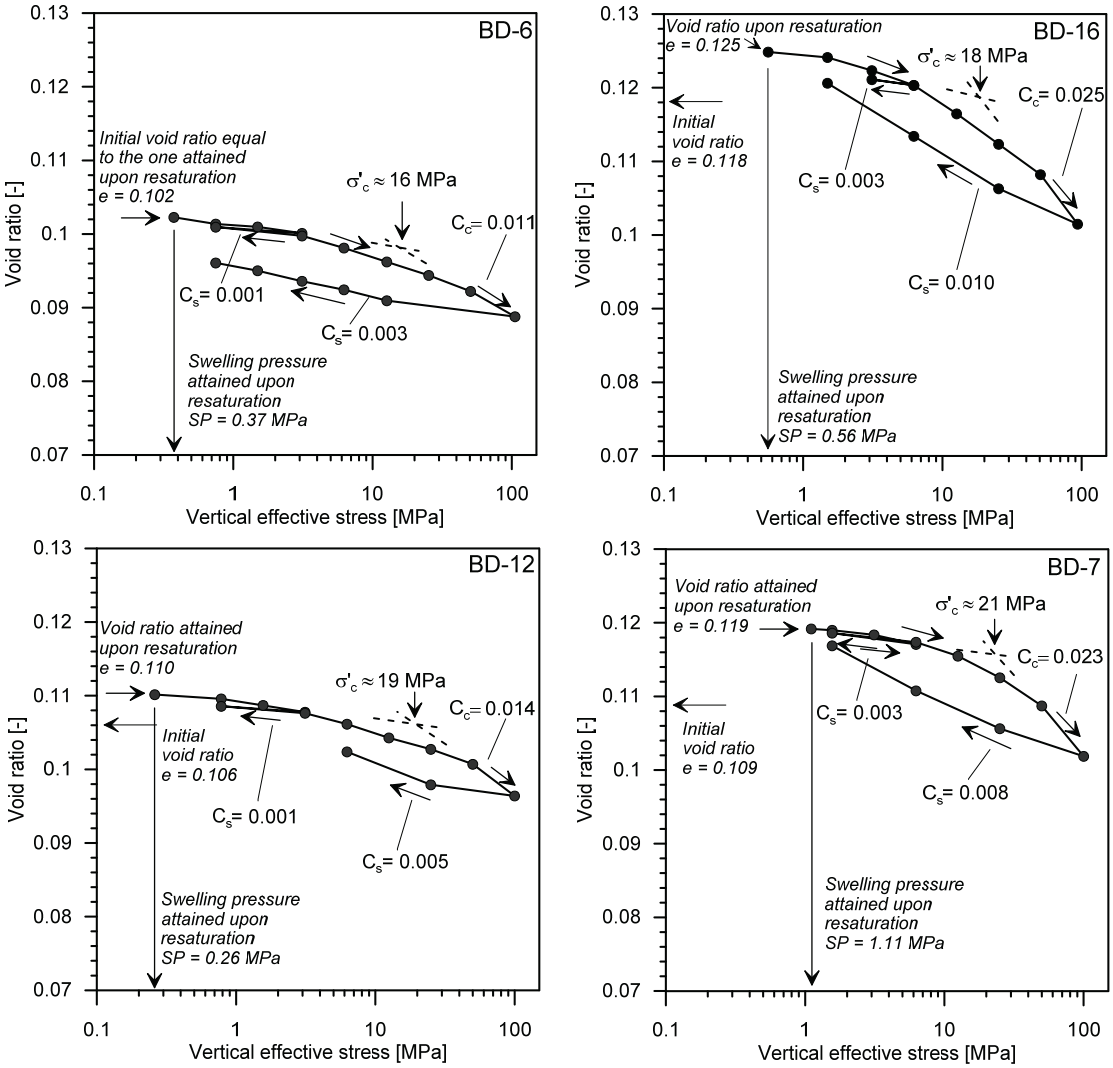

Figure 3-29: End-of-primary oedometric curves of BD shale cores

The values of the oedometric modulus (E_{oed}) and of the coefficient of consolidation (c_v) are reported in Figure 3-30 as a function of the vertical effective stress applied at the beginning of the loading-unloading steps. The results of both first loading and unloading steps are reported. The values of the oedometric modulus present some variability, even when only the first loading is considered. However, a clear increase of oedometric modulus with vertical effective stress can be observed. The impact of damage due to the maximum stress level reached is recognised in the fact that the values of the oedometric modulus during the final unloading phase are lower with respect to the ones obtained during previous unloading-reloading phases. The values of the coefficient of consolidation present less variability for BD shale with respect to OPA-deep, with a clear decrease of the coefficient of consolidation with increasing stress during first loading. The coefficient of consolidation decreases during unloading-reloading phases for the same vertical effective stress and significantly lower values are observed during the final unloading phase, in agreement with the behaviour of OPA-shallow and OPA-deep shales presented in section 3.2.4.1.

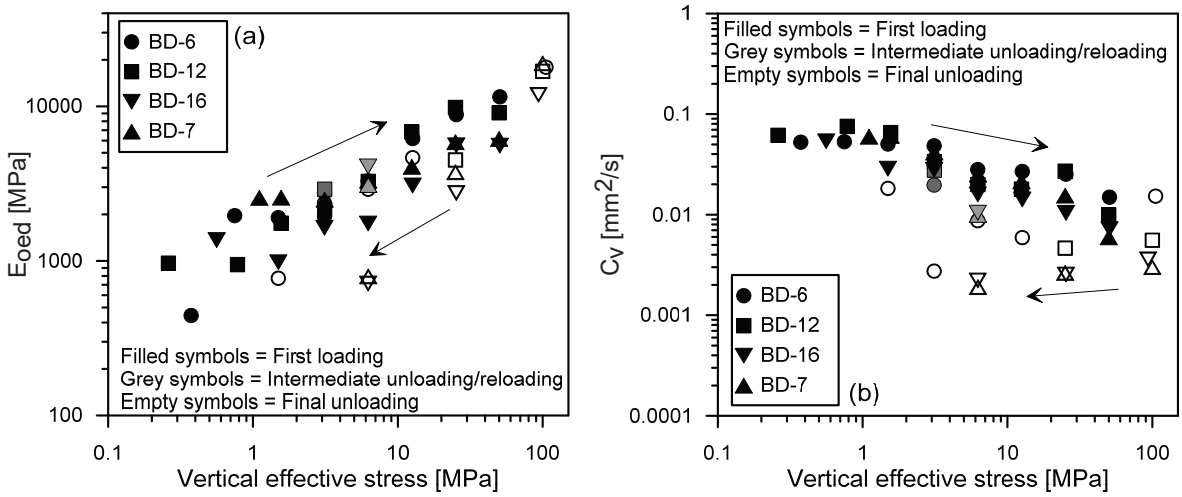

Figure 3-30: Oedometric modulus and coefficient of consolidation as a function of the vertical effective stress for BD shale cores.

The values of the secondary compression coefficient as a function of the vertical effective stress are reported in Figure 3-31. The coefficient appears to be approximately constant and presents values lower than 10^{-3}. The poroelastic coefficients α and C are reported in Figure 3-32 as a function of the vertical effective stress. The obtained values are observed to decrease as the maximum vertical effective stress increases, in agreement with the results on OPA-shallow and OPA-deep.

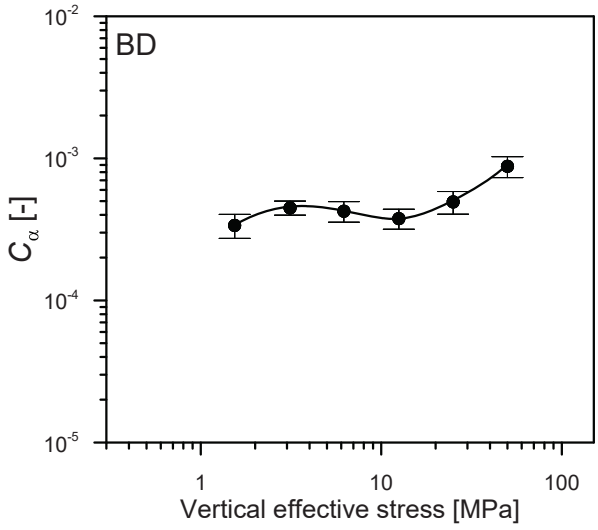

Figure 3-31: Secondary compression coefficient as a function of vertical effective stress for BD shale.

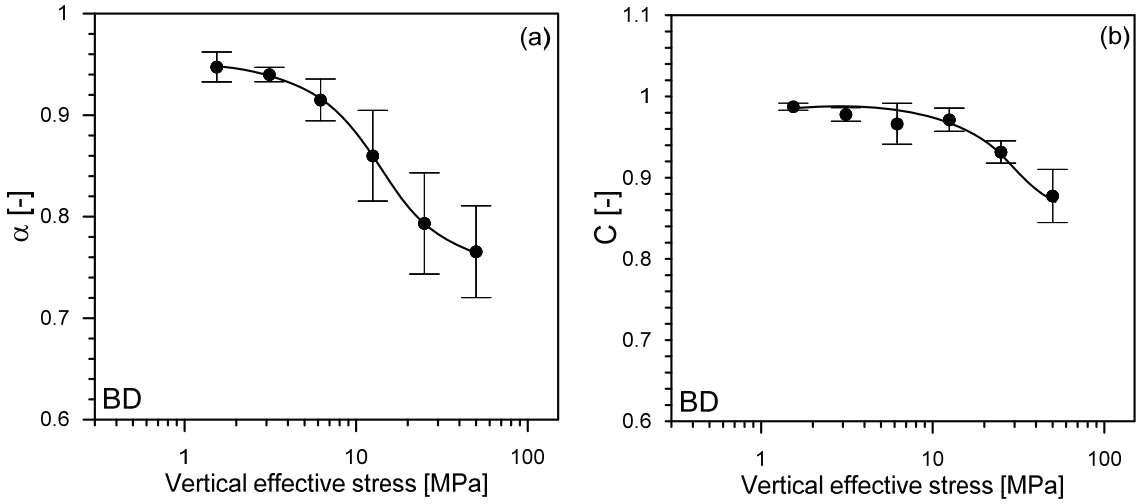

Figure 3-32: Poroelastic coefficients α and C as a function of the vertical effective stress for BD shale.

3.4.3. On the swelling behaviour of Opalinus Clay

The oedometric apparatus is often used to characterize the swelling behaviour of soils in the laboratory, in order to derive either the free swelling deformation or the swelling pressure (Mesri et al., 1994; ASTMD4546, 1996; Di Maio et al., 2004; Wang et al., 2012). Swelling pressure is defined as the external pressure that has to be applied to a sample in order to prevent any swelling upon resaturation (Gonçalvès et al., 2010). When adopting the oedometric apparatus to investigate the swelling behaviour of shales, it is important to take into account the impact of the intrinsic anisotropy of the material which may cause a different swelling behaviour as a function of the orientation of the loading with respect to the bedding planes. The swelling pressure correlation with index properties and density has been extensively studied for soils since the works of Holtz and Gibbs (1956) and Komornik and David (1969). The investigation of the swelling behaviour of shales was also initiated more than thirty years ago fostered by the several stability problems encountered in construction, mining and petroleum activities (Madsen and Muller-Vonmoos, 1985; Huang et al., 1986; Steiger, 1993; Mesri et al., 1994; Van Oort, 2003). With the intent to provide a solution to shale-water interaction issues, the majority of the studies focused on the impact of the pore fluid composition on the swelling behaviour of shales (Steiger, 1993; Van Oort, 2003; Ewy, 2014). The volume change/swelling pressure development during wetting under different boundary conditions (free swelling, constant volume and constant mean stress) was investigated by Mesri et al. (1994) for Taylor shale and by Powell et al. (2013) for Bearpaw Shale. The results of these studies show that the swelling response is related to the initial stress and initial volume of the material, in addition to the boundary conditions during wetting. In particular, a decrease of the initial void ratio induces an increase of the swelling pressure when constant volume wetting is carried out; while a decrease of the mean stress induces an increase in swelling deformation upon wetting in free-volume conditions.

In this section, an insight on the swelling behaviour of Opalinus Clay is carried out, based on the results obtained during the resaturation phases of several high-pressure oedometric tests. Some of the considered tests have been described in section 3.2 and 3.4.1; the results of the resaturation phases of other high-pressure oedometric tests presented further in Chapters 4 and 5, are also considered for a

more comprehensive analysis. As described in section 3.2.2.3, the resaturation phase of all the considered tests is carried out using synthetic water (which reproduces the in-situ pore water composition) and by limiting the volume expansion ($\Delta e < 0.2\%$); therefore the maximum external pressure applied to maintain constant volume conditions provides the measurement of the swelling pressure. In few tests a greater volume increase was accorded during resaturation; this fact allows to highlight the impact of a certain volume change on the observed swelling pressure. The obtained results are presented in Figure 3-33 for the OPA-shallow and in Figure 3-34 for the OPA-deep; all the results are obtained on specimens tested perpendicular to the bedding planes (S-samples).

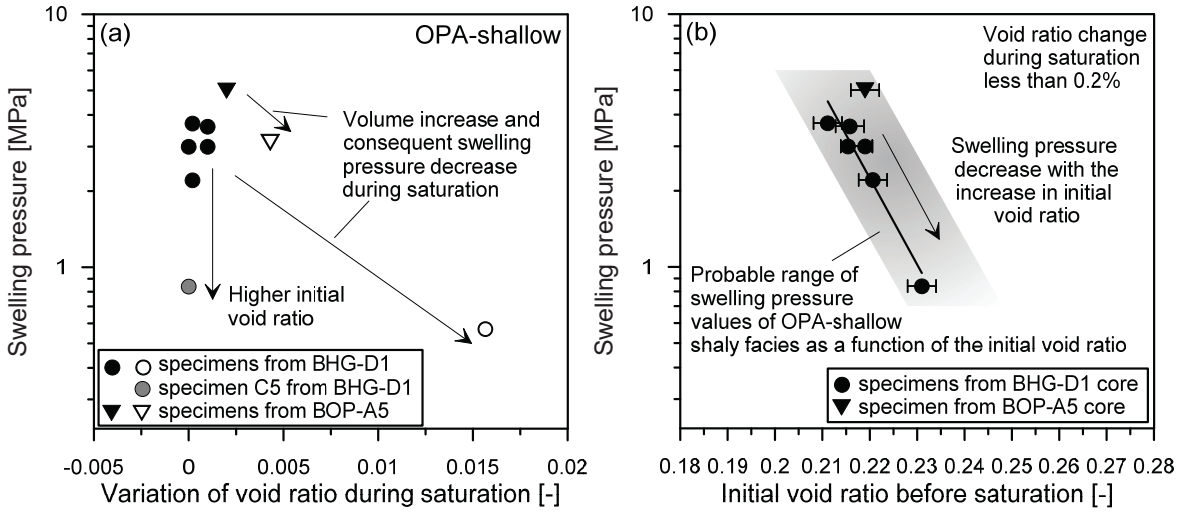

Figure 3-33: Swelling pressure values of OPA-shallow as a function of the void ratio variation during wetting (a) and of the initial void ratio before saturation (b).

The swelling pressure values measured on OPA-shallow specimens as a function of the void ratio variation during wetting are presented in Figure 3-33a. The figure shows that, as expected, when void ratio variations greater than 0.2% are allowed, a lower swelling pressure is measured, due to the dissipation of the swelling potential caused by the increase in volume. When void ratio variations during wetting are prevented ($\Delta e < 0.1\%$ for BHG-D1 and $\Delta e < 0.2\%$ for BOP-A5) a maximum swelling pressure value of 3.7 MPa and 5 MPa is obtained for BHG-D1 and BOP-A5, respectively. Figure 3-33b depicts the swelling pressure values as a function of the initial void ratio before wetting for the tests where the void ratio change during wetting is kept lower than 0.2%. The figure shows that even if Δe is kept lower than 0.2%, the swelling pressure value observed is not constant: it decreases with the increase of the initial void ratio before wetting. Previous studies on shales (Mesri et al., 1994; Powell et al., 2013) have highlighted this behavioural feature, where the greater the initial void ratio, the lower the swelling pressure measured during wetting in constant volume conditions. The initial greater void ratio of a specimen, and therefore the lower swelling pressure, may be due to same disturbance or humidification during the phases of specimen preparation and emplacement in the cell. A probable range of swelling pressure values as a function of the initial void ratio before wetting for OPA-shallow shaly facies is proposed in Figure 3-33b. This analysis helps in identifying the sealing capacity of this shale in relation to its initial volume state.

The swelling pressure values obtained for OPA-deep specimens as a function of the void ratio variation during wetting are presented in Figure 3-34; the initial void ratio before saturation is also indicated in Figure 3-34. The results clearly show that if a certain volume increase is allowed during saturation, a marked decrease in swelling pressure is obtained when about the same initial void ratio is found. Some differences in the mineralogical composition of the OPA-deep cores have been highlighted in Chapter 1 (see Table 1-9), where a greater clay content induces a higher void ratio in the material, due to the fact that the interconnected porosity is mainly observed at the level of the clay matrix. The results presented in Figure 3-34 highlight the impact of the mineralogical composition both on the initial void ratio and on the swelling behaviour. In fact, the OPA-deep core called OPA-2 presents a considerably greater clay content and lower quartz content with respect to other OPA-deep cores; accordingly, it manifests a greater initial void ratio, but also a greater swelling tendency, even though a greater void ratio variation during saturation is encountered with respect to the other tested specimens.

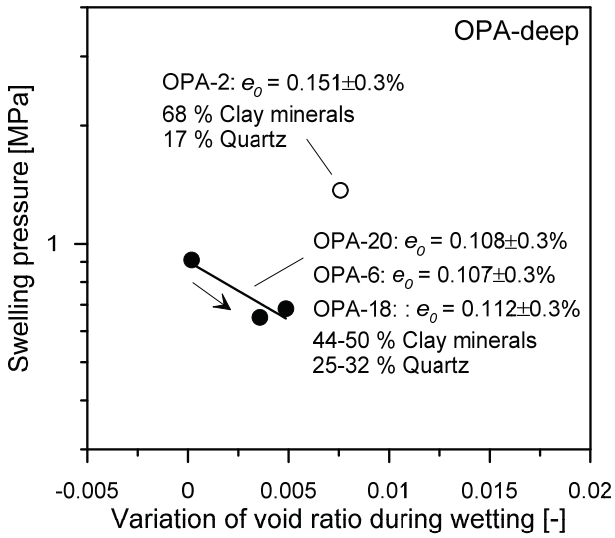

Figure 3-34: Swelling pressure values of OPA-deep as a function of the void ratio variation during wetting.

The swelling pressure values do not show correlation with the initial degree of saturation for the tested specimens. This is due to the fact that the initial degree of saturation of the considered OPA-shallow and OPA-deep specimens is in the range of 0.61-0.88: according to the retention behaviour of the OPA-shallow and OPA-deep analysed in Chapter 2 (Figure 2.5 and Figure 2.7), this range corresponds to total suction values between 20-40 MPa for the former, and between 30-70 MPa for the latter. The analysis of the volume change behaviour during wetting and drying paths conducted in Chapter 2 (Figure 2.8) shows that the majority of the swelling manifests mainly when total suction is reduced to values below 10 MPa for the OPA-shallow, and below 30 MPa for the OPA-deep, so that about the same volume change response is expected during wetting when the initial suction is within the above-mentioned total suction ranges for the same initial void ratio. As a consequence, the swelling behaviour of the considered specimens is found to depend mainly on the allowed deformation during wetting, on the initial void ratio of the material, and on the mineralogical composition of the tested cores.

3.4.4. Analysis of permeability-void ratio relationship

The coefficient of permeability is computed according to Eq.(3.44), which was derived from the consolidation equation for a poroelastic geomaterial (section 3.2.3.4.2). The values of the coefficient of permeability for OPA-shallow, OPA-deep and BD are presented in Figure 3-35 as a function of the void ratio at the end of each loading step normalized with respect to the initial void ratio before oedometric compression (e_i). This procedure allows to remove the scatter in the initial void ratio values, which is due to several factors: the presence of an error in the measured quantities used to compute the initial void ratio, the possibility of having some irregularities in the shape of the prepared specimens which cause artefacts during their volume measurement (since perfect cylindrical shape is assumed for the specimens), as well as the different mineralogy of the tested cores which may induce different effective porosity values (i.e. the ratio of the volume of the conducting pores to the total volume (Koponen et al., 1997)). In fact, in low porosity geomaterials part of the total void ratio is not relevant to the flow (Koponen et al., 1997). In the case of Opalinus Clay this is mainly due to either non-connected (isolated) pores, or to the presence of large storage pores.

The results depicted in Figure 3-35 show that the decrease in void ratio due to mechanical compaction induces a relevant decrease in permeability. Such trend of permeability reduction with decreasing void ratio is well defined for the three tested shales. Reducing the void ratio to 80% of its initial value induces a decrease in permeability of about one order of magnitude for OPA-shallow and of about two orders of magnitude for OPA-deep and BD shales (Figure 3-35). The normalised void ratio values found on the oedometric curve at the in-situ vertical effective stress are also represented in Figure 3-35. The figure shows that the reduction in permeability with decreasing void ratio is more significant in the initial recompression phase, when void ratio values are greater or close to the ones found at the in-situ stress; this is observed especially for the OPA-deep and BD cores. On the other hand, less marked reduction in permeability with decreasing void ratio is observed when the material is compressed at void ratio values lower than the ones found at the in-situ stress. The observed behaviour can be interpreted in light of the knowledge concerning the response of shales during coring processes, sampling, unloading and re-wetting (Pham et al., 2007; Mohajerani et al., 2011; Sarout et al., 2014; Ewy, 2015; Zhang, 2015), as well as considering the pore network microstructure of the studied shales as described in Section 3.3.3.2. The fast reduction of permeability with void ratio in the initial recompression phase is likely due to the closure of coring/sampling/wetting- induced micro-fissures. Zhang (2015) investigated the permeability evolution of an argillite during re-compaction to the in-situ stress and found a significant and irreversible decrease in permeability of some orders of magnitude, which was attributed to the closure of sampling-induced microcracks. Once the material is brought to the in-situ stress, the majority of the micro-fissures are closed and further compaction causes the closure of connecting and storage pores. The closure of storage pores has less impact on the permeability variation with respect to the closure of connecting pores, since the latter mainly dictate the transport properties of the material. If no volume change is allowed during resaturation, the initial marked change in permeability is limited as in the case of OPA-shallow, while almost all the OPA-deep and BD specimens experienced some swelling during resaturation, which

might have induced some damage to the material. In fact, a severe impact on the permeability is noticed.

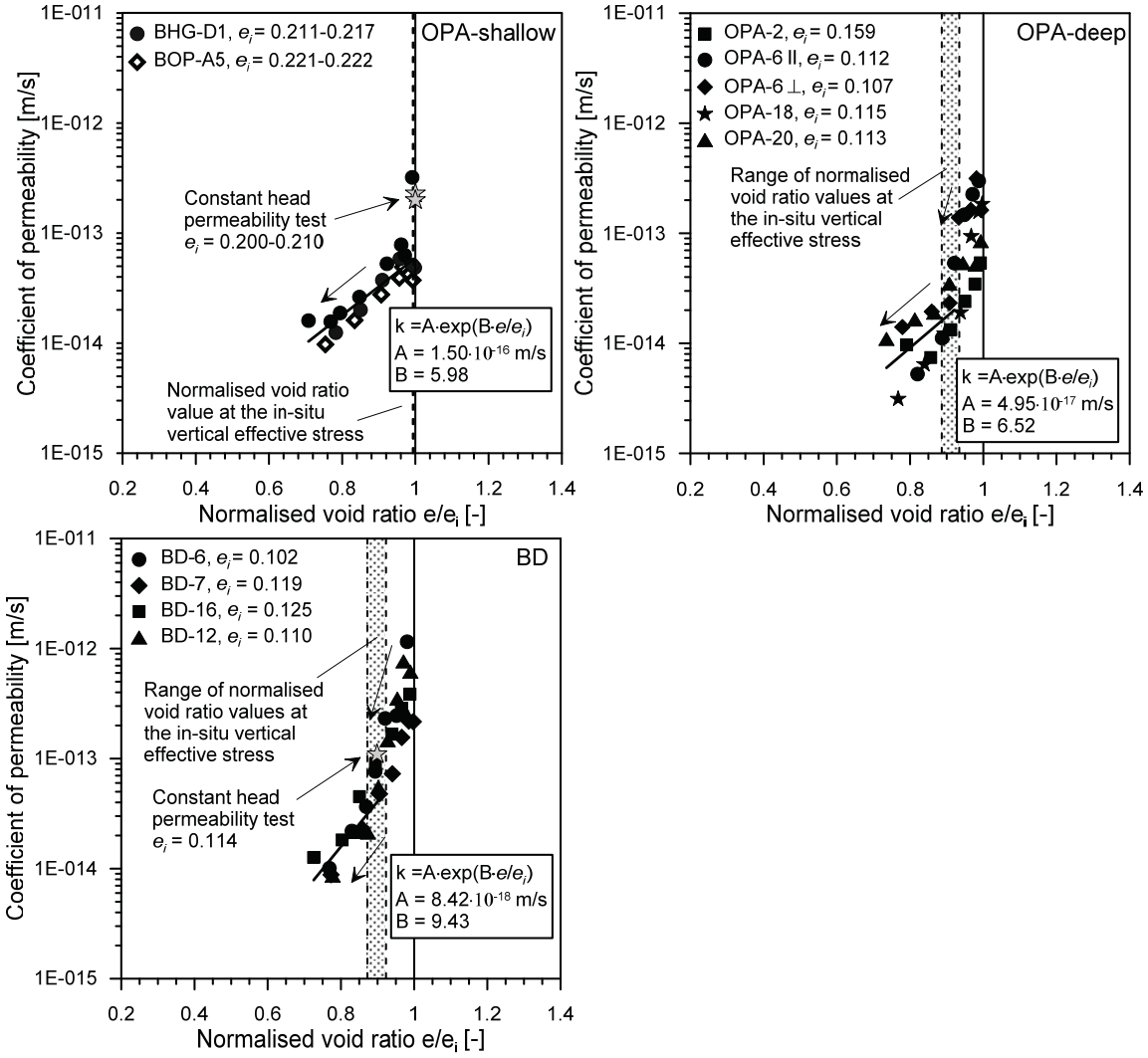

Figure 3-35: Coefficient of permeability as a function of the normalised void ratio for the three tested Swiss shales.

The permeability- void ratio relationship, for normalized void ratio values lower than the identified threshold representing in-situ conditions, is fitted through an exponential equation indicated in Figure 3-35 for the three shales. The results of constant head permeability tests on OPA-shallow and BD shale specimens are also reported in Figure 3-35, revealing good agreement with the permeability values obtained from consolidation tests. The results presented in Figure 3-35 are also in good agreement with the permeability-void ratio values reported in Romero et al. (2013) for the three tested shales.

3.5. Conclusions

An advanced experimental tool and a new rigorous and comprehensive technique for investigating the one-dimensional volumetric behaviour and consolidation of shales have been presented in section 3.2. Testing materials with high yield stresses requires the design of a high-pressure oedometric cell, as presented here; the proposed approach enabled the successful testing of the mechanical behaviour of Opalinus Clay shale specimens and the observation of the transition from the pre- to the post-yield phase. An analytical solution was rigorously derived to enable the analysis of the time-dependent settlement curves of the tested shales; the developed method allows for the interpretation of the experimental results in light of the deformation of the testing device and secondary consolidation phenomenon. In addition, the analytical expression accounts for time-dependent loading conditions to address the delay in load application.

Results on Opalinus Clay shale specimens from different depths and different sites were presented. The proposed experimental procedure and analytical technique for investigating the consolidation behaviour of Opalinus Clay enabled the analysis of the fundamental hydro-mechanical features of the material. The results were reported in terms of the stiffness and consolidation coefficient, and their dependency on the stress level and stress path was successfully addressed. The values of the secondary compression coefficient were also reported, allowing information to be gathered on the creep behaviour of the tested shale as a function of the vertical effective stress. Significant information regarding the poroelastic behaviour of the tested material was derived, extending the available knowledge concerning the poroelastic parameters of Opalinus Clay. A rigorous procedure for computing the coefficient of permeability from consolidation tests on poroelastic materials was presented, together with select results for deep Opalinus Clay. Porosity variations due to consolidation processes or creep effects are of major concern in all applications involving shales. The results of this work can provide guidance regarding consolidation and settlement during tunnel excavation, swelling phenomena during resaturation, and displacements related to delayed convergence due to creep effects.

An experimental study aimed at characterizing the behaviour of the Opalinus Clay shale in the remoulded state has been presented in section 3.3. Such characterization helps understanding (i) the significance of diagenesis and depth for Opalinus Clay shale and their impact on the hydro-mechanical behaviour of the material and (ii) the extent to which the remoulded material can be used for gathering information on the behaviour of the natural shale. The procedure for the preparation of remoulded specimens was reported together with the testing protocol and the analysis of the results. Significant diagenetic effects have been highlighted for Opalinus Clay shale from Northern Switzerland. Diagenetic processes that have developed during the burial history of Opalinus Clay have caused a certain degree of cementation and bonding of the material structure, with significant consequences on the mechanical behaviour in terms of compressibility, swelling properties, porosity reduction and creep effects. A greater stiffness is observed in response to diagenetic processes, while a lower swelling sensitivity is registered: the greater swelling tendency of the remoulded material during mechanical unloading is likely to be related to bond breakage during the remoulding process.

A considerable reduction in porosity is observed as a consequence of diagenesis, as the void ratio of the intact material cannot be reached simply by mechanical compaction of the remoulded one. Diagenesis does not seem to a have a strong impact on the permeability of the tested shales, as the storage pores are likely to be filled and cemented rather than the connecting pores. Creep effects are observed to be greater when the material is remoulded. In conclusion, the relevant roles of depth and diagenesis have been highlighted for Opalinus Clay, as the mechanical properties of this shale found at shallow depths are different from those observed for the same shale found at greater depths. In addition, particular attention has to be paid when testing remoulded Opalinus Clay, as the hydro-mechanical behaviour may substantially differ from that of the natural shale.

The last section of this chapter presented further analysis on the hydro-mechanical behaviour of OPA-deep cores highlighting the impact of mineralogical compositions and the limited role of anisotropy on the hydro-mechanical response of the material. The one-dimensional compression behaviour of BD shale cores retrieved at the Schlattingen site was also investigated and compared to Opalinus Clay.

An insight into the swelling behaviour of Opalinus Clay was carried out based on the results of the resaturation phases of several high-pressure oedometric tests. The obtained results highlight that the swelling pressure values measured during resaturation are highly influenced by the allowed deformation during wetting, as well as by the mineralogical composition of the tested core. An impact of the initial void ratio prior to wetting is also recognised.

The permeability-void ratio relationship of the tested shales has been analysed in detail. The analysis highlighted the peculiar relationship between permeability and normalised void ratio values, where a rapid decrease in permeability with decreasing void ratio is observed in the initial recompression phase until about the void ratio value at the in-situ vertical effective stress is reached; while the rate of permeability decrease with decreasing void ratio reduces when the material is compressed at void ratio values lower than the ones found at the in-situ stress. The observed behaviour is justified taking into account the impact of the coring/sampling/rewetting processes on the material, as well as its pore network microstructure.

3.6. References

Addis, M.A. and Jones, M.E. Volume changes during diagenesis. Marine and Petroleum Geology (1985) 2(3): 241-246.

Ali, S.A., Clark, W.J., Moore, W.R. and Dribus, J.R. Diagenesis and reservoir quality. Oilfield Review (2010) 22(2): 14-27.

Alonso, E. and Alcoverro, J. Swelling and degradation of argillaceous rocks. In: Proceedings of the 3rd international conference on unsaturated soils, Recife, Brazil: 951–969, (2002). 951–969.

Asef, M. and Farrokhrouz, M. Shale engineering: Mechanics and mechanisms, CRC Press, (2013).

ASTMD4546 (1996). Standard Test Methods for One-Dimensional Swell or Settlement Potential of Cohesive Soils. Annual book of ASTM Standards, vol. 04.08. West Conshohocken, PA.

Aversa, S., Evangelista, A., Leroueil, S. and Picarelli, L. (1993). Some aspects of the mechanical behaviour of structured soils and soft rocks. Geotechnical Engineering of hard soils-weak rocks. A. Anagnostopoulos, F. Schlosser, N. Kalteziotis and R. Frank. Rotterdam, Balkema. 1**:** 359-366.

Bass, J. (1995). Elasticity of minerals, glasses and melts. Mineral physics and crystallography: a handbook of physical constants. T. J. Ahrens. Washington DC, Am. Geophys. Union, AGU Reference Shelf 2**:** 45-63.

Biot, M.A. General theory of three-dimensional consolidation. Journal of applied physics (1941) 12(2): 155-164.

Bjerrum, L. The third Terzaghi lectures; Progressive failure in slopes of overconsolidated plastic clay and clay shales. Journal of the Soil Mechanics and Foundations Division (1967) 93(5): 1-49.

Bjørlykke, K. and Høeg, K. Effects of burial diagenesis on stresses, compaction and fluid flow in sedimentary basins. Marine and Petroleum Geology (1997) 14(3): 267-276.

Bock, H. RA Experiment. Updated review of the rock mechanics properties of the Opalinus Clay of the Mont Terri URL based on laboratory and field testing. Unpublished Mont Terri Technical Report (2009).

Bossart, P. (2012). Characteristics of the Opalinus Clay at Mont Terri. http://www.mont-terri.ch/internet/mont-terri/de/home/geology/key_characteristics.html.

Burland, J. On the compressibility and shear strength of natural clays. Geotechnique (1990) 40(3): 329-378.

Casagrande, A. The determination of the pre-consolidation load and its practical significance. Proceedings of the international conference on soil mechanics and foundation engineering, Harvard University Cambridge, (1936). 60-64.

Chan, A. Determination of the coefficient of consolidation using a least squares method. Geotechnique (2003) 53(7): 673-678.

Chandler, R. Stiff sedimentary clays: geological origins and engineering properties. Geotechnique (2010) 60(12): 891-902.

Cheng, A.-D. Material coefficients of anisotropic poroelasticity. International Journal of Rock Mechanics and Mining Sciences (1997) 34(2): 199-205.

Conte, E. and Troncone, A. One-dimensional consolidation under general time-dependent loading. Canadian geotechnical journal (2006) 43(11): 1107-1116.

Cook, J. The effects of pore pressure on the mechanical and physical properties of shales. Oil & Gas Science and Technology (1999) 54(6): 695-701.

Corkum, A.G. and Martin, C.D. The mechanical behaviour of weak mudstone (Opalinus Clay) at low stresses. International Journal of Rock Mechanics and Mining Sciences (2007) 44(2): 196-209.

Cotecchia, F. and Chandler, R. A general framework for the mechanical behaviour of clays. Geotechnique (2000) 50(4): 431-447.

Cotecchia, F. and Chandler, R.J. The influence of structure on the pre-failure behaviour of a natural clay. Geotechnique (1997) 47(3): 523-544.

Coussy, O. Mécanique des milieux poreux. Paris, Editions Technip, (1991).

Detournay, E. and Cheng, A. (1993). Fundamentals of Poroelasticity. Comprehensive rock engineering: principles, practice & projects. H. J. (ed). Oxford, Pergamon Press. 2**:** 113-171.

Dewhurst, D.N., Aplin, A.C., Sarda, J.P. and Yang, Y. Compaction-driven evolution of porosity and permeability in natural mudstones: An experimental study. Journal of Geophysical Research: Solid Earth (1998) 103(B1): 651-661.

Di Maio, C., Santoli, L. and Schiavone, P. Volume change behaviour of clays: the influence of mineral composition, pore fluid composition and stress state. Mechanics of Materials (2004) 36(5): 435-451.

Djéran-Maigre, I., Tessier, D., Grunberger, D., Velde, B. and Vasseur, G. Evolution of microstructures and of macroscopic properties of some clays during experimental compaction. Marine and Petroleum Geology (1998) 15(2): 109-128.

Ewy, R.T. Shale swelling/shrinkage and water content change due to imposed suction and due to direct brine contact. Acta Geotechnica (2014) 9(5): 869-886.

Ewy, R.T. Shale/claystone response to air and liquid exposure, and implications for handling, sampling and testing. International Journal of Rock Mechanics and Mining Sciences (2015) 80: 388-401.

Favero, V., Ferrari, A. and Laloui, L. On the hydro-mechanical behaviour of remoulded and natural Opalinus Clay shale. Engineering Geology (2016) 208: 128-135.

Ferrari, A., Favero, V. and Laloui, L. One-dimensional compression and consolidation of shales. International Journal of Rock Mechanics and Mining Sciences (2016) 88: 286-300

Ferrari, A., Favero, V., Manca, D. and Laloui, L. Geotechnical characterization of core samples from the geothermal well Schlattingen SLA-1. Nagra Arb. Ber. NAB (2013): 12-50.

Flemings, P. and Betts, W. Permeability and Compressibility of Resedimented Gulf of Mexico Mudrocks. Fourth EAGE Shale Workshop, (2014).

Gibson, R. The progress of consolidation in a clay layer increasing in thickness with time. Geotechnique (1958) 8(4): 171-182.

Gonçalvès, J., Rousseau-Gueutin, P., de Marsily, G., Cosenza, P. and Violette, S. What is the significance of pore pressure in a saturated shale layer? Water Resources Research (2010) 46(4).

Gradstein, F.M., Ogg, J.G., Schmitz, M. and Ogg, G. The Geologic Time Scale 2012 2-Volume Set, elsevier, (2012).

Gutierrez, M., Katsuki, D. and Tutuncu, A. Determination of the continuous stress-dependent permeability, compressibility and poroelasticity of shale. Marine and Petroleum Geology (2015) 68: 614-628.

Hanna, D., Sivakugan, N. and Lovisa, J. Simple approach to consolidation due to constant rate loading in clays. International Journal of Geomechanics (2011) 13(2): 193-196.

Head, K. (1984). Manual of Soil Laboratory Testing, 1, Soil Classification and Compaction Tests. ELE International Ltd, Fentech Press, London.

Hedberg, H.D. Gravitational compaction of clays and shales. American Journal of Science (1936) (184): 241-287.

Hill, R. The elastic behaviour of a crystalline aggregate. Proceedings of the Physical Society. Section A (1952) 65(5): 349-354.

Holtz, W.G. and Gibbs, H.J. Engineering properties of expansive clays. Transactions of the American Society of Civil Engineers (1956) 121(1): 641-663.

Hong, Z.-S., Zeng, L.-L., Cui, Y.-J., Cai, Y.-Q. and Lin, C. Compression behaviour of natural and reconstituted clays. Geotechnique (2012) 62(4): 291-301.

Hong, Z. Correlating compression properties of sensitive clays using void index. Geotechnique (2006) 56(8): 573-578.

Hong, Z., Yin, J. and Cui, Y.-J. Compression behaviour of reconstituted soils at high initial water contents. Geotechnique (2010) 60(9): 691-700.

Houben, M., Desbois, G. and Urai, J. Pore morphology and distribution in the Shaly facies of Opalinus Clay (Mont Terri, Switzerland): insights from representative 2D BIB–SEM investigations on mm to nm scale. Applied Clay Science (2013) 71: 82-97.

Hsu, T.-W. and Lu, S.-C. Behavior of one-dimensional consolidation under time-dependent loading. Journal of Engineering Mechanics (2006) 132(4): 457-462.

Huang, S., Aughenbaugh, N. and Rockaway, J. Swelling pressure studies of shales. International Journal of Rock Mechanics and Mining Sciences & Geomechanics Abstracts, Elsevier, (1986). 371-377.

Jahns, E. Geomechanical laboratory tests on Opalinus Clay cores from the bore hole Schlattingen SLA-1. Nagra Work Report NAB (2013): 13-18.

Jones, M.E. and Addis, M.A. On changes in porosity and volume during burial of argillaceous sediments. Marine and Petroleum Geology (1985) 2(3): 247-253.

Jones, M.E. and Addis, M.A. Volume change during sediment diagenesis and the development of growth faults. Marine and Petroleum Geology (1984) 1(2): 118-122.

Keller, L.M., Schuetz, P., Erni, R., Rossell, M.D., Lucas, F., Gasser, P. and Holzer, L. Characterization of multi-scale microstructural features in Opalinus Clay. Microporous and mesoporous materials (2013) 170: 83-94.

Komornik, A. and David, D. Prediction of swelling pressure of clays. J. Soil Mech. Found. Div., Am. Soc. Civ. Eng.;(United States) (1969) 95.

Koponen, A., Kataja, M. and Timonen, J. Permeability and effective porosity of porous media. Physical Review E (1997) 56(3): 3319.

Lambe, T.W. and Whitman, R.V. Soil Mechanics, Wiley and Sons, (1979).

Leroueil, S. and Vaughan, P. The general and congruent effects of structure in natural soils and weak rocks. Geotechnique (1990) 40(3): 467-488.

Lovisa, J., Sivakugan, N. and Ameratunga, J. Discretisation of constant rate loading. In: ANZ 2012 Conference Proceedings. From: Ground Engineering in a Changing World: 11th Australia - New Zealand Conference on Geomechanics, Melbourne, VIC, Australia, (2012). 864-870.

Mäder, U. Recipe and preparation of a simplified artificial pore water for Opalinus Clay and Brown Dogger. NAGRA AN (2011): 11-159.

Madsen, F.T. and Muller-Vonmoos, M. Swelling pressure calculated from mineralogical properties of a Jurassic opalinum shale, Switzerland. Clays and Clay Minerals (1985) 33(6): 501-509.

Martin, C. and Lanyon, G. Measurement of in-situ stress in weak rocks at Mont Terri Rock Laboratory, Switzerland. International Journal of Rock Mechanics and Mining Sciences (2003) 40(7): 1077-1088.

Mesri, G. and Hayat, T. The coefficient of earth pressure at rest. Canadian geotechnical journal (1993) 30(4): 647-666.

Mesri, G., Pakbaz, M. and Cepeda-Diaz, A. Meaning, measurement and field application of swelling pressure of clay shales. Geotechnique (1994) 44(1): 129-145.

Mesri, G., Ullrich, C. and Choi, Y. The rate of swelling of overconsolidated clays subjected to unloading. Geotechnique (1978) 28(3): 281-307.

Mohajerani, M., Delage, P., Monfared, M., Tang, A.M., Sulem, J. and Gatmiri, B. Oedometric compression and swelling behaviour of the Callovo-Oxfordian argillite. International Journal of Rock Mechanics and Mining Sciences (2011) 48(4): 606-615.

Nagra (2002). Projekt Opalinuston: Synthese der geowissenschaftlichen Untersuchungsergebnisse. Entsorgungsnachweis für abgebrannte Brennelemente, verglaste hochaktive sowie langlebige mittelaktive Abfälle. Nagra Technischer Bericht. NTB 02-03. Nagra, Wettingen.

Nagra (2014b). SGT Etappe 2: Vorschlag weiter zu untersuchender geologischer Standortgebiete mit zugehörigen Standortarealen für die Oberflächenanlage. Geologische Grundlagen. Nagra Technischer Bericht. NTB 14-02. Nagra, Wettingen. .

Nagra (2014a). Sicherheitstechnischer Bericht zu SGT-Etappe 2: Sicherheitstechnischer Vergleich und Vorschlag der in Etappe 3 weiter zu untersuchenden geologischen Standortgebiete. Nagra Technischer Bericht. NTB 14-01. Nagra, Wettingen. .

Nygård, R., Gutierrez, M., Gautam, R. and Høeg, K. Compaction behavior of argillaceous sediments as function of diagenesis. Marine and Petroleum Geology (2004) 21(3): 349-362.

Olson, R.E. Consolidation under time-dependent loading. Journal of the Geotechnical Engineering Division (1977) 103(1): 55-60.

Pearson, F. (1998). Opalinus clay experimental water: A1 Type, Version 980318. PSI Internal report TM-44-98-07. V. P. Paul Scherrer Institut, Switzerland.

Pham, Q., Vales, F., Malinsky, L., Minh, D.N. and Gharbi, H. Effects of desaturation–resaturation on mudstone. Physics and Chemistry of the Earth, Parts A/B/C (2007) 32(8): 646-655.

Picarelli, L. Discussion on the paper: “The general and congruent effects of structure in natural soils and weak rocks” by S. Leroueil and PR Vaughan. Geotechnique (1991) 41(2): 281-284.

Powell, J., Siemens, G., Take, W. and Remenda, V. Characterizing the swelling potential of Bearpaw clayshale. Engineering Geology (2013) 158: 89-97.

Reuss, A. Berechnung der Fließgrenze von Mischkristallen auf Grund der Plastizitätsbedingung für Einkristalle. ZAMM-Journal of Applied Mathematics and Mechanics/Zeitschrift für Angewandte Mathematik und Mechanik (1929) 9(1): 49-58.

Romero, E., Senger, R., Marschall, P. and Gómez, R. (2013). Air tests on low-permeability claystone formations. Experimental results and simulations. In: Multiphysical Testing of Soils and Shales, Springer**:** 69-83.

Salager, S., Ferrari, A. and Laloui, L. (2010). New experimental tools for the characterization of highly overconsolidated clayey materials in unsaturated conditions. In: Mechanics of unsaturated geomaterials. L. L. (ed.), John Wiley & sons**:** 113-126.

Sarout, J., Esteban, L., Delle Piane, C., Maney, B. and Dewhurst, D.N. Elastic anisotropy of Opalinus Clay under variable saturation and triaxial stress. Geophysical Journal International (2014) 198(3): 1662-1682.

Savage, W.Z. and Braddock, W. A model for hydrostatic consolidation of Pierre shale. International journal of rock mechanics and mining sciences & geomechanics abstracts (1991) 28(5): 345-354.

Schmertmann, J.H. The mechanical aging of soils. Journal of Geotechnical Engineering (1991) 117(9): 1288-1330.

SHARC (2014). Annual Report. Shale Research Centre (SHARC) Consortium.

Shukla, M. and Padial, N. A calculation of the Debye characteristic temperature of cubic crystals. Rev. Bras. de Fis (1973) 3(1): 39-45.

Skempton, A. The pore-pressure coefficients A and B. Geotechnique (1954) 4(4): 143-147.

Skempton, A.W. The consolidation of clays by gravitational compaction. Quarterly Journal of the Geological Society (1969) 125(1-4): 373-411.

Steiger, R.P. Advanced triaxial swelling tests on preserved shale cores. International journal of rock mechanics and mining sciences & geomechanics abstracts, Elsevier, (1993). 681-685.

Terzaghi, K. Die berechnung der durchlassigkeitsziffer des tones aus dem verlauf der hydrodynamischen spannungserscheinungen. Sitzungsber. Akad. Wissen., Wien Math. Naturwiss. Kl., Abt. IIa (1923) 132: 105-124.

Van Oort, E. On the physical and chemical stability of shales. Journal of Petroleum Science and Engineering (2003) 38(3): 213-235.

Vanorio, T., Prasad, M. and Nur, A. Elastic properties of dry clay mineral aggregates, suspensions and sandstones. Geophysical Journal International (2003) 155(1): 319-326.

Voigt, W. Lehrbuch der Kristallphysik. Teubner, Leipzig. (1928).

Wang, H. Theory of linear poroelasticity with applications to geomechanics and hydrogeology, Princeton University Press, (2000).

Wang, Q., Tang, A.M., Cui, Y.-J., Delage, P. and Gatmiri, B. Experimental study on the swelling behaviour of bentonite/claystone mixture. Engineering Geology (2012) 124: 59-66.

William, E. Engineering performance of Bringelly shale. (2005).

William, E. and Airey, D. (2009). The role of fabric in evaluating the failure mode of the stiffened Bringelly Shale. 10th IAEG International Congress IAEG 2006. United Kingdom: Geological Society of London.

Wong, R. Swelling and softening behaviour of La Biche shale. Canadian geotechnical journal (1998) 35(2): 206-221.

Zeng, L.-L., Hong, Z.-S. and Cui, Y.-J. Determining the virgin compression lines of reconstituted clays at different initial water contents. Canadian geotechnical journal (2015) 52(999): 1-8.

Zhang, C.-L. The stress–strain–permeability behaviour of clay rock during damage and recompaction. Journal of Rock Mechanics and Geotechnical Engineering (2015).

Chapter 4
Thermo-Mechanical Volume Change Behaviour of Opalinus Clay

4.1. Foreword

This chapter examines the thermo-mechanical volume change behaviour of Opalinus Clay in relation to different stress conditions and overconsolidation ratio (OCR) values and evaluates the impact of temperature on some hydro-mechanical properties of this material. To this aim, a focused experimental campaign consisting in high-temperature/high-pressure oedometric tests has been carried out.

The following sections are based on the paper entitled "Thermo-Mechanical Volume Change Behaviour of Opalinus Clay" - Favero et al. (2016), which is published in the International Journal of Rock Mechanics and Mining Science. The content of the paper is reported here and adjusted in order to avoid repetitions with respect to the previous chapters of the Thesis.

4.2. Introduction

In recent years, several shale formations have been involved in geo-energy related engineering fields that foresee the presence of high thermal loads or significant temperature variations. Such thermal conditions are related to a need to reach great depths (several hundred of meters), as in the case of CO_2 sequestration and Enhanced Geothermal System (EGS) technologies, or to the presence of thermal sources, as in the context of nuclear waste geological disposal. In addition, thermal changes can occur in shale formations through the injection of drilling and fracturing fluids at great depths, where a higher temperature with respect to the one of the injected fluid is encountered as a result of the geothermal gradient. Therefore questions are raised on the impact of temperature variations on the hydro-mechanical properties of shale formations and on the thermal response of the material at different stress conditions. The Opalinus Clay shale formation is considered as host-material for the construction of a deep geological repository for radioactive waste in Switzerland. The formation is expected to be exposed to higher temperatures relative to those found in-situ due to the disposal of the canister containing radioactive waste (Gaus et al., 2014; Dupray and Laloui, 2016); as a consequence, the thermo-mechanical behaviour of Opalinus Clay shale must be thoroughly analysed.

The thermo-mechanical behaviour of clays has been widely studied in the past, and extensive knowledge in this area has been acquired. The elastic domain has been found to reduce with an increase in temperature (Baldi et al., 1988; Tidfors and Sällfors, 1989; Boudali et al., 1994; Sultan et al., 2002; Di Donna and Laloui, 2015), and negligible thermal effects on the elastic and plastic compressibility of clays have been found by several authors (Campanella and Mitchell, 1968; Baldi et al., 1988; Boudali et al., 1994; Towhata et al., 1995; Burghignoli et al., 2000; Di Donna and Laloui, 2015). The volumetric behaviour due to temperature changes has been found to be strongly dependent on the degree of overconsolidation (Campanella and Mitchell, 1968; Baldi et al., 1988; Towhata et al., 1995; Burghignoli et al., 2000; Sultan et al., 2002; Cekerevac and Laloui, 2004; Di Donna and Laloui, 2015), as heating a normally consolidated clay results in volumetric contraction, slightly overconsolidated samples show initial expansion followed by thermal contraction, and highly overconsolidated samples undergo thermal expansion. Uncertainties remain with respect to basic mechanisms involved in the thermal compaction phenomenon, which is generally attributed to

physico-chemical interactions between clay and water where a change of temperature produces a variation in the thickness of the double layer. In particular, thermal perturbations caused by an increase in temperature would result in the removal of bound water molecules and thus in an irreversible decrease in double layer thickness as sustained in Olson and Mesri (1970) and in Morin and Silva (1984). On the other hand, an increase in temperature causes also a rearrangement of particles (Burghignoli et al., 2000) and generates structural disturbance together with mineral and adsorbed water thermal expansion (Romero et al., 2005). The combination of such phenomena may lead to either thermal expansion or thermal compaction based on the predominant mechanism: both irreversible compaction (Campanella and Mitchell, 1968; Baldi et al., 1988; Boudali et al., 1994; Towhata et al., 1995; Burghignoli et al., 2000; Sultan et al., 2002; Cekerevac and Laloui, 2004; Di Donna and Laloui, 2015) and irreversible expansive behaviour (Romero et al., 2005) have been experimentally observed. The effects of temperature on the coefficient of consolidation of clays have also been addressed in the past: in general an increase in temperature appears to generate an increase in the coefficient of consolidation, mainly due to a decrease in water viscosity at high temperatures (Towhata et al., 1995).

In recent years, attention has been paid to the study of the thermo-mechanical behaviour of argillites and shales given their involvement in the development of energy-related geo-engineering applications. Most studies on argillites have focused on the impacts of temperature on strength properties of this material and have found a slight decrease in strength with an increase in temperature up to 100 °C (Wang et al., 2013; Masri et al., 2014; Zhang et al., 2014). The thermoplastic behaviour of an argillite has been studied in Mohajerani et al. (2014), who highlighted a thermoplastic response similar to that observed for clays. While shales are heavily involved in energy-related fields, their thermo-mechanical behaviour has been poorly studied. Irreversible thermal compaction has been observed in Pierre shale (Bauer et al., 2014) and for a Canadian shale (Xu et al., 2011); a thermo-elasto-plastic response under temperature variations similar to that observed in clays has been reported for Opalinus Clay (Monfared et al., 2011) together with a decrease of the failure strength at high temperatures (Hunsche et al., 2004). On the other hand, the evolution of hydro-mechanical properties of the shale with temperature at different stress levels has not been extensively examined thus far; this is of relevance when predictions of the response of the material are sought via the use of numerical tools.

The impact of the degree of overconsolidation and the effect on the yield stress and on the position of the compression line, are critical aspects in the analysis of the thermo-mechanical behaviour of clays; it is thus important to clarify these concepts in the context of the analysis of the thermo-mechanical behaviour of shales. Several studies on argillites and shales have highlighted the elasto-plastic response of these materials where both reversible and irreversible deformations can be produced upon mechanical loading and where a yield threshold defines the limit of the elastic domain (Sultan et al., 2002; Nygård et al., 2004; Gutierrez et al., 2014). The compression line describes the material behaviour upon virgin compression; when the stress state of the material lies on the compression line it is found in normally consolidated conditions and manifests elasto-plastic behaviour. Significant efforts have been made to develop elasto-plasticity based models for argillites and shales (Gens et al.,

2005; Chen et al., 2010) which can also take into account the presence of some degree of plasticity before the main yield surface is reached (Hujeux, 1979; Mroz et al., 1979; Mroz et al., 1981). The ratio of the maximum stress level ever experienced by a material (preconsolidation pressure) to the actual effective stress is commonly expressed as "overconsolidation ratio" (OCR) (Lambe and Whitman, 1979). This quantity refers to a pure mechanical compaction process. The overburden, which have occurred throughout the geologic history of shales, is among the factors that determine the value of the yield stress, but it is not the only one: particles and water-cations system rearrangement (Mitchell and Soga, 1976), cementation processes (Leroueil and Vaughan, 1990) that occur during diagenesis and degradation phenomena, may induce a variation in the yield stress which becomes an apparent preconsolidation pressure. When the actual stress state has to be compared to the yield stress in the case of a material which has been subjected to chemical processes during its burial history, the term "yield stress ratio" (YSR) is to be used, which is the ratio of the effective yield stress of the material to the actual or imposed effective stress (Cotecchia and Chandler, 1997). When dealing with shales, the need to distinguish between the two concepts of OCR and YSR is encountered, due to the relevance of the geologic history for these geomaterials. In this paper, both the concept of YSR and OCR should be adopted in order to distinguish between the yield stress exhibited by the material and the yield stress induced by mechanical loading in the laboratory. However, the term "OCR" is used here to identify the ratio of the vertical effective yield stress to the actual vertical effective stress, regardless of the way in which the yield stress is induced in the material.

In the context of this study, evidences are sought regarding the impact of temperature on the yield stress for shales, and the effect of the OCR on their thermal volume change behaviour. The thermal cyclic behaviour and thus the dependency of the thermal volumetric response on the temperature history have not been widely studied, and no discussion concerning the temperature induced variation in porosity in shales has ever been raised. An investigation on the thermo-mechanical volume change behaviour of Opalinus Clay is carried out and presented in this chapter. More specifically, this comprehensive experimental campaign aims (i) at analysing the thermal behaviour of Opalinus Clay in relation to different stress conditions and (ii) at examining the impact of temperature on hydro-mechanical properties of the shale formation. The first task involves examining the phase in which the radioactive waste is emplaced in the repository tunnels with the consequent heating of surrounding materials. The second task involves clarifying how the mechanical response of the material is altered by thermal perturbations. To address these issues, the experimental program foresees mechanical loading and unloading paths under different constant temperatures and heating-cooling phases under varying levels of constant vertical effective stress. A high-pressure/high-temperature oedometer cell was developed, set up and calibrated to allow for the analysis of the volume change behaviour of shales under high temperatures (up to 100°C) and under high stress levels (up to 100 MPa). Temperatures exceeding 100 °C are not expected for the host geomaterial in the Swiss concept for the construction of geological repositories for nuclear waste disposal (Gaus et al., 2014; Dupray and Laloui, 2016), while testing under high-pressure conditions allows to observe the transition from the pre-yield phase to the post-yield phase of the material and to cover a broad

range of possible depths and vertical stresses for the repository. The testing tools used, the experimental procedure employed and the studied shale are first described; the results of the experimental campaign are then presented and discussed in the second part of the chapter.

4.3. Experimental methodology

4.3.1. Testing equipment

Shale testing requires the application of high pressures in order to observe the transition from the pre-yield to the post-yield phase. In addition, a broad range of vertical stress levels must be explored in order to capture potential effects of an additional variable (e.g., effects of temperature on the yield stress and on mechanical properties of the material). To examine the thermo-mechanical behaviour of shales, the high-pressure oedometer cell presented in Chapter 3 was used; the cell is equipped with a temperature control system: the layout of the testing apparatus is presented in Figure 4-1.

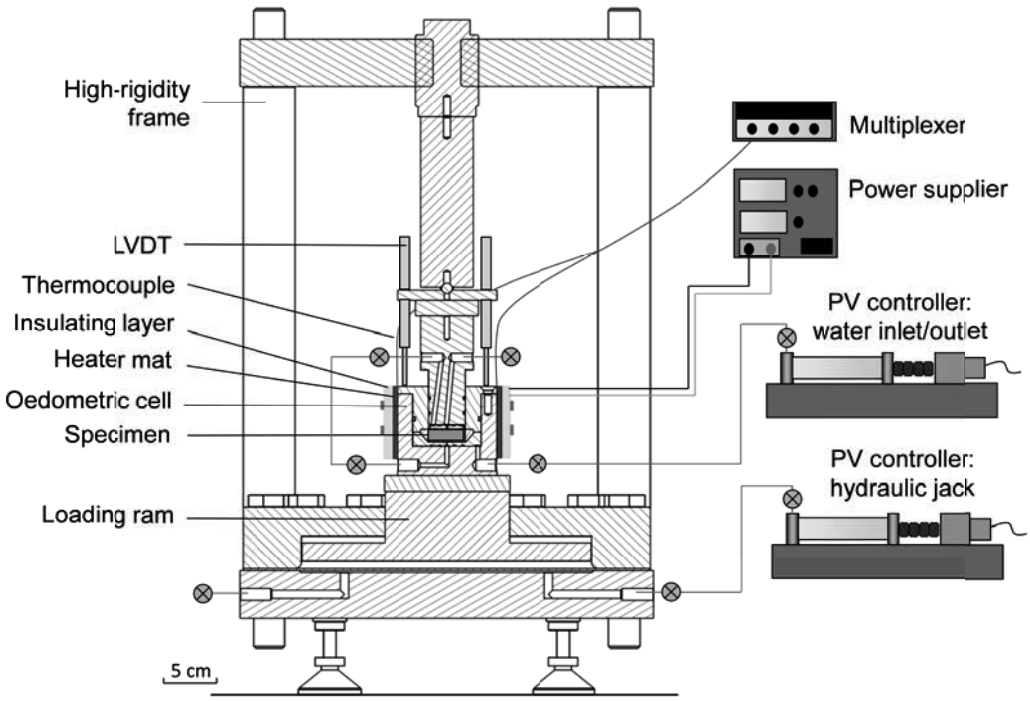

Figure 4-1: The high-pressure oedometric cell modified for controlled-temperature testing.

The cell is heated by a silicon heater mat: heating is achieved through an electrical resistance placed between two layers of woven fibreglass impregnated with a silicon elastomer. Heater mats allow one to easily modify testing devices when introducing temperature control (Di Donna et al., 2015). The heater mat is approximately 3 mm thick, and the permissible surface temperature ranges from – 60 °C

to + 200 °C. The heating section is covered by a 10 mm insulation layer made of silicone foam. The heating mat wraps the cell and it is fixed in place by steel rings. A laboratory power supplier (©Weir 4000 30V-2A) is connected to the heater mat and it is used to control the temperature of the specimen by setting the voltage level. To this purpose the relationship between the applied voltage, the heater mat temperature and the temperature inside the cell is carefully determined (Figure 4-2) using a series of thermocouples (resolution of 0.1 °C): two are permanently placed at the contact interface between the cell and heater mat to allow us to monitor the evolution of the temperature over the entire testing campaign, and another thermocouple is inserted into the cell through the drainage lines and is situated in contact with a shale specimen specifically devoted to this calibration stage.

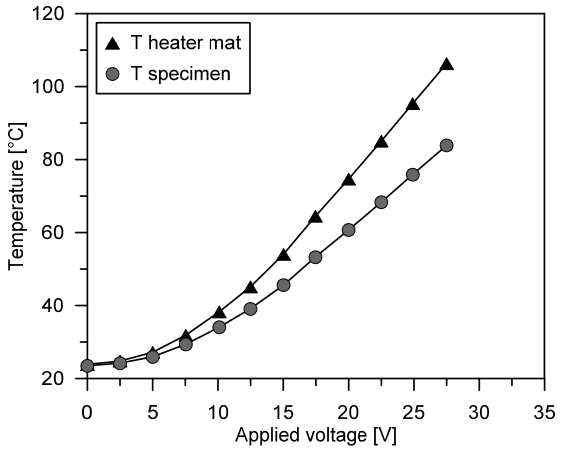

Figure 4-2: Relationship between applied voltage and temperature.

The vertical displacement of the specimen due to temperature variations is measured using a system of LVDTs (resolution of 1 μm); the measured values must account for the thermal deformation of the device. In order to correct the measured vertical displacement, thermal deformations of the apparatus were monitored during thermal loading cycles ranging from 20 °C to 80 °C with temperature steps of approximately 10 °C. A steel specimen with a known thermal expansion coefficient was used during the procedure, and its thermal expansion was taken into account in computing overall apparatus deformations. Apparatus thermal deformations were assessed both vertically and radially under different imposed vertical pressures, and two thermal loading-unloading cycles were carried out for each vertical pressure imposed: the magnitude of vertical pressure applied did not significantly affect the thermal deformation in the device. In order to carefully assess the radial expansion of the cell, four strain gauges were positioned at the interface between the cell and the heater mater. The results highlight a radial thermal expansion coefficient of the cell equal to 1.2×10^{-5} °C^{-1}, which was constant for all the performed heating-cooling cycles (Figure 4-3a). This unwanted radial expansion of the oedometric ring during heating needs to be carefully taken into account during the evaluation of the linear thermal expansion coefficient, as well as during the estimation of the volume changes of the tested material along non-isothermal paths. Indeed, vertical expansion is allowed on the specimen, while the radial expansion is controlled by the radial thermal deformation of the cell. Therefore, the volume change of the tested material is computed as the sum of the measured axial strain and twice

the radial strain, which are obtained by considering the radial thermal expansion of the cell. Assuming isotropic thermo-elastic behaviour, the relationship between the measured thermal expansion coefficient ($\alpha_{measured}$) and the linear thermal expansion coefficient (α_l) is derived as follows:

$$\alpha_{measured} = \alpha_l \frac{(1+\nu)}{(1-\nu)} - \alpha_c \frac{2\nu}{(1-\nu)} \tag{4.1}$$

where α_c is the radial thermal expansion coefficient of the cell and ν is the Poisson's ratio of the material. It has to be noted that the radial deformations of the tested material and of the oedometric ring will result in some radial stress change. In particular, the thermal expansion of the material produces radial stress increase, while radial stress decrease is rather caused by the expansion of the ring and by the thermal compaction behaviour of the material. These radial stress variations have been quantified in this work for all the performed non-isothermal paths, and they appear considerably lower with respect to the radial stress induced by the presence of the vertical load. Therefore, some radial stress is always present during non-isothermal paths and the contact between the specimen and the oedometric ring is never lost.

When high pressures are considered, device deformations resulting from the applied load must be taken into account. Mechanical deformations of the apparatus at different temperatures were assessed: the cell was subjected to mechanical loading - unloading cycles at ambient temperature, at 60 °C and at 80 °C. The loading phase was performed over incremental steps that correspond to loading steps applied during an oedometric test on shale specimens. A steel specimen was used during this calibration stage, and its deformation as a result of the mechanical load was taken into account. Apparatus deformations were slightly more pronounced under high temperature conditions relative to those found at room temperature, however, no significant difference was found between deformations generated under 60 °C and 80 °C conditions (Figure 4-3b).

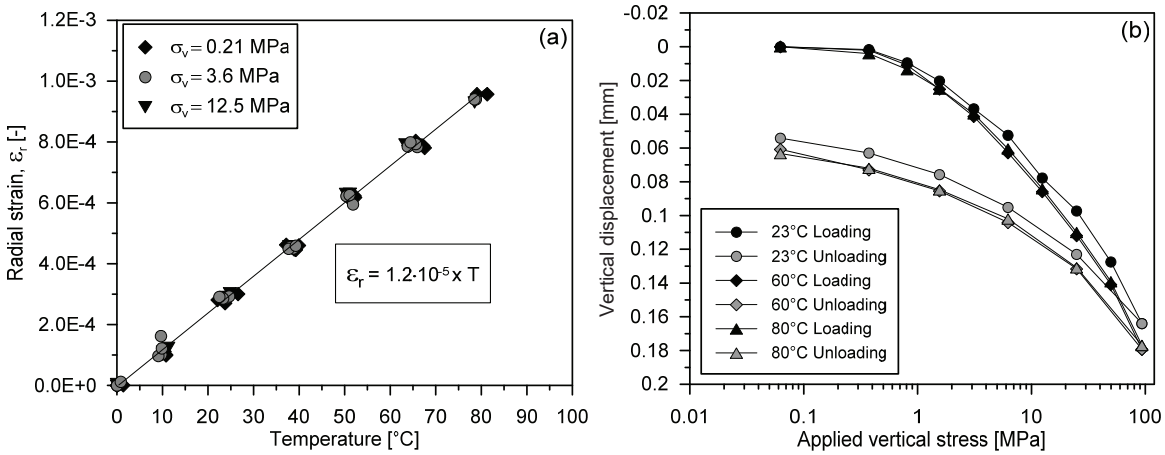

Figure 4-3: Thermo-mechanical calibration of the oedometric cell: radial strains versus applied temperature at different constant vertical stresses (a) and vertical displacement versus vertical stress at different constant temperatures (b).

4.3.2. Tested material

The Opalinus Clay core considered in this experimental campaign is named BHG-D1 and it was retrieved from the Mont Terri Underground Rock Laboratory (URL) in Northern Switzerland. The description and the geotechnical characterization of this core are presented in Chapter 1: the core belongs to the shaly facies, and it was cored perpendicular to the bedding planes. Synthetic water was used in the experiments in order to recreate the in-situ pore water composition of Mont Terri (Pearson, 1998). The Opalinus Clay specimens used were 35 mm in diameter and approximately 12.5 mm in height, and they were obtained following the ad hoc procedure that was described in detail in Section 3.2.2.2.

4.3.3. Experimental program

The experimental campaign aims at characterizing the thermo-mechanical volumetric response of Opalinus Clay; it consists of saturated high-pressure oedometric tests where elaborated thermo-mechanical stress paths are followed and where non-isothermal conditions are applied. The controlled variables are temperature and vertical effective stress defined, according to Terzaghi, as the vertical total stress minus the pore water pressure. Three tests are performed in total (test 1, test 2 and test 3) that involve heating-cooling cycles at different constant vertical effective stresses and at different OCR values, and mechanical loading-unloading cycles under different constant temperatures. The thermo-mechanical stress paths of the three tests are depicted in Figure 4-4. During all three tests, the initial saturation phase is carried out by limiting the vertical expansion in order to preserve the initial void ratio of the material and in order to measure the swelling pressure upon re-saturation. The saturation phase is carried out by initially flushing the specimen from the bottom base while applying zero pore water pressure at the upper base and by then subsequently applying the same pore water pressure on both the lower and upper bases of the specimen.

The importance of maintaining constant volume conditions when measuring swelling pressures is highlighted in Figure 4-4a (Test 1): when the shale specimen was left to partially swell (due to a lack of vertical displacement control at night), a vertical expansion equal to 1.4% was obtained, and a swelling pressure equal to approximately 0.6 MPa was found. The heating phase (up to 80 °C) was performed immediately after saturation, and it was followed by mechanical loading-unloading cycles up to 25 MPa. The specimen was subsequently cooled at laboratory temperature (23 °C), and a complete mechanical loading-unloading cycle up to 80 MPa was carried out. The stress-path of test 2 is presented in Figure 4-4b: greater control over swelling during saturation was achieved compared to that achieved in test 1, as a maximum vertical expansion of 0.12% and a swelling pressure of 3.7 MPa were registered. In this case, loading-unloading cycles up to 90 MPa were performed before temperature was increased; once the specimen was unloaded, it was heated to 80 °C at a constant stress equal to approximately 6.0 MPa and was then reloaded up to approximately 90 MPa. Figure 4-4c depicts the stress-path of test 3. In this last test, good control of the volume during saturation was also achieved: a maximum vertical expansion of 0.04% was measured together with a swelling pressure equal to approximately 3.0 MPa. The first heating-cooling cycle up to 80 °C was then

performed. Once the specimen was cooled to 23 °C, the vertical load was increased in phases up to 50 MPa. Once unloaded, two complete heating-cooling cycles up to 80 °C were carried out. Finally, heating up to 80 °C was followed by a final mechanical loading-unloading cycle up to approximately 90 MPa.

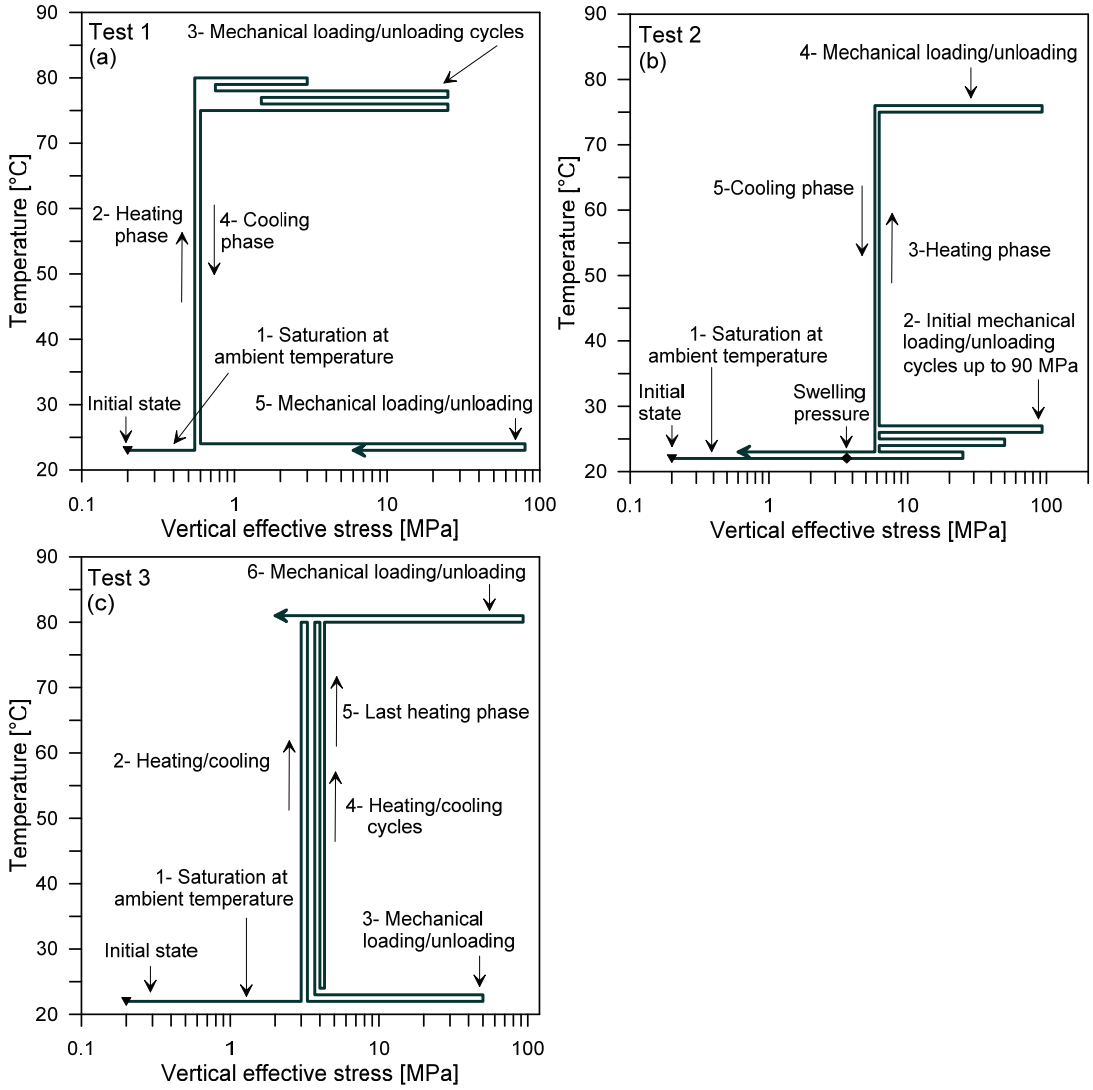

Figure 4-4: Thermo-mechanical stress paths.

As for the non-isothermal phases, due to low porosity and permeability typical of shales, particular attention was paid to heating and cooling rates to avoid the generation of excess pore water pressure. Xu et al. (2011) examined the influence of heating rates from 0.3 to 0.04°C/min on a shale sample from Canada. The slowest value (corresponding to 2.4°C/h) was found to induce uniform pore pressure distribution within shale samples of 15 cm in length and 7 cm in diameter. Monfared et al. (2011) conducted numerical investigations to evaluate the most suitable heating rate for Opalinus Clay and found that a rate of 1°C/h for a drainage path of 10 mm prevented significant pore pressure

build up. In the high-pressure oedometric tests conducted in the present study, the drainage path length was approximately 6 mm, and a heating rate of 2.0°C/h was considered suitable. To ensure the complete dissipation of possible excess pore water pressures, after five increments (i.e., for about every ten degrees of temperature increase), the complete dissipation of excess pore water pressure was permitted. The next heating step was applied when the excess pore water pressure had fully dissipated and when thermal expansion/contraction in the material had fully stabilized (less than two microns over 10 hours). Figure 4-5 presents a full heating phase (the first heating phase after mechanical loading-unloading during test 3) to illustrate the observed behaviour of the specimen under the imposed temperature variations: vertical displacements evolved as the temperature was increased by 2 °C each hour; once the target temperature was reached, displacement stabilization was fairly rapid, suggesting that the adopted heating rate is suitable for the tested material.

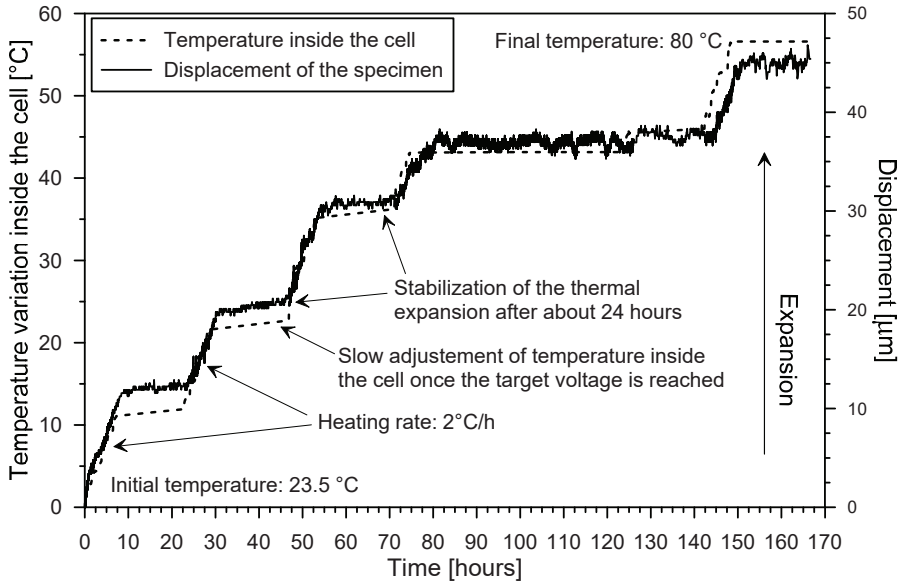

Figure 4-5: Vertical thermal expansion of the material versus time.

Regardless, roughly 24 hours were allowed to pass before the subsequent thermal step was initiated to ensure vertical displacement stabilization. Thermal expansion/contraction in the material was evaluated based on the 10-degree increments, i.e., when complete vertical expansion/contraction stabilization for a certain temperature increment was observed.

4.4. Experimental results

In the following sections the results obtained on the thermo-mechanical volume change behaviour of Opalinus Clay are reported and analysed in detail. Section 4.4.1 focuses on the impact of temperature on the hydro-mechanical properties of the shale and highlights how hydro-mechanical properties of the material are affected by temperature variations. Section 4.4.2 describes the volumetric behaviour of the shale when subjected to temperature changes, taking into account the role of the applied stress state and OCR.

4.4.1. Temperature effects on hydro-mechanical properties of Opalinus Clay

In this section, the hydro-mechanical behaviour of Opalinus Clay is analysed at ambient and high temperature with a particular focus on the effect of this variable on the response of the material.

The tests were performed by incremental loading and the results of each loading/unloading step in terms of settlement versus time curves were analysed using the analytical method presented in Chapter 3 (Section 3.2), which allows one to separate end-of-primary consolidation settlement from secondary consolidation settlement and from the settlement due to the mechanical deformation of the testing apparatus. The best fit between the experimental results and analytical model allows one to obtain information on the oedometric modulus E_{oed}, on the coefficient of consolidation c_v and on the secondary compression coefficient C_α, which are parameters of the model itself. The oedometric curves are presented in terms of void ratio versus vertical effective stress. Void ratio values were referred to the end-of-primary consolidation settlement, and particular attention was paid to the computation of the void ratio variations due to changes in temperature. In fact, the volume of the solid constituents (V_s) changes with temperature together with the overall specimen volume (V) (Campanella and Mitchell, 1968). Consequently, the thermal expansion/contraction of the solid constituents must be taken into account when computing the void ratio. When void ratio variations are simply derived from the measured volumetric strain and when variations in solid particles volume are not taken into account, overestimation during thermal expansion or underestimation during thermal compaction occur in terms of void ratio variation, producing misleading results (Mašín and Khalili, 2012). The void ratio variation due to temperature changes is given by equation (4.2) (after Romero (1999)):

$$\Delta e = \left(\frac{\Delta V}{V_i} - \alpha_s \Delta T \right) \frac{1 + e_i}{1 + \alpha_s \Delta T} \tag{4.2}$$

where V_i and e_i are the initial volume and initial void ratio of the specimen prior to heating (or cooling), respectively, and where α_s is the thermal expansion coefficient of the solid constituents equal to 2.4×10^{-5} °C^{-1}, which is estimated here as a weighted average based on the mineralogical composition of Opalinus Clay and based on the thermal expansion coefficient of each mineralogical component. The thermal expansion coefficient of each mineralogical constituent is reported in Table 4-1.

Table 4-1: Thermal expansion coefficients of each mineralogical constituent (*Fei, 1995; **Horseman and McEwen, 1996).

Mineralogical constituent	Quartz	Feldspar	Calcite	Dolomite	Siderite	Pyrite	Clay
Thermal expansion coefficient	(x10^{-5} °C^{-1})	(x10^{-5} °C^{-1})	(x10^{-5} °C^{-1})	(x10^{-5} °C^{-1})	(x10^{-5} °C^{-1})	(x10^{-5} °C^{-1})	(x10^{-5} °C^{-1})
	2.43*	0.97*	0.38*	0.23*	0.27*	0.26*	2.9**

Loading cycles up to 25 MPa at a constant temperature of 80 °C are presented in Figure 4-6, where the results of test 1 are depicted. The specimen was heated after the saturation phase, and an increase in the void ratio was obtained as a result of thermal expansion of the material. Mechanical loading up to 25 MPa was then carried out: a clear transition from a pre-yield domain to a post-yield domain can be observed as the vertical load increased. The value of the vertical effective yield stress obtained according to Casagrande (1936) method is about 6 MPa. The reversible unloading-reloading cycle at 3 MPa reveals that a certain degree of plasticity is found before the vertical effective yield stress is reached; this feature is often observed in natural geomaterials where small plastic strains can occur before the vertical effective yield stress is reached.

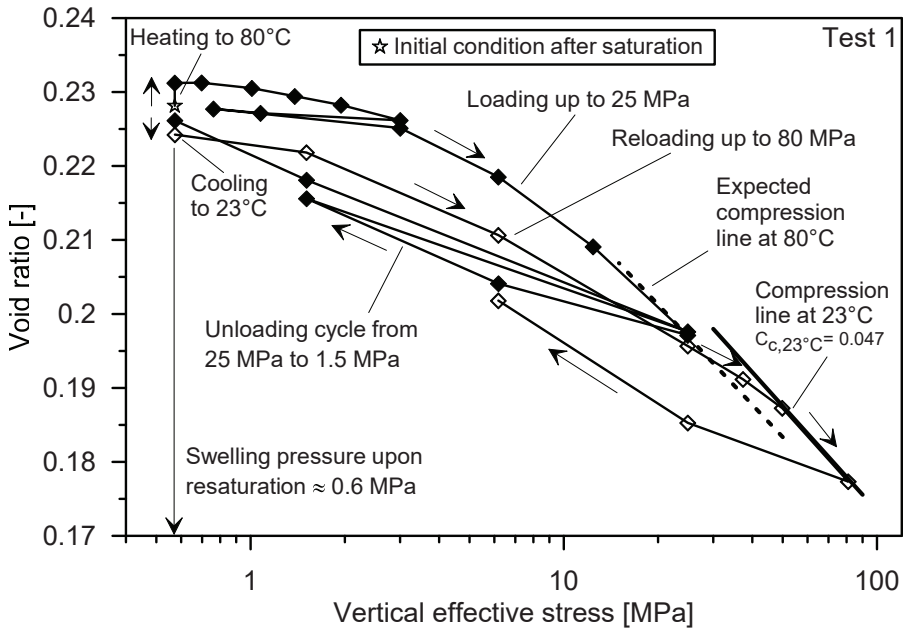

Figure 4-6: Test 1 – Void ratio versus vertical effective stress.

Once unloaded, an additional loading/unloading cycle was carried out at the same temperature to observe the behaviour of the material during isothermal mechanical loading cycles at high vertical stresses. The material did not present a significant axial strain accumulation after reloading to 25 MPa, and approximately the same void ratio was reached for the same vertical effective stress. Once unloaded to 0.6 MPa, the specimen was cooled to 23 °C, and a reduction in the void ratio was observed as a result of thermal contraction. To examine the effects of a lower temperature on the yield threshold, the specimen was subsequently reloaded to up to 80 MPa at a constant temperature of 23 °C as illustrated in Figure 4-4a. During reloading, the material reached the previous yield threshold of 25 MPa, however no shift from a lower (elastic) compressibility to a higher (elasto-plastic) compressibility was observed until a higher vertical effective stress (approximately 50 MPa) was applied (Figure 4-6). The yielding of the material seems to occur at a higher vertical effective stress than expected, therefore, the decrease in temperature appears to induce an increase in the vertical effective yield stress.

Loading cycles up to 90 MPa at constant ambient temperature that refer to test 2 are presented in Figure 4-7. Several unloading/reloading cycles were performed after the specimen was saturated under constant volume conditions in order to study the rebound upon mechanical unloading at different maximum vertical stresses: a steeper unloading branch slope with the increase in maximum stress level reached is observed.

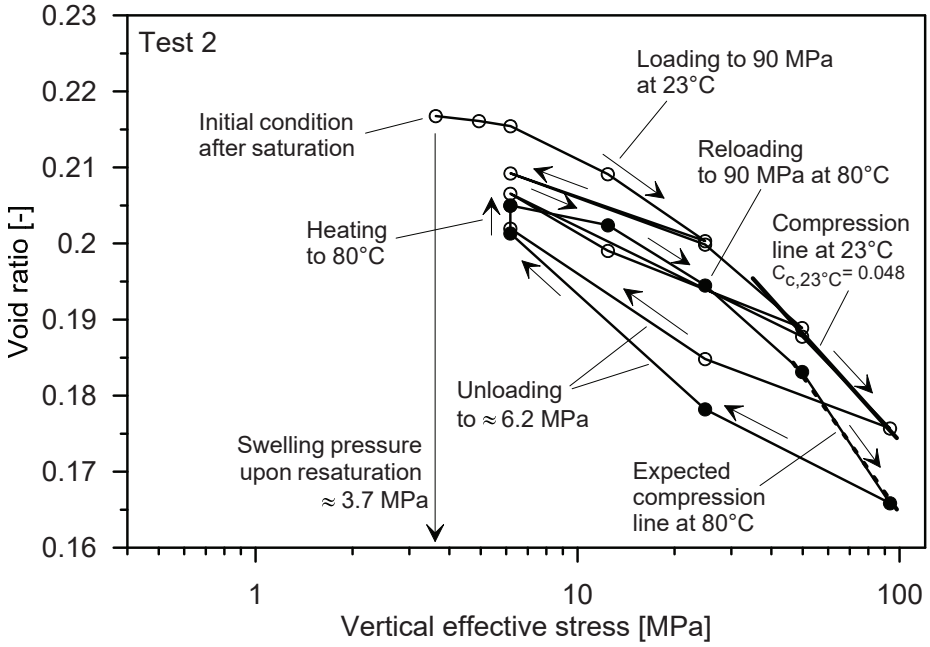

Figure 4-7: Test 2 – Void ratio versus vertical effective stress.

In this second stress path, the effect of a higher temperature (80 °C) on the yield stress was addressed; once unloaded, the specimen was heated to 80 °C under 6 MPa. Once again, an increase in the void ratio was found as a result of thermal expansion. The specimen was subsequently reloaded up to the previous maximum vertical effective stress: a significantly lower void ratio value was reached after reloading at high temperature with respect to the void ratio value found during compression at ambient temperature; in addition, a change in slope is found before the previous yield stress was encountered, in clear contrast with the behaviour observed in Figure 4-6. This last observation suggests that the yield threshold, which was previously brought to about 90 MPa, decreased with the increase in temperature.

To more thoroughly examine the post-yield behaviour of the material at high temperatures, the stress path of test 3 was applied, where the vertical effective stress during compression at 80 °C reached higher values relative to those reached at ambient temperature. The results are presented in Figure 4-8: the temperature was raised to about 80 °C after the saturation phase under 3 MPa, and a decrease in void ratio was obtained (this aspect is further discussed in Section 4.4.2). The specimen was then cooled to 23 °C, and mechanical loading was carried out at constant temperature up to 50 MPa. After unloading, the specimen was subjected to a series of heating-cooling cycles up to 80 °C and was subsequently reloaded to approximately 90 MPa at high temperature. The specimen reached a lower

void ratio value when compressed again at 50 MPa at high temperature relative to the void ratio value found during compression at ambient temperature; moreover a transition from a lower elastic compressibility to higher elasto-plastic compressibility seems to be observed before the previous ambient temperature yield threshold was reached.

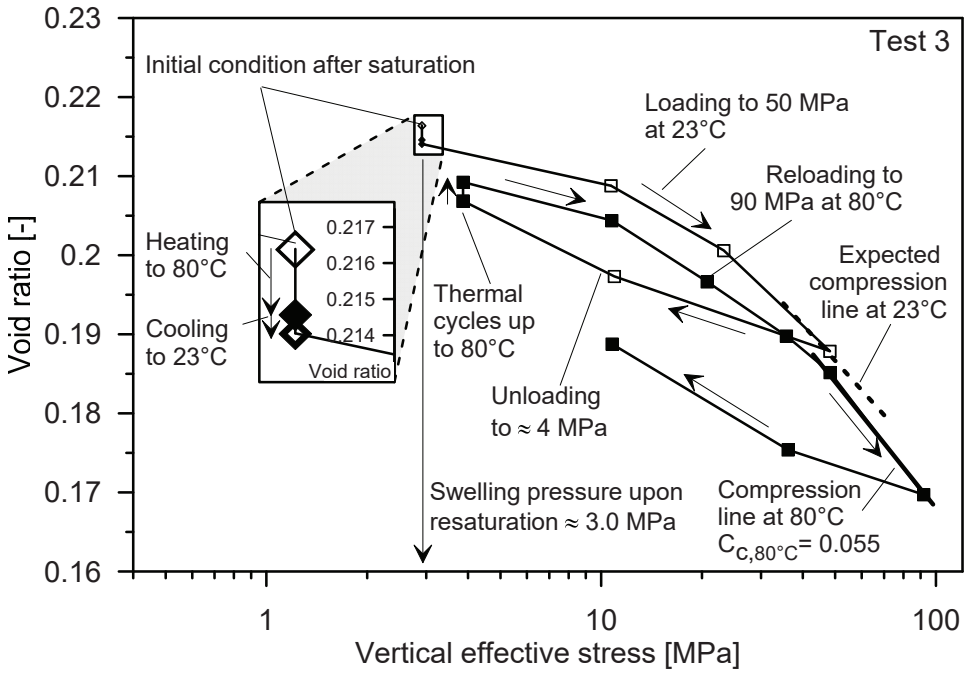

Figure 4-8: Test 3 – Void ratio versus vertical effective stress.

The compression behaviour of the material can be better described by computing the compression (C_c) and swelling (C_s) indexes. The former describes the compressibility of a material in the post-yield domain, while the latter describes the relationship between void ratio and vertical effective stress in the pre-yield domain. The compression index was computed based on a vertical effective stress range between 50 MPa and 100 MPa; the swelling index was computed for each entire unloading branch of the oedometric curves. The compression index at 23 °C is derived from test 1 and test 2, where values equal to 0.047 and 0.048 are computed respectively, while the C_c at 80 °C is derived from test 3 where a value equal to 0.055 is found. The results seem to highlight a slight increase in the elasto-plastic compressibility with temperature; the behaviour of the material during recompression at 80 °C in test 2 seems to confirm this observation. However the measured increase is quite low and can be considered negligible for Opalinus Clay in the studied temperature range in line with the behaviour typically observed for clays. The C_s computed for a stress level of about 25 MPa is equal to 0.015 regardless of temperature which is equal to 80 °C in test 1 and to 23 °C in test 2. The C_s computed at about 100 MPa are equal to 0.022 at 23 °C (tests 1 and 2), while it varies between 0.022 and 0.030 at 80 °C (test 3 and test 2 respectively). Temperature effects on the swelling index appear to be negligible, while an increase in C_s with the increase in maximum stress level reached is found under both ambient and high temperatures, likely due to damage effects and to the formation of micro cracks when high levels of vertical stress are applied (Mohajerani et al., 2011).

The oedometric modulus (E_{oed}) of Opalinus Clay is presented in Figure 4-9 as a function of the vertical effective stress at the beginning of each loading step (Figure 4-9a) and as a function of the void ratio value (derived from the end-of-primary consolidation settlement) at the end of each loading step (Figure 4-9b); only values related to the first loading branches are presented. High temperatures seems to induce a slight decrease in stiffness for the same vertical effective stress and void ratio value, however, given the variability of this material, the effect of temperature on the oedometric modulus appears to be quite negligible, in particular for vertical effective stresses greater than approximately 6.0 MPa. This observation is in good agreement with the negligible dependence of the compression index on temperature. The initially higher values of the oedometric modulus found at ambient temperature for vertical effective stresses less than 6.0 MPa can be related to non-perfect initial saturation in the specimens at low pressures together with the effect of the transition from the initial reloading branch to the virgin loading branch.

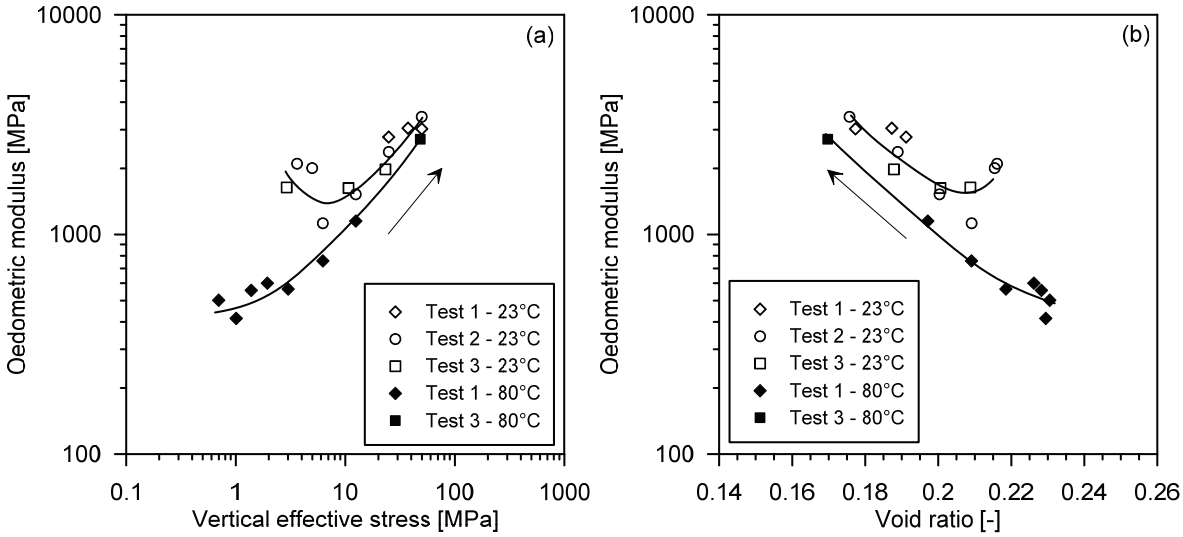

Figure 4-9: Oedometric modulus as a function of the vertical effective stress (a) and of the void ratio (b).

Values of the coefficient of consolidation (c_v) for the first loading branches are reported in Figure 4-10a as a function of vertical effective stress and in Figure 4-10b as a function of the void ratio computed from the end-of-primary consolidation settlement. The coefficient of consolidation is clearly higher when compression is applied at high temperature suggesting a faster dissipation of generated excess pore water pressure. This phenomenon occurs because as the temperature increases, the viscosity of pore water decreases, enhancing the dissipation of excess pore water pressure and thus the consolidation process (Towhata et al., 1995; Di Donna and Laloui, 2015). Figure 4-11 presents values of the secondary compression coefficient (C_α) found at ambient and high temperatures as a function of vertical effective stress at the beginning of each loading step. The dependence of C_α on temperature does not appear to be significant in agreement with the results presented in Di Donna and Laloui (2015) and in Laloui et al. (2008) on clays.

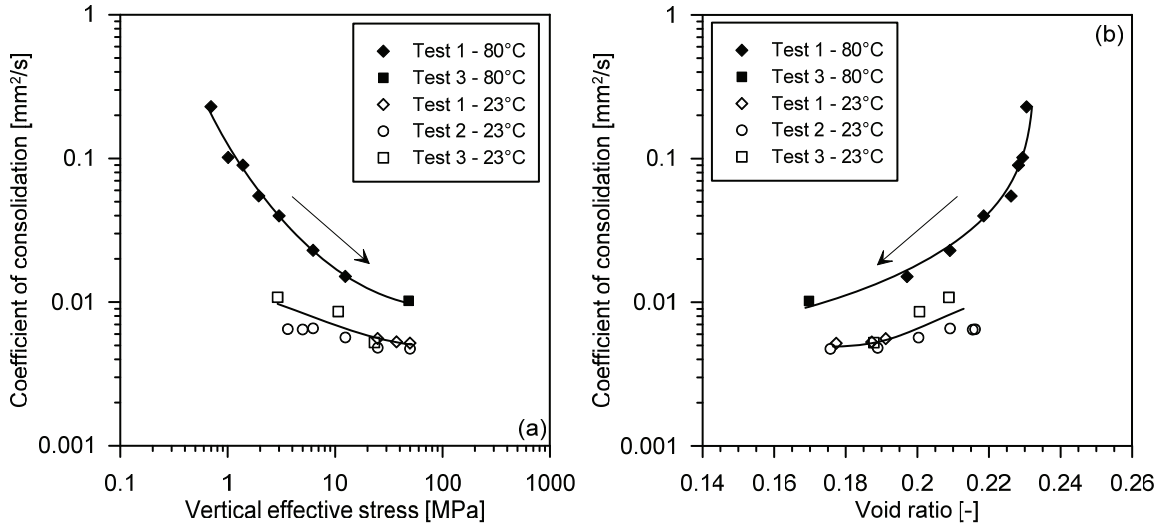

Figure 4-10: Coefficient of consolidation as a function of vertical effective stress (a) and of void ratio (b).

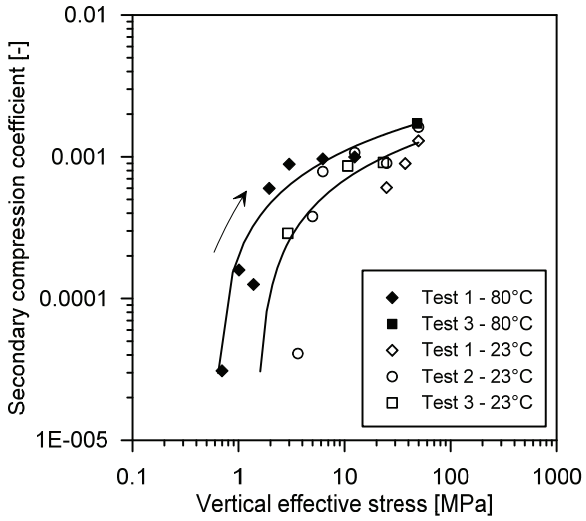

Figure 4-11: Secondary compression coefficient as a function of vertical effective stress.

4.4.2. Volumetric behaviour of Opalinus Clay under non-isothermal conditions

The volumetric response of Opalinus Clay upon heating and cooling is analysed in this section. Non-isothermal phases were carried out under different stress conditions; therefore, the effect of the vertical effective stress and of the different values of the OCR on the thermal behaviour of the material is investigated. Figure 4-12 depicts the measured axial strain behaviour and the computed volumetric strain behaviour of Opalinus Clay (taking into account the radial thermal deformation of the oedometric ring) during "first-heating" phases: the material undergoes thermal expansion at high OCR values, with an overall increase in volume, while no thermal expansion but rather thermal compaction is observed when the vertical effective stress at which heating is carried out approaches the vertical effective yield stress (low OCR).

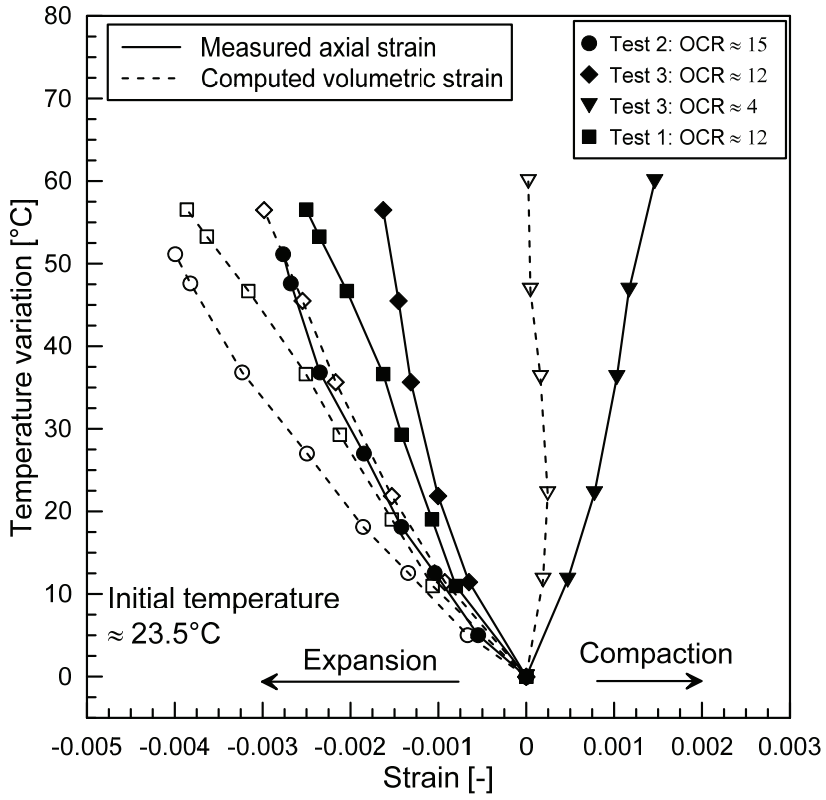

Figure 4-12: Strain behaviour of Opalinus Clay during heating as a function of the OCR: solid lines represent the measured axial strain behaviour while dashed lines represent the corrected volumetric behaviour during heating.

In particular, a more significant volume increase is observed in test 2, where a mechanical loading-unloading cycle up to 90 MPa was carried out before the specimen was heated at a constant vertical effective stress equal to 6.0 MPa: the loading induced an OCR equal to 15. A smaller volume increase was found for the specimens used in tests 1 and 3 once they were subjected to heating at a OCR between 11 and 12. In particular, during test 3, heating was carried out at a constant vertical effective stress equal to approximately 4.0 MPa after having experienced a mechanical loading cycle up to 48 MPa at ambient temperature; by contrast, the specimen used in test 1 was heated after initial saturation at a constant vertical effective stress equal to 0.6 MPa, and the vertical effective yield stress was estimated according to Casagrande (1936) method. The results reveal a decrease in thermal expansion of the material with the decrease in OCR. However, some differences in the degree of thermal volume change are observed even when about the same OCR is considered: the shale specimen used in test 1 exhibits a larger volume increase compared to the shale specimen used in test 3 at a similar OCR value. This behaviour may be justified by two observations: the shale specimen used in test 1 was allowed to swell partially during the initial saturation phase, and this condition may have induced some disturbance to the shale specimen, resulting in bond breakage and in the generation of micro-fissures; as a consequence this specimen would be more prone to expansion relative to a specimen that has not experienced structural disturbance due to swelling (like the specimen used in test 3). In addition, the examined heating phases were carried out at different

constant vertical effective stresses (0.6 MPa and 4.0 MPa for tests 1 and 3, respectively), and thus the effective stress conditions under which heating was carried out may have also affected the volumetric behaviour observed. However, such discrepancy is mainly observed in higher ranges of temperature variation (from approximately 45 °C to 80 °C), while the response of the two specimens remained in relative agreement up to 45 °C. Consequently, additional insights are needed to support this observation.

The linear thermal expansion coefficients computed between 23 °C and 40 °C by taking into account the radial deformation of the cell (Equation (4.1), assuming a Poisson's ratio equal to 0.33 (Bossart, 2012)) are equal to 3.6 x 10^{-5} °C^{-1} for the heating phase in test 1, 4.4 x 10^{-5} °C^{-1} for the heating phase in test 2, and 3.0 x 10^{-5} °C^{-1} for the first heating after mechanical loading-unloading in test 3. The decrease in thermal expansion with decreasing OCR values is further confirmed in test 3, where the heating phase was carried out at a OCR equal to 4 (the yield stress in this case was estimated from the oedometric curve of test 2): the shale specimen did not experience any increase in volume upon heating, but rather manifested thermal compaction, exhibiting behavioural features similar to those observed in clayey materials. It is interesting to notice that, even though very little volumetric thermal compaction strain is observed during heating (Figure 4-12), the void ratio decrease experienced by the material is relevant (Figure 4-8). This is due to the thermal expansion of the solid particles, which, together with the plastic structural rearrangement, contribute to the material porosity reduction.

The thermal cyclic behaviour of Opalinus Clay is presented in Figure 4-13: heating-cooling cycles were carried out at OCR values equal to 4 and 12 for constant values of vertical effective stress equal to 3.0 MPa and 4.0 MPa, respectively (Figure 4-4c, Test 3). Heating and cooling the shale specimen at an OCR equal to 4 induced an irreversible reduction in volume. The linear thermal expansion coefficient obtained upon cooling in the lower temperature range, is equal to 1.23 x 10^{-5} °C^{-1}. Heating-cooling cycles at an OCR equal to 12, show that the shale specimen initially expanded as shown in Figure 4-12; however, the increase in volume caused by the temperature increase was not recovered upon subsequent cooling: the material showed irreversible expansive strain. On the other hand, during the subsequent heating-cooling-heating cycle, a fairly reversible behaviour was observed together with a minor degree of hysteresis: a linear trend was identified for the entire temperature range examined, suggesting a lower linear thermal expansion coefficient with respect to the one observed upon first heating and equal to 1.21 x 10^{-5} °C^{-1} according to equation (4.1). Irreversible features of the thermal volumetric behaviour were mainly observed during the first-heating phases, when a certain degree of structural accommodation (Di Donna and Laloui, 2015) took place until a more stable configuration was achieved.

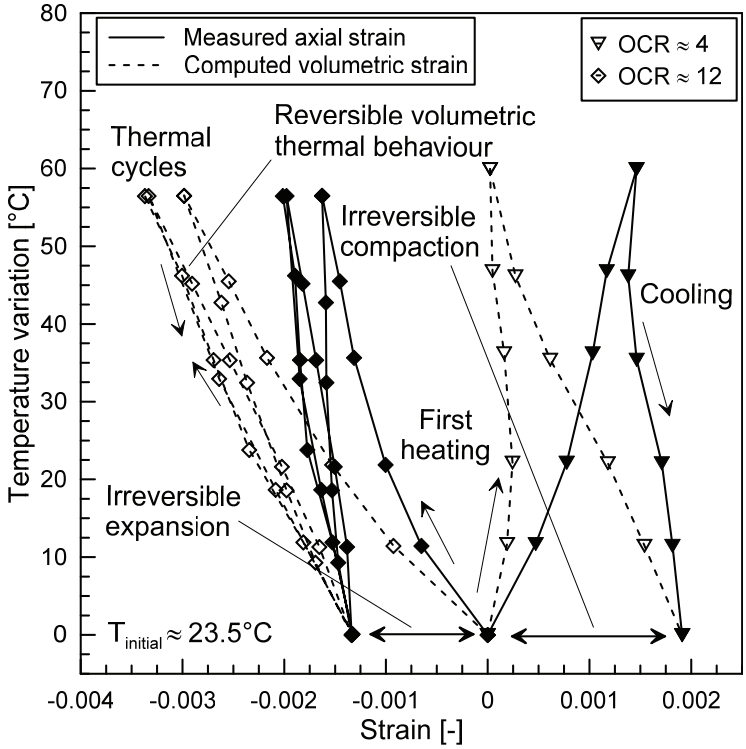

Figure 4-13: Cyclic thermal behaviour of Opalinus Clay under different values of OCR: solid lines represent the measured axial strain behaviour while dashed lines represent the volumetric behaviour.

4.5. Discussion

In the following section the obtained results are further discussed: the thermal volume change behaviour of Opalinus Clay is addressed first, while further discussion on the impact of temperature on the mechanical behaviour of the shale is subsequently carried out. The results on the thermal expansive behaviour of shales upon first-heating at high OCR values (Figure 4-12) show that the expected linear trend of thermal expansion is not clearly detectable: the initial tendency toward expansion seems to progressively decline as temperature increases, highlighting the fact that the obtained thermal expansion coefficient is dependent on the range of temperature variation considered. Figure 4-12 shows that the thermal response of Opalinus Clay shale to temperature variation is rather complex, as it is related to the temperature range involved and to the stress conditions in which the material is found. Jobmann and Polster (2007) presented experimental results on Opalinus Clay specimens cored at 45° with respect to the bedding orientation: a certain linear expansive behaviour was observed by these authors at temperatures below 40 °C, while no further significant increase in length was measured under higher temperatures; the volumetric behaviour upon heating was not found to be linear for the entire temperature range considered, in good agreement with the findings obtained in this study. The authors reported a linear thermal expansion coefficient value equal to 1.5 x 10^{-5} $°C^{-1}$ for temperatures lower than 40 °C. The thermal expansion coefficient values obtained in this paper upon first heating are higher than those obtained in Jobmann and Polster (2007). Such

differences are justified by two factors: the linear thermal expansion coefficient presents anisotropic features and is thus related to the bedding orientation, exhibiting higher levels of sensitivity when measured perpendicular to the bedding (Bock, 2009; Mohajerani et al., 2014). Furthermore, the stress history experienced by the material and the testing conditions of the specimens are also fundamental in determining the degree of volume increase (or decrease) during heating.

The macroscopic thermoplastic response observed for the Opalinus Clay shale is in agreement with the thermal behavioural features of clays, showing that the clayey component of the shale plays a fundamental role in the thermo-mechanical response of Opalinus Clay. Previous studies on clays have reported that high temperatures affect some clay properties (e.g., particle size, water content, specific gravity, activity index, swelling behaviour, compressibility and strength) (Yilmaz, 2011; Bai et al., 2014) and that this is associated with the effects of temperature on free and adsorbed water (Bai et al., 2014). Irreversible features observed in clays and shales are also associated with microscopic phenomena that are related to an interaction between the structural components of these materials. These microscopic phenomena consist in different processes (Di Donna and Laloui, 2015) among which a decrease in the thickness of the adsorbed water layer (Pusch, 1986), the different thermal responses of the microstructural components (Kingery and Bowen, 1976) that may induce a change in the contact forces among them, and the variation in Van der Waals attractive forces due to the thermal expansion of water and grains (Laloui, 2001). The overall combination of these factors may induce irreversible deformations resulting from particles rearrangement (Campanella and Mitchell, 1968) and accommodation, which can correspond to either an increase or a decrease in volume depending on the OCR of the material.

The results of the oedometric compression tests highlight the elasto-plastic features of Opalinus Clay, where irrecoverable changes in the void ratio are observed upon oedometric compression together with a transition from a pre-yield elastic compressibility during unloading-reloading branches to a post-yield elasto-plastic compressibility. A yield threshold can be identified where the material is found in normally consolidated conditions, and where the vertical effective stress corresponds to the vertical effective yield stress. The analysis of the compression behaviour at different temperatures has highlighted an effect of temperature on the yield threshold of the material: Figure 4-6 suggests that the yield threshold at 23 °C has been moved to greater stress values with respect to the yield stress imposed at 80 °C. This phenomenon is better highlighted if the compression lines are drawn (see Figure 4-6): the compression line at 23 °C is clearly located at the right side of the expected compression line at 80 °C, thus highlighting an increase of the elastic domain at low temperature. On the other hand, when the results of test 2 and of test 3 are considered (Figure 4-7 and Figure 4-8), a decrease of the yield threshold can be noticed when the material is compressed at 80 °C since the transition from a pre-yield compressibility to a post-yield compressibility seems to occur at lower vertical effective stress values with respect to the ones previously induced at 23 °C. The compression lines for test 2 are represented in Figure 4-7: the early change in compressibility seems to highlight a decrease of the elastic domain at high temperature, in such a way that the expected compression line at 80 °C is moved to the left side of the compression line at 23 °C. The compression lines for test 3 are represented in Figure 4-8 and they appear to be in line with the previous considerations since the

compression line at 80 °C is located at the left side of the expected compression line at 23 °C. In order to examine more closely the decrease in vertical effective yield stress with temperature, the effect of the void ratio on vertical effective yield stress must also be taken into account, as the former also affects the latter. For this reason, the minimum void ratio achieved during compression at ambient temperature in tests 2 and 3 are used as reference values, while the corresponding vertical effective stress values found on the expected compression lines at 80 °C and at 23 °C are derived from Figure 4-7 and Figure 4-8, respectively. This procedure is based on the theoretical concept that all the points located on the compression line belong to the yield surface; therefore the selected points on the compression lines can be considered as the vertical effective yield stress values corresponding to the reference void ratio values for the two selected temperatures. The data points obtained following the procedure described above are plotted in Figure 4-14 as a function of the temperature and of the reference void ratio.

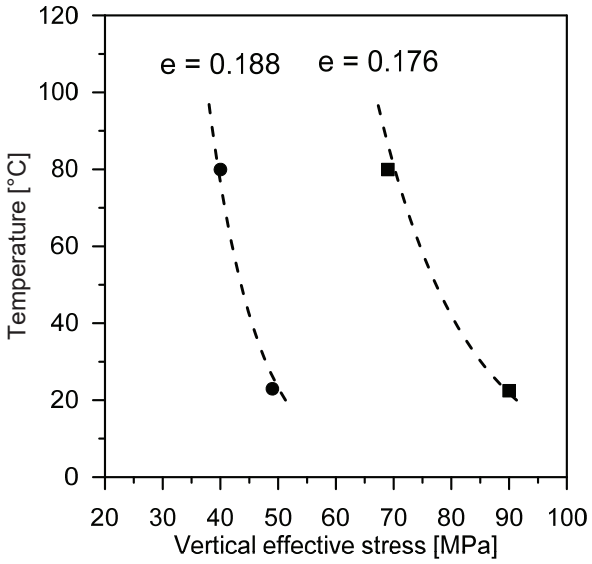

Figure 4-14: Position of the theoretical yield surface as a function of temperature.

The data are fitted with the following expression (Laloui and François, 2009):

$$\frac{\sigma'_c}{\sigma'_{c0}} = 1 - \gamma_T \ln\left(\frac{T}{T_0}\right) \tag{4.3}$$

where σ'_{c0} is the reference vertical effective yield stress at a reference temperature T_0 and where γ_T is a parameter. In Figure 4-14, the reference temperature T_0 is taken equal to 23 °C, while the reference vertical effective yield stress σ'_{c0} must be adjusted as a function of the void ratio: values equal to 90 MPa and 50 MPa are assumed for tests 2 and 3, respectively, which correspond to the maximum vertical effective stress reached (vertical effective yield stress) at a temperature of 23 °C. A good fitting of the data is found when the γ_T parameter is taken equal to 0.17. Equation (4.3) describes the evolution of the vertical effective yield stress with temperature for Opalinus Clay when the γ_T parameter is taken equal to 0.17.

4.6. Conclusions

The continuous development of energy-related engineering applications involving shale formations requires taking into account the impact of high temperatures and high mechanical loads on the response of this material. The results presented in this chapter on the Opalinus Clay shale highlight the fact that the hydro-mechanical behaviour of shales is affected by thermal variations. The results of the experimental campaign show that the volumetric behaviour of the material during heating is heavily dependent on the OCR: thermal expansion is observed when the material is heated at high OCR values, whereas thermal compaction and porosity reduction are observed when the material is subjected to heating at a vertical effective stress that is close to the vertical effective yield stress (low OCR). The volumetric behaviour of Opalinus Clay when subjected to heating/cooling cycles was analysed: the first heating cycle caused irreversible compaction or irreversible expansion depending on the value of the OCR. Additional heating/cooling cycles revealed a reversible behaviour.

Effects of thermal variations on the hydro-mechanical behaviour of Opalinus Clay were examined via oedometric compression tests conducted at different temperatures. An increase in the yield threshold is observed upon compression at 23 °C relative to the vertical effective yield stress value previously induced at 80 °C. In addition, the yield threshold appears to decrease upon compression at high temperatures relative to the vertical effective yield stress value previously induced at 23 °C. The dependence of vertical effective yield stress on temperature may be better described through the introduction of an analytical expression and of a thermal parameter γ_T. Such dependence should be carefully taken into account, as an increase in temperature induced by the emplacement of a heat source and thus the decrease in the yield stress in the considered shale formation may result in the development of plastic settlements when the in-situ stress is sufficiently close to the yield stress. On the other hand, when heating is conducted at an in-situ stress that is sufficiently low relative to the yield stress, thermal expansion is expected together with an increase in the material void ratio under constant effective stress conditions. In general, hydro-mechanical properties of Opalinus Clay vary as a function of void ratio values; however, as the changes in void ratio induced by thermal variations within the examined temperature range were found to be quite low, hydro-mechanical properties would not be affected considerably due to this change in volume.

The negligible effects of temperature on the oedometric modulus, on compressibility and on the secondary compression coefficient suggest that the overall mechanical performance of the shale formation would not be altered considerably when heated within the specified temperature range. On the other hand, consolidation processes would be improved upon heating, with a faster dissipation of induced excess pore water pressures thanks to an increase in the coefficient of consolidation with an increase in temperature.

The obtained results serve as a comprehensive description of the thermo-mechanical behaviour of Opalinus Clay, broadening scientific knowledge on the thermal behaviour of shales under different stress conditions and on the effects of temperature on their hydro-mechanical properties. The results obtained are especially relevant, as Opalinus Clay shale has been selected as the host formation for high-level nuclear waste disposal in Switzerland.

4.7. References

Bai, B., Guo, L. and Han, S. Pore pressure and consolidation of saturated silty clay induced by progressively heating/cooling. Mechanics of Materials (2014) 75: 84-94.

Baldi, G., Hueckel, T. and Pellegrini, R. Thermal volume changes of the mineral-water system in low-porosity clay soils. Canadian geotechnical journal (1988) 25(4): 807-825.

Bauer, A., Stenebråten, J., Nes, O.-M., Sønstebø, E., Holt, R. and Marøen, L. Thermally Induced compaction of shales. 48th US Rock Mechanics/Geomechanics Symposium, American Rock Mechanics Association, (2014).

Bock, H. RA Experiment: Updated Review of the Rock Mechanics Properties of the Opalinus Clay of the Mont Terri URL based on Laboratory and Field Testing. TECHNICAL REPORT 2008-04 (2009).

Bossart, P. (2012). Characteristics of the Opalinus Clay at Mont Terri. http://www.mont-terri.ch/internet/mont-terri/de/home/geology/key_characteristics.html.

Boudali, M., Leroueil, S. and Murthy, B.S. Viscous behaviour of natural clays. Proceedings of the International Conference on Soil Mechanics and Foundation Engineering - International Society for Soil Mechanics and Foundation Engineering, AA BALKEMA, (1994). 411-411.

Burghignoli, A., Desideri, A. and Miliziano, S. A laboratory study on the thermomechanical behaviour of clayey soils. Canadian geotechnical journal (2000) 37(4): 764-780.

Campanella, R.G. and Mitchell, J.K. Influence of temperature variations on soil behavior. Journal of Soil Mechanics & Foundations Div (1968).

Casagrande, A. The determination of the pre-consolidation load and its practical significance. Proceedings of the international conference on soil mechanics and foundation engineering, Harvard University Cambridge, (1936). 60-64.

Cekerevac, C. and Laloui, L. Experimental study of thermal effects on the mechanical behaviour of a clay. International Journal for Numerical and Analytical Methods in Geomechanics (2004) 28(3): 209-228.

Chen, L., Shao, J.-F. and Huang, H. Coupled elastoplastic damage modeling of anisotropic rocks. Computers and Geotechnics (2010) 37(1): 187-194.

Cotecchia, F. and Chandler, R.J. The influence of structure on the pre-failure behaviour of a natural clay. Geotechnique (1997) 47(3): 523-544.

Di Donna, A., Ferrari, A. and Laloui, L. Experimental investigations of the soil-concrete interface: physical mechanisms, cyclic mobilisation and behaviour at different temperatures. Canadian geotechnical journal, 10.1139/cgj-2015-0294. (2015).

Di Donna, A. and Laloui, L. Response of soil subjected to thermal cyclic loading: experimental and constitutive study. Engineering Geology (2015) 190: 65-76.

Dupray, F. and Laloui, L. Numerical analysis of canister movements in an engineered barrier system. Acta Geotechnica (2016) (11): 145–159.

Favero, V., Ferrari, A. and Laloui, L. Thermo-mechanical volume change behaviour of Opalinus Clay. International Journal of Rock Mechanics and Mining Sciences (2016) 90: 15-25.

Fei, Y. Thermal expansion. Mineral physics and crystallography: a handbook of physical constants (1995) 2: 29-44.

Gaus, I., Garitte, B., Senger, R., Gens, A., Vasconcelos, R., Garcia-Sineriz, J., Trick, T., Wiecozorek, K., Czaikowski, O. and Schuster, K. The HE-E Experiment: Lay-out, Interpretation and THM Modelling. NAGRA Arbeitsbericht NAB (2014): 14-53.

Gens, A., Vaunat, J. and Garitte, B. Elastoplastic modelling of hard soils and soft rocks: formulation and application. Proceedings of the VIII International Conference on Computational Plasticity, COMPLAS VIII, Barcelona, (2005).

Gutierrez, M., Katsuki, D. and Tutuncu, A. Determination of the continuous stress-dependent permeability, compressibility and poroelasticity of shale. Marine and Petroleum Geology (2014) In press.

Horseman, S., Harrington, J. and Noy, D. Swelling and osmotic flow in a potential host rock. Physics and Chemistry of the Earth, Parts A/B/C (2007) 32(1): 408-420.

Hujeux, J.-C. (1979). Calcul numérique de problèmes de consolidation élastoplastique.

Hunsche, U., Walter, F. and Schnier, H. Evolution and failure of the Opalinus clay: relationship between deformation and damage, experimental results and constitutive equation. Applied Clay Science (2004) 26(1): 403-411.

Jobmann, M. and Polster, M. The response of Opalinus clay due to heating: A combined analysis of in situ measurements, laboratory investigations and numerical calculations. Physics and Chemistry of the Earth, Parts A/B/C (2007) 32(8): 929-936.

Kingery, B. and Bowen, H. Uhlmann, introduction to Ceramics. John Wiley&Sons, New York (1976).

Laloui, L. (2001). Thermo-mechanical behaviour of soils. Environmental geomechanics. E. Press. Lausanne**:** 809-843.

Laloui, L. and François, B. ACMEG-T: soil thermoplasticity model. Journal of Engineering Mechanics (2009) 135(9): 932-944.

Laloui, L., Leroueil, S. and Chalindar, S. Modelling the combined effect of strain rate and temperature on one-dimensional compression of soils. Canadian geotechnical journal (2008) 45(12): 1765-1777.

Lambe, T.W. and Whitman, R.V. Soil Mechanics, Wiley and Sons, (1979).

Leroueil, S. and Vaughan, P. The general and congruent effects of structure in natural soils and weak rocks. Geotechnique (1990) 40(3): 467-488.

Mašín, D. and Khalili, N. A thermo-mechanical model for variably saturated soils based on hypoplasticity. International Journal for Numerical and Analytical Methods in Geomechanics (2012) 36(12): 1461-1485.

Masri, M., Sibai, M., Shao, J.-F. and Mainguy, M. Experimental investigation of the effect of temperature on the mechanical behavior of Tournemire shale. International Journal of Rock Mechanics and Mining Sciences (2014) 70: 185-191.

Mitchell, J.K. and Soga, K. Fundamentals of soil behavior, Wiley New York, (1976).

Mohajerani, M., Delage, P., Monfared, M., Tang, A.M., Sulem, J. and Gatmiri, B. Oedometric compression and swelling behaviour of the Callovo-Oxfordian argillite. International Journal of Rock Mechanics and Mining Sciences (2011) 48(4): 606-615.

Mohajerani, M., Delage, P., Sulem, J., Monfared, M., Tang, A.M. and Gatmiri, B. The Thermal Volume Changes of the Callovo–Oxfordian Claystone. Rock mechanics and rock engineering (2014) 47(1): 131-142.

Monfared, M., Sulem, J., Delage, P. and Mohajerani, M. A laboratory investigation on thermal properties of the Opalinus claystone. Rock mechanics and rock engineering (2011) 44(6): 735-747.

Morin, R. and Silva, A.J. The effects of high pressure and high temperature on some physical properties of ocean sediments. Journal of Geophysical Research: Solid Earth (1984) 89(B1): 511-526.

Mroz, Z., Norris, V. and Zienkiewicz, O. Application of an anisotropic hardening model in the analysis of elasto–plastic deformation of soils. Geotechnique (1979) 29(1): 1-34.

Mroz, Z., Norris, V. and Zienkiewicz, O.C. An anisotropic, critical state model for soils subject to cyclic loading. Geotechnique (1981) 31(4): 451-469.

Nygård, R., Gutierrez, M., Gautam, R. and Høeg, K. Compaction behavior of argillaceous sediments as function of diagenesis. Marine and Petroleum Geology (2004) 21(3): 349-362.

Olson, R.E. and Mesri, G. Mechanisms controlling compressibility of clays. Journal of Soil Mechanics & Foundations Div (1970) 96(SM6).

Pearson, F. (1998). Opalinus clay experimental water: A1 Type, Version 980318. PSI Internal report TM-44-98-07. V. P. Paul Scherrer Institut, Switzerland.

Pusch, R. Permanent crystal lattice contraction, a primary mechanism in thermally induced alteration of Na bentonite. MRS Proceedings, Cambridge Univ Press, (1986). 791.

Romero, E. (1999). Characterisation and thermo-hydro-mechanical behaviour of unsaturated Boom clay: an experimental study.

Romero, E., Villar, M. and Lloret, A. Thermo-hydro-mechanical behaviour of two heavily overconsolidated clays. Engineering Geology (2005) 81(3): 255-268.

Sultan, N., Delage, P. and Cui, Y. Temperature effects on the volume change behaviour of Boom clay. Engineering Geology (2002) 64(2): 135-145.

Tidfors, M. and Sällfors, G. Temperature effect on preconsolidation pressure. (1989).

Towhata, I., Kuntiwattanakul, P., Seko, I. and Ohishi, K. Volume change of clays induced by heating as observed in consolidation tests (closure). Soils and Foundations (1995) 35(3): 124-127.

Wang, W., Xie, S. and Xu, W. Experimental study and numerical modelling of thermo-mechanical behaviour of Tournemire argillite. European Journal of Environmental and Civil Engineering (2013) 17(sup1): s174-s186.

Xu, B., Yuan, Y. and Wang, Z. Thermal impact on shale deformation/failure behaviors---laboratory studies. 45th US Rock Mechanics/Geomechanics Symposium, American Rock Mechanics Association, (2011).

Yilmaz, G. The effects of temperature on the characteristics of kaolinite and bentonite. Scientific Research and Essays (2011) 6(9): 1928-1939.

Zhang, F., Hu, D., Xie, S. and Shao, J.-F. Influences of temperature and water content on mechanical property of argillite. European Journal of Environmental and Civil Engineering (2014) 18(2): 173-189.

Chapter 5
Coupled Chemo-Mechanical Processes in Opalinus Clay

5.1. Foreword

In the geo-energy fields involving the exploitation of shale formations, the chemical interactions between shales and pore fluid may play a relevant role in determining the performance of the material. Opalinus Clay is the shale formation considered for the construction of a nuclear waste repository in Switzerland, therefore great interest is addressed on the impact of variations in pore fluid chemical concentration on its hydro-mechanical performance. In fact, variations in the chemical concentration of the pore fluid lead to changes in the osmotic suction of the shale, which are likely to trigger volumetric deformation. The following chapter is dedicated to the investigation and analysis of coupled chemo-mechanical processes in Opalinus Clay shale.

5.2. Introduction

Chemo-osmotic effects in shales have been addressed in the past mainly in relations to issues concerning wellbore stability and drilling activities (Bunger et al. 2014). The impact of water based fluids on shale formations is a major issue for wellbore stability and for the transport properties of the material during drilling or hydraulic fracturing operations. The involvement of shale formations in the construction of nuclear waste repositories brings ahead concerns about the impact of variations in chemical concentration of the pore fluid on the mechanical and hydraulic performance of the candidate host material. In fact the change in salinity and therefore in osmotic suction may impact the swelling and self-sealing properties as well as the hydro-mechanical behaviour of the shale. The salinity of the ground water is commonly found to increase with depth (Siddiqua et al., 2011) partially due to the reduction in the diluting effect of the surface water (Gascoyne et al., 1987). Gascoyne et al. (1987) reports data on the Canadian Shield area, which show that salinity of the groundwater, in terms of total dissolved solids (TDS), may reach values between 100-500 g/l at depths between 1500-2000 m. This is related mainly to the consistent increase in the concentration of chloride. In a long-term prospective it is important to take this aspect into account to correctly assess the performance of the repository at different possible depths. The knowledge on the impact of testing shales with a pore fluid having a different osmotic suction value than the one of the in-situ pore fluid is also of relevance.

With the goal of addressing the concerns related to wellbore stability and to shale-fluid interaction during drilling and hydraulic fracturing operations, the majority of the studies carried out in the past have focused on the impact of the pore fluid composition on strength (Al-Bazali et al., 2008; AL-Bazali, 2011) and on swelling behaviour of shales (Kwon et al., 2001; Van Oort, 2003; Wakim et al., 2009; Ewy, 2014). In particular, the available experimental evidences reveal that an increase in pore fluid osmotic suction generally leads to an increase in strength and reduces the amount of swelling upon exposure to the pore fluid. On the other hand, a deeper investigation of the coupled chemo-mechanical interactions is strongly needed in order to develop a better understanding of the chemo-osmotic phenomena and to formulate suitable analytical and numerical tools capable of predicting the chemo-mechanical behaviour of shales.

Broad information is available concerning the chemo-mechanical behaviour of reconstituted and natural clays (Barbour and Fredlund, 1989; Di Maio and Fenelli, 1994; Di Maio, 1996; Di Maio and Fenelli, 1997; Di Maio, 1998; Di Maio et al., 2004; Siddiqua et al., 2011; Witteveen et al., 2013; Mokni et al., 2014; Manca et al., 2015). The major outcomes of these studies provide a wide picture on the chemo-mechanical behaviour of active clays (Di Maio, 1996; Musso et al., 2003; Di Maio et al., 2004; Castellanos et al., 2008; Manca et al., 2015) and non-active clays (Sridharan and Rao, 1973; Sridharan and Rao, 1979; Di Maio and Fenelli, 1994; Chen et al., 2000; Wahid et al., 2010; Witteveen et al., 2013). In general, the increase in osmotic suction of the pore fluid causes a decrease in the volume of clays; this chemically induced volume change is caused by two principle mechanisms that operate simultaneously (Laird, 2006; Yukselen-Aksoy et al., 2008; Wahid et al., 2010): (i) a decrease of the diffuse double layer (DDL) repulsive forces and (ii) a variation in the inter-particle forces, which leads to the sliding between particles at their contact points and thus to a structural rearrangement. Sridharan and Rao (1973) showed that the first mechanism is predominant in active clays like montmorillonite, while the second mechanism is dominant in non-active clays such as kaolinite and illite. The two mechanisms dictate also the reversible or irreversible nature of the chemical settlements (Quirk et al., 1986): active clays are observed to experience recoverable chemically induced variations in volume (Di Maio, 1996; Wahid et al., 2010) while non-active clays present irrecoverable chemical settlements (Di Maio, 1996; Wahid et al., 2010; Mokni et al., 2014). Previous investigations on clays have also highlighted the impact of stress level and void ratio on the amount of volume change (Di Maio, 1996; Di Maio, 1998; Chen et al., 2000; Di Maio et al., 2004; Wahid et al., 2010; Mokni et al., 2014), while the stress history does not appear to have a significant impact (Mokni et al., 2014). In particular Di Maio (1998) explains the dependency of the chemical settlement on the stress level with two main factors: i) changes in thermodynamic conditions of the double layer which cause a different interaction with the diffusing ions and ii) the formation of regions where it would be more or less difficult for the ions to diffuse. No evidences concerning the impact of stress level, void ratio and stress history on the chemically induced settlements in shales have been reported so far (Bunger et al., 2014). Chemical loads appear to affect the compressibility of active clays only (Di Maio et al., 2004; Yukselen-Aksoy et al., 2008), while the compression and swelling indexes of non-active clays are not significantly affected (Di Maio et al., 2004; Yukselen-Aksoy et al., 2008; Wahid et al., 2010; Witteveen et al., 2013; Mokni et al., 2014). As to the impact of osmotic suction on the transport properties, no relevant effect on the coefficient of permeability and on the coefficient of consolidation is highlighted for clays, and the impact of a change in osmotic suction is equal to the one induced by an equivalent change in void ratio (Chen et al., 2000; Di Maio et al., 2004; Wahid et al., 2010).

Despite the large information available on the chemo-mechanical behaviour of clays, few studies are available on the chemo-osmotic effects on shales. Bunger et al. (2014) reports experimental evidences on the settlement induced by an increase in osmotic suction in a shale. Ewy (2015) reports results on the swelling magnitude of shales as a function of stress and void ratio. On the other hand, no experimental evidences on the dependency of the chemically induce settlements on the stress state, porosity or loading history are found. The reversibility concept for the chemically induced settlements

in shales has not been addressed, and no analysis on the impact of a chemical load on the pore network evolution has ever been carried out. This work provides an insight about the chemo-osmotic effects on the volume change behaviour of Opalinus Clay shale and analyses the chemo-osmotic consolidation behaviour. The effect of the chemical loading on the mechanical properties and on the pore network evolution is also addressed. This investigation is fundamental to gain information on the impact of osmotic suction on the self-sealing and hydraulic performance of the shale formation as well as on the mechanical response of the material. The analysis is also of utmost importance when the chemo-mechanical behaviour of shales has to be predicted by the use of numerical tools.

In the past, attempts have been made in order to elaborate numerical models capable of predicting the chemo-mechanical behaviour of clays (e.g. Gajo et al., 2002; Loret et al., 2002; Gajo and Loret, 2003; Guimarães et al., 2007; Gens, 2010; Guimarães et al., 2013; Witteveen et al., 2013). Following the wide experimental investigation on the chemo-mechanical behaviour of active clays having barrier functions, Gajo et al. (2002), Loret et al. (2002) and Gajo and Loret (2003) presented an elasto-plastic model where the chemical behaviour is governed by the mass fraction and mass balance of all the species. Differently, Guimarães et al. (2007) and Gens (2010) elaborated a double-structure model where osmotic suction is considered as the variable governing the chemical effects. As experimentally observed for active clays, these models consider reversible chemically induced strains. Guimarães et al. (2013) further expanded their formulation in order to include not only the effect of osmotic suction but also the influence of the nature of the exchangeable cations. The experimental investigations on non-active clays have highlighted the irreversible nature of the chemically induced settlements: Witteveen et al. (2013) presented an elasto plastic chemo-mechanical constitutive model which reproduces the irreversibility of the chemical consolidation settlements. The increasing interest in shales performance concerning wellbore stability and shale-fluid interaction, led to the development of chemo-poro-elastic models for predicting the chemo-mechanical behaviour of shales (Sarout and Detournay, 2011; Bunger et al., 2014). However the irreversible nature of the chemical settlements is not taken into account as well as the impact of the stress conditions on the chemo-mechanical behaviour. In this chapter an elasto-plastic chemo-mechanical constitutive framework is presented, which is capable of reproducing both the irreversibility of the chemically induced settlements as well as their stress dependency. The framework is calibrated and applied for back analysing the experimental results presented in the first part of this chapter. The model results are presented and discussed in the second part of the chapter.

5.3. Materials

5.3.1. Tested Opalinus Clay cores

The Opalinus Clay cores considered in this experimental campaign belong to the so called OPA-shallow (Mont Terri URL) and are named BOP-A5 and BHG-D1. The description and the geotechnical characterization of these cores are presented in Chapter 1. The cores belong to the shaly facies and all the specimens were cut perpendicular to the bedding orientation.

5.3.2. Pore fluids

Different pore fluids are considered in this work with the aim to impose different values of osmotic suction. Among the five considered pore fluids, a synthetic water is used which is made in order to reproduce the in-situ pore water chemical composition (Pearson, 1998): the measured osmotic suction of this water is 1.2 MPa. The remaining four pore fluids are sodium chloride (NaCl) solutions at different concentrations; the use of NaCl is justified by the fact that the main cation type present in the pore water of Opalinus Clay is sodium, therefore possible cation exchange effects are minimized (Manca et al., 2015).

The osmotic suction is usually derived from the chemical concentration according to Van't Hoff equation:

$$\pi = \nu RTc \tag{5.1}$$

where π is the osmotic suction [kPa], ν is the number of constituent ions, c is the concentration of the pore fluid [M = mol/L], R is the universal gas constant [8.32 kPa/K M] and T is the absolute temperature [K]. However, this relationship is valid in a limited range of concentrations (up to approximately 2 M). Witteveen et al. (2013) presented a detail correlation between the chemical concentration of NaCl solution and osmotic suction up to 6 M concentration (almost saturated solution):

$$\pi = 0.407c^2 + 3.888c + 0.61 \tag{5.2}$$

The considered pore fluids are reported in Table 5-1 together with the corresponding salt concentration and osmotic suction values.

Table 5-1: Pore fluids used in the chemo-mechanical experimental campaign on Opalinus Clay.

Fluids	Salinity [g/l]	Osmotic suction [MPa]
Distilled water (DW)	0	~0
Synthetic water (SW)	-	1.2
0.5 M NaCl	29.22	2.4
1 M NaCl	58.44	4.4
2 M NaCl	116.88	9.8
3 M NaCl	175.32	15.3

5.4. Experimental methodologies

The laboratory program was elaborated with the aim of providing a comprehensive picture of the coupled chemo/osmotic-mechanical processes in Opalinus Clay. A first series of experiments was conducted with the aim of analysing the impact of pore fluid osmotic suction on the water content and void ratio of the shale after wetting in free volume conditions (swelling behaviour). A second campaign of chemo-mechanical oedometric tests was conducted with the goal of studying the chemo-osmotic impact on the mechanical behaviour and the influence of stress state and mechanical loading

history on the chemo-osmotic volume change behaviour. Finally, mercury intrusion porosimetry (MIP) tests were carried out with the goal of understanding the effects of osmotic suction on the pore network evolution. The following sections provide details on the laboratory procedures.

5.4.1. Chemo-osmotic impact on water content and void ratio upon wetting

Preliminary analyses have been conducted in order to establish suitable procedures to impose and control the osmotic suction of the material at saturation. Osmotic suction is defined here as the solute suction, which is related to the salt concentration in the pore fluid. Whereas matric suction is defined as the suction generated by the presence of the matrix; it includes capillary forces, and osmotic and electrostatic phenomena on the clay particles surface. Saturated conditions are meant here as zero-matric suction conditions: the experimental analysis of the water retention behaviour of Opalinus Clay (see Chapter 2, Figure 2-5) has highlighted the fact that when zero-matric suction conditions are reached along a wetting path in free-volume condition, the degree of saturation is equal to about one. For this reason, when zero-matric suction is achieved, it is consistent to assume a degree of saturation equal to one. The following procedures have been considered to impose and control the osmotic suction in the specimens:

a) Direct contact and saturation with different pore fluids having different salt concentrations;

b) Initial saturation by direct contact with synthetic water, followed by direct exposure to different pore fluids having different salt concentrations.

To this aim, small cubic Opalinus Clay samples (~0.5 cm^3) were cut from the original core (BHG-D1 core). Subsequently, six specimens (referred as saturated specimens) were treated according to procedure (a): they were placed in different closed environments corresponding to different saline solutions imposing different values of osmotic suction (as specified in Table 5-1). The specimens were laid on bases composed by porous stones covered by filter paper, which were immersed in the different saline solutions (Figure 5-1). Since the specimen is in contact with the fluid, water infiltrates by capillary action and by osmotic processes related to the presence of the clay matrix: matric suction is thus brought to zero. However, the presence of a pore fluid having a certain chemical concentration induces an osmotic suction in the material that is therefore equal to the total suction.

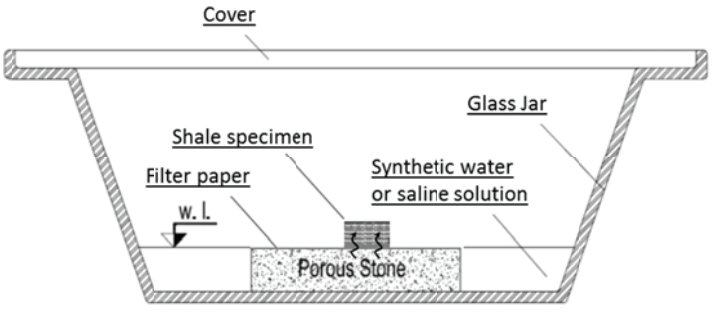

Figure 5-1: System used to impose the osmotic suction in the shale specimens.

Procedure (b) was applied on five specimens (referred as exposed specimens): the material was first saturated with synthetic water using the same methodology described above and subsequently exposed to the saline solutions, being in direct contact with them through a porous stone and filter paper which were located in closed environments as described in Figure 5-1. After equilibrium was achieved, the total suction of the saturated and exposed specimens was measured by a dew-point chilled-mirror psychrometer (Decagon, WP4C) (accuracy of ±0.05 MPa for total suction from 0 to 5 MPa and ±1% for total suction in the range of 5 – 300 MPa), the water content (w) was subsequently determined by oven-drying at 105°C and the void ratio (e) was finally computed, using the specific gravity of solids (G_s) and assuming full saturation of the samples, as:

$$e = w\, G_s \tag{5.3}$$

Preliminary tests were conducted in order to evaluate the time required for saturation of the specimens and for osmotic suction equilibration. The time for saturation was evaluated by measuring the mass evolution in time of a specimen of Opalinus Clay under saturation in the same conditions foreseen during the tests. The weight of the specimen was monitored using a precision balance (0.0001 g), and saturation was considered achieved once no further mass evolution was observed (after 8-10 days). As to the time for osmotic suction equilibration, about 30 days were allowed, considering a diffusion coefficient (D) of about 2.5×10^{-11} m^2/s (corresponding to an effective diffusion coefficient D_e of about 4.3×10^{-12} m^2/s), based on the analysis carried out in Section 5.5.3 on the diffusion behaviour of Opalinus Clay. The results of the total suction measurements on the saturated and exposed specimens highlight that the osmotic suction of the pore fluid is transmitted well to the material both by direct contact saturation and by direct exposure after saturation with synthetic water (Figure 5-2).

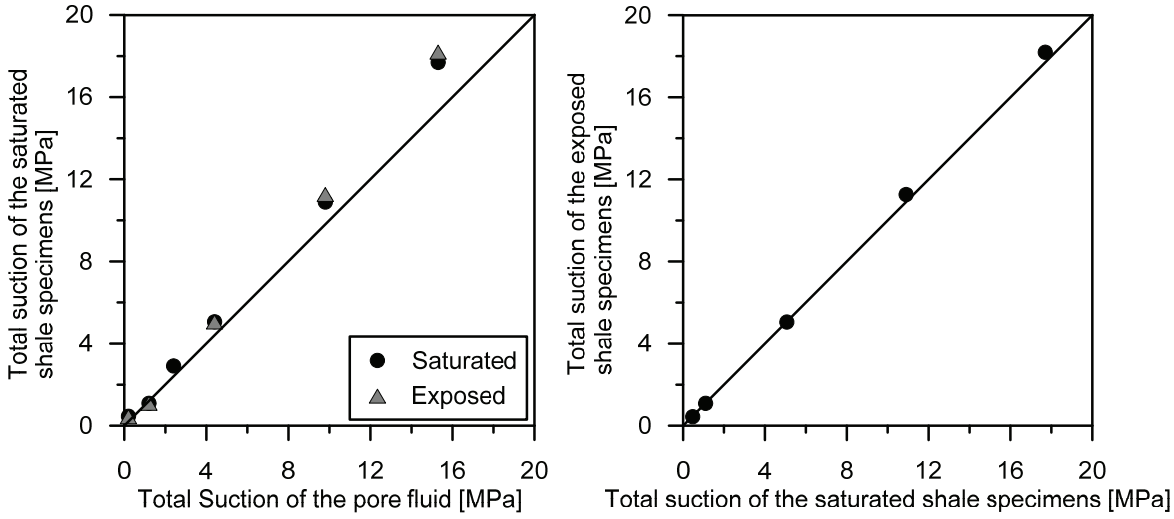

Figure 5-2: Comparison between the measured osmotic suction of the pore fluid, of the saturated specimens and of the exposed specimens.

The slightly greater values of osmotic suction measured for the specimens with respect to the ones of the solutions may be due to some matric suction development during the equalization stage in the WP4C chamber since small specimens are involved. The lower water content in the specimens equalized at high osmotic suction with respect to those equalized at low osmotic suction (see Figure 5-6) may induce a greater impact of water losses in the former during the equalization stages in the WP4C. The osmotic suction of the saturated specimens and the one of the exposed ones is very close: this evidence highlights that the process of diffusion is a relevant mechanism to impose a change in osmotic suction.

5.4.2. Chemo-mechanical oedometric testing

In order to investigate the coupled chemo-mechanical behaviour of Opalinus Clay a series of chemo-mechanical oedometric tests was carried out where the osmotic suction was considered as an independent variable. The high-pressure oedometric cell presented in Chapter 3 was used in this experimental campaign. A suitable interface cell (GDS Toxic Interface Unit) was adopted and connected between the cell and the pore fluid volume-pressure controller (VPC) in order to provide the possibility to apply high salinity pore fluids in the system using a back pressure and without damaging the VPC. The chemo-mechanical stress paths have been elaborated with the aim of analysing the influence of stress state, void ratio and overconsolidation ratio (OCR) on the volume change behaviour of the material during changes in osmotic suction, as well as with the aim of analysing the impact of the osmotic suction on the hydro-mechanical properties of the material. For this reason, osmotic suction changes are foreseen at different values of vertical effective stress and at different OCR values, while mechanical loading is carried out at different osmotic suction values. The stress paths of the tests are presented in Figure 5-3, the initial osmotic suction value corresponds, in all cases, to the one of the in-situ brine (1 MPa). Test 1and 2 were carried out on specimens obtained from the BOP-A5 core, while the specimens used in Test 3 to 6 belonged to the BHG-D1 core.

In the considered testing configuration, the specimens were in contact with the pore fluid in the drainage system through the top and bottom bases. All the tested shale specimens were initially saturated with synthetic water by keeping the volume constant in order to avoid any damage to the material, and the swelling pressure (corresponding to the maximum vertical stress that had to be applied to prevent any swelling of the material) was registered. Saturation was initially carried out by flushing the specimen from the bottom base under the action of an imposed hydraulic gradient, and subsequently applying the same back pressure (200 kPa) both from the top and bottom bases. Several days were needed to achieve saturation (i.e. constant swelling pressure was observed and no more water flowing into the cell was recorded). Subsequently the mechanical or chemical loads were applied according to the elaborated stress paths. Test 1 is a reference test where no chemical load is applied. In test 2, test 3, test 4 and test 6, the chemical load is applied during first loading phases at different values of vertical effective stress. In test 5 the chemical load is applied after a mechanical loading-unloading cycle which provides a high value of OCR. Quantitative details are reported in Figure 5-3.

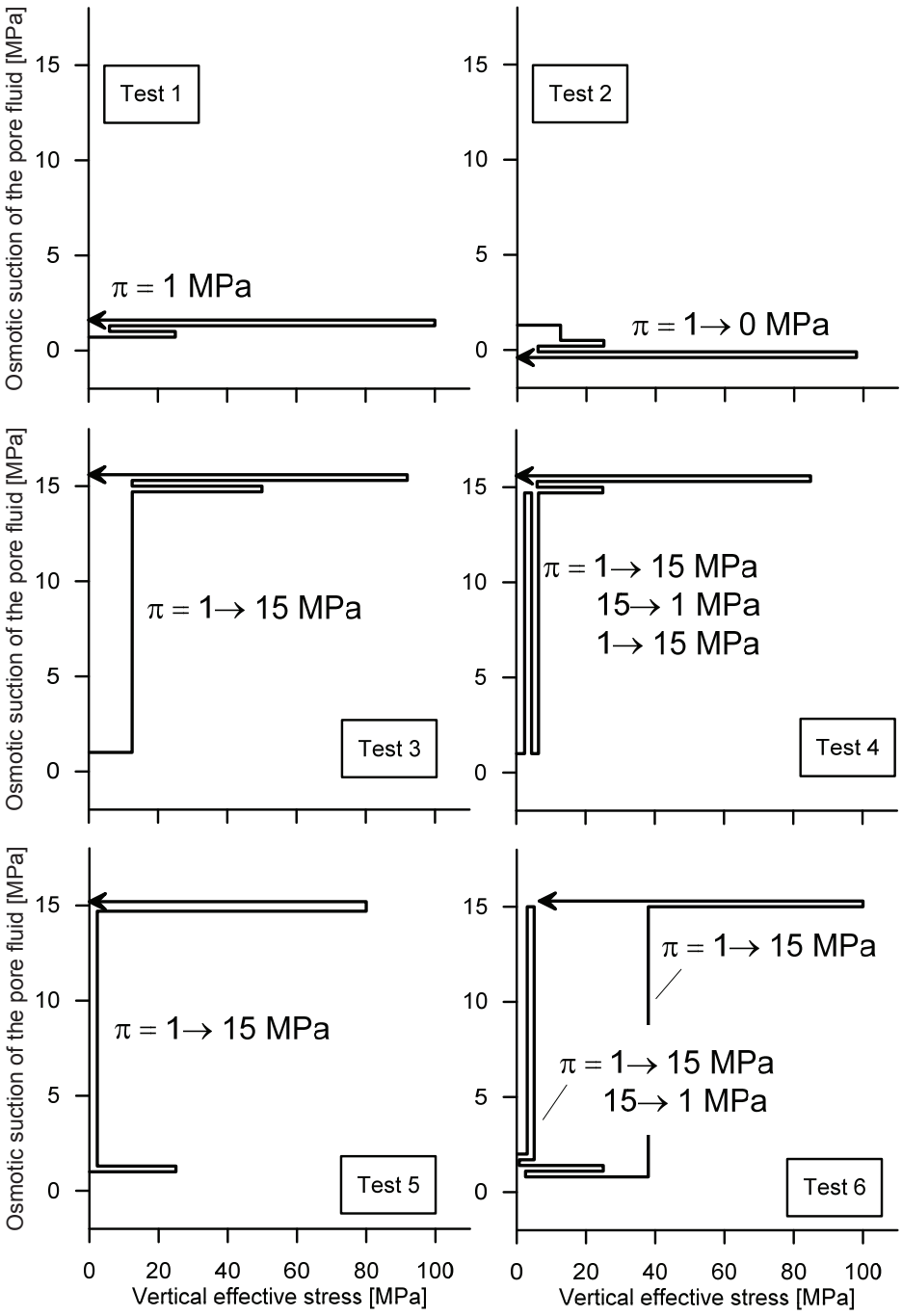

Figure 5-3: Stress paths for the chemo-mechanical oedometric tests.

5.4.3. Impact of osmotic suction on the evolution of the dominant pore size

A series of Mercury Intrusion Porosimetry (MIP) tests was carried out in order to study the pore network evolution under variations in osmotic suction. Six Opalinus Clay specimens from the BHG-D1 core, prepared with a diameter of about 30 mm and a height of about 7 mm, were closed in ad-hoc designed micro-cells which are represented in Figure 5-4 (Seiphoori et al., 2014).

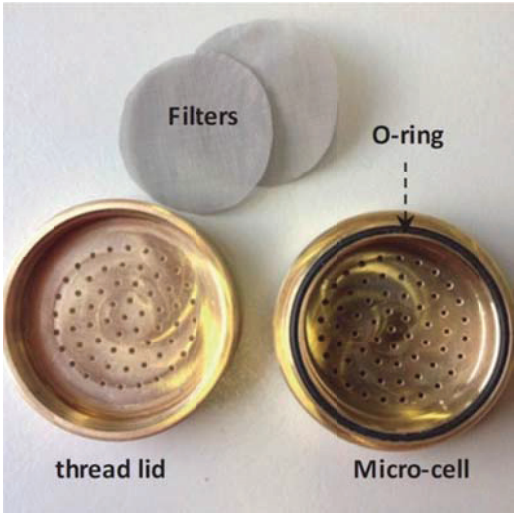

Figure 5-4: Micro-cell components (Seiphoori et al., 2014).

The use of these cells allows putting the specimens in contact with different pore fluids thanks to the presence of small holes in the rigid top and bottom bases of the cell, therefore the specimens are saturated while keeping constant volume conditions during wetting. Any void between the specimens and the cell which was due to a non-perfect geometry of the prepared specimens, was filled with a plastic metal (Weicon) which has greater stiffness with respect to the tested material (about 5 GPa). Different osmotic suction paths were elaborated concerning this testing phase (Figure 5-5): all the considered specimens, closed in the micro-cells, were initially immersed and saturated in synthetic water. To this aim the micro-cells were inserted in a greater cell, which was used in order to impose a back pressure of 150 kPa through the use of a VPC. After saturation, MIP tests were carried out on two of the six specimens, while the remaining four, closed in their microcells, were immersed in a 3M NaCl solution in order to impose an osmotic suction of 15 MPa by diffusion; the back pressure was imposed by the use of the interface cell and a VPC. Time for diffusion was estimated from the analysis of the chemo-osmotic loading phases of the chemo-mechanical oedometric tests (see further section 5.5.3). In fact, the size of the specimens inserted in the micro-cells is smaller than the one of the specimens used in the chemo-mechanical oedometric tests, therefore, an ions diffusion time between 20-30 days was considered suitable. Subsequently MIP tests were again conducted on two out of the four specimens equilibrated at 15 MPa of osmotic suction, while the remaining two specimens were again immersed in synthetic water under back pressure. After 30 days, MIP tests were carried out on the last two specimens. All the specimens subjected to MIP tests were freeze dried before testing.

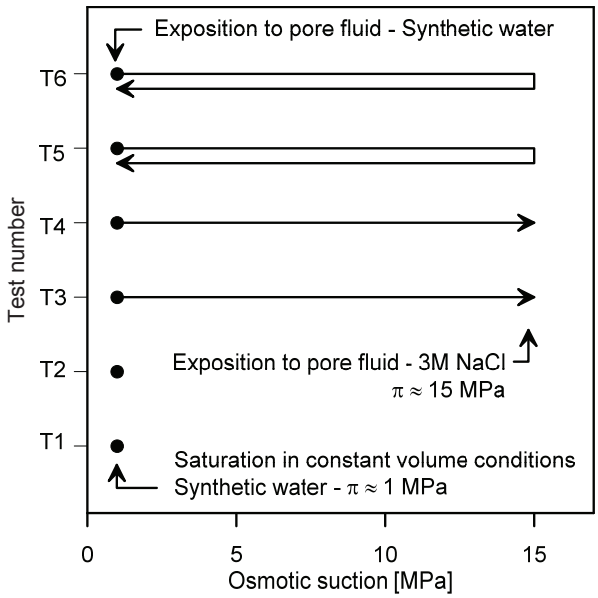

Figure 5-5: Osmotic suction paths for the specimens subjected to MIP testing.

5.5. Results and analysis

5.5.1. Chemo-osmotic impact on water content and void ratio upon wetting

The water content and void ratio of Opalinus Clay as a function of osmotic suction are presented in Figure 5-6 both for saturated specimens and exposed specimens: the water content and void ratio decrease as the osmotic suction increases at zero-matric suction conditions. Moreover, when the shale specimens are exposed to distilled water, a considerable amount of water uptake is observed, in good agreement with the results reported by Zhang (2007); also an important increase in volume is obtained, probably due to the opening of micro-fissures. Figure 5-6 shows that high values of osmotic suction of the pore fluid lead to a considerably lower amount of swelling upon wetting: the increase in void ratio with respect to the initial value of the core is considerably lower when saturation is carried out with high osmotic suction pore fluids with respect to the volume change observed when low osmotic suction pore fluids are adopted. The obtained results show that the use of solutions imposing high osmotic suction inhibits the swelling during wetting and, therefore, reduces the amount of volume change upon decrease in matric suction.

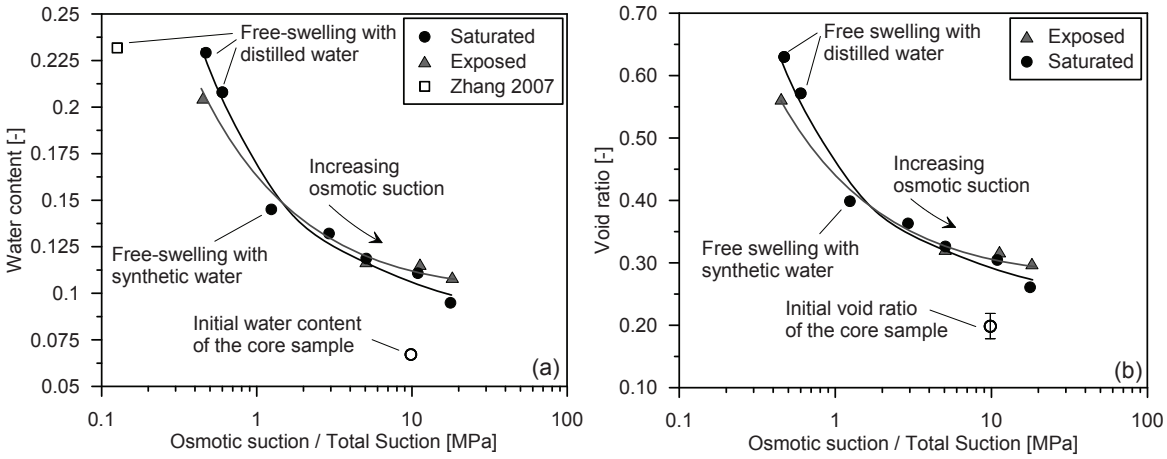

Figure 5-6: Water content (a) and void ratio (b) variations upon changes in pore fluid osmotic suction.

5.5.2. Coupled chemo-mechanical processes in chemo-mechanical oedometric tests

5.5.2.1. Chemo-mechanical oedometric behaviour

The experimental results presented so far have highlighted the impact of osmotic suction on the volume change behaviour of Opalinus Clay. In this section the results of the chemo-mechanical oedometric testing campaign are presented and discussed.

Test 1 was conducted at constant osmotic suction equal to the one of the in-situ pore fluid (1 MPa). The results of this test are reported in Chapter 3 (Test 1 on OPA-shallow) and are recalled here in Figure 5-7: the test allows obtaining the mechanical properties such as the compression index and swelling indices of the shale at the reference osmotic suction of 1 MPa.

The impact of different chemical loads at constant vertical effective stress is analysed in Figure 5-8 and Figure 5-9 where the osmotic suction of the pore fluid was respectively decreased to 0 MPa (Test 2) or increased to 15 MPa (Test 3) at about 12.5 MPa of vertical effective stress. The substitution of the pore fluid with distilled water has a negligible impact on the volume change: this is probably due to the fact that the imposed vertical effective stress was greater than the swelling pressure of the material. Ewy (2015) also show limited swelling of shale specimen when suction is decreased under stress. On the other hand, the imposition of a high osmotic suction equal to 15 MPa induced a decrease in void ratio: this process is defined as chemo-osmotic consolidation (Barbour and Fredlund, 1989; Kaczmarek and Hueckel, 1998). Further explanations on the physical mechanisms involved in the chemo-osmotic consolidation are given in Section 5.5.3.

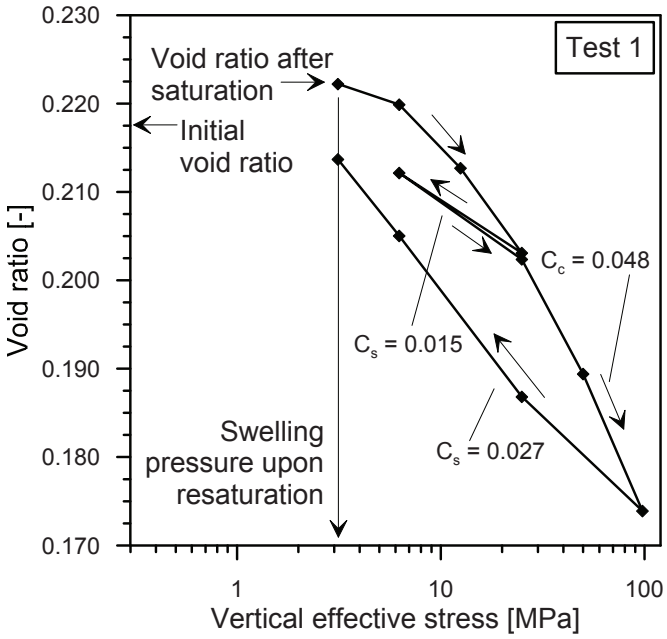

Figure 5-7: Oedometric compression at constant osmotic suction of 1 MPa.

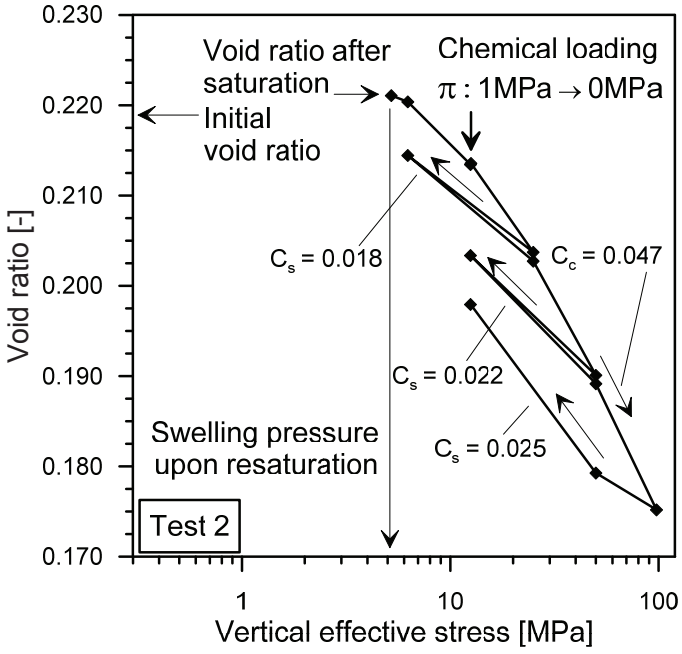

Figure 5-8: Oedometric compression with reduction of pore fluid osmotic suction at about 12.5 MPa of vertical effective stress.

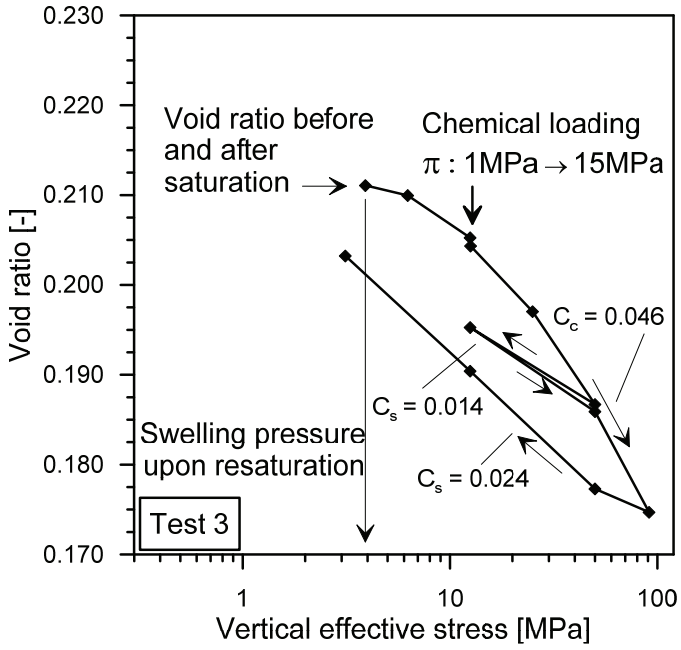

Figure 5-9: Oedometric compression with increase of pore fluid osmotic suction at about 12.5 MPa vertical effective stress.

Figure 5-10 refers to Test 3 and depicts the evolution of the vertical displacement due to the application of the mechanical load step from 6.5 to 12.5 MPa, and due to the application of the chemical load from 1 to 15 MPa of osmotic suction. Osmotic suction was increased only once the primary consolidation settlement had stabilized. The chemical settlement manifested shortly after the increase in osmotic suction, and it was allowed to develop until a displacement rate of 0.18 μm/day was reached after at least 12 days: in general about 3-4 weeks were required to satisfy the criterion.

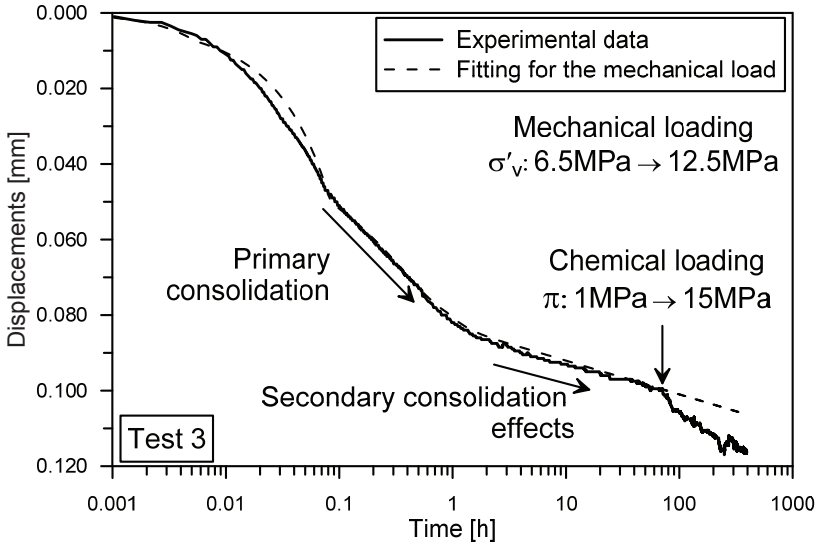

Figure 5-10: Mechanical and chemical load versus time.

The development of chemical settlements required significant amount of time, for this reason the secondary consolidation effects due to the applied mechanical load may play a role. The settlements due to secondary consolidation have been quantified thanks to the knowledge of the secondary compression coefficient C_α (obtained from the analysis of the previous mechanical loading step), and they have been taken into account when computing the chemical settlement (Figure 5-10) under the hypothesis that C_α is not affected by changes in osmotic suction.

The impact of the stress level on the chemical settlement is investigated in Figure 5-11 which depicts the results of test 4: the osmotic suction was increased to 15 MPa immediately after saturation at a vertical effective stress equal to 2.4 MPa. The chemical load induced a chemical strain equal to 0.15% which is significantly greater with respect to the chemical strain obtained at 12.5 MPa vertical effective stress and equal to 0.08%. The results highlight a dependency of the chemical settlements on the stress level where an increasing vertical effective stress reduces the induced chemical settlements for the same variation in osmotic suction.

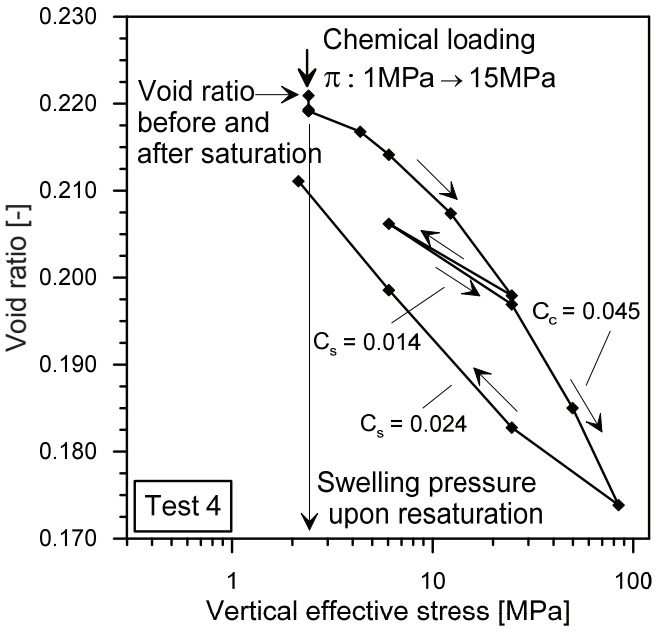

Figure 5-11: Oedometric compression with increase of pore fluid osmotic suction at 2.4 MPa vertical effective stress.

Figure 5-12 presents the evolution of the settlement in time after the chemical load was applied in test 4: once the chemical settlement induced by the increase in osmotic suction had stabilized (after about 20 days), the osmotic suction of the pore fluid was decreased to the initial value equal to 1 MPa. The previously induced chemical settlement was not recovered after the subsequent decrease in osmotic suction, thus highlighting the irreversible nature of the chemical settlements for Opalinus Clay. More than the 80% of the clayey component in Opalinus Clay is made up of non-active clay minerals such as illite, kaolinite and chlorite (Bossart, 2012). Non-active clays are observed to manifest irreversible

strains upon chemical loading; therefore, the chemo-mechanical behaviour of Opalinus Clay is in line with the behaviour of clayey geomaterials taking into account its mineralogical composition.

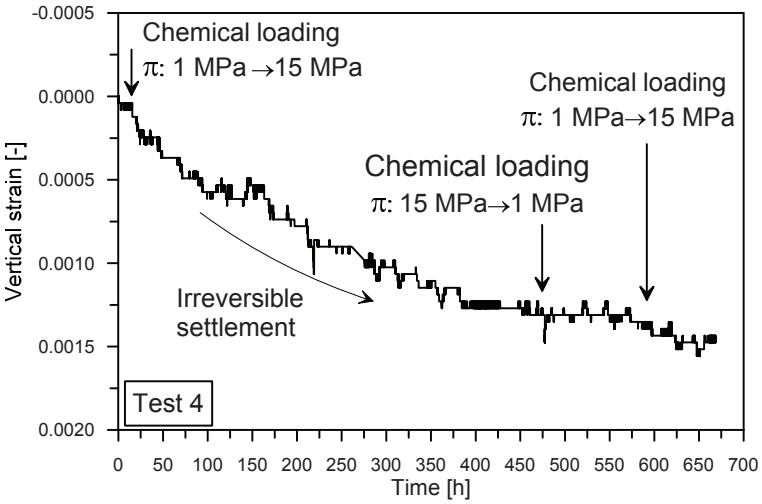

Figure 5-12: Evolution of the chemical strain at 2.4 MPa vertical effective stress in time.

The effect of the stress history and OCR is investigated through the performance of a chemo-mechanical oedometric test where the chemical loading is applied after a mechanical unloading-reloading cycle (Figure 5-13- Test 5). The increase up to 15 MPa osmotic suction is carried out at about the same vertical effective stress as in test 4 while the different mechanical loading history has induced a great vertical effective yield stress (25 MPa). The obtained value of the chemical settlement is much lower in test 5 (0.04%) compared to the one obtained in test 4.

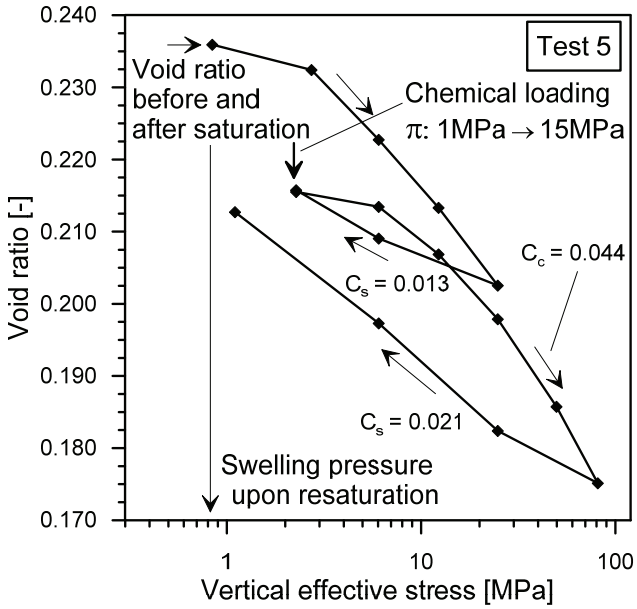

Figure 5-13: Oedometric compression with increase of pore fluid osmotic suction after a mechanical unloading-reloading cycle.

Figure 5-14 presents the results of test 6: a first chemical loading cycle was applied in steps, after saturation was completed, at a vertical effective stress equal to 3 MPa and an irreversible chemical deformation was obtained equal to 0.15% which is in good agreement with the value measured in test 4. After the decrease of the osmotic suction to the initial value of 1 MPa, the mechanical load was carried out in steps, including two unloading-reloading cycles, up to 37 MPa of vertical effective stress. At this point the osmotic suction was again increased up to 15 MPa at constant vertical effective stress: the process induced a small chemical consolidation settlement.

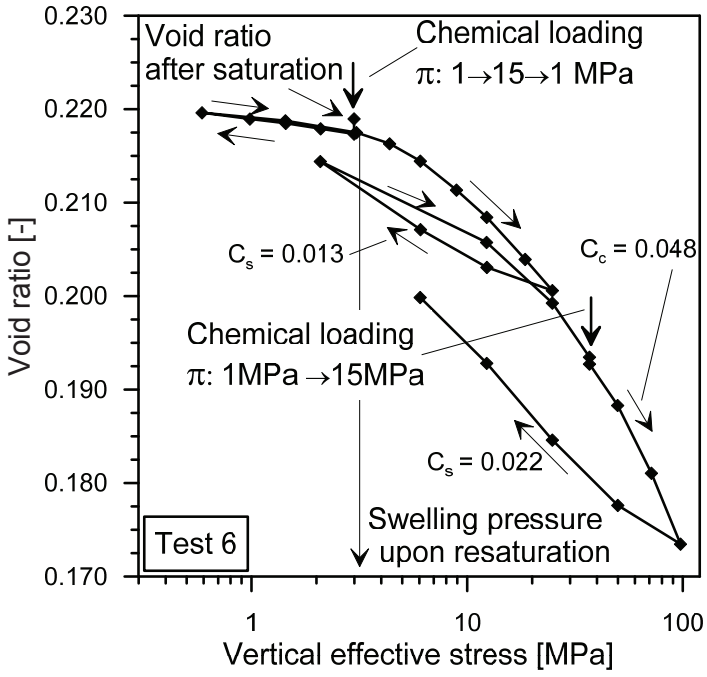

Figure 5-14: Oedometric compression with chemical loading-unloading cycles at 3 MPa vertical effective stress and final increase of pore fluid osmotic suction at 37 MPa vertical effective stress.

The chemical settlements are depicted in Figure 5-15 with respect to the applied osmotic suction for all the first chemical loading phases of the different tests. The maximum vertical effective stress reached before the application of the chemical load is also indicated in the figure. The first chemical loading cycle carried out in test 6 reveals a linear increase of the vertical strain with osmotic suction. The unloading branches in test 4 and test 6 highlight the irreversible nature of the chemical settlements.

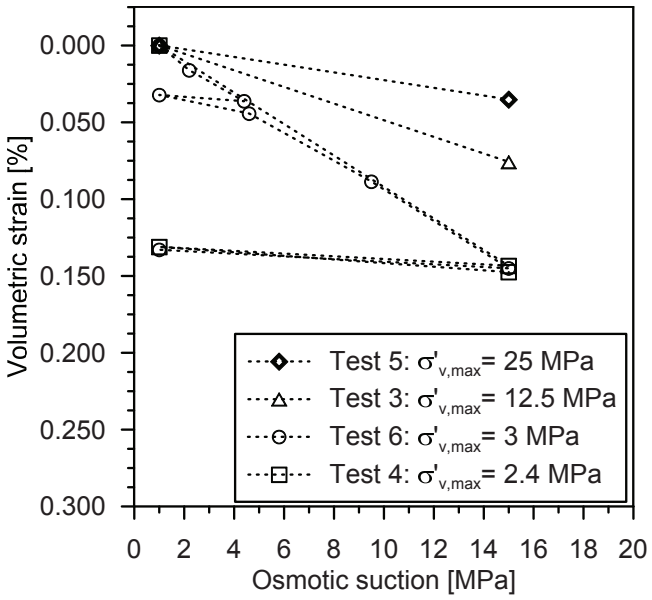

Figure 5-15: Chemical loading phases for the different tests: volumetric strains versus osmotic suction.

5.5.2.2. Effect of osmotic suction on the hydro-mechanical properties

The compression index expresses the compressibility of the material in the elasto-plastic domain while the swelling indexes express the compressibility of the material in the elastic domain; these indexes are derived from the oedometric compression results and they are represented in Figure 5-16 as a function of the osmotic suction. The swelling indexes are reported also as a function of the maximum stress level reached, highlighting the damage features of Opalinus Clay, where the increase in the stress level induces an increase in the compressibility of the material upon unloading. Figure 5-16 reports also the results of an additional oedometric test carried out at the reference osmotic suction of 1 MPa and presented in Chapter 3 (Test 2 on OPA-shallow). The results highlight that osmotic suction has negligible impact on the elastic and elasto-plastic compressibility of Opalinus Clay in the investigated range of osmotic suction.

Figure 5-17 depicts the oedometric modulus as a function of the vertical effective stress at the beginning of the loading steps and as a function of the osmotic suction. The oedometric modulus is clearly a function of the vertical effective stress since a greater stiffness is found at high vertical effective stress levels. The impact of damage is also well highlighted when the unloading-reloading branches are considered: the elastic modulus upon unloading-reloading decreases as the maximum effective stress reached increases. However, a negligible impact of the osmotic suction on the oedometric modulus is found, in line with the results on the compressibility values.

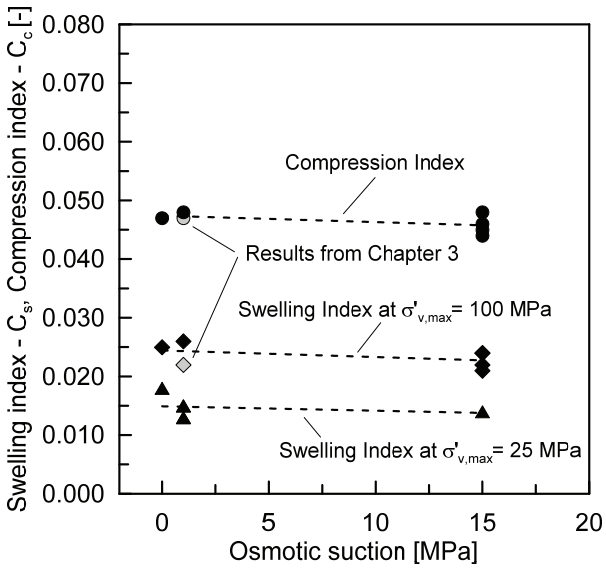

Figure 5-16: Compression index and swelling indexes as a function of the osmotic suction.

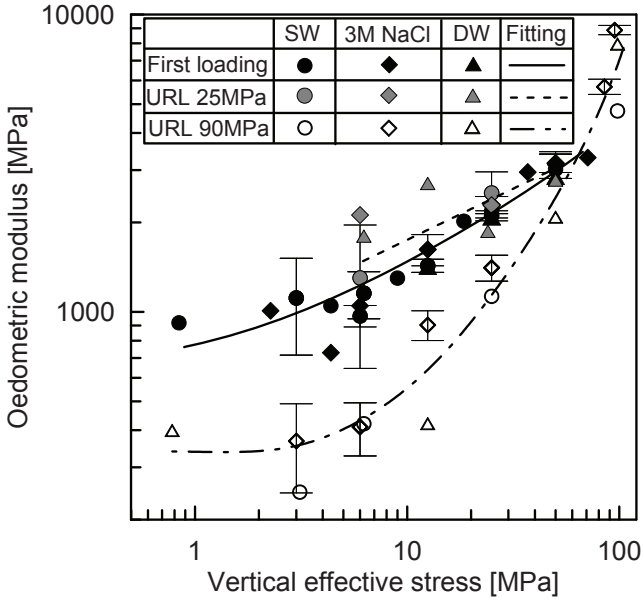

Figure 5-17: Oedometric modulus as a function of the vertical effective stress and osmotic suction.

The values of the coefficient of consolidation are reported in Figure 5-18 as a function of the vertical effective stress at the beginning of the loading steps and of the osmotic suction. Similarly to the previous considerations, a dependency of the coefficient of consolidation on the stress level is highlighted while the osmotic suction has a negligible impact. The results suggest that the compressibility of Opalinus Clay and the consolidation behaviour are not affected in a significant way by the osmotic suction of the pore fluid for the range of osmotic suction considered in this experimental campaign, in line with the behavioural features of non-active clays (e.g. Di Maio et al., 2004; Wahid et al., 2010).

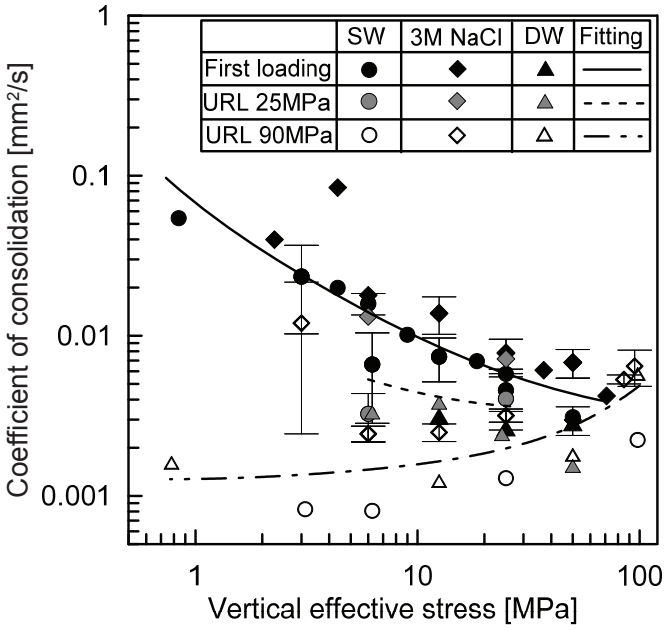

Figure 5-18: Coefficient of consolidation as a function of the vertical effective stress and osmotic suction.

5.5.3. Chemo-osmotic consolidation mechanisms and analysis

In this section an insight into the analysis of the chemo-osmotic consolidation mechanisms is carried out. Two primary chemo-osmotic consolidation mechanisms have been recognised in clays: they are named osmotic consolidation and chemical consolidation (Barbour and Fredlund, 1989; Kaczmarek and Hueckel, 1998; Peters and Smith, 2004; Witteveen et al., 2013). Osmotic consolidation develops due to the presence of an osmotic pressure gradient which generates a flow of water out of the specimen inducing negative pore water pressures inside the specimen and increasing the effective stress, which causes a decrease in volume. However, the induced negative pore water pressures and thus the increase in the effective stress are destined to decrease and go back to zero as the ions diffuse into the specimen and the osmotic pressure gradient diminishes. Therefore, the volume change induced by this type of process has to be recovered under the condition of elastic behaviour. Moreover the relevance of this process is strictly related to the capability of the material to exclude ions and to maintain the osmotic pressure gradient, behaving as a semi-permeable osmotic membrane. This property is expressed through the osmotic membrane efficiency (ω) which is defined as the ratio of the osmotically induced hydrostatic pressure to the imposed osmotic pressure variation, and varies between 0 (for negligible osmotic membrane properties) and 1 (for ideal membranes) (Marine and Fritz, 1981; Fritz, 1986). Chemical consolidation occurs when ions are capable of entering the specimen and are attracted to the negatively charged clay surface, thus decreasing the electrical repulsive forces and allowing the clay particles to move closer inducing a decrease in volume of the specimen. The term “diffused double layer” (DDL) indicates the system composed by the negatively charged surface of the clay particles, the water molecules and the ions distributed in the vicinity of the clay surface attracted by the negative charge (Mitchell and Soga, 2005). A higher concentration of

ions decreases the negative charge, reducing the thickness of the DDL and the repulsive forces among the clay particles. As a consequence a change in ion concentration of the pore fluid, and thus of the osmotic suction, would be directly related to a change in volume of the material.

Several authors have investigated the role and the effects of the two mechanisms on the chemo-osmotic volume change behaviour of clays (e.g. Barbour and Fredlund, 1989; Kaczmarek and Hueckel, 1998; Peters and Smith, 2004). They highlighted that the time-frame, the settlement evolution process as well as the entity of the induced pore water pressure, are very different for the two mechanisms: the osmotic mechanism develops much faster with respect to the chemical mechanism, in a time-frame that is close to the one of the mechanical consolidation, while chemical consolidation develops much more slowly. This is because the pore pressure diffusion front is expected to exceed the ion diffusion front of about one to two orders of magnitude (Van Oort, 2003). The settlements induced by the osmotic consolidation are completely recovered as the osmotic pressure gradient dissipates, while the settlements induced by the chemical consolidation are not recovered at the end of the process. Kaczmarek and Hueckel (1998) showed that chemical consolidation induces a small pore water pressure build up in the specimen while the osmotic consolidation causes the development of large negative pore water pressures. Since clayey geomaterials are recognised to have non-ideal osmotic membrane properties, the two mechanisms may act in parallel or one may predominates on the other according to the osmotic efficiency of the material: the osmotic mechanism is expected to be significant when the migration of ions is hindered and thus for high osmotic membrane efficiency, while the chemical consolidation is expect to prevail at low osmotic efficiency. However, the analysis conducted by Barbour and Fredlund (1989) leads to the main conclusion that the dominant chemo-osmotic mechanism of volume change in clays is chemical consolidation (Witteveen et al., 2013).

The evolution of the chemical settlement in time after the application of the chemical load during the different chemo-mechanical oedometric tests is depicted from Figure 5-19 until Figure 5-23. The experimental evidences suggest that chemical consolidation is the main mechanism causing the settlements development: in fact, the analysis of the transient phases reveals that a much wider time frame is involved with respect to the mechanical consolidation process widely illustrated in Chapter 3. In addition, the settlements are not recovered as it would be expected if osmotic consolidation would have played a significant role. Moreover, the results presented in section 5.5.1 show that the total suction of a specimen exposed to a given pore fluid, matches closely its suction, confirming the ion diffusion process. Very low osmotic-membrane efficiency has been measured for Opalinus Clay: Horseman et al. (2007) reported a value of 0.04. Low osmotic efficiency values have been measured also for other shales: Van Oort (2003) reports values of osmotic efficiencies between 0.02 and 0.08 for Pierre shale, while AL-Bazali (2011) reports a compilation of osmotic efficiency values for several shales where an average value of 0.05 is found with more than half of the reported data displaying osmotic membrane efficiencies lower than 0.034. The low osmotic efficiency values observed for these shales mean that ions are easily capable of entering the material, avoiding the development of significant osmotic pressure gradients. As a consequence, the generation of chemo-osmotic consolidation settlements is related mainly to ions transport and to a variation in chemical

concentration inside the specimen (chemical consolidation). AL-Bazali (2011) conducted some studies on the chemical impact on shales and recognised that the process of ion diffusion may be much more relevant with respect to the one related to osmotic consolidation, in agreement with the previous consideration on Opalinus Clay.

The experimental data on the transient behaviour during chemical loading have been back analysed using an analytical model for chemo-mechanical consolidation (Kaczmarek and Hueckel, 1998). The complete derivation of the equations is reported in Appendix C. Hereafter only the relevant equations are reported. The variation in ion concentration along z-direction is described by equation (5.4):

$$D_e \frac{\partial^2 c}{\partial z^2} = n\frac{\partial c}{\partial t} + c\omega k \frac{\partial^2 h}{\partial z^2} + \frac{\partial c}{\partial z}\left(-k\frac{\partial h}{\partial z} + \frac{\omega k}{\rho_w g}\frac{\partial \pi}{\partial z} + \omega k \frac{\partial h}{\partial z} \right) \tag{5.4}$$

where D_e is the effective diffusion coefficient, k is the hydraulic conductivity, n is the porosity, ω is the osmotic membrane efficiency, ρ_w is the density of water and g is the specific gravity. The first term on the right-hand side corresponds to storage of ions. The second term expresses ultrafiltration (i.e. flow of ions due to a hydraulic gradient generated due to the presence of an osmotic potential) and the coupling terms inside the brackets on the right side are the contribution to ion transport due to advection, chemical-osmosis and ultrafiltration, respectively. Advection is usually disregarded due to the different time scale involved with respect to the diffusive process (Kaczmarek and Hueckel, 1998; Peters and Smith, 2004; Horseman et al., 2007; AL-Bazali, 2011), ultrafiltration can also be neglected as well as the contribution to the ion transport due to chemo-osmosis since very low osmotic membrane efficiency values are involved. The significance of the chemo-osmotic coupling terms has been investigated by Soler (2001) for Opalinus Clay, who studied the potential effects of the different coupled transport phenomena on ions transport in the vicinity of a repository for high level nuclear waste. The author's analysis shows that the only coupled transport mechanism that has an impact on the ions transport is thermal osmosis, while the other coupling terms have only a minor impact. Taking into account the above considerations, the variation in ion concentration along z-direction is thus described by the following equation which takes the form of the second Fick's law:

$$D\frac{\partial^2 c}{\partial z^2} = \frac{\partial c}{\partial t} \tag{5.5}$$

Assuming a linear relationship between c and π (Van't Hoff equation), equation (5.5) can be written as follows:

$$D\frac{\partial^2 \pi}{\partial z^2} = \frac{\partial \pi}{\partial t} \tag{5.6}$$

where D is the diffusion coefficient defined as (Horseman et al., 1996):

$$D = \frac{D_e}{n} \tag{5.7}$$

where the intrinsic parameter D_e is the effective diffusion coefficient, which is different from the well-known Fick's diffusion coefficient D_0 due to the geometry of the porous material:

$$D_e = n\frac{\chi}{\tau^2}D_0 \tag{5.8}$$

where χ is the constrictivity, which takes into account the pore narrowing, and τ is the tortuosity, which takes into account the path lengthening (Horseman et al., 1996).

The volume reduction caused by chemical consolidation may generate a positive increase in pore water pressure which would subsequently dissipate, causing further consolidation. This phenomenon is expressed through equation (5.9) (Kaczmarek and Hueckel, 1998):

$$\frac{\partial u}{\partial t} = \frac{m_\pi}{m_v} RT \frac{\partial c}{\partial t} \tag{5.9}$$

where m_v is the coefficient of volume change and m_π is the osmotic coefficient of volume change. Equation (5.9) describes the change in pore pressure in time through the coupling with the porosity variation induced by chemical consolidation. The relevance of this phenomenon is related to the ratio between the osmotic and the mechanical compressibility (expressed by the osmotic coefficient of volume change and the coefficient of volume change, respectively). If the osmotic compressibility is low with respect to the mechanical one, this term has a negligible impact on the consolidation process. Kaczmarek and Hueckel (1998) carried out numerical simulations in order to understand the contribution of this term in a clayey medium and found that a low positive pore water pressure (less than 1 kPa) was generated under a chemical load of 4M of NaCl (about 20 MPa osmotic suction). As a consequence the contribution of this process to the development of chemical consolidation settlements is neglected.

The solution of equation (5.6) under the initial condition (t=0) of constant osmotic suction π_0 along z-direction, and the boundary condition of null osmotic suction at the top and bottom bases of the specimen (for t>0), allows obtaining the variation of osmotic suction along z-direction and in time:

$$\pi(z,t) = \sum_{m=0}^{\infty} \frac{2\pi_0}{M}\left(\sin\frac{Mz}{H}\right) e^{-M^2\frac{Dt}{H^2}} \tag{5.10}$$

where π_0 is the imposed variation in osmotic suction, H is the diffusion path length (half of the height of the specimen) and $M = 0.5\pi(2m+1)$, with m being an integer. A variation in osmotic suction induces a change in volume and in particular an increase in osmotic suction induces a settlement according to the following constitutive relationship (volumetric strains are considered positive when compressive):

$$-\frac{\Delta V}{V}(z,t) = \varepsilon(z,t) = m_\pi \Delta\pi(z,t) = m_\pi\left[\pi_0 - \pi(z,t)\right] \tag{5.11}$$

The settlement induced by an increase in osmotic suction is expressed as follows:

$$\delta(\mathrm{t}) = \int_0^{2H} \varepsilon(t,z)dz = \int_0^{2H} m_\pi \Delta\pi(t,z)dz = m_\pi \int_0^{2H} \left[\pi_0 - \pi(z,t)\right]dz \tag{5.12}$$

$$\delta(\mathrm{t}) = m_\pi \int_0^{2H} \left[\pi_0 - \sum_{m=0}^{\infty} \frac{2\pi_0}{M} \left(\sin\frac{Mz}{H} \right) e^{-M^2 \frac{Dt}{H^2}} \right] dz \tag{5.13}$$

$$\delta(\mathrm{t}) = 2Hm_\pi\pi_0 \left[1 + \sum_{m=0}^{\infty} \frac{1}{M^2} e^{-M^2 \frac{Dt}{H^2}} (\cos 2M - 1) \right] \tag{5.14}$$

$$\delta(\mathrm{t}) = 2Hm_\pi\pi_0 \left[1 - \sum_{m=0}^{\infty} \frac{2}{M^2} e^{-M^2 \frac{Dt}{H^2}} \right] \tag{5.15}$$

The parameters involved in the computation of the settlement evolution in time are the apparent diffusion coefficient D and the osmotic compressibility m_π; the osmotic stiffness modulus is defined as the inverse of the osmotic compressibility. These parameters are assumed constant during the chemical loading step and they are determined by fitting the experimental data with the proposed model through the minimization of the sum of the squared differences between the computed and measured settlements. The chemical loading steps of test 3, test 4, test 5 and test 6 have been analysed and the results are presented from Figure 5-19 to Figure 5-23 (only the last two steps for the initial chemical loading phase in test 6 are reported).

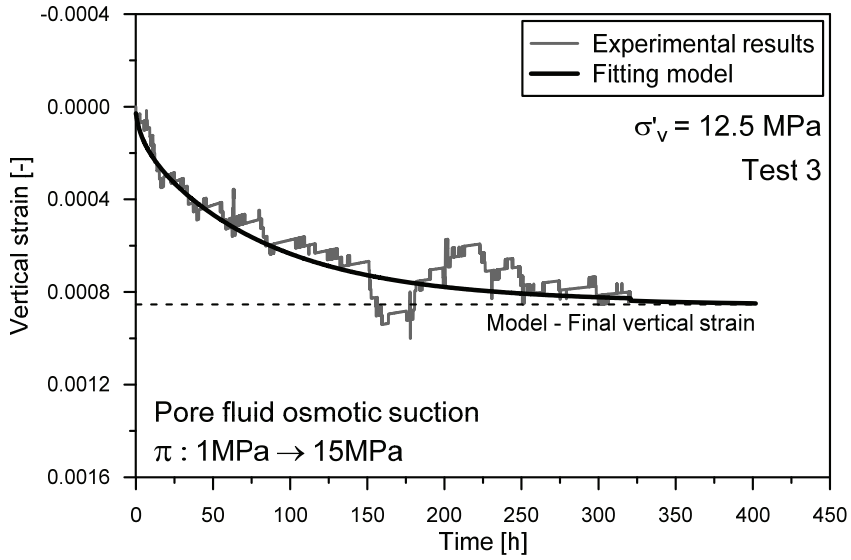

Figure 5-19: Chemical consolidation phase in Test 3.

The model describes well the behaviour experimentally observed, supporting the consideration that the predominant chemo-osmotic mechanism acting on the tested material is chemical-consolidation. The model predicts well the final chemical settlements in almost all the chemo-osmotic loading

phases, highlighting a degree of chemical consolidation greater than 95%. As to test 5, the model reveals that slightly longer time would have been required in order to reach 95% of chemical consolidation: the average degree of chemical consolidation for Test 5 is equal to 81%.

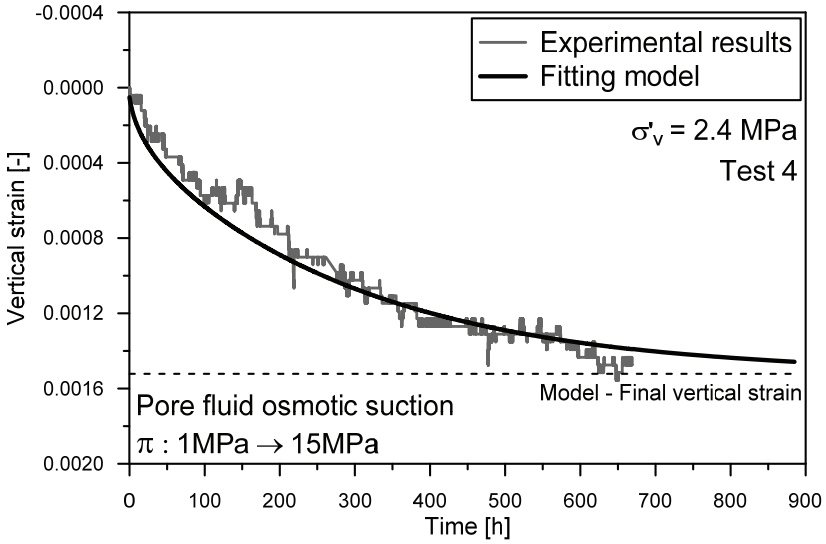

Figure 5-20: Chemical consolidation phase in Test 4.

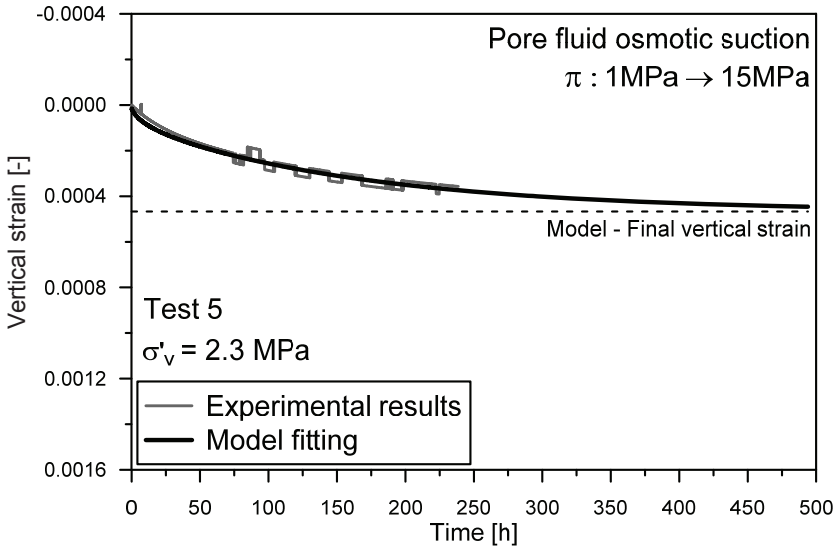

Figure 5-21: Chemical consolidation phase in Test 5.

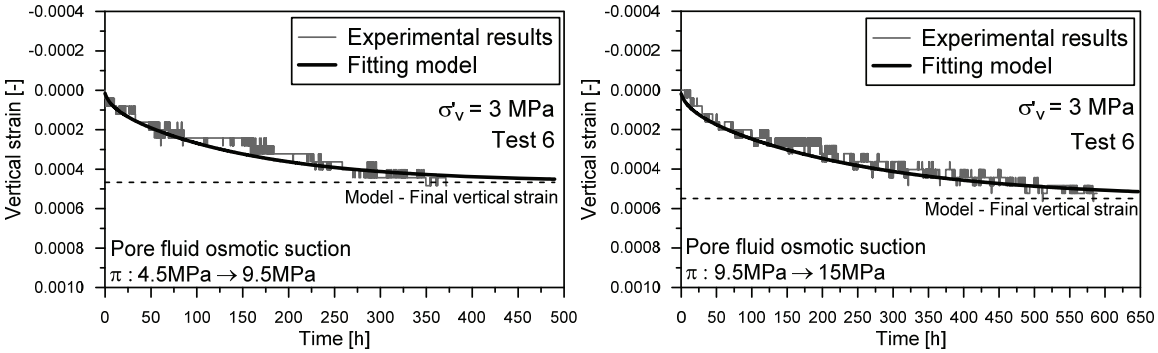

Figure 5-22: Chemical consolidation phases at 3 MPa vertical effective stress in Test 6.

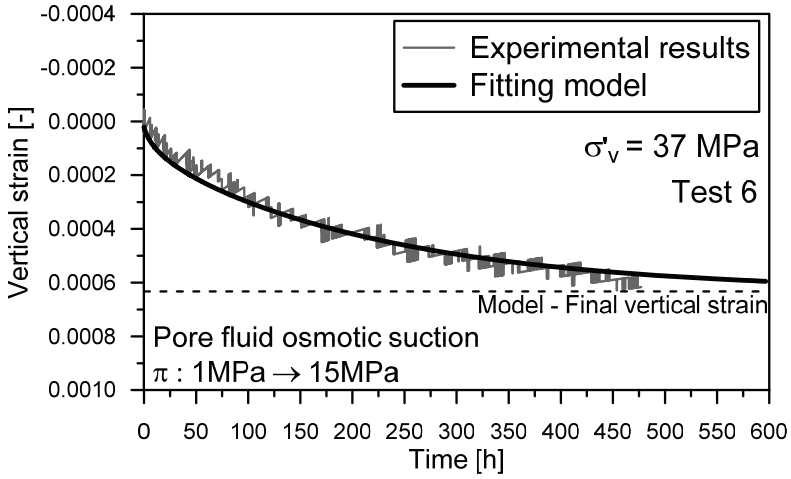

Figure 5-23: Chemical consolidation phase at 37 MPa vertical effective stress in Test 6.

The results in terms of effective diffusion coefficient (D_e) (computed from Eq.(5.7) assuming n equal to total porosity) and osmotic stiffness modulus are reported in Figure 5-24 and Figure 5-25 as a function of the vertical effective stress and of the void ratio; both first loading conditions and high OCR conditions are presented. The effective diffusion coefficient is observed to be independent on the void ratio and vertical effective stress, and varies between 10^{-11} m^2/s and 10^{-12} m^2/s in good agreement with the values reported in Soler (2001) and Bossart (2012) (10^{-11} - 10^{-12} m^2/s and 4.8 x 10^{-12} m^2/s, respectively). The values of the osmotic stiffness modulus are presented in Figure 5-25 as a function of the vertical effective stress and of the void ratio. When first loading conditions are considered, the osmotic stiffness increases with decreasing void ratio and with increasing vertical effective stress. However, when high OCR conditions are found, the chemical loading induces a lower deformation, manifesting very high osmotic stiffness. This behaviour may be due to the fact that a structural rearrangement has already taken place during the previous mechanical loading at high stress. The values of the osmotic stiffness modulus are presented in Figure 5-26 as a function of the vertical effective yield stress: a better correlation is found, suggesting that the response of the material to changes in osmotic suction is rather related to the maximum stress level experienced.

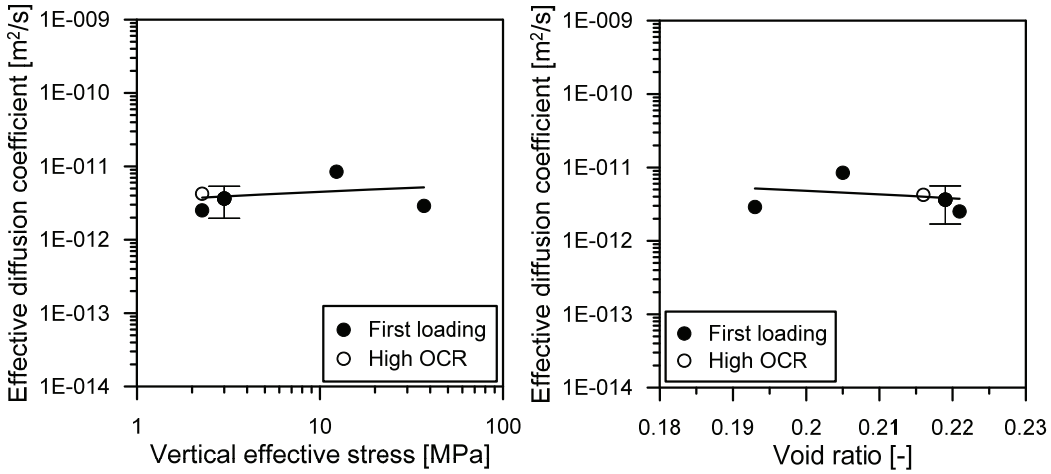

Figure 5-24: Effective diffusion coefficient as a function of the vertical effective stress and void ratio.

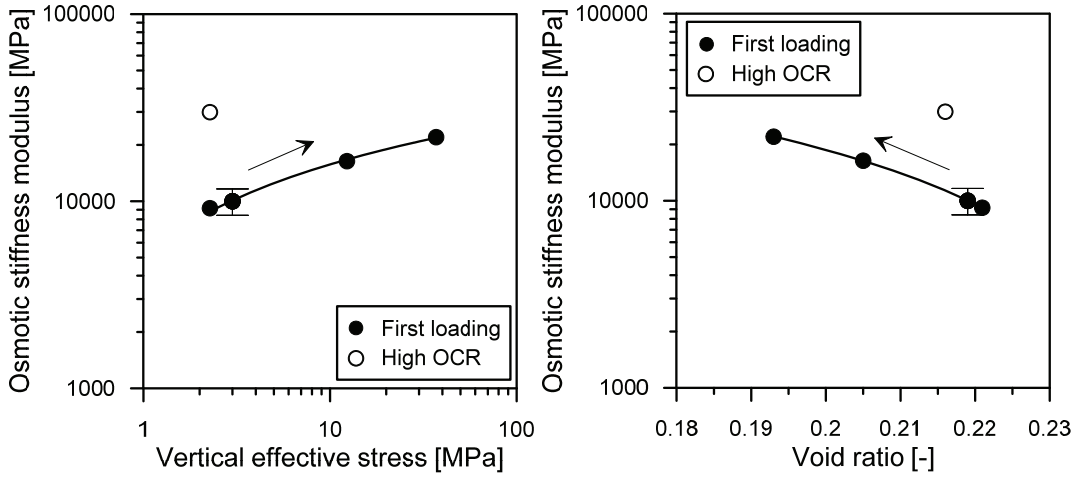

Figure 5-25: Osmotic stiffness modulus as a function of the vertical effective stress and void ratio.

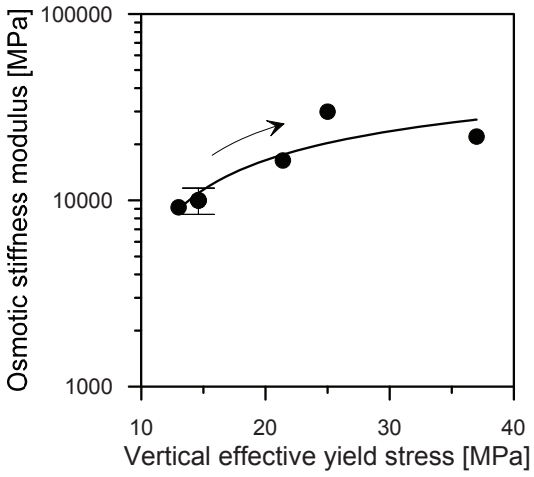

Figure 5-26: Osmotic stiffness modulus as a function of the vertical effective yield stress.

5.5.4. Impact of osmotic suction on the evolution of the dominant pore size

The MIP technique is used in this work in order to investigate possible microstructural changes related to osmotic suction variations in Opalinus Clay. A relevant aspect in the analysis of MIP results is the effect of the surface roughness: scanning electro-microscopy (SEM) images of Opalinus Clay microstructure have shown that the maximum pore diameters are in the order of 1 μm – 10 μm, while the mercury intrusion process identifies greater diameters due to the surface roughness of the specimen, thus overestimating the porosity (Houben et al., 2013). For this reason Houben et al. (2013) suggested to correct the intruded volume down to maximum access diameters between 100 nm and 10 μm. In this work the intruded volume is corrected down to a pore diameter of 1 μm. The results on the evolution of the dominant entrance pore size upon changes in osmotic suction are presented in Figure 5-27. The exposition of the material to a pore fluid characterized by an osmotic suction equal to 15 MPa induces a visible reduction in the dominant entrance pore size from about 20 nm to about 12 nm (Figure 5-27a). On the other hand, when the material is subjected to a complete osmotic suction cycle and further re-exposed to the initial osmotic suction equal to 1 MPa, a reversible behaviour is highlighted where the dominant entrance pore size returns to the initial value (Figure 5-27b). As to quantitative variations in the void ratio of the material, the MIP tests results do not allow to observe significant volume change. In fact, the maximum irreversible volume reduction induced by chemical consolidation in the oedometric tests was about 0.15% (Figure 5-15) which corresponds to a void ratio variation of about 0.18%: such a small variation is within the accuracy of the MIP technique for any quantitative prediction of the intruded void ratio. Moreover, this technique presents two major limits when it is applied to low porosity materials: the first one is related to the incapacity of the apparatus to investigate the smallest pores of the material which constitute the so called non-intruded porosity; the second one is related to the presence of pores that are accessible only through smaller ones. These pores are defined as constricted porosity and they are not detected until the smaller pores are penetrated (Tarantino et al., 2009). Therefore, the above mentioned limits of this technique when applied to shales, which have very low porosity and a complex and heterogeneous pore structure, do not allow any quantitative evaluation in terms of porosity change.

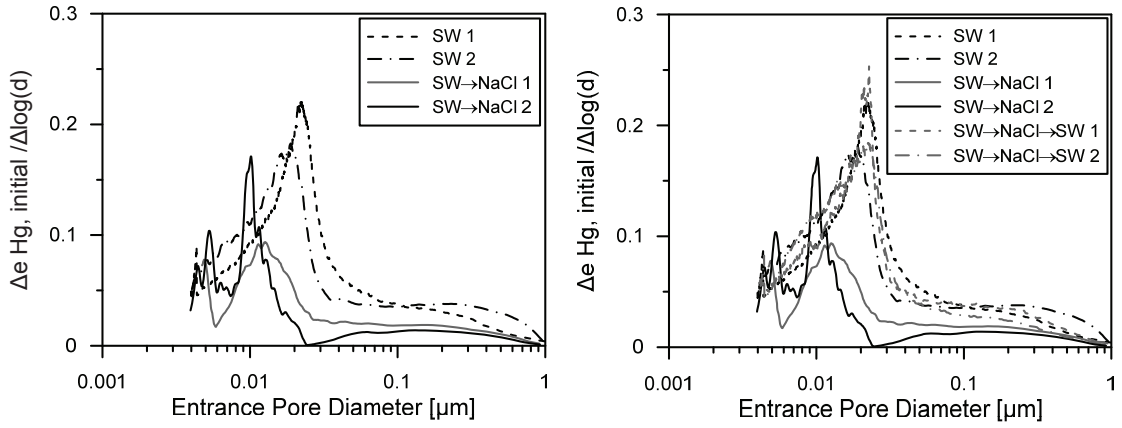

Figure 5-27: Dominant entrance pore size evolution upon changes in osmotic suction for Opalinus Clay.

5.6. Discussion

The experimental evidences obtained both from the chemo-osmotic consolidation results and from the MIP tests can be well explained from a qualitative point of view, taking into account the complex pore structure of Opalinus Clay. Microstructural investigations (e.g. Keller et al., 2013; Houben et al., 2013) have shown that the interconnected pore network is mainly found in the clay matrix and it is characterized and controlled by pore throats as low as few tenths of nanometres. These small pore throats constitute the connection between bigger pores (few hundreds of nanometres) which are found either in the clay matrix at the irregular contact boundaries between different clay domains, or at the contact boundaries between clay matrix and non-clayey particles.

The variation in pore fluid osmotic suction has a double effect: the first one is reversible and consists in the interaction of the ions with the DDL. A DDL may not exist inside a clay domain, due to the very low distance between clay layers, however it may exists between different clay domains. Houben et al. (2013) revealed that the interconnected porosity in Opalinus Clay is mainly formed by: (i) elongated pores between clay domains oriented in a similar manner, (ii) crescent-shaped pores in saddles of folded clay domains, (iii) large pores surrounding non-clayey grains. Therefore, DDL effects may affect the size of small pores in the clay matrix, causing a narrowing of the pore throats and reducing the distance between clay domains.

The second effect consists in an irreversible variation in volume upon osmotic suction cycles which is likely to take place where the contact forces between different particles are lower. In fact, the morphology of the Opalinus Clay microstructure and the knowledge about the chemo-osmotic behaviour of non-active clays (which constitute the majority of the clay component in Opalinus Clay) can well explain the latter phenomenon. The consolidation settlements induced by the application of a chemical load in non-active clays are due to a variation in the inter-particle forces, which leads to the sliding between particles at their contact points and thus to a structural rearrangement (Sridharan and Rao, 1973; Di Maio and Fenelli, 1997; Wahid et al., 2010). This rearrangement of the structure produces an irreversible decrease in volume (Di Maio, 1996; Wahid et al., 2010; Mokni et al., 2014). The same mechanism seems to manifests also for Opalinus Clay. Constricted pores greater than the dominant entrance pore size are widely found in Opalinus Clay (Houben et al., 2013), especially at the boundaries with non-clayey particles (Keller et al., 2013). It is thus possible that the majority of the irreversible volume reduction manifests in correspondence to these bigger pores where sliding between different particles is more likely to take place. When highly overconsolidated conditions are found, the chemical effects are less relevant as observed in Section 5.5.2.1. This behaviour may be due to the fact that a microstructural rearrangement has already taken place during the previous mechanical loading at high stresses, thus a chemical load would not induce further significant structural rearrangement at the current stress conditions. The results from the MIP tests allows to draw the conclusion that the irreversibility in the volume change is not at the level of the porosity involved in the pore network (connecting pores) but it is rather attributed to a structural rearrangement involving bigger pores which are more prone to collapse upon a reduction in the inter-particles forces.

5.7. Chemo-mechanical constitutive framework

An elasto-plastic chemo-mechanical framework is formulated in this section, which takes into account the chemo-mechanical behavioural features experimentally observed in Opalinus Clay. The framework is applied in order to back analyse the results of the chemo-mechanical testing campaign presented in Section 5.5.2.

5.7.1. A chemo-mechanical elasto-plastic framework

The proposed constitutive framework is based on the well-known ACMEG model (François and Laloui, 2008), which have been modified with the aim to better tackle the chemo-mechanical response of Opalinus Clay. Chapter 7 of this Thesis provides a more detailed description of the elaborated mechanical framework; in this section only the most relevant equations concerning the mechanical part of the model are reported, while more attention is dedicated to the introduction and description of the chemo-osmotic equations and their interaction with the mechanical part.

5.7.1.1. Non-linear anisotropic elasticity

The increment in total strain $d\varepsilon_{ij}$ is given by the sum of the elastic strain increment $d\varepsilon_{ij}^{e}$ and plastic strain increment $d\varepsilon_{ij}^{p}$ (positive sign is considered as compression):

$$d\varepsilon_{ij} = d\varepsilon_{ij}^{e} + d\varepsilon_{ij}^{p} \tag{5.16}$$

The reversible elastic strains are computed through the definition of the transversely isotropic elastic stiffness matrix D_{ijkl}:

$$d\varepsilon_{ij}^{e} = D_{ijkl}^{-1} d\sigma'_{kl} \tag{5.17}$$

In fact, Opalinus Clay manifests an anisotropic elastic behaviour, where the material is more compliant when loaded perpendicular to the anisotropic planes (bedding planes) rather than when loaded parallel to them. This type of anisotropy is called transverse isotropy and the elastic behaviour of the material is determined through the definition of five independent elastic parameters: the Young modulus E_1 and Poisson's ratio ν_1 parallel to the bedding planes, the Young modulus E_2 and Poisson's ratio ν_2 perpendicular to the bedding planes, and the shear modulus G_2 for shear loads in the bedding planes. Further details on the definition of the elastic transversely isotropic stiffness matrix and its implementation are given in Chapter 7. Moreover, the non-linear elastic response is described through the dependency of the elastic moduli on the mean effective stress p', according to a power law:

$$E_1 = E_{1\,ref} \left(\frac{p'}{p'_{ref}} \right)^{n_{el}} \tag{5.18}$$

$$E_2 = E_{2\,ref}\left(\frac{p'}{p'_{ref}}\right)^{n_{el}} \tag{5.19}$$

where E_{1ref} and E_{2ref} are the elastic moduli parallel and perpendicular to the bedding planes respectively, at a reference mean effective stress equal to 1 MPa and n_{el} is the elastic exponent. The mean effective stress p' is defined as follows:

$$p' = \frac{\sigma'_x + \sigma'_y + \sigma'_z}{3} \tag{5.20}$$

The deviatoric stress q is also introduced as follows:

$$q = \sqrt{\frac{\left(\sigma'_x - \sigma'_y\right)^2 + \left(\sigma'_x - \sigma'_z\right)^2 + \left(\sigma'_y - \sigma'_z\right)^2 + 3\tau_{xy}^2 + 3\tau_{xz}^2 + 3\tau_{yz}^2}{2}} \tag{5.21}$$

5.7.1.2. Elasto-plasticity

The elastic domain is limited by an isotropic yield limit, which evolves with the volumetric plastic strains, and by a bilinear Mohr-Coulomb failure surface, where a progressive plasticity process is considered through the introduction of the bounding surface theory (Dafalias and Popov, 1975; Krieg, 1975; Dafalias and Popov, 1977).

The isotropic yield limit is expressed as follows:

$$f_{iso} = p' - p'_c = 0 \tag{5.22}$$

where p'_c is the mean effective yield stress, which evolves with the mechanical volumetric plastic strains $\varepsilon_v^{p,m}$ and depends on the osmotic suction as follows:

$$p'_c = p'_{c0}\exp\left(\beta \cdot \varepsilon_v^{p,m}\right)\left(1 - \gamma_\pi \ln\frac{\pi}{\pi_0}\right) \tag{5.23}$$

where p'_{c0} is the mean effective yield stress at the reference osmotic suction π_0, β is the plastic stiffness index and γ_π is a parameter describing the variation of the yield stress with osmotic suction.

The bilinear Mohr-Coulomb failure surface in the p'- q plane is expressed through the definition of two domains:

For $p' < p'_{tr}$: $\qquad f_{MC} = q - M_2 p' r_{dev} = 0$ (5.24)

For $p' > p'_{tr}$: $$f_{MC} = q - M_1\left(p' + \frac{c_{pq}}{M_1}\right) r_{dev} = 0 \tag{5.25}$$

where c_{pq} is a cohesive component that allows to describe the bi-linearity of the failure surface, p'_{tr} is a threshold mean effective stress, and r_{dev} is the bounding surface deviatoric radius. The threshold mean effective stress represent the values of the mean effective stress at which the change in slope of the failure envelope occurs:

$$p'_{tr} = \frac{c_{pq}}{\left(M_2 - M_1\right)} \tag{5.26}$$

The failure envelope is therefore defined only by the parameter M_2 in the lower mean effective stress range, while both M_1 and c_{pq} are to be defined for the higher mean effective stress range. The parameter M_1 and M_2, and the cohesive component c_{pq} are defined as follows:

$$M_1 = \frac{6\sin\phi'_1}{3 - \sin\phi'_1} \tag{5.27}$$

$$M_2 = \frac{6\sin\phi'_2}{3 - \sin\phi'_2} \tag{5.28}$$

$$c_{pq} = \frac{c' \cdot M_1}{\tan\phi'_1} \tag{5.29}$$

where ϕ'_1 is the friction angle for the domain $p' > p'_{tr}$ and c' is the cohesion for the same domain, while ϕ'_2 is the friction angle for the domain $p' < p'_{tr}$. The deviatoric radius r_{dev} allows to have plasticity before reaching the failure conditions thanks to the evolution of the bounding surface with the deviatoric plastic strain, and it is expressed as follows:

$$r_{dev} = r_{dev}^{el} + \frac{\varepsilon_{dev}^{p}}{a + \varepsilon_{dev}^{p}} \tag{5.30}$$

and

$$\partial r_{dev} = \frac{\left(1 - r_{dev} + r_{dev}^{el}\right)^2}{a} \partial\varepsilon_{dev}^{p} \tag{5.31}$$

where r_{dev}^{el} is the initial value of the deviatoric radius, a is a material parameter and ε_{dev}^{p} is the deviatoric plastic strain.

5.7.1.3. Osmotic mechanism

A new osmotic plastic mechanism is introduced. The yield function for the osmotic mechanism is expressed as follows:

$$f_\pi = \pi - \pi_c = 0 \tag{5.32}$$

where π_c is the yield osmotic suction, which is a function of the osmotic volumetric plastic strain $\varepsilon_v^{p,\pi}$ (strain produced by the activation of the osmotic mechanisms):

$$\pi_c = \pi_{c0} + \beta_\pi \varepsilon_v^{p,\pi} \tag{5.33}$$

where π_{c0} is the initial yield osmotic suction and β_π is the osmotic stiffness modulus which is considered as function of the mean effective yield stress:

$$\beta_\pi = f(p'_c) \tag{5.34}$$

The following logarithmic expression is considered here, according to the experimental evidences reported in Figure 5-26:

$$\beta_\pi = \beta_{\pi 0} + A \ln p'_c \tag{5.35}$$

where $\beta_{\pi 0}$ and A are material parameters.

The model flow rules are associated for the isotropic and osmotic mechanisms, therefore $f_{iso} = g_{iso}$ and $f_\pi = g_\pi$; while non-associated flow rule is considered for the deviatoric part. In this last case the shape of the plastic potential is taken after the work of Nova and Wood (1979) and modified as follows:

$$g_{dev} = q - M_1 \left(p' + \frac{c_{\mathrm{pq}}}{M_1} \right) \left(1 - \ln \frac{2\left(p' + \frac{c_{\mathrm{pq}}}{M_1} \right)}{p'_c} \right) = 0 \tag{5.36}$$

Therefore the plastic flows are expressed as follows:

$$d\varepsilon_v^{p,m} = \lambda_{iso}^p \frac{\partial g_{iso}}{\partial p'} + \lambda_{dev}^p \frac{\partial g_{dev}}{\partial p'} \tag{5.37}$$

$$d\varepsilon_{dev}^p = \lambda_{dev}^p \frac{\partial g_{dev}}{\partial q} \tag{5.38}$$

$$d\varepsilon_v^{p,\pi} = \lambda_\pi^p \frac{\partial g_\pi}{\partial \pi} \tag{5.39}$$

where λ_{iso}^{p} and λ_{dev}^{p} are the mechanical plastic multipliers, while λ_{π}^{p} is the osmotic plastic multiplier. The plastic multipliers are defined through the respect of the consistency conditions:

$$\partial f_{iso} = \frac{\partial f_{iso}}{\partial p'}\partial p' + \frac{\partial f_{iso}}{\partial \pi}\partial \pi + \frac{\partial f_{iso}}{\partial p'_{c}}\frac{\partial p'_{c}}{\partial \varepsilon_{v}^{p,m}}\partial \varepsilon_{v}^{p,m} = 0 \tag{5.40}$$

$$\partial f_{MC} = \frac{\partial f_{MC}}{\partial q}\partial q + \frac{\partial f_{MC}}{\partial p'}\partial p' + \frac{\partial f_{MC}}{\partial r_{dev}}\frac{\partial r_{dev}}{\partial \varepsilon_{dev}^{p}}\partial \varepsilon_{dev}^{p} = 0 \tag{5.41}$$

$$\partial f_{\pi} = \frac{\partial f_{\pi}}{\partial \pi}\partial \pi + \frac{\partial f_{\pi}}{\partial \pi_{c}}\frac{\partial \pi_{c}}{\partial \varepsilon_{v}^{p,\pi}}\partial \varepsilon_{v}^{p,\pi} = 0 \tag{5.42}$$

The resolution of the consistency equations allows obtaining the plastic multipliers and thus the magnitude of the plastic strains.

5.7.2. Determination of the model parameters

The analysis of the experimental results presented in Section 5.5.2 allows to derive relevant information for the calibration of the model parameters. The relationship between the Oedometric modulus, the Young moduli E_1 and E_2, and the Poisson's ratios ν_1 and ν_2 for an S-sample is derived as follows:

$$E_{oed} = \frac{E_2}{1 - \frac{2\nu_2^{\,2}}{E_2}\frac{E_1}{(1-\nu_1)}} \tag{5.43}$$

The experimental evidences reported in Chapter 6 as well as in Bock (2009) suggest that the average anisotropy factor for the Young Modulus (E_1/E_2) can be assumed as equal to 2. Moreover, based on the same experimental evidences mentioned above, ν_1 is taken equal to 0.29 while ν_2 is taken equal to 0.32. Therefore the elastic coefficients can be determined using Eq. (5.43) once the Oedometric modulus is known. The wide analysis of the oedometric compression behaviour of Opalinus Clay reported in Chapter 3 allows to assume an initial value for the Oedometric modulus equal to around 1000 MPa. The adopted values for the elastic parameters are reported in Table 5-2. The failure envelope parameters ϕ'_1, ϕ'_2 and c' for Opalinus Clay have been determined through a series of triaxial tests which are presented in Chapter 6: a value of ϕ'_2 equal to 45° has been assumed for the low mean effective stress range ($p' < p'_{tr}$), while values of 22° and 2.6 MPa have been assumed for the friction angle and cohesion, respectively, in the higher mean effective stress range ($p' \geq p'_{tr}$). The remaining mechanical parameters (n_{el}, β, r_{dev}^{el} and a) are calibrated by curve fitting based on the results of the oedometric test 1 (Figure 5-7), while the remaining oedometric tests are used for blind prediction. The yield stress is derived from the analysis of the oedometric curve of test 1, through the use of

Casagrande (1936) method, which allows the estimation of the vertical effective yield stress σ'_c. The mean effective yield stress is subsequently obtained considering the K_0 coefficient, which is computed according to Jaky (1948):

$$K_0 = 1 - \sin\phi' \tag{5.44}$$

and

$$p'_c = \frac{\sigma'_c\left(1+2K_0\right)}{3} \tag{5.45}$$

A value for the mean effective yield stress equal to 9.1 MPa is obtained for test 1. However, the value of the mean effective yield stress is strictly related to the void ratio of the material in relation to the compression line. Therefore, during the simulation of the remaining five oedometric tests, the corresponding value of the mean effective yield stress have been estimated based on the initial void ratio of the tested sample and on slope of the compression line, which is identified through the compression index C_c taken equal to 0.46 (Figure 5-16). The values of the mean effective yield stress for each test are reported in Table 5-3 together with the void ratio values.

As to the model parameters related to the chemo-osmotic behaviour (γ_π, $\beta_{\pi 0}$ and A), the results of the chemo-osmotic phases of test 6 have been used for their calibrations, while the chemo-osmotic phases of the remaining tests (test 3, 4 and 5) have been used for blind prediction. The adopted model parameters are reported in Table 5-2.

Table 5-2: Chemo-mechanical model parameters.

Parameter	Unit	Value
$E_{1\,\mathrm{ref}}$	[MPa]	1030
$E_{2\,\mathrm{ref}}$	[MPa]	530
ν_1	[-]	0.29
ν_2	[-]	0.32
$G_{2\,\mathrm{ref}}$	[MPa]	200
n_{el}	[-]	0.5
β	[-]	60
ϕ'_2	[°]	45
ϕ'_1	[°]	22
c'	[MPa]	2.6
r_{dev}^{el}	[-]	0.1
a	[-]	0.003
γ_π	[-]	0.02
$\beta_{\pi 0}$	[GPa]	212
A	[GPa]	13.8

Table 5-3: Mean effective yield stress value adopted for each modelled test.

Test number	Initial void ratio [-]	Mean effective yield stress [MPa]
Test 5	0.236	4.2
Test 1	0.222	9.1
Test 2	0.221	9.3
Test 4	0.221	9.5
Test 6	0.219	10.2
Test 3	0.211	16.0

5.7.3. Numerical simulations

The simulation of test 1, test 2, test 3 and test 4 are reported in Figure 5-28, Figure 5-29 and Figure 5-30; the details of the chemo-osmotic loading steps for test 3 and 4 are reported in Figure 5-29b and Figure 5-30b, respectively. The overall mechanical behaviour of the material is well reproduced; the chemo-osmotic response is also well captured since the proposed model takes into account both the variation in the osmotic stiffness with the maximum stress level reached, as well as the irreversible nature of the chemo-osmotic settlements.

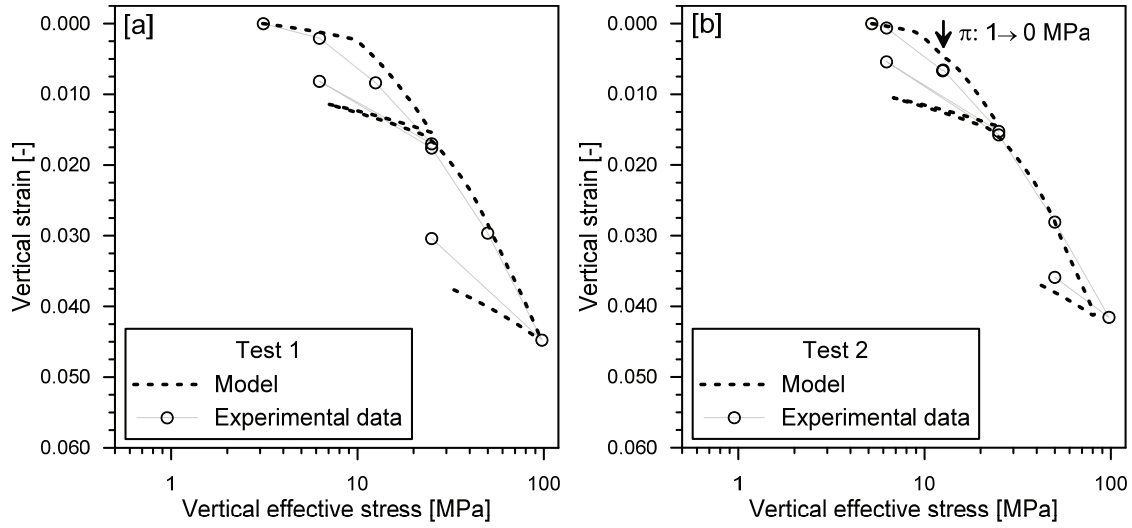

Figure 5-28: Simulation of oedometric test 1 [a] and test 2 [b]: vertical strain versus vertical effective stress [a].

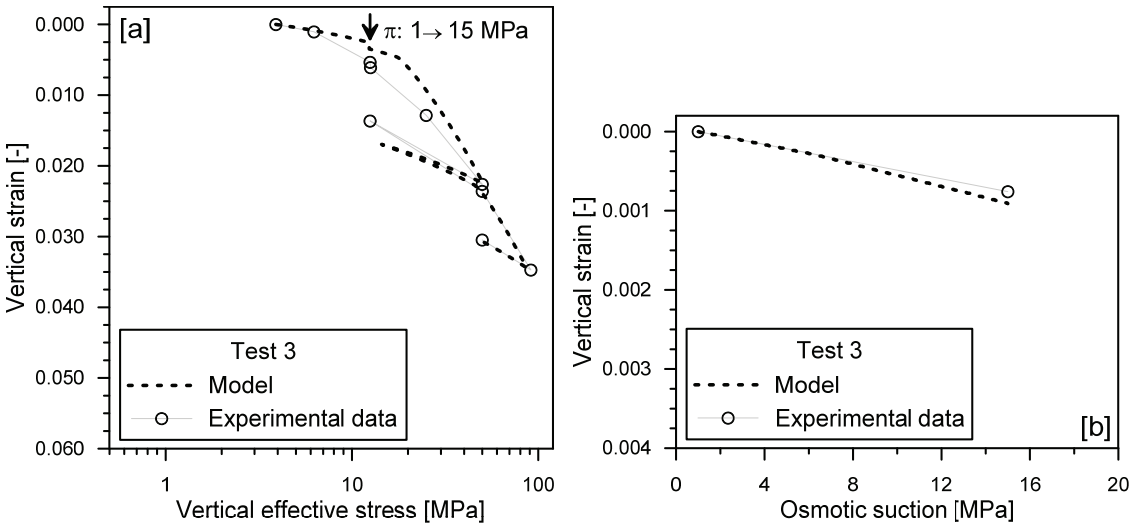

Figure 5-29: Simulation of chemo-mechanical oedometric test 3: vertical strain versus vertical effective stress [a] and osmotic suction [b].

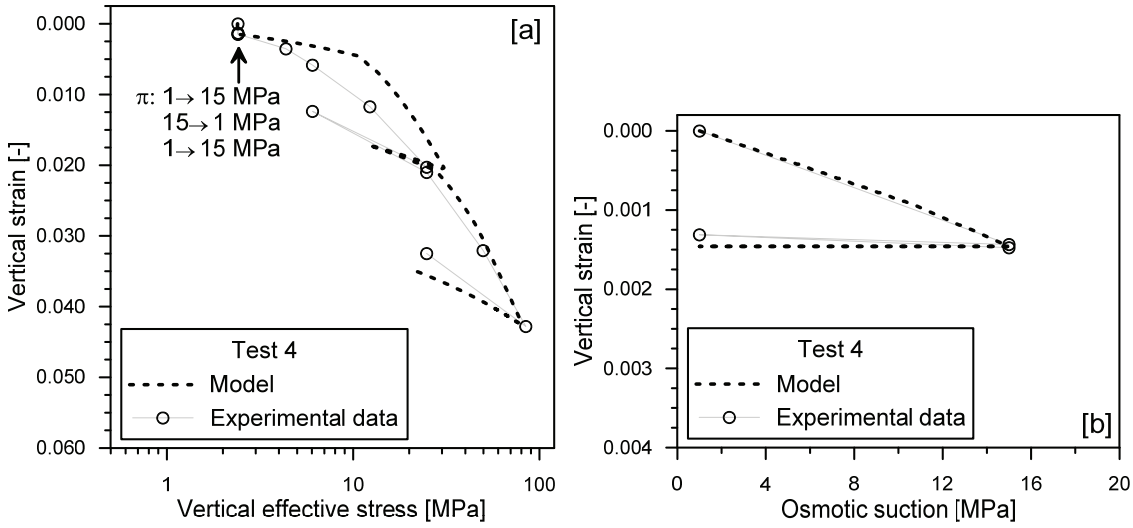

Figure 5-30: Simulation of chemo-mechanical oedometric test 4: vertical strain versus vertical effective stress [a] and osmotic suction [b].

Figure 5-31 presents the results of the simulation of test 5: the model captures well the decrease of the osmotic stiffness with the increasing yield stress, since a lower chemical settlement is predicted with respect to the one obtained in test 4.

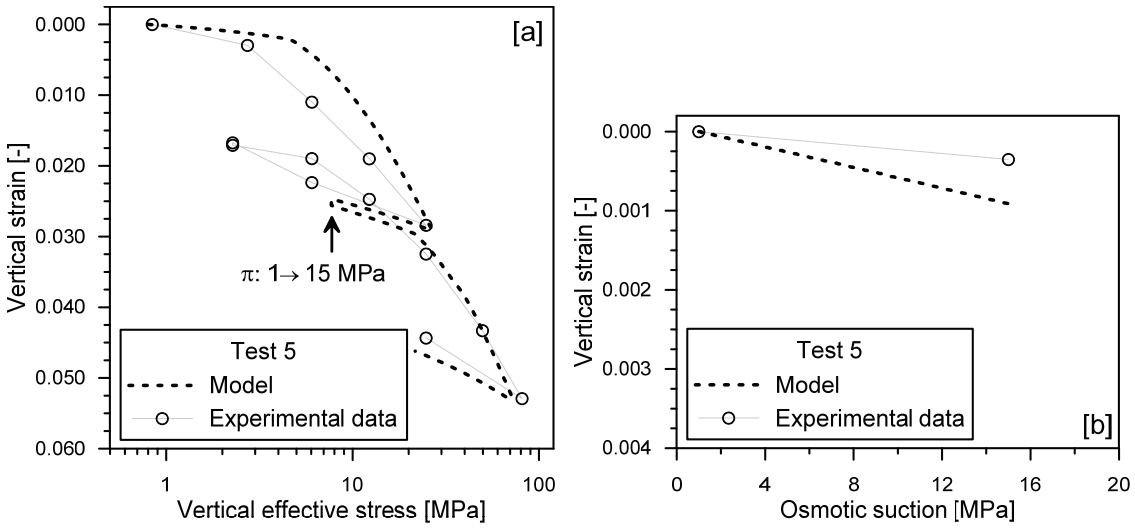

Figure 5-31: Simulation of chemo-mechanical oedometric test 5: vertical strain versus vertical effective stress [a] and osmotic suction [b].

The results of the simulation of test 6 are presented in Figure 5-32. The details of the two chemical loading phases are depicted in Figure 5-32b and Figure 5-32c: the irreversible response is reproduced well when the osmotic suction cycles are simulated (Figure 5-32b). The chemical settlement observed during the second chemical loading phase at high vertical stress (Figure 5-32c) is modelled thanks to the dependency of the mechanical yield surface on the osmotic suction: in fact, the chemo-osmotic yield surface has already evolved during the first chemical loading cycle. On the other hand, since the stress state is found on the first loading compression line when the second chemical load is applied, the decrease of the mechanical yield surface with increasing osmotic suction induces its evolution for consistency, therefore volumetric plastic strains are produced.

The framework presented in Section 5.7.1 reproduces well the chemo-mechanical behaviour of Opalinus Clay, both from a qualitative and quantitative point of view. The irreversibility of the chemo-osmotic settlements is well taken into account; moreover, the magnitude of the chemo-osmotic settlements is related to the stress history of the material, as highlighted in the experimental evidences.

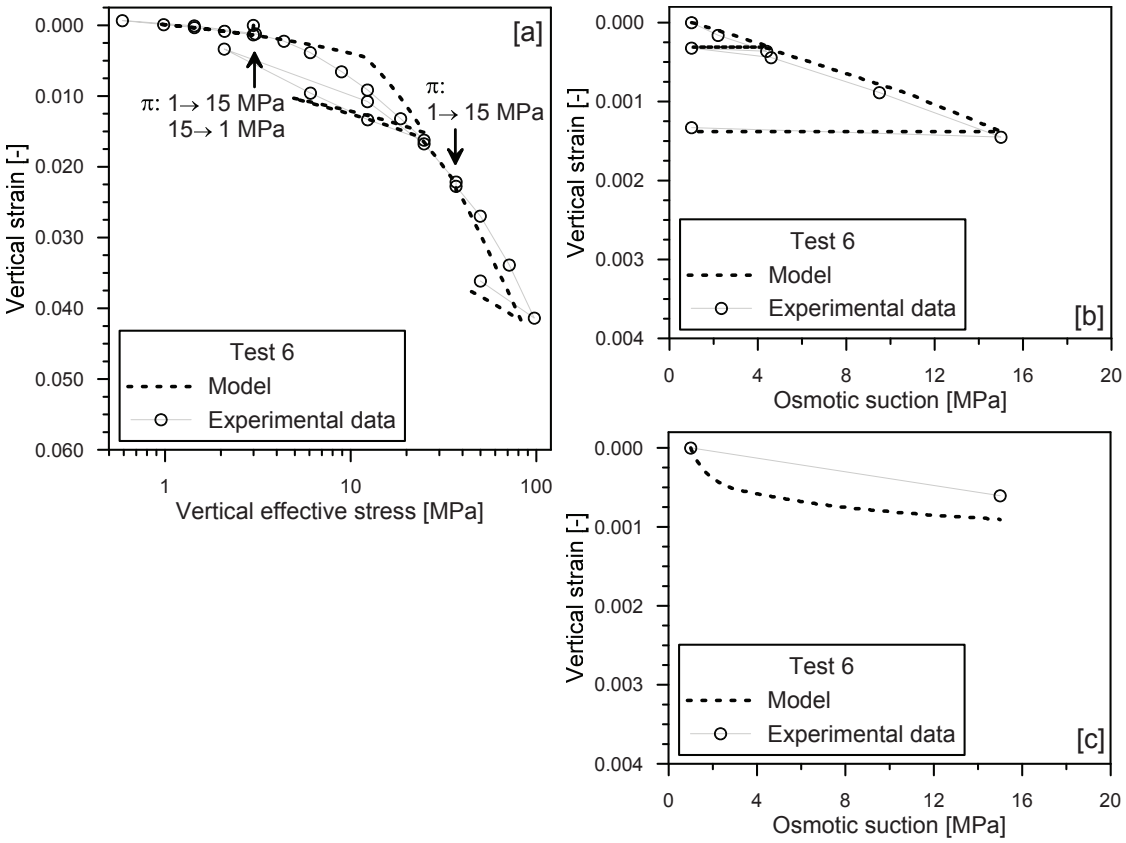

Figure 5-32: Simulation of oedometric test 6: vertical strain versus vertical effective stress [a], first cycles of osmotic suction loading at low vertical stress [b] and osmotic suction loading at high vertical stress [c].

5.8. Conclusions

An experimental investigation on the coupled chemo-mechanical behaviour of Opalinus Clay was presented in this chapter. A comprehensive testing campaign was carried out with the aim of characterizing the chemo-osmotic behaviour of Opalinus Clay under different stress conditions and mechanical loading histories, as well as to investigate the impact of osmotic suction on the swelling behaviour, mechanical properties and consolidation behaviour.

The research highlights that the swelling potential of the material decreases if the osmotic suction of the pore fluid is increased; therefore the sealing properties of the material are reduced at high osmotic suction values. The chemo-mechanical oedometric investigation reveals that the increase in osmotic suction at constant vertical effective stress leads to irreversible chemical settlements development; the magnitude of these settlements is related to the stress conditions and stress history of the material. Moreover, the results of the chemo-mechanical experimental campaign suggest that there is no significant impact of the osmotic suction on the stiffness and consolidation coefficient, for the investigated range of osmotic suction values; therefore, the hydro-mechanical performance of the shale would not be altered in a significant way.

A deep analysis of the chemical consolidation behaviour of Opalinus Clay allowed deriving the effective diffusion coefficient for the shale: the information is useful in order to estimate the time for ions diffusion processes to take place. The combined analysis of the chemical consolidation mechanism, of the MIP tests results and of the knowledge concerning chemo-osmotic affects in clays, allows to discuss possible microstructural changes during osmotic suction variations. Irreversible chemical settlements are likely to generate from the collapse of bigger pores where the contact forces among particles are lower; whereas the reversible reduction in the dominant entrance pore size is likely due to reversible double layer effects which take place in the clay matrix of the shale.

The experimental evidences collected in the presented experimental campaign widen significantly the knowledge on the coupled chemo-mechanical behaviour of shales, providing a base for a better understanding of the material performance under multiphysical conditions, and allowing possible further advances for the developments of numerical tools to reproduce and predict the coupled chemo-mechanical behaviour of shales.

A chemo-mechanical elasto-plastic framework was formulated in the last part of this chapter, in order to take into account the chemo-mechanical behavioural features of Opalinus Clay. The framework includes a dependency of the osmotic stiffness on the maximum stress level reached, as well as the possibility to reproduce irreversible chemical settlements. The framework has been calibrated and successfully applied in order to back analyse the results of the chemo-mechanical testing campaign on Opalinus Clay.

5.9. References

Al-Bazali, T., Zhang, J., Chenevert, M.E. and Sharma, M.M. Factors controlling the compressive strength and acoustic properties of shales when interacting with water-based fluids. International Journal of Rock Mechanics and Mining Sciences (2008) 45(5): 729-738.

AL-Bazali, T.M. The consequences of using concentrated salt solutions for mitigating wellbore instability in shales. Journal of Petroleum Science and Engineering (2011) 80(1): 94-101.

Barbour, S. and Fredlund, D. Mechanisms of osmotic flow and volume change in clay soils. Canadian geotechnical journal (1989) 26(4): 551-562.

Bock, H. RA Experiment: Updated Review of the Rock Mechanics Properties of the Opalinus Clay of the Mont Terri URL based on Laboratory and Field Testing. TECHNICAL REPORT 2008-04 (2009).

Bossart, P. (2012). Characteristics of the Opalinus Clay at Mont Terri. http://www.mont-terri.ch/internet/mont-terri/de/home/geology/key_characteristics.html.

Bunger, A.P., Sarout, J., Kear, J., Delle Piane, C., Detournay, E., Josh, M. and Dewhurst, D.N. Experimental chemoporoelastic characterization of shale using millimeter-scale specimens. Journal of Petroleum Science and Engineering (2014) 118: 40-51.

Casagrande, A. The determination of the pre-consolidation load and its practical significance. Proceedings of the international conference on soil mechanics and foundation engineering, Harvard University Cambridge, (1936). 60-64.

Castellanos, E., Villar, M., Romero, E., Lloret, A. and Gens, A. Chemical impact on the hydro-mechanical behaviour of high-density febex bentonite. Physics and Chemistry of the Earth, Parts A/B/C (2008) 33: S516-S526.

Chen, J., Anandarajah, A. and Inyang, H. Pore fluid properties and compressibility of kaolinite. Journal of Geotechnical and Geoenvironmental Engineering (2000) 126(9): 798-807.

Dafalias, Y. and Popov, E. A model of nonlinearly hardening materials for complex loading. Acta mechanica (1975) 21(3): 173-192.

Dafalias, Y.F. and Popov, E.P. Cyclic loading for materials with a vanishing elastic region. Nuclear Engineering and Design (1977) 41(2): 293-302.

Di Maio, C. Exposure of bentonite to salt solution: osmotic and mechanical effects. Geotechnique (1996) 46(4): 695-707.

Di Maio, C. Exposure of bentonite to salt solution: osmotic and mechanical effects. Geotechnique (1998) 48: 433-436.

Di Maio, C. and Fenelli, G. Residual strength of kaolin and bentonite: the influence of their constituent pore fluid. Geotechnique (1994) 44(2): 217-226.

Di Maio, C. and Fenelli, G. Clayey soil deformability: the influence of physico-chemical interactions. Ital. Geotechnical J (1997) 1: 43-54.

Di Maio, C., Santoli, L. and Schiavone, P. Volume change behaviour of clays: the influence of mineral composition, pore fluid composition and stress state. Mechanics of Materials (2004) 36(5): 435-451.

Ewy, R.T. Shale swelling/shrinkage and water content change due to imposed suction and due to direct brine contact. Acta Geotechnica (2014) 9(5): 869-886.

Ewy, R.T. Shale/claystone response to air and liquid exposure, and implications for handling, sampling and testing. International Journal of Rock Mechanics and Mining Sciences (2015) 80: 388-401.

François, B. and Laloui, L. ACMEG-TS: A constitutive model for unsaturated soils under non-isothermal conditions. International Journal for Numerical and Analytical Methods in Geomechanics (2008) 32(16): 1955-1988.

Fritz, S.J. Ideality of clay membranes in osmotic processes: a review. Clays and Clay Minerals (1986) 34(2): 214-223.

Gajo, A. and Loret, B. Finite element simulations of chemo-mechanical coupling in elastic–plastic homoionic expansive clays. Computer Methods in Applied Mechanics and Engineering (2003) 192(31): 3489-3530.

Gajo, A., Loret, B. and Hueckel, T. Electro-chemo-mechanical couplings in saturated porous media: elastic–plastic behaviour of heteroionic expansive clays. International journal of solids and structures (2002) 39(16): 4327-4362.

Gascoyne, M., Davison, C.C., Ross, J. and Pearson, R. (1987). Saline groundwaters and brines in plutons in the Canadian Shield. Saline Water and Gases in Crystalline Rocks, Geol. Assoc. Can. 33**:** 53-68.

Gens, A. Soil–environment interactions in geotechnical engineering. Geotechnique (2010) 60(1): 3-74.

Guimarães, L.d.N., Gens, A. and Olivella, S. Coupled thermo-hydro-mechanical and chemical analysis of expansive clay subjected to heating and hydration. Transport in Porous Media (2007) 66(3): 341-372.

Guimarães, L.D.N., Gens, A., Sanchez, M. and Olivella, S. A chemo-mechanical constitutive model accounting for cation exchange in expansive clays. Geotechnique (2013) 63(3): 221-234.

Horseman, S., Harrington, J. and Noy, D. Swelling and osmotic flow in a potential host rock. Physics and Chemistry of the Earth, Parts A/B/C (2007) 32(1): 408-420.

Horseman, S., Higgo, J., Alexander, J. and Harrington, J. Water, gas and solute movement through argillaceous media. Nuclear Energy Agency Rep. CC-96/1. OECD, Paris (1996).

Houben, M., Desbois, G. and Urai, J. Pore morphology and distribution in the Shaly facies of Opalinus Clay (Mont Terri, Switzerland): insights from representative 2D BIB–SEM investigations on mm to nm scale. Applied Clay Science (2013) 71: 82-97.

Jaky, J. Pressure in soils. Proceedings of the 2nd international conference on soil mechanics and foundation engineering, (1948). 103-107.

Kaczmarek, M. and Hueckel, T. Chemo-mechanical consolidation of clays: analytical solutions for a linearized one-dimensional problem. Transport in Porous Media (1998) 32(1): 49-74.

Keller, L.M., Schuetz, P., Erni, R., Rossell, M.D., Lucas, F., Gasser, P. and Holzer, L. Characterization of multi-scale microstructural features in Opalinus Clay. Microporous and mesoporous materials (2013) 170: 83-94.

Krieg, R. A practical two surface plasticity theory. Journal of applied mechanics (1975) 42(3): 641-646.

Kwon, O., Kronenberg, A.K., Gangi, A.F. and Johnson, B. Permeability of Wilcox shale and its effective pressure law. Journal of Geophysical Research: Solid Earth (1978–2012) (2001) 106(B9): 19339-19353.

Laird, D.A. Influence of layer charge on swelling of smectites. Applied Clay Science (2006) 34(1): 74-87.

Loret, B., Hueckel, T. and Gajo, A. Chemo-mechanical coupling in saturated porous media: elastic–plastic behaviour of homoionic expansive clays. International journal of solids and structures (2002) 39(10): 2773-2806.

Manca, D., Ferrari, A. and Laloui, L. Fabric evolution and the related swelling behaviour of a sand/bentonite mixture upon hydro-chemo-mechanical loadings. Geotechnique (2015) 66(1): 41-57.

Marine, I.W. and Fritz, S.J. Osmotic model to explain anomalous hydraulic heads. Water Resources Research (1981) 17(1): 73-82.

Mitchell, J. and Soga, K. Fundamentals of soil behavior." John Wiley and Sons, Inc., Hoboken, NJ. (2005).

Mokni, N., Romero, E. and Olivella, S. Chemo-hydro-mechanical behaviour of compacted Boom Clay: joint effects of osmotic and matric suctions. Geotechnique (2014) 64(9): 681-693.

Musso, G., Morales, E.R., Gens, A. and Castellanos, E. The role of structure in the chemically induced deformations of FEBEX bentonite. Applied Clay Science (2003) 23(1): 229-237.

Nova, R. and Wood, D.M. A constitutive model for sand in triaxial compression. International Journal for Numerical and Analytical Methods in Geomechanics (1979) 3(3): 255-278.

Pearson, F. (1998). Opalinus clay experimental water: A1 Type, Version 980318. PSI Internal report TM-44-98-07. V. P. Paul Scherrer Institut, Switzerland.

Peters, G.P. and Smith, D.W. The influence of advective transport on coupled chemical and mechanical consolidation of clays. Mechanics of Materials (2004) 36(5): 467-486.

Quirk, J., Pereira, C. and Tanton, T. Soil permeability in relation to sodicity and salinity [and discussion]. Philosophical Transactions of the Royal Society of London A: Mathematical, Physical and Engineering Sciences (1986) 316(1537): 297-317.

Sarout, J. and Detournay, E. Chemoporoelastic analysis and experimental validation of the pore pressure transmission test for reactive shales. International Journal of Rock Mechanics and Mining Sciences (2011) 48(5): 759-772.

Seiphoori, A., Ferrari, A. and Laloui, L. Water retention behaviour and microstructural evolution of MX-80 bentonite during wetting and drying cycles. Geotechnique (2014) 64(9): 721-734.

Siddiqua, S., Blatz, J. and Siemens, G. Evaluation of the impact of pore fluid chemistry on the hydromechanical behaviour of clay-based sealing materials. Canadian geotechnical journal (2011) 48(2): 199-213.

Soler, J.M. The effect of coupled transport phenomena in the Opalinus Clay and implications for radionuclide transport. Journal of Contaminant Hydrology (2001) 53(1): 63-84.

Sridharan, A. and Rao, G.V. Shear strength behaviour of saturated clays and the role of the effective stress concept. Geotechnique (1979) 29(2): 177-193.

Sridharan, A. and Rao, G.V. Mechanisms controlling volume change of saturated clays and the role of the effective stress concept. Geotechnique (1973) 23(3): 359-382.

Tarantino, A., Romero, E. and Cui, Y.J. Laboratory and field testing of unsaturated soils, Springer, (2009).

Van Oort, E. On the physical and chemical stability of shales. Journal of Petroleum Science and Engineering (2003) 38(3): 213-235.

Wahid, A., Gajo, A. and Di Maggio, R. Chemo-mechanical effects in kaolinite. Part 2: exposed samples and chemical and phase analyses. Geotechnique (2010) 61(6): 449-457.

Wakim, J., Hadj-Hassen, F. and De Windt, L. Effect of aqueous solution chemistry on the swelling and shrinkage of the Tournemire shale. International Journal of Rock Mechanics and Mining Sciences (2009) 46(8): 1378-1382.

Witteveen, P., Ferrari, A. and Laloui, L. An experimental and constitutive investigation on the chemo-mechanical behaviour of a clay. Geotechnique (2013) 63(3): 244-255.

Yukselen-Aksoy, Y., Kaya, A. and Ören, A.H. Seawater effect on consistency limits and compressibility characteristics of clays. Engineering Geology (2008) 102(1): 54-61.

Chapter 6
Triaxial testing of Opalinus Clay

6.1. Foreword

This chapter is dedicated to the analysis of the stiffness and strength behaviour of Opalinus Clay, taking into account the anisotropic features of this shale. The laboratory program consists in consolidated and drained (CD) triaxial tests (single stage and multistage) on Opalinus Clay specimens from the Mont Terri URL. The anisotropic behaviour of the shale is investigated by testing both P-samples (where the vertical load is applied parallel to the bedding planes) and S-samples (where the vertical load is applied perpendicular to the bedding planes). Particular attention is paid to the control of the testing conditions in order to ensure saturation and consolidated conditions, as well as to the correct selection of the strain rate for the application of the axial strain during triaxial testing.

6.2. Tested material

The tested specimens were obtained from the Opalinus Clay cores BFE-B019, BFE-B022 and BDR-B7, the index properties of the tested cores are reported in Chapter 1. Cores BFE-B019 and BFE-B022 were used in order to obtain P-samples, while core BDR-B7 was used to prepare the S-samples. The tested specimens are 50 mm in diameter and 100 mm in height. The complete list of tested specimens and the corresponding confining effective stress (defined as total stress minus pore water pressure), at which the shear phase is carried out, are reported in Table 6-1.

Table 6-1: List of tested specimens.

Name	Test type	Orientation	Confining effective stress [MPa]
P-1	Single stage	P-sample	5 MPa
P-2	Multistage	P-sample	2 - 5 - 10 MPa
S-1	Single stage	S-sample	2 MPa
S-2	Single stage	S-sample	5 MPa
S-3	Single stage	S-sample	12 MPa

The specimens are prepared shortly before initiating the test: a slice of about 110 mm is cut from the original core, the packaging is subsequently removed and the sample is placed in a lathe which is used to progressively reduce the diameter of the specimen to the desired value. The lathe is used also to obtain smooth and parallel top and bottom bases. No water, air or any other fluid was used during the cutting phase in order to preserve the original water content and reduce the disturbance of the material as much as possible. A small piece of material coming from the trimmings of the specimen is used to measure the initial water content of the specimen. The specimen is then immediately inserted into the testing device. The initial characteristics of the tested specimens are reported in Table 6-2.

Table 6-2: Initial characteristics of the tested specimens

Core	ρ (Mg/m^3)	w (%)	e (-)	S_r (%)
P-1	2.41	6.7	0.20	85
P-2	2.40	6.0	0.23	72
S-1	2.43	4.2	0.19	60
S-2	2.42	6.6	0.20	90
S-3	2.42	7.4	0.21	97

6.3. Testing device and experimental procedure

6.3.1. The high-pressure triaxial cell

The triaxial tests are carried out using a high-pressure triaxial system which is described in detail in Seiphoori et al. (2011). However, while in Seiphoori et al. (2011) an inner-cell was used in order to measure the volume change of the specimen from the inflow/outflow, in the current configuration the inner-cell has been removed in order to accommodate a circumferential linear variable differential transformer (LVDT) for direct measurement of the circumferential displacement of the specimen. The layout of the triaxial cell is presented in Figure 6-1, and the description of the device is briefly recalled here. The cell holds specimens 100 mm high and 50 mm in diameter. Two compressed steel porous plates are disposed at the top and bottom bases of the specimen in order to ensure a uniform distribution of the pore water pressure. The specimen is inserted into a neoprene membrane in order to prevent the contact with the confining fluid. The axial load is applied by controlling the pressure in a hydraulic press by means of a pressure controller; the maximum applicable force is 450 kN which corresponds to an axial total stress of 230 MPa. Axial compression can be applied either in load-controlled mode or in displacement-controlled mode. The confinement is applied through a confining fluid (mineral oil), whose pressure is controlled by a pressure/volume controller (PVC – resolution of 1 kPa): the confining pressure can reach values up to 30 MPa. Two pressure/volume controllers are used to separately control the pore water pressure at the top and bottom bases of the specimen: the maximum applicable pore water pressure at the top base is 6 MPa, while the maximum applicable pore water pressure at the bottom base is 10 MPa. The independent control of the pore water pressure at the two extremes of the specimen allows running constant head permeability tests by applying a hydraulic gradient along the specimen. The vertical displacement is measured by an external LVDT which monitors the displacement of the loading piston at the bottom of the cell with a resolution of 1 μm. As anticipated above, the circumferential displacement of the specimen is measured by a circumferential LVDT (resolution of 1 μm) mounted with a spring-chain system at the mid-height of the specimen. The measurement of the circumferential and vertical displacements allows to compute the axial strain (ε_a) and radial strain (ε_r), and therefore the volumetric deformation of the specimen is obtained as $\varepsilon = \varepsilon_a + 2\varepsilon_r$.

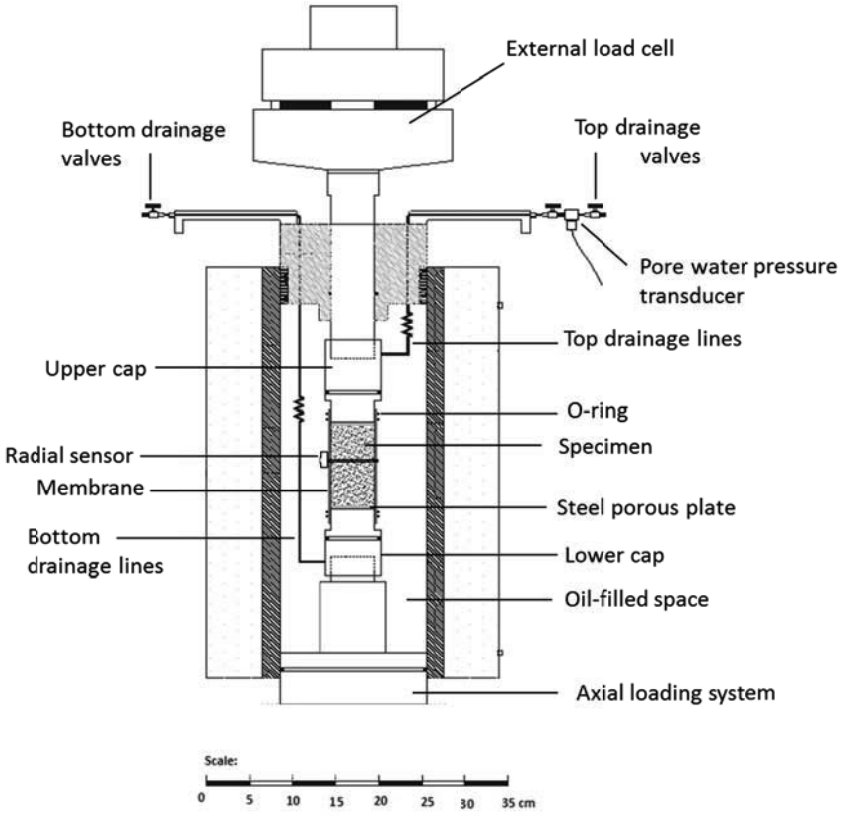

Figure 6-1: Layout of the triaxial cell (modified from Seiphoori et al. (2011)).

Careful calibration is carried out in order to take into account the compressibility of the testing device and to obtain the correct stress-strain behaviour of the tested specimen. To this aim, the compressibility of each involved component of the cell has been assessed. Once the response of the cell components to an applied load was quantified, the measurements of the vertical displacement were corrected as follows:

$$\delta\rho_{sp} = \delta\rho_{measured} - \delta\rho_{top} - \delta\rho_{bottom} - \delta\rho_{plates} \tag{6.1}$$

where $\delta\rho_{sp}$ is the displacement of the specimen, $\delta\rho_{measured}$ is the measured displacement by the LVDT, $\delta\rho_{top}$ is the displacement of the cell components above the specimen, $\delta\rho_{bottom}$ is the displacement of the cell components below the specimen and $\delta\rho_{plates}$ is the contribution of the two porous plates. The calibration was subsequently validated using a porous PVC (Polyvinyl Chloride) specimen whose mechanical properties are known. The PVC specimen was placed inside the triaxial cell and axially loaded up to 45kN. The measured displacements were corrected in light of the compressibility of the cell components: a good reproduction of the mechanical response of the PVC specimen was obtained as shown in Figure 6-2, thus validating the performed calibration and highlighting the negligible effect of the piston friction, as already observed in Seiphoori (2014).

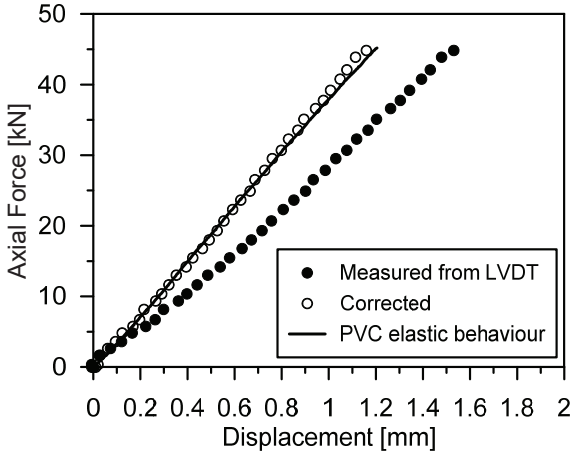

Figure 6-2: Validation of the triaxial cell calibration procedure with a PVC specimen.

High-pressure valves are placed at the inlets and outlets of the internal top and bottom drainage lines in order to isolate the internal drainage system (bottom and top caps, steel tubes and porous plates) from the external one (external tubes and PV controllers). A pore water pressure transducer is mounted between the outlet of the top drainage lines and the high-pressure valve, and it is used to measure the pore water pressure response during B-check tests. The maximum measurable pore water pressure by the transducer is 16 MPa, with a resolution of 1 kPa. The dead volume of water inside the internal drainage system was quantified in order to assess its impact on the undrained response of the material during B-check tests. In fact, it is recognised that the pore fluid compressibility have a relevant influence on the measurement of the real pore pressure response in stiff geomaterials that are subjected to undrained loading (e.g. Bishop, 1976; Mesri et al., 1976; Ghabezloo and Sulem, 2010). The total dead volume of water in the internal drainage system is equal to about 22 cm^3.

6.3.2. Experimental procedures

An overview of the stress path for the multistage triaxial testing is provided in Figure 6-3; the stress path for the single stage triaxial test is analogous except for the fact that only one consolidation phase and one shearing phase are carried out. The following sections describe in detail the different phases of the testing procedure. Both single stage and multistage triaxial tests comprise four main phases:

1- Saturation

2- B-check test

3- Isotropic consolidation

4- Drained shear

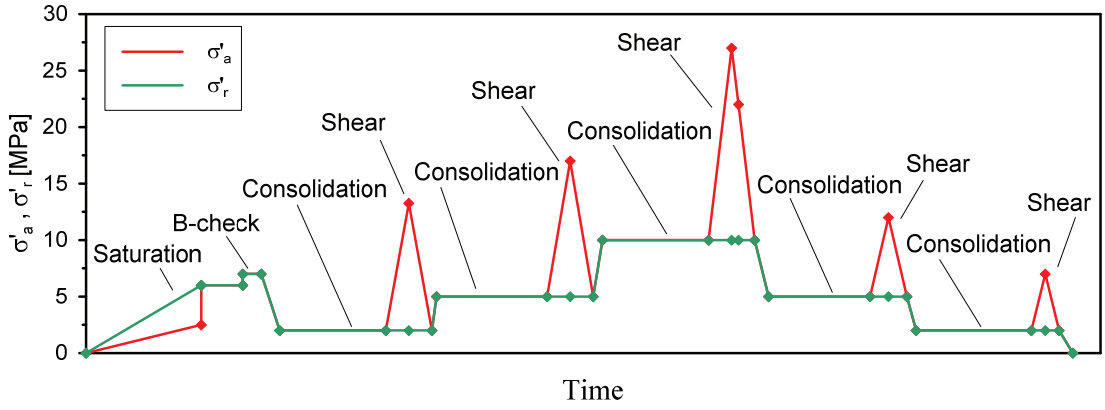

Figure 6-3: Stress path for the multistage triaxial test (P-Sample).

When the multistage triaxial test is carried out, steps 3 and 4 have been repeated 5 times to measure peak and ultimate strength of the material at the three different selected confining pressure values. The four phases are described in details below.

6.3.2.1. Saturation

The saturation phase is carried out in constant volume conditions: the specimen is put in contact with distilled and de-aired water at initially low values of pore water pressures (few tents of kPa), while vertical and confining stresses are raised as soon as some swelling is detected. Subsequently, the saturation is enhanced by raising the pore water pressure in the range of about 1-2.5 MPa and imposing a differential pore water pressure at the two extremes of the specimen. The material is thus flushed in the upward direction and the inflow and outflow volumes are monitored. The procedure is continued until no more swelling is detected and the outflow approaches the inflow. The adopted procedure allows avoiding any damage due to the material swelling during re-saturation.

6.3.2.2. B-check phase

The achievement of saturated conditions is subsequently ensured through the performance of a B-check test. The B-check test consists in measuring the B-Skempton pore water pressure coefficient (Skempton, 1954), which is defined as the ratio of the pore water pressure variation to the mean total stress variation when isotropic compression is carried out in undrained conditions. For saturated soils the B value is equal or very close to unity, while for stiff geomaterials, such as shales, this coefficient may assume values lower than 1 at saturation. This is due to the fact that the compressibility of the solid skeleton is comparable to the compressibility of the pore water and of the solid particles. When saturation is not fully achieved, the measured B value increases with increasing back pressure. This is due to the increasing degree of saturation and decreasing compressibility of the pore fluid as the back pressure is increased (Wissa, 1969). Undrained conditions are imposed by closing the valves at the inlet and outlet of the cell drainage lines, total stress is increased isotropically and the pore water pressure response is registered thanks to the presence of the pressure transducer. A mean total stress increment of 0.4 MPa has been selected for all the B-check tests. The procedure is repeated at

different values of back pressure after the re-establishment of drained conditions in between each undrained loading, and the B coefficient is computed for each step. The procedure is carried out until a constant or slightly decreasing value of B is obtained with increasing back pressure values: if the B coefficient remains constant or manifests a small decrease, saturated conditions can be considered achieved (Wissa, 1969).

6.3.2.3. Isotropic consolidation phase

After B-check is accomplished, drained conditions are re-established; subsequently, the specimen is isotropically loaded or unloaded to the desire confining pressure and enough time is allowed for ensuring the dissipation of the generated excess pore water pressures (primary consolidation). A constant back pressure of 3 MPa is maintained throughout the consolidation and shear phases of the tests. Different methodologies are adopted between P and S samples in order to carry out the isotropic consolidation: P-samples are isotropically compressed and enough time is allowed for the complete development of the volume change vs time curve, which includes not only the primary consolidation phase but also the secondary compression phase. The time t_{100} (time at the end of the primary consolidation phase) can thus be graphically determined from the plot of the volumetric strain vs square root of time, and the coefficient of consolidation can be computed (Head, 1992):

$$c_v = \frac{\pi d^2}{\lambda_d t_{100}} \tag{6.2}$$

where d is the diameter of the specimen and λ_d is a coefficient related to the drainage conditions and equal to 4 for drainage at the top and bottom bases of the specimen. The coefficient of consolidation is useful not only for the characterization of the anisotropic hydro-mechanical properties of the material, but also for the computation of the strain rate to be used during the shear phase.

The consolidation behaviour of S-samples has been widely studied in Chapter 3. The coefficient of consolidation presents values greater than 0.004 mm^2/s for effective stress values below 20 MPa. As a consequence, this value is adopted to compute the time required for the primary consolidation to take place, as well as for the estimation of the strain rate to be used during the shear phase.

6.3.2.4. Shear phase

The shear phase is carried out in drained conditions by applying a vertical strain rate and maintaining constant radial stress and constant pore water pressure. The strain rate is computed according to Renner et al. (2000), who observed from experiments on rock samples that the strain rate at which the internal fluid pressure is maintained constant can be expressed as:

$$\dot{\varepsilon}_a = \frac{\Delta\varepsilon_a}{H^2} c_v \tag{6.3}$$

where c_v is the coefficient of consolidation and H is the drainage path length. As to the axial strain increment $\Delta\varepsilon_a$, Renner et al. (2000) suggests the adoption of values between 0.1% and 1% for brittle

failure and semi-brittle failure, respectively. Opalinus Clay manifests a semi-brittle behaviour during compression (Corkum and Martin, 2007; Siegesmund et al., 2014) with accumulation of plastic strains. However, the material rheology highlights different behaviours between S and P samples: S-samples produce greater elasto-plastic strains upon compression with respect to P-samples. Therefore, the latter can be considered more semi-brittle than the former. For this reason, $\Delta\varepsilon_a$ is fixed to 1% for S-samples, and to 0.5% for P-samples.

The consolidation curves for the P-samples (presented further in Section 6.4.2) allow to derive values of the coefficient of consolidation between 0.011-0.013 mm^2/s, revealing that a faster consolidation occurs with respect to S-samples (coefficient of consolidation greater than 0.004 mm^2/s). Taking into account the mentioned values for the coefficient of consolidation and $\Delta\varepsilon_a$, Eq.(6.3) allows computing strain rates between $2x10^{-8}$ s^{-1} and $3x10^{-8}$ s^{-1}. For all the tests a strain rate of $3x10^{-8}$ s^{-1} was adopted. The respect of the drainage conditions was further tested during the shear phase by halting the shearing process, possibly close to the peak strength, and by allowing several hours before continuing with shearing the specimen: no gain of resistance (which would be caused by further dissipation of residual excess pore water pressures) was observed during the continuation of the shearing phase, meaning that the drained conditions could be considered as respected.

6.4. Results

6.4.1. B-check tests results

The measured B values as a function of the applied back pressure are reported in Figure 6-4 for the P-samples and in Figure 6-5 for the S-samples. The detailed behaviour in terms of total stress and pore water pressure evolution in time is depicted and analysed in Appendix D for all the tested specimens.

The B-check test on specimen P-1 was carried out at an initial mean effective stress value equal to 3 MPa and an initial pore water pressure of 1.25 MPa (Figure 6-4a). An initial increase of the measured B value with increasing back pressure reveals that the specimen was not fully saturated; saturated conditions are achieved at back pressures greater than 2 MPa since the measured B coefficient did not increase further. The B-check test on specimen P-2 was carried out at an initial mean effective stress value equal to 7 MPa and an initial pore water pressure of 2.0 MPa (Figure 6-4b). Undrained conditions were imposed and the mean total stress was increased in steps of 0.4 MPa while the response of the pore water pressure was recorded at each step. The value of the measured B coefficient did not increase further showing that saturation was achieved at a back pressure of 2 MPa.

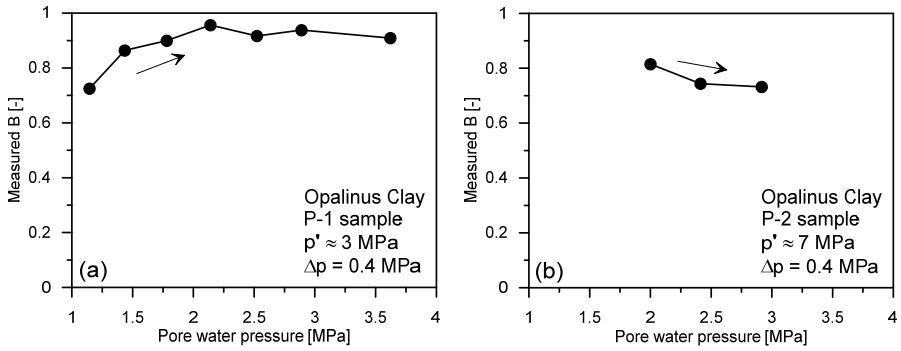

Figure 6-4: Measured B coefficient as a function of the back pressure for P-samples.

The B-check test on specimen S-1 was carried out at an initial mean effective stress value equal to 10 MPa and an initial pore water pressure of 2.0 MPa (Figure 6-5a), specimen S-2 was carried out at an initial mean effective stress value equal to 7 MPa and an initial pore water pressure of 2.5 MPa (Figure 6-5b), while specimen S-3 was carried out at an initial mean effective stress value equal to 12 MPa and an initial pore water pressure of 2.0 MPa (Figure 6-5c). Greater back pressure values appear to be necessary for S-samples with respect to P-samples in order to observe a certain stabilization of the B-values. Saturated conditions are considered achieved at back pressure values between 2.5 and 3.5 MPa.

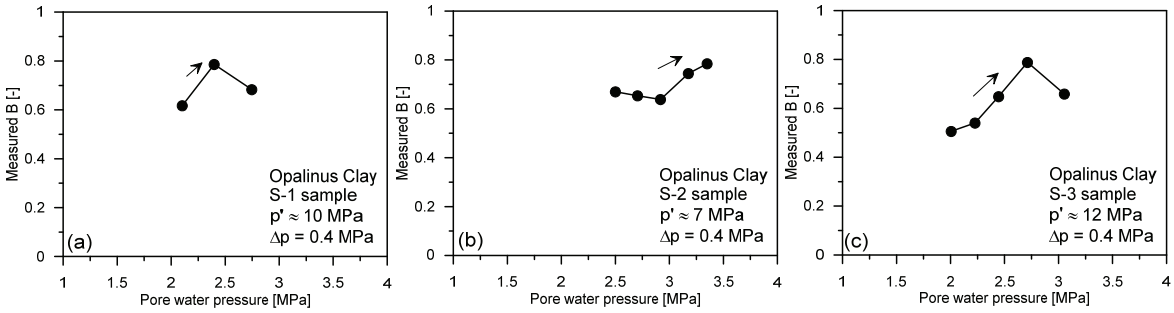

Figure 6-5: Measured B coefficient as a function of the back pressure for S-samples.

The performance of B-check tests at different values of mean effective stress allows deriving information on the dependency of the B coefficient on the stress conditions. The values of the B coefficient at saturation are plotted as a function of the mean effective stress in Figure 6-6 for both P and S samples. The B values clearly tend to decrease as the mean effective stress increases. This is a typical behaviour of stiff geomaterials, for whom the poroelastic properties play a significant role, as largely observed in literature (e.g. Cook, 1999; Gutierrez et al., 2014; Wild et al., 2015).

As previously mentioned, the measurement of the pore pressure response in undrained conditions is affected by the compressibility of the system. Wissa (1969) and Bishop (1976) proposed an expression for computing the corrected value of coefficient B taking into account the compressibility of the pore fluid dead volume and the compressibility of the system (tubing and transducers). However, thanks to the development of modern testing apparatuses, Ghabezloo and Sulem (2010)

proved that the impact of the compressibility of the system can be considered negligible, and modified the formulation for computing the corrected B values as follows:

$$B_{correct} = \frac{1}{\left(1/B_{obs}\right) - \frac{V_L}{V}\frac{K}{K_f\left(1-\frac{K}{K_s}\right)}} \tag{6.4}$$

where B_{obs} is the measured B value, $B_{correct}$ is the corrected B value, V_L is the dead volume of the pore fluid, V is the volume of the specimen, K is the bulk modulus, K_f is the bulk modulus of the pore fluid, and K_s is the bulk modulus of the solid phase. The bulk modulus of the solid phase (K_s) for OPA-shallow is taken equal to 14 GPa (see Chapter 3); K_f is taken as the bulk modulus of water, equal to 2.2 GPa; K is derived either from the isotropic compression results or it is computed from the bulk modulus of the solid phase assuming a value of the Biot coefficient according to the analysis conducted in Chapter 3 ($\alpha \approx 0.9$). The assumption of this formulation for the correction of the measured B values and neglecting the correction due to the system compressibility is justified by the fact that the tubes and sensors are mainly made of stainless steel and thus have negligible compressibility.

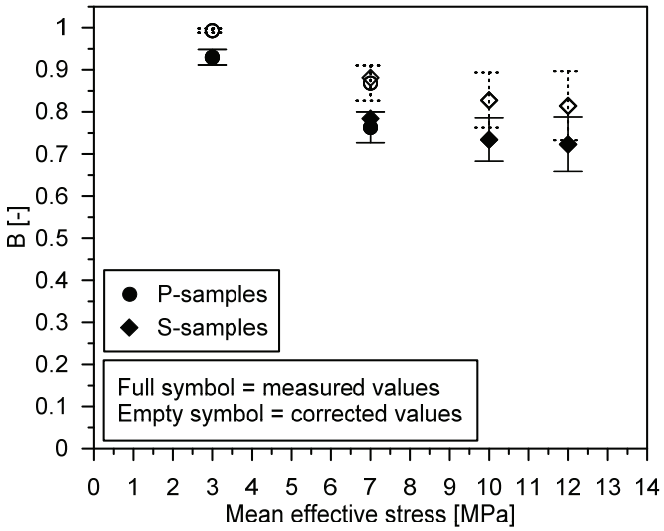

Figure 6-6: Measured and corrected values of the B coefficient as a function of the mean effective stress for the tested specimens.

6.4.2. Consolidation phases results

The isotropic consolidation of specimen P-1 was performed at a mean effective stress of 5 MPa and a back pressure value of 3 MPa. For some reasons, during the testing of specimen P-1 the radial sensor was not working, therefore the consolidation process was assessed only from the vertical settlement. The evolution of the vertical deformation versus square root of time for specimen P-1 is reported in

Figure 6-7. The time at which theoretical 100% consolidation is achieved (t_{100}) was estimated using a graphical construction (Head, 1992): the axial strain is plotted against the square-root of time; the line intercepting the initial linear portion of the graph is extended until intersecting the horizontal line representing the final part of the curve as shown in Figure 6-7. The t_{100} is the time corresponding to this intersection point, and was equal to 43 h for P-1 specimen, corresponding to a coefficient of consolidation c_v equal to 0.013 mm^2/s.

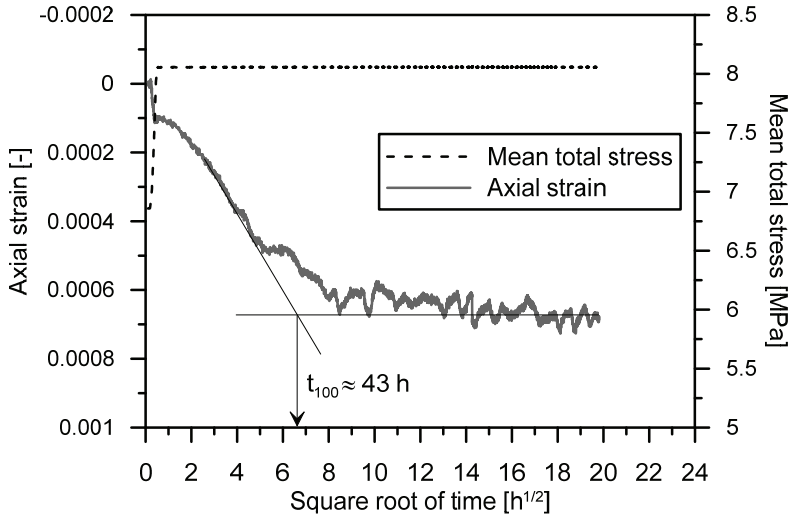

Figure 6-7: Consolidation phase at p' = 5 MPa for specimen P-1.

Since specimen P-2 was subjected to a multistage triaxial test, three different isotropic consolidation phases at different mean effective stress were carried out prior to each deviatoric loading stage. In particular, the isotropic consolidation of specimen P-2 was performed at mean effective stress values of 2 MPa, 5 MPa and 10 MPa with pore water pressure equal to 3 MPa.

Since the isotropic mean effective stress after the B-check phase was equal to 7 MPa, the specimen was unloaded to 2 MPa and swelling was obtained. The swelling appeared to require significant amount of time for equilibration with respect to the consolidation behaviour of P-1 specimen; equilibration was considered achieved when a strain rate of 0.03% volumetric strain/day was reached (Figure 6-8). This first isotropic unloading step required about two weeks to be completed.

The results of the second isotropic compression stage of specimen P-2 at a mean effective stress of 5 MPa are reported in Figure 6-9. The t_{100} at 5 MPa was found to be equal to the one derived from the consolidation curve of specimen P-1 (43 hours) for the same mean effective stress, thus increasing the confidence in the result. The coefficient of consolidation results again equal to 0.013 mm^2/s, since the dimensions of the specimen did not differ significantly.

The results of the third isotropic compression stage of specimen P-2 at a mean effective stress of 10 MPa are reported in Figure 6-10. The t_{100} was derived as described above and is equal to 51.5 h. The coefficient of consolidation computed according to Eq.(6.2) is equal to 0.011 mm^2/s.

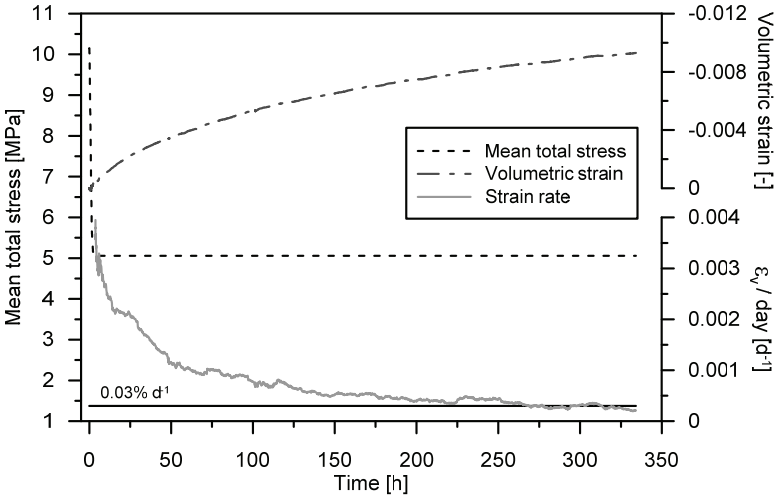

Figure 6-8: Unloading phase at p' = 2 MPa for specimen P-2.

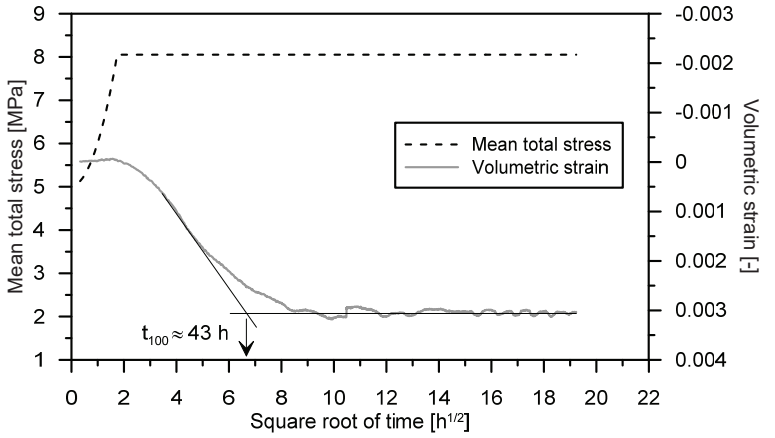

Figure 6-9: Consolidation phase at p' = 5 MPa for specimen P-2.

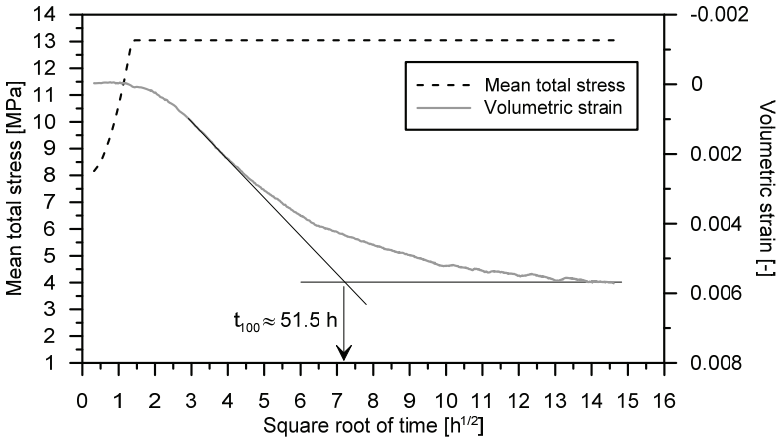

Figure 6-10: Consolidation phase at p' = 10 MPa for specimen P-2.

The isotropic unloading steps, which are carried out before the determination of the residual strength at 5 MPa and at 2 MPa of mean effective stress, are performed taking into account the same criterion that was adopted during the first unloading step at 2 MPa (equilibration was considered achieved when a strain rate of 0.03% days^{-1} was reached). However, at this stage, the specimen is no more intact, and cannot be analysed as if it was a continuum. The same criterion used in the first unloading step is adopted for consistency.

As described in Section 6.3.2, a value for the coefficient of consolidation equal to 0.004 mm^2/s has been adopted to compute the time required for the primary consolidation to take place for S-samples. Considering a drainage path of 50 mm, the required time to achieve consolidation is about 174 hours. The consolidation phases for specimens S-1 and S-2 are depicted in Figure 6-11 and Figure 6-12, respectively. The consolidation phase of specimen S-3 was not carried out since the desired mean effective stress was achieved at the end of the B-check test; therefore the shear phase was directly carried out once equilibration was achieved after the establishment of drained conditions.

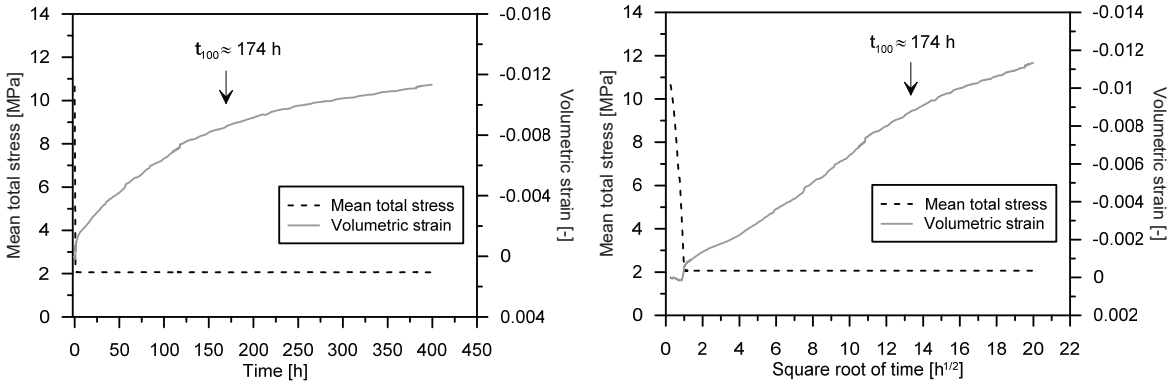

Figure 6-11: Consolidation phase at p' = 2 MPa for specimen S-1.

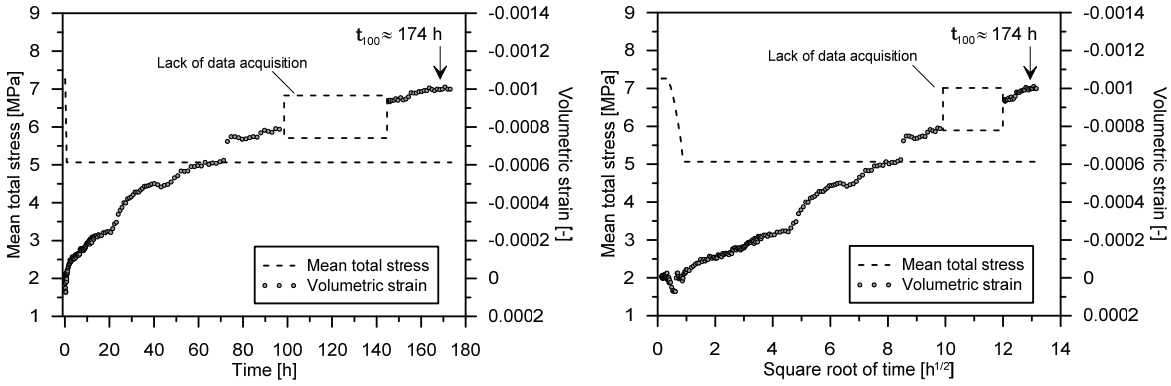

Figure 6-12: Consolidation phase at p' = 5 MPa for specimen S-2.

6.4.3. Drained shear phases results

The results of the shear phases of the triaxial tests on P-samples and on S-samples are reported in this section. In Figure 6-13 the deviatoric stress $q = \sigma_1 - \sigma_3$, is plotted as a function of the axial, radial and volumetric strains for the three stages of the multistage triaxial test on P-2 sample. The results from the single stage P-1 test are not represented here, since the radial and volumetric strains could not be computed due to the failure of the radial LVDT. In the first two stages of the multistage test (at 2 MPa and at 5 MPa confining effective stress), as soon as a peak was detected, the shearing process was halted overnight with the intent to verify the adopted strain rate: if any excess pore water pressure was present due to a too fast strain rate, the equilibration time would allow its dissipation and thus a gain in resistance. During the night a decrease of the deviatoric stress was observed due to relaxation. As soon as the shearing process was re-started, the deviatoric stress gradually increased until reaching about the same deviatoric stress value as before. No significant gain of strength was observed: the adopted strain rate was proved to be suitable for drained testing, in addition, the fact that about the same deviatoric stress was obtained after the continuation of the shearing process reveals that no significant damage was caused to the specimen. In the last stage, at 10 MPa of effective radial confining pressure, the shearing process was applied until the peak and subsequently maintained to obtain the post peak response and the ultimate shear strength. The deviatoric load was subsequently decreased until an isotropic stress state was re-established. The specimen was then isotropically unloaded to 5 MPa mean effective stress allowing for the equilibration of the volumetric strain and subsequently sheared to obtain information on the ultimate strength. The same procedure was re-applied to obtain information on the ultimate strength at 2 MPa mean effective stress. However, it has to be noted that once the specimen is brought to failure during the last stage of the multistage triaxial tests, the failure surface has formed, and the material cannot be treated as a continuum anymore. Therefore, the measurement of the radial displacement is no more representative and the computation of the lateral and volumetric deformations is no more possible.

In Figure 6-14 the deviatoric stress q is plotted as a function of the axial, radial and volumetric strains for the three single stage triaxial tests on S-samples. Again the shearing process was halted for several hours during the execution of the tests in order to analyse the response of the material in term of strength during further shearing as explained above.

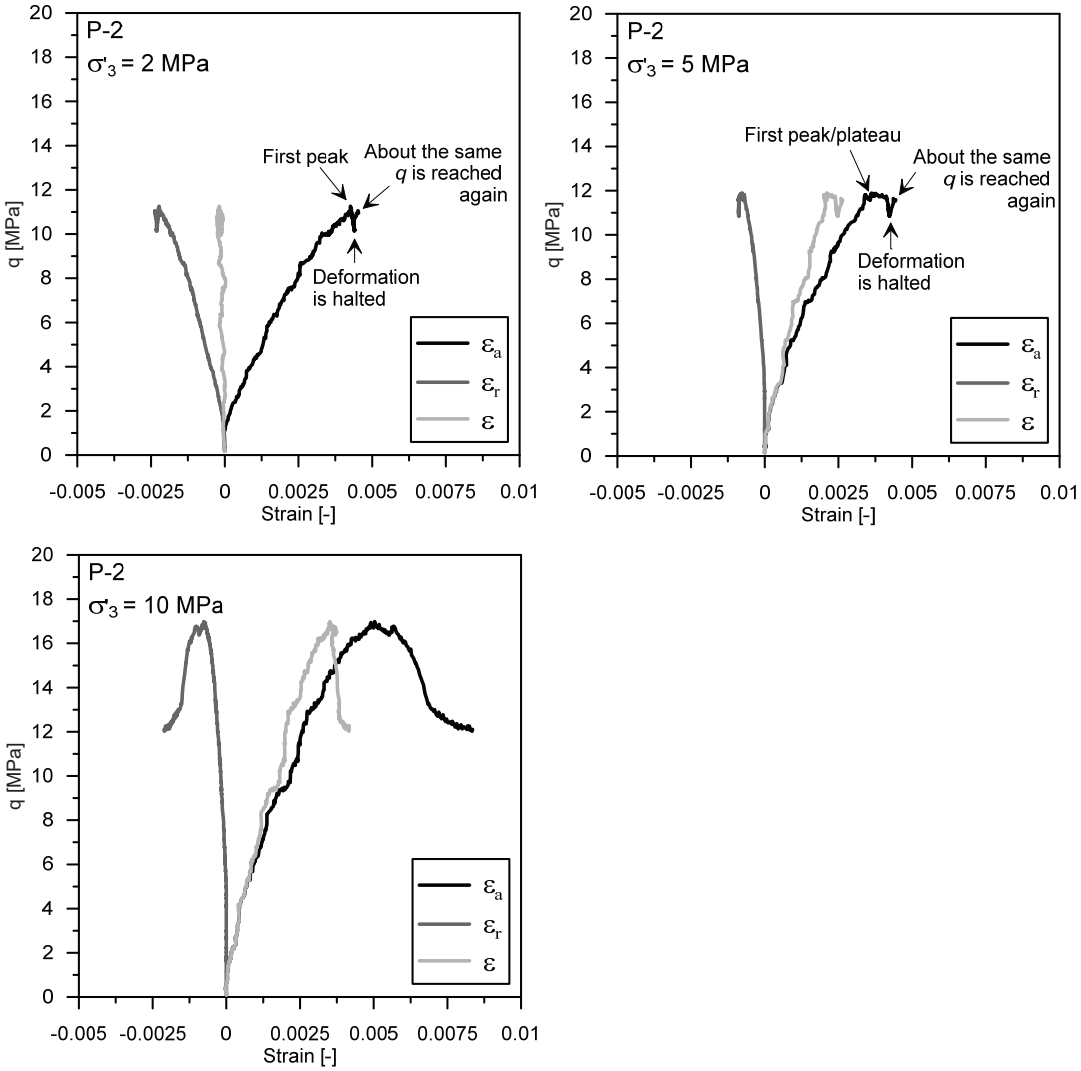

Figure 6-13: Deviatoric stress as a function of the axial, radial and volumetric strain for P-2 sample at σ'_3 = 2 MPa, 5 MPa and 10 MPa (multistage triaxial test).

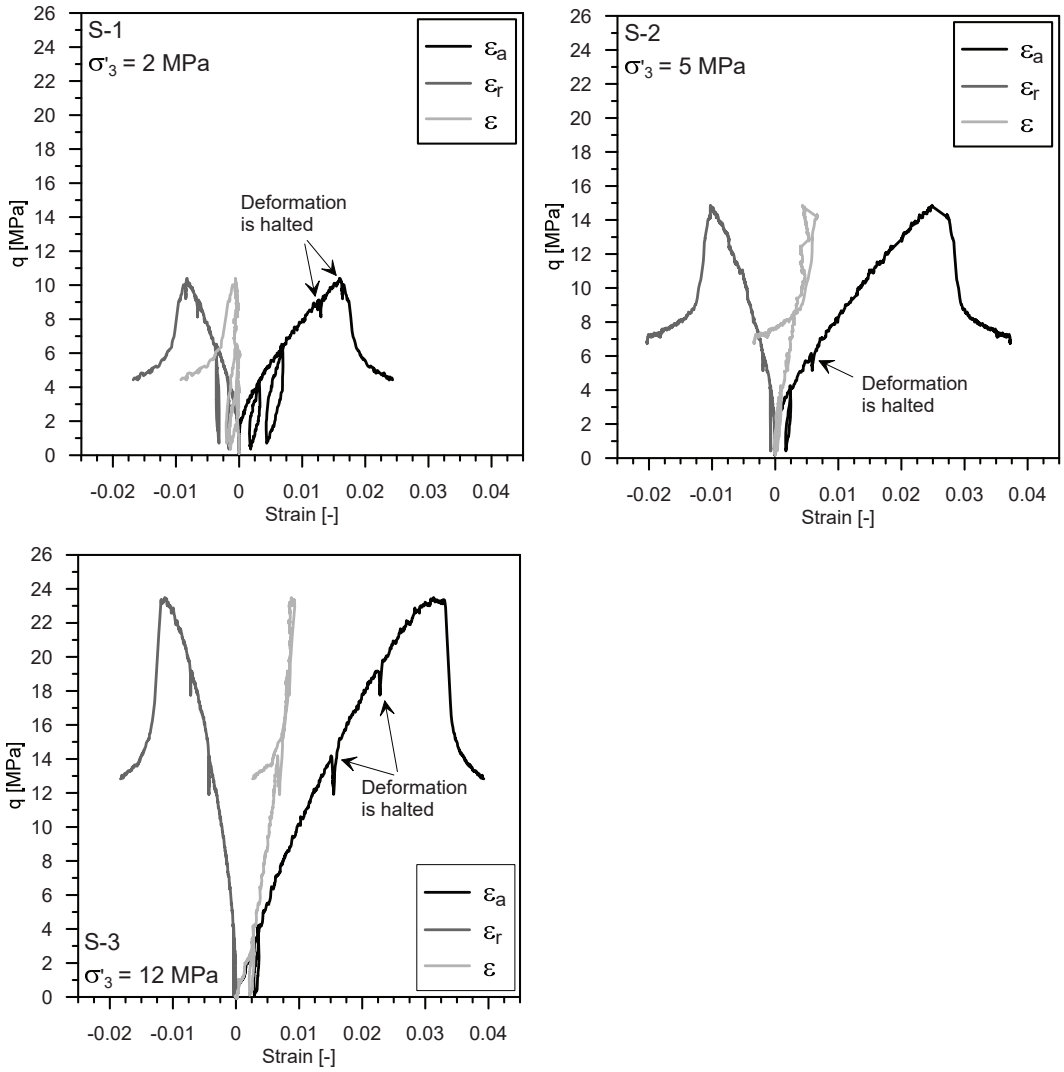

Figure 6-14: Deviatoric stress as a function of the axial, radial and volumetric strain for S-samples at σ'3 = 2 MPa, 5 MPa and 12 MPa.

The results of all triaxial tests are reported in Figure 6-15 for the P-samples and in Figure 6-16 for the S-samples, in terms of deviatoric stress (q) versus mean effective stress (p'), in terms of deviatoric stress versus axial strain (ε_a), and in terms of radial strain (ε_r) and volumetric strain (ε) versus axial strain. The mean effective stress p' is computed as follows:

$$p' = \frac{\sigma'_a + 2\sigma'_r}{3} \tag{6.5}$$

The results of the ultimate shear strength determination for the P-sample in the multistage test are also reported in Figure 6-15. The peak observed at 5 MPa effective radial stress in the single stage triaxial test is about 2 MPa higher with respect to the one observed in the multistage test at the same radial stress: this might be due to a certain damage caused during the achievement of the previous peak;

however this difference may also be related to the heterogeneity of the material since the two specimens are derived from different Opalinus Clay cores. However, a good agreement is observed between single stage and multistage tests in relation to the determination of the ultimate shear strength at 5 MPa effective radial stress, since a value of about 7 MPa of deviatoric stress is obtained from the two tests.

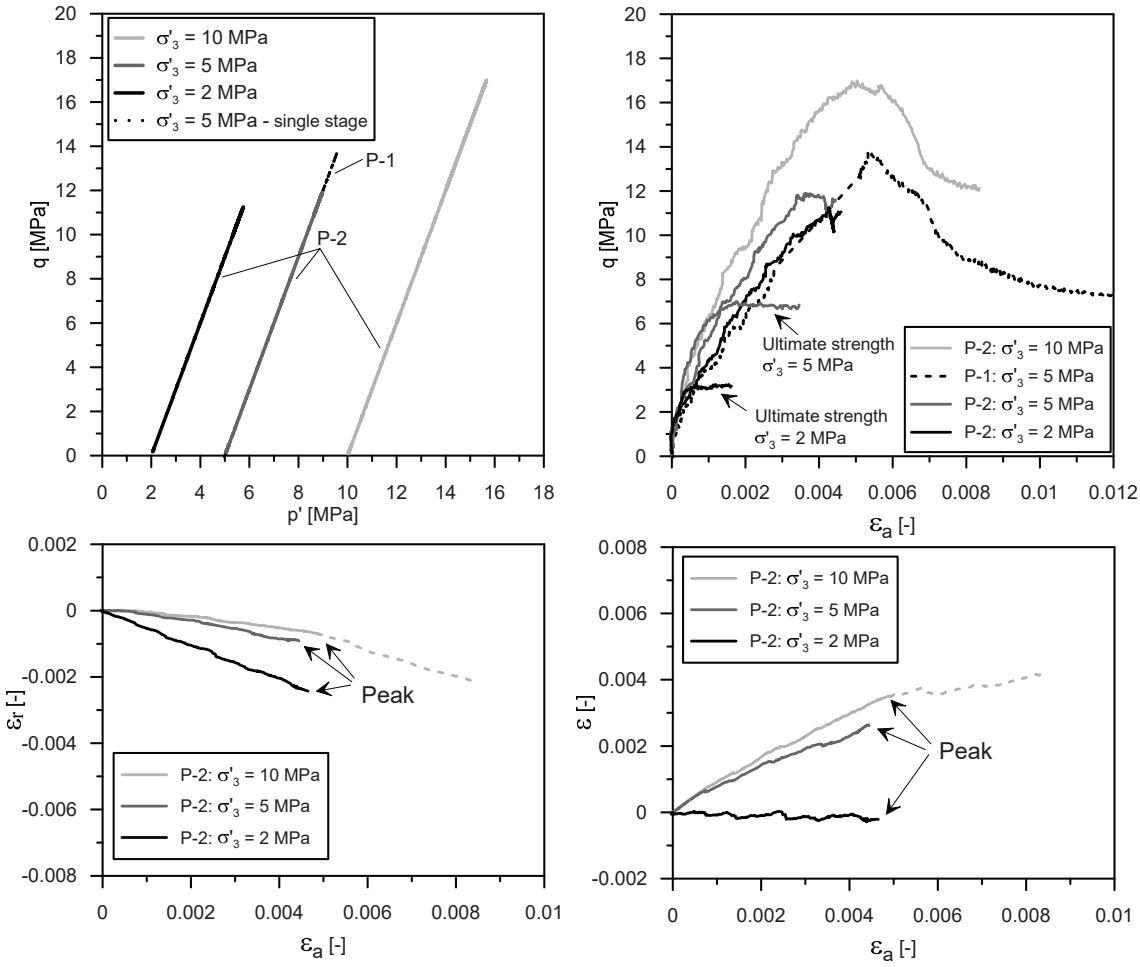

Figure 6-15: Triaxial test results for P-samples.

The comparison between Figure 6-15 and Figure 6-16 highlights that the application of higher axial strains is necessary for the S-samples in order to reach the peak with respect to the P-samples, revealing a much more compliant behaviour of the former with respect to the latter. However, the shear strength at the peak and ultimate states is comparable for the two loading directions at the same effective radial stress.

Regarding the behaviour of the material in terms of radial strain (ε_r) and volumetric strain (ε) versus axial strain (ε_a), reported in Figure 6-15 for the P-samples and in Figure 6-16 for the S-samples, no relevant dilatant behaviour is recognised, especially for the higher confining pressure values.

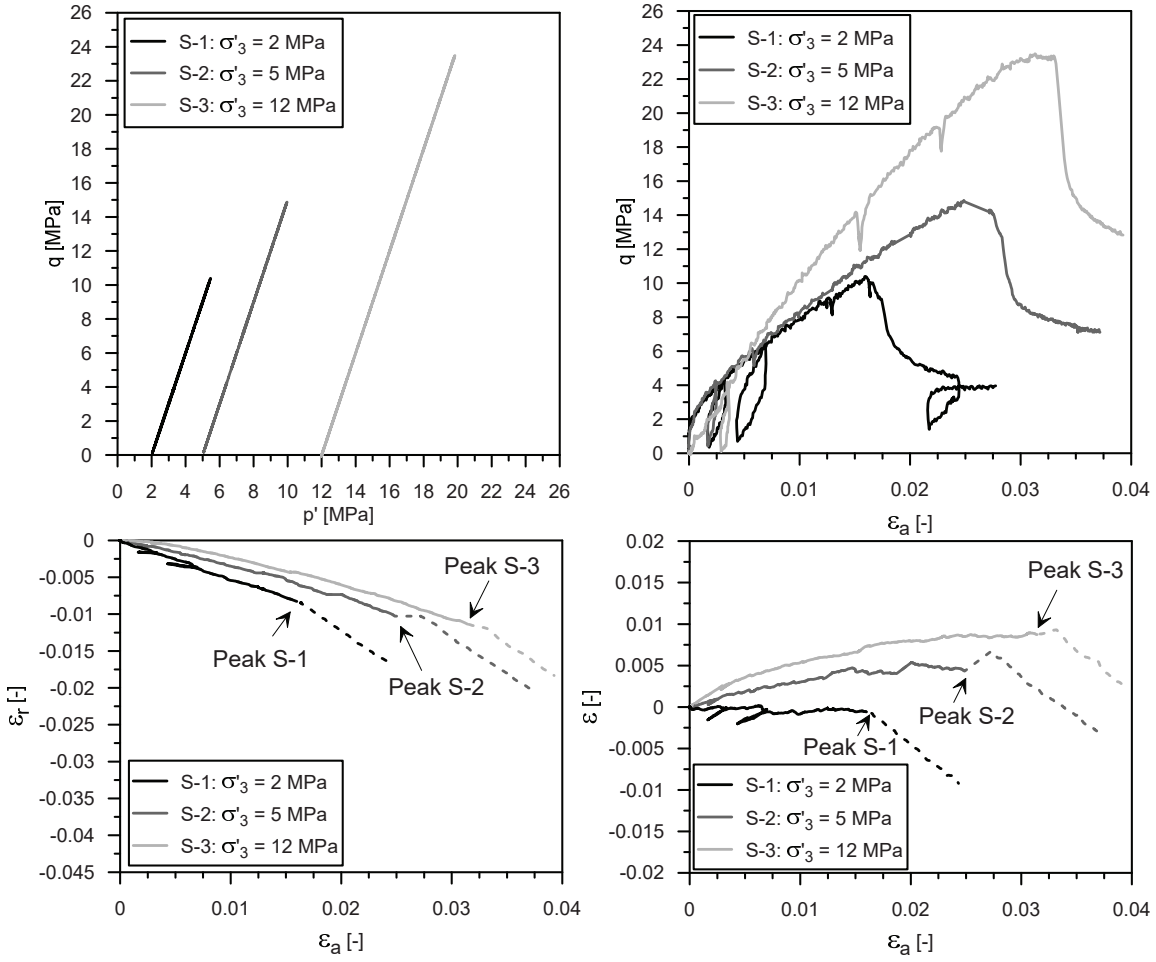

Figure 6-16: Triaxial test results for S-samples.

6.5. Analysis: shear strength and stiffness of Opalinus Clay

6.5.1. Shear strength

The results obtained on both P- and S- samples are plotted in Figure 6-17 in terms of deviatoric stress versus mean effective stress. The peak strength and ultimate strength envelopes are thus determined in the *p'- q* space, for the two loading directions, independently. The envelopes are expressed through the following equation:

$$q = \mathrm{a} + \mathrm{M}p' \tag{6.6}$$

where a is the intercept with the *q*- axis and M is the slope. Such parameters are reported in Figure 6-17 for the peak strength envelope and for the ultimate strength envelope for both P- and S- samples.

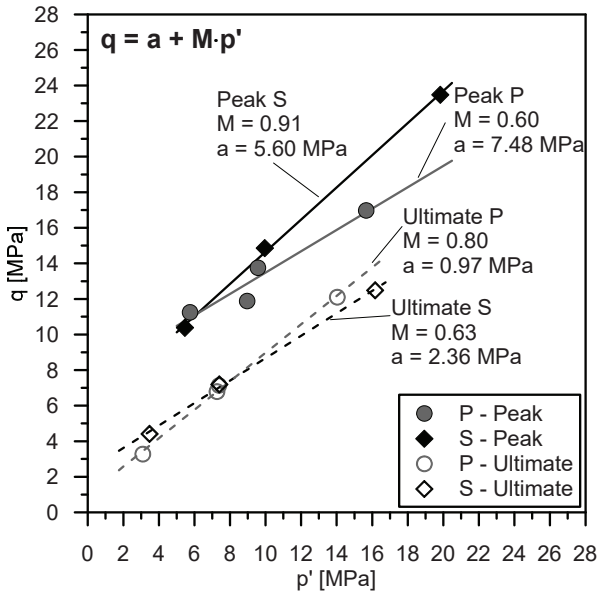

Figure 6-17: Envelopes for peak and ultimate shear strength of Opalinus Clay: separate envelopes are proposed for P- and S- samples.

Previous studies have reported results on the strength behaviour of Opalinus Clay (e.g. Naumann et al., 2007; Popp and Salzer, 2007; Bock, 2009; Gräsle, 2011; Siegesmund et al., 2014; Wild et al., 2015). However, contradictory results have been found: Gräsle (2011) and Naumann et al. (2007) found a distinct anisotropic behaviour in terms of strength properties; Bock (2009) reports very close strength parameters for the P- and S- loading orientations; finally Popp and Salzer (2007), Siegesmund et al. (2014) and Wild et al. (2015) did not find a significant anisotropy in the strength behaviour of Opalinus Clay. The reasons of these discrepancies are still not clear and further investigation on the microstructural interactions involving the presence of bedding planes, sandy lenses, and clay-rich layers, should be conducted, in parallel with a careful analysis of the experimental procedure adopted. In this work, the ultimate strength behaviour appears to be very similar for the two loading orientations; however, this is not the case for the peak strength behaviour as analysed in Figure 6-17. Different peak strength parameters are identified, with the greater M parameter observed for the S-samples. This observation appears contradictory with respect to previous findings on Opalinus Clay (Naumann et al., 2007; Gräsle, 2011; Jahns, 2013), where P-samples usually manifest greater strength with respect to S-samples. Moreover, the different slope for the P- and S- envelopes at peak conditions, and in particular the low M parameter for the P- envelope, is probably caused by the point defining the peak strength of P-2 specimen at the initial mean effective stress p' = 10 MPa. This peak was obtained through a multistage triaxial loading procedure, after two previous loading cycles. Therefore, some damage may have happened in the last stage of the test, inducing lower peak strength with respect to the value that would be obtained using a single stage triaxial procedure. Further testing would clarify this aspect. The remaining peak strength results appear to be very similar among the two loading orientations, therefore, a unique failure envelope is

also proposed for both peak and ultimate shear strength. The analysis is reported in Figure 6-18. The photos of the tested specimens after triaxial testing are reported in Appendix C.

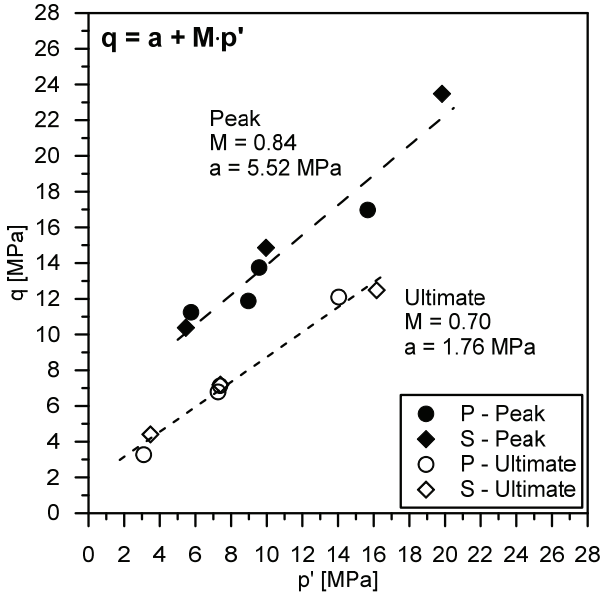

Figure 6-18: Envelopes for peak and ultimate shear strength of Opalinus Clay: unique envelopes are proposed which are valid for both P- and S- samples.

The parameter a and M can be used in order to derive the well-known Mohr-Coulomb parameters according to the following relationships:

$$\sin\phi' = \frac{3M}{M+6} \tag{6.7}$$

$$c' = \frac{a \cdot \tan\phi'}{M} \tag{6.8}$$

The obtained Mohr-Coulomb parameters are reported in Table 6-3 for both the hypothesis of separated strength envelopes (Figure 6-17) and unique strength envelopes (Figure 6-18).

Table 6-3: Mohr-Coulomb parameters for separated envelopes and for unique envelopes.

	Peak		*Ultimate*	
	ϕ' (°)	c' (MPa)	ϕ' (°)	c' (MPa)
Separate envelopes				
P-samples	16	3.5	21	0.5
S-samples	23	2.6	17	1.1
Unique envelope				
All	22	2.6	18	0.8

The results presented in Fig 6-18 are compared with data reported in Wild et al. (2015) on Opalinus Clay (Figure 6-19). The comparison shows that a bilinear Mohr-Coulomb criterion captures well the failure behaviour of Opalinus Clay. In fact, a threshold mean effective stress p'_{tr} equal to about 5 MPa can be identified: the M and a parameters related to the case when $p' < p'_{tr}$ and to the case when $p' > p'_{tr}$, are reported in Figure 6-19. The corresponding Mohr-Coulomb parameters are reported in Table 6-4 for the two cases.

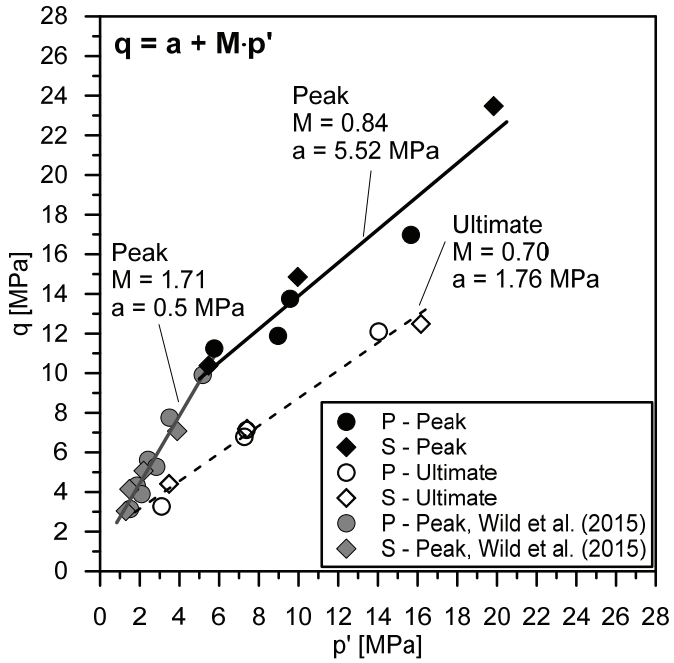

Figure 6-19: Envelopes for peak and ultimate shear strength of Opalinus Clay.

The observed bi-linearity in the failure behaviour of Opalinus Clay should be carefully taken into account in order to develop suitable constitutive model for this material. In fact, the stress range to be considered in the applications involving Opalinus Clay comprises both $p' < p'_{tr}$ and $p' > p'_{tr}$.

Table 6-4: Bilinear Mohr-Coulomb failure parameters for Opalinus Clay

$p' < p'_{tr}$		$p' > p'_{tr}$	
ϕ' (°)	c' (MPa)	ϕ' (°)	c' (MPa)
42	0.5	22	2.6

The ultimate shear strength behaviour can be well reproduced by a linear Mohr-Coulomb criterion, for the considered stress range. Moreover, the ultimate shear strength response appears to be similar for the two considered loading orientations.

6.5.2. Elastic behaviour

The analysis of the results presented in Section 6.4.3 allows determining the elastic properties of the material in terms of Young modulus and Poisson's ratio. According to the norm ASTM D 3148, different criteria can be adopted for the determination of the Young modulus; in this work it is derived from the linear part of the unloading-reloading loops for the S-samples. As to the P-samples, no unloading-reloading cycles have been carried out; therefore, the Young modulus is derive from the initial linear part of the deviatoric stress versus axial strain curve in the stress range between about 0 and 25% of the peak shear strength. However, the analysis of the deviatoric stress versus axial strain curves for the S-samples reveals that the slope of the initial linear portion of the curve is very similar to the slope of the unloading-reloading part (Figure 6-16). Therefore, the two followed procedures are considered to produce comparable results.

The determination of the Poisson's ratio is often affected by non-linearity in the material behaviour (ASTM D3148); according to the norm, the best procedure for the determination of the Poisson's ratio, and the one used in this work, is to consider the slope of the initial linear portion of the radial strain versus axial strain curve (Figure 6-15 and Figure 6-16). The obtained values of Young modulus and Poisson's ratio are plotted in Figure 6-20 as a function of the confining effective stress.

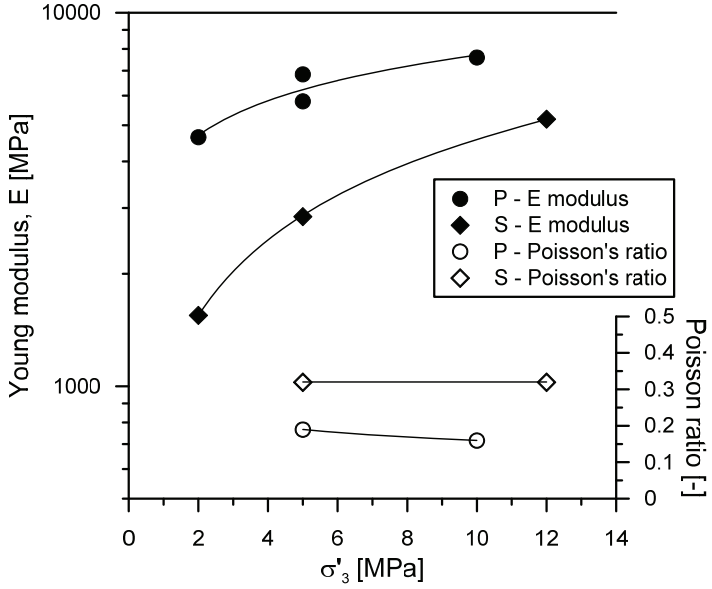

Figure 6-20: Young modulus and Poisson's ratio for the tested Opalinus Clay samples as a function of the confining radial effective stress.

The analysis of the elasto-plastic behaviour of Opalinus Clay during one-dimensional loading, unloading and reloading cycles in the oedometric cell has been presented in Chapter 3, in terms of oedometric modulus versus vertical effective stress. Further data have also been presented in Chapters 4 and 5, in the context of the analysis of the thermo-mechanical response and of the coupled chemo-mechanical processes in Opalinus Clay. In order to compare these results with those presented in Figure 6-20, the relationship between a vertical effective stress increment and the corresponding

radial effective stress increment during oedometric compression perpendicular to the bedding planes must be determined, in order to compute the mean effective stress from Eq.(6.5). Moreover, the relationship between oedometric modulus and Young moduli must be defined. For the case when the stress state is within the elastic domain, this is achieved taking into account the transversely isotropic elastic behaviour of the material and considering oedometric loading perpendicular to the bedding planes. The following relationships between a vertical effective stress increment and the corresponding radial effective stress increment, as well as between oedometric modulus and Young moduli are obtained:

$$\delta\sigma'_r = \delta\sigma'_v \frac{\nu_2}{E_2} \frac{E_1}{(1-\nu_1)} \tag{6.9}$$

$$E_{oed} = \frac{E_2}{\left(1 - \frac{2\nu_2^2}{E_2} \frac{E_1}{(1-\nu_1)}\right)} \tag{6.10}$$

where E_1 and ν_1 are the Young modulus and the Poisson's ratio parallel to the bedding planes, while E_2 and ν_2 are the Young modulus and Poisson's ratio perpendicular to the bedding planes.

However, the response of the material during oedometric loading appears to be elasto-plastic: when the elastic domain is overcome, Eq.(6.9) does not apply anymore, and the computation of the radial stress increment requires to make some assumptions. In this work the elasto-plastic radial stress increments are computed using Jaky's (1948) relationship in order to estimate the K_0 coefficient:

$$K_0 = 1 - \sin\phi' \tag{6.11}$$

And:

$$\delta\sigma'_r = K_0 \, \delta\sigma'_v \tag{6.12}$$

However, since the validity of Jaky's formula has not been proved for shales, this assumption may cause some errors in the evaluation of the mean effective stress when the stress state overcomes the elastic domain during oedometric compression. The values of the oedometric modulus, computed on elastic branches of the oedometric curves, are reported in Figure 6-21 as a function of the mean effective stress at the beginning (end) of the loading (unloading) branches. They are compared in Figure 6-21 with the results derived from the triaxial tests converted in terms of oedometric modulus using Eq.(6.10). The mean effective stress, for the case of oedometric compression, is derived from the vertical effective stress through Eq.(6.5), and using Eq.(6.9) for stress increments in the elastic domain, and Eq.(6.12) for stress increments in the elasto-plastic domain. Oedometric elastic branches carried out up to a maximum of 25 MPa of vertical effective stress have been considered in order to limit the stress increments in the elasto-plastic domain. Good accordance between oedometric tests results and triaxial tests results is observed at low mean effective stress values, while lower values of the Oedometric modulus are found from the analysis of the oedometric tests results as the mean

effective stress increases. This may be due to several factors: (i) some differences in the tested materials (such as density or mineralogical composition) since the specimens used in the oedometric testing were obtained from a different core with respect to the one used for obtaining the specimens tested in triaxial conditions; (ii) some disturbance to the specimens due to oedometric compression rather than isotropic compression; (iii) some uncertainties in the estimation of the mean effective stress as explained above; (iv) finally some uncertainties are also present in the determination of the elastic parameters that are used in Eq.(6.9) and Eq.(6.10).

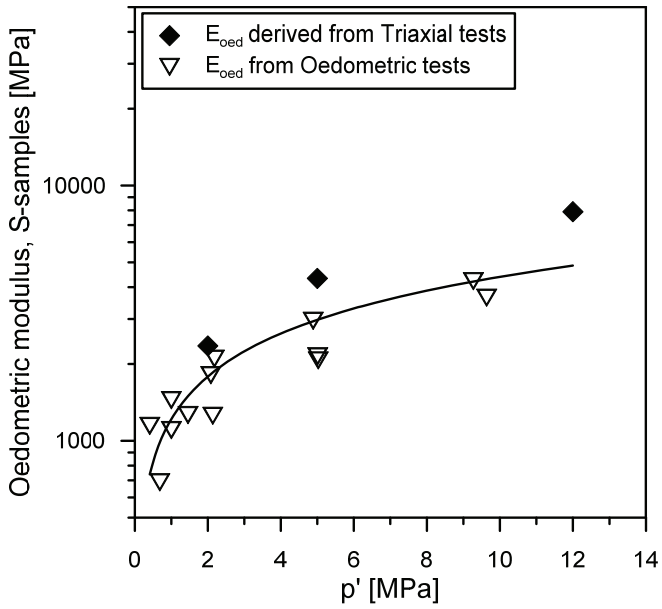

Figure 6-21: Oedometric modulus as a function of the mean effective stress estimated from triaxial tests results and computed from oedometric tests results.

6.6. Conclusions

The results of CD triaxial tests on P-samples and on S-samples from the Opalinus Clay from Mont Terri URL have been presented and analysed in this chapter, in order to derive information on the strength and stiffness properties of Opalinus Clay. Particular attention has been paid to the experimental procedure in order to ensure saturated conditions; in fact the degree of saturation and the presence of suction influence the strength and the elastic properties of shales in a relevant way. As a consequence, a proper resaturation of the specimen before mechanical testing is fundamental. Particular attention has also been adopted in the estimation of the strain rate during the shearing phase of the triaxial tests in order to avoid the generation of unwanted excess pore water pressure and thus to ensure drained conditions. Single stage and multistage triaxial testing procedures are both adopted in this experimental campaign. Multistage triaxial testing allows to gain several results with the use of a single specimen, as a consequence this procedure has the advantages to reduce the amount of material needed and to save several time, since the resaturation phase is performed only once rather than several times. In addition, the scatter of the results due to the natural variability of the material is completely eliminated. On the other hand, multistage testing may introduce the risk of damaging the specimen with the increase in the number of stages. However, if the risk (and probability) of underestimation of the strength for the last stages is taken into account, the results derived from multistage testing still provide meaningful information on the strength, with the benefit of coming from well controlled experimental conditions.

The results of the triaxial tests on P- and S- samples highlight that the material behaves in a similar manner in terms of both peak and ultimate shear strength, regardless the considered direction of loading (P and S directions) with respect to the bedding orientation. Therefore, separate failure envelopes for the two loading orientations, as well as a unique failure envelope are proposed for both peak and ultimate shear strength. The comparison of the results with additional recent data available in the literature shows that the failure behaviour of Opalinus Clay, in the investigated range, can be well reproduced through a bilinear Mohr-Coulomb criterion. No anisotropy is observed in the ultimate shear strength response of Opalinus Clay, where the ultimate shear strength behaviour can be well reproduced by a linear Mohr-Coulomb criterion, using the same parameters for both P and S samples.

A clear anisotropic elastic behaviour is observed for the tested shale, where S-samples present a much more compliant behaviour than P-samples. Moreover, the Young moduli are found to increase with the increase in mean effective stress, according to a power law.

The results presented in this chapter have been obtained following meticulous experimental procedures, and they have been analysed in order to derive relevant parameters for the prediction of the hydro-mechanical behaviour of Opalinus Clay. This study is believed to be of utmost importance for the development and calibration of constitutive and numerical tools, with the aim to model and predict the hydro-mechanical response of the tested shale.

6.7. References

Bishop, A. The influence of system compressibility on the observed pore-pressure response to an undrained change in stress in saturated rock. Geotechnique (1976) 26(Analytic).

Bock, H. RA Experiment: Updated Review of the Rock Mechanics Properties of the Opalinus Clay of the Mont Terri URL based on Laboratory and Field Testing. TECHNICAL REPORT 2008-04 (2009).

Cook, J. The effects of pore pressure on the mechanical and physical properties of shales. Oil & Gas Science and Technology (1999) 54(6): 695-701.

Corkum, A.G. and Martin, C.D. The mechanical behaviour of weak mudstone (Opalinus Clay) at low stresses. International Journal of Rock Mechanics and Mining Sciences (2007) 44(2): 196-209.

Jahns, E. Geomechanical laboratory tests on Opalinus Clay cores from the bore hole Schlattingen SLA-1. Nagra Work Report NAB (2013): 13-18.

Ghabezloo, S. and Sulem, J. Effect of the volume of the drainage system on the measurement of undrained thermo-poro-elastic parameters. International Journal of Rock Mechanics and Mining Sciences (2010) 47(1): 60-68.

Gräsle, W. Multistep triaxial strength tests: Investigating strength parameters and pore pressure effects on Opalinus Clay. Physics and Chemistry of the Earth, Parts A/B/C (2011) 36(17): 1898-1904.

Gutierrez, M., Katsuki, D. and Tutuncu, A. Determination of the continuous stress-dependent permeability, compressibility and poroelasticity of shale. Marine and Petroleum Geology (2014) In press.

Head, K. (1992). Manual of Soil Laboratory Testing, Volume 3, Effective Stress Tests. Volume 3, Pentech Press London.

Jaky, J. Pressure in soils. Proceedings of the 2nd international conference on soil mechanics and foundation engineering, (1948). 103-107.

Mesri, G., Adachi, G. and Ullrich, C. Pore-pressure response in rock to undrained change in all-round stress. Geotechnique (1976) 26(2): 317-330.

Naumann, M., Hunsche, U. and Schulze, O. Experimental investigations on anisotropy in dilatancy, failure and creep of Opalinus Clay. Physics and Chemistry of the Earth, Parts A/B/C (2007) 32(8): 889-895.

Popp, T. and Salzer, K. Anisotropy of seismic and mechanical properties of Opalinus clay during triaxial deformation in a multi-anvil apparatus. Physics and Chemistry of the Earth, Parts A/B/C (2007) 32(8): 879-888.

Renner, J., Evans, B. and Hirth, G. On the rheologically critical melt fraction. Earth and Planetary Science Letters (2000) 181(4): 585-594.

Seiphoori, A., Ferrari, A. and Laloui, L. An advanced calibration process for a thermo-hydro-mechanical triaxial testing system. Deformation Characteristics of Geomaterials: Proceedings of the

Fifth International Symposium on Deformation Characteristics of Geomaterials, IS-Seoul 2011, 1-3 September 2011, Seoul, Korea, IOS Press, (2011). 396.

Seiphoori, A. Thermo-hydro-mechanical characterisation and modelling of MX-80 granular bentonite. (2014).

Siegesmund, S., Popp, T., Kaufhold, A., Dohrmann, R., Gräsle, W., Hinkes, R. and Schulte-Kortnack, D. Seismic and mechanical properties of Opalinus Clay: comparison between sandy and shaly facies from Mont Terri (Switzerland). Environmental earth sciences (2014) 71(8): 3737-3749.

Skempton, A. The pore-pressure coefficients A and B. Geotechnique (1954) 4(4): 143-147.

Wild, K., Amann, F., Martin, C., Wassermann, J., David, C. and Barla, M. Dilatancy of clay shales and its impact on pore pressure evolution and effective stress for different triaxial stress paths. 49th US Rock Mechanics/Geomechanics Symposium, American Rock Mechanics Association, (2015).

Wissa, A.E. Pore pressure measurement in saturated stiff soils. Journal of the Soil Mechanics and Foundations Division (1969) 95(4): 1063-1074.

Chapter 7
A Constitutive Framework for Opalinus Clay

7.1. Foreword

During the different phases of the life of an underground waste disposal facility, the surrounding host geomaterial will experience various hydro-mechanical conditions. The realistic prediction of the hydro-mechanical response of the host formation requires the development of a suitable constitutive framework, capable to take into account the behavioural features of the material. A wide knowledge on the hydro-mechanical behaviour of Opalinus Clay has been acquired through the development of a comprehensive experimental database, presented and analysed in the previous chapters of this PhD Thesis. In particular, Chapter 6 has highlighted typical behavioural features of the studied material such as the intrinsic structural anisotropy, the quasi-brittle behaviour, and the stiffness and strength dependency on the mean effective stress.

A constitutive modelling framework is presented in this chapter, which is developed in order to take into account the observed behavioural features of Opalinus Clay. The proposed constitutive approach includes the introduction of the disturbed state concept (DSC) (Desai, 2000) in order to reproduce the softening behaviour after peak.

7.2. Introduction

The database available in the literature on the mechanical behaviour of shales, even though often affected by a lack of good experimental procedures and testing protocols, has shown the predominant features in the mechanical response of these materials e.g. (Niandou et al., 1997; Wong, 1998; Hsu and Nelson, 2002; Corkum and Martin, 2007; Naumann et al., 2007; Islam and Skalle, 2013), giving rise to a research branch dedicated to the reproduction of the observed behaviour through the development of constitutive laws. When dealing with the constitutive modelling of shales, whose behaviour can be considered as intermediate between that of a soil and of a rock, major attention has to be paid to their brittle or quasi-brittle response and to the softening behaviour after peak. As a proof of this fact, damage models have been largely developed and used to reproduce the softening behaviour of shales: an extended review on this subject has been carried out by Parisio et al. (2015). However, such models present a complex formulation, and the calibration of the model parameters is often difficult.

Opalinus Clay shale manifests a quasi-brittle behaviour during compression e.g. (Corkum and Martin, 2007; Siegesmund et al., 2014) with accumulation of plastic strains; softening is observed once failure is reached, until the ultimate conditions are achieved. Therefore, a constitutive framework capable of predicting this response must be taken into account: in this chapter the disturbed state concept (DSC) proposed by Desai (2000) has been considered, in order to model the softening behaviour of Opalinus Clay. The DSC has been introduced into the framework of an elasto-plastic constitutive model, which has been further developed in order tackle the behavioural features of Opalinus Clay. A brief description of the relevant behavioural characteristics of shales and in particular of Opalinus Clay, which have been taken into consideration for the development of the constitutive framework, is given in the following paragraphs.

The experimental analysis of Opalinus Clay behaviour has highlighted the anisotropic response of the material. In particular, due to the particular configuration of its oriented structure and due to the presence of bedding planes, the behaviour of the material can be defined as transversely isotropic, where the elastic properties perpendicular to the bedding planes are different than those parallel to the bedding planes. Moreover, Figure 6.20 in the previous Chapter 6 has shown that the elastic moduli are stress-dependent, where the stiffness of the material increases with increasing mean effective stress level.

Several experimental investigations on Opalinus Clay have highlighted the dependency of the peak strength on the loading orientation with respect to the bedding planes. As to the strength behaviour of P-samples (specimens loaded parallel to the bedding planes) and of S-samples (specimens loaded perpendicular to the bedding planes), contradictory results are found in the literature. Gräsle (2011), Naumann et al. (2007) and Jahns (2013) found a distinct anisotropic behaviour in terms of strength properties, where the P-samples manifests greater strength than S-samples; Bock (2009) reports very close strength parameters for the P- and S- loading orientations, while Popp and Salzer (2007), Siegesmund et al. (2014) and Wild et al. (2015) did not find a significant anisotropy in the strength behaviour of P-samples and S-samples of Opalinus Clay. These last studies are in line with the experimental findings of this PhD work, as widely discussed in Chapter 6. However, several investigation on the mechanical behaviour of shales e.g. (Niandou et al., 1997; Naumann et al., 2007; Islam and Skalle, 2013; Jahns, 2013) clearly highlight that the strength is lower when the shale is loaded with an angle of 30°-45° with respect to the bedding planes orientation. This is probably due to the fact that the failure surface approaches the orientation of the bedding planes. Therefore, the possibility to reproduce this intrinsic anisotropic strength response should also be consider and included in the model.

The following Section 7.3 provides a description of the developed constitutive framework. The DSC concept and formulation are widely presented and described in Section 7.4. Finally, the triaxial tests results presented in Chapter 6 are back-analysed in order to demonstrate the performance of the proposed framework. The results of the back-analysis are presented in Section 7.5.

7.3. The elasto-plastic constitutive framework

In this section, the elasto-plastic constitutive framework for Opalinus Clay is formulated. The proposed constitutive framework takes origin from the well-known ACMEG model (François and Laloui, 2008), which has been modified with the aim to better tackle the mechanical response of Opalinus Clay. The anisotropic elastic component of the model is described first; afterwards, the elasto-plastic components of the model are introduced.

7.3.1. Anisotropic Elasticity

As introduced in Section 7.2, Opalinus Clay manifests a transversely isotropic elastic behaviour; therefore, the transversely isotropic elasticity equations must be considered in order to correctly reproduce the elastic stress-strain response of the material. Moreover, the five independent elastic parameters, which constitute the transversely isotropic elastic stiffness matrix, are defined in order to manifest stress dependency of the elastic moduli and of the shear moduli.

The stiffness matrix **D** for a transversely isotropic material is defined as follows:

$$\mathbf{D} = \begin{bmatrix} E_1 \dfrac{1-\frac{E_1}{E_2}\nu_2^{\,2}}{(1+\nu_1)\cdot(1-\nu_1-2\frac{E_1}{E_2}\nu_2^{\,2})} & E_1 \dfrac{\nu_1+\frac{E_1}{E_2}\nu_2^{\,2}}{(1+\nu_1)\cdot(1-\nu_1-2\frac{E_1}{E_2}\nu_2^{\,2})} & \dfrac{E_1\cdot\nu_2}{(1-\nu_1-2\frac{E_1}{E_2}\nu_2^{\,2})} & 0 & 0 & 0 \\ E_1 \dfrac{\nu_1+\frac{E_1}{E_2}\nu_2^{\,2}}{(1+\nu_1)\cdot(1-\nu_1-2\frac{E_1}{E_2}\nu_2^{\,2})} & E_1 \dfrac{1-\frac{E_1}{E_2}\nu_2^{\,2}}{(1+\nu_1)\cdot(1-\nu_1-2\frac{E_1}{E_2}\nu_2^{\,2})} & \dfrac{E_1\cdot\nu_2}{(1-\nu_1-2\frac{E_1}{E_2}\nu_2^{\,2})} & 0 & 0 & 0 \\ \dfrac{E_1\cdot\nu_2}{(1-\nu_1-2\frac{E_1}{E_2}\nu_2^{\,2})} & \dfrac{E_1\cdot\nu_2}{(1-\nu_1-2\frac{E_1}{E_2}\nu_2^{\,2})} & \dfrac{E_2\cdot(1-\nu_1)}{(1-\nu_1-2\frac{E_1}{E_2}\nu_2^{\,2})} & 0 & 0 & 0 \\ 0 & 0 & 0 & \dfrac{E_1}{2(1+\nu_1)} & 0 & 0 \\ 0 & 0 & 0 & 0 & G_2 & 0 \\ 0 & 0 & 0 & 0 & 0 & G_2 \end{bmatrix} \tag{7.1}$$

where five independent elastic parameters are introduced: the Young modulus E_1 and Poisson's ratio ν_1 parallel to the bedding planes; the Young modulus E_2 and Poisson's ratio ν_2 perpendicular to the bedding planes; and the shear modulus G_2 for shear loads in the bedding planes. The meaning of these parameters is better presented in Figure 7-1. The remaining elastic parameters can be derived from the five independent ones.

From a numerical point of view, the elastic properties for a transversely-isotropic material are specified on the basis of coordinate axes, and such coordinate axes are strictly related to the orientation of the anisotropic planes. In the case described by the stiffness matrix **D** (Eq.(7.1)), the z-axis corresponds to the direction perpendicular to the bedding planes. It is therefore necessary to transfer the stiffness matrix to a rotated coordinate system (x', y', z'), which could be oriented in a convenient way with respect the previous reference system (x, y, z) (Figure 7-2). For this reason, a rotation matrix **K** is introduced. The rotated elastic stiffness matrix $\mathbf{D}^{\text{rotated}}$ is thus obtained:

$$\mathbf{D}^{\text{rotated}} = \mathbf{K}\ \mathbf{D}\ \mathbf{K}^{\text{T}} \tag{7.2}$$

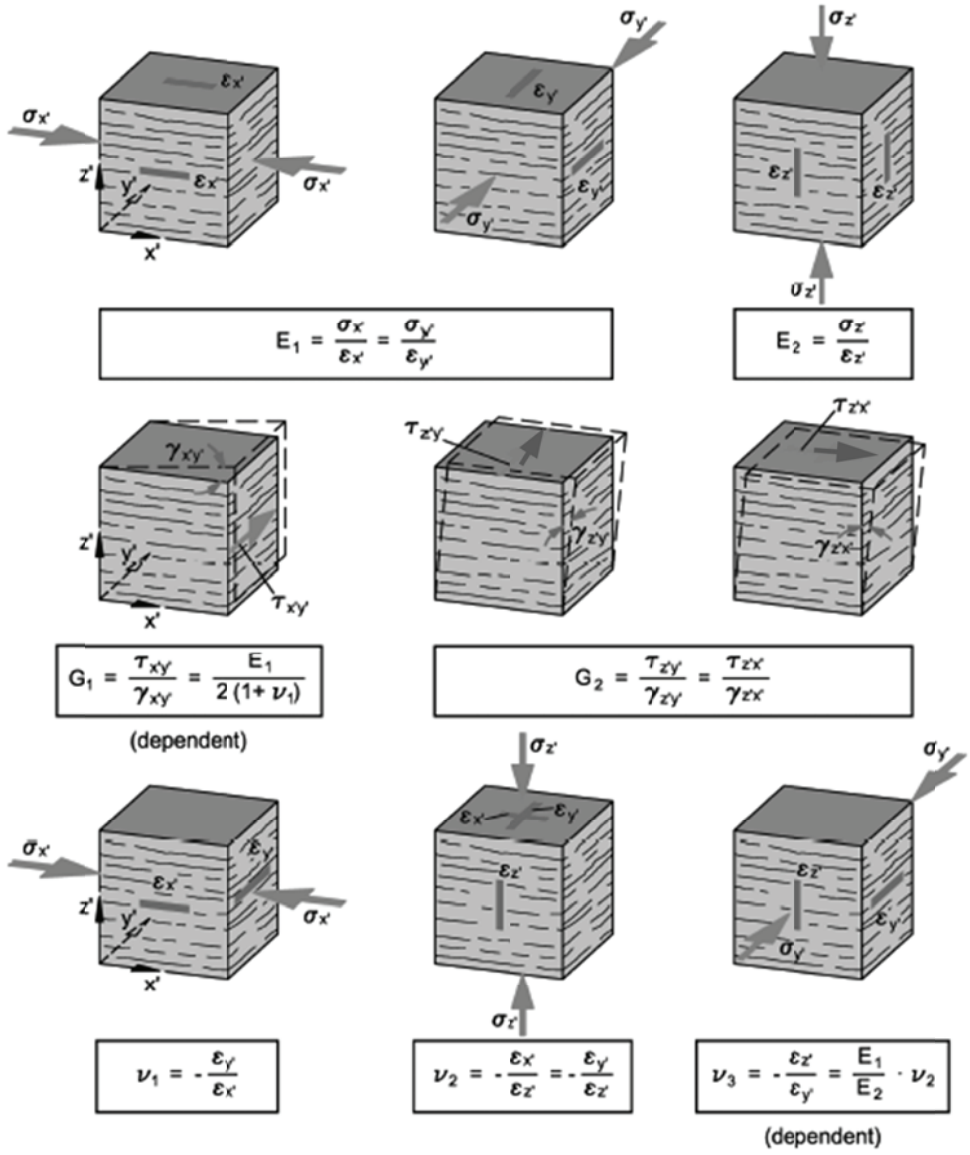

Figure 7-1: Definition of the transversely isotropic elastic parameters (Wittke, 2014).

For the case of rotation of an angle η about the y-axis (Figure 7-2) the rotation matrix is expressed as follows:

$$\mathbf{K} = \begin{bmatrix} c^2 & 0 & s^2 & 0 & 2cs & 0 \\ 0 & 1 & 0 & 0 & 0 & 0 \\ s^2 & 0 & c^2 & 0 & -2cs & 0 \\ 0 & 0 & 0 & c & 0 & -s \\ -cs & 0 & cs & 0 & c^2 - s^2 & 0 \\ 0 & 0 & 0 & s & 0 & c \end{bmatrix} \tag{7.3}$$

where $c = \cos\eta$ and $s = \sin\eta$. The elastic matrix **D** is defined for the condition where the z-axis of the reference system is perpendicular to the anisotropic plane, therefore when the angle between the z-axis of the reference system and the anisotropy plane θ is equal to 90°, η is equal to 0°. Consequently, the following relationship holds: $\eta = 90° - \theta$.

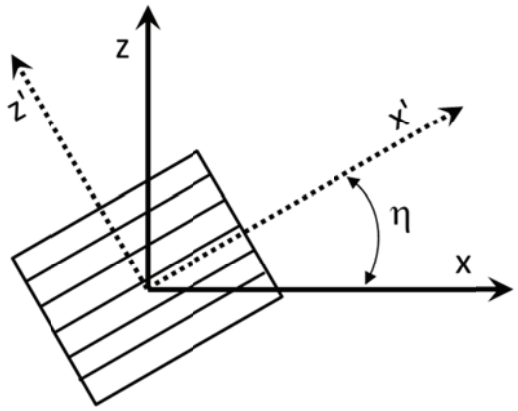

Figure 7-2: Rotation of the reference system of the transversely isotropic elastic stiffness matrix of an angle η about the y-axis.

The non-linear elastic response is described through the dependency of the Young moduli on the mean effective stress, according to a power law:

$$E_1 = E_{1\,ref}\left(\frac{p'}{p'_{ref}}\right)^{n_{el}} \tag{7.4}$$

$$E_2 = E_{2\,ref}\left(\frac{p'}{p'_{ref}}\right)^{n_{el}} \tag{7.5}$$

where E_{1ref} and $E_{2\,ref}$ are the Young moduli parallel and perpendicular to the bedding planes respectively, at a reference mean effective stress equal to 1 MPa, and n_{el} is the elastic exponent. The mean effective stress p' is defined as follows:

$$p' = \frac{\sigma'_x + \sigma'_y + \sigma'_z}{3} \tag{7.6}$$

The deviatoric stress q is also introduced as follows:

$$q = \sqrt{\frac{\left(\sigma'_x - \sigma'_y\right)^2 + \left(\sigma'_x - \sigma'_z\right)^2 + \left(\sigma'_y - \sigma'_z\right)^2 + 3\tau_{xy}^2 + 3\tau_{xz}^2 + 3\tau_{yz}^2}{2}} \tag{7.7}$$

7.3.2. Elasto - Plasticity

The elastic domain is limited by an isotropic yield limit, which evolves with the volumetric plastic strains, and by a bilinear Mohr-Coulomb failure surface, where a progressive plasticity process is considered through the introduction of the bounding surface theory (Dafalias and Popov, 1975; Krieg, 1975; Dafalias and Popov, 1977). The choice of a bilinear Mohr-Coulomb failure criterion is justified by the experimental evidences reported in Chapter 6, where the shear strength behaviour of Opalinus Clay has been investigated and the results have been compared with data available in the literature (Figure 6.19). The elastic domain limited by the yield surface and bounding surface, as well as the bilinear failure surface are depicted in Figure 7-3.

The isotropic yield limit is expressed as follows:

$$f_{iso} = p' - p'_c = 0 \tag{7.8}$$

where p'_c is the mean effective yield stress, which evolves with the volumetric plastic strains $\varepsilon_v^{\,p}$ as follows:

$$p'_c = p'_{c0} \exp\left(\beta \cdot \varepsilon_v^{\,p}\right) \tag{7.9}$$

where β is the plastic stiffness index and p'_{c0} is the initial reference mean effective yield stress.

The bilinear Mohr-Coulomb failure surface in the p'- q plane is expressed through the definition of two domains:

For $p' < p'_{tr}$: $$f_{MC} = q - M_2 p' r_{dev} = 0 \tag{7.10}$$

For $p' \geq p'_{tr}$: $$f_{MC} = q - M_1 \left(p' + \frac{c_{\mathrm{pq}}}{M_1} \right) r_{dev} = 0 \tag{7.11}$$

where c_{pq} is a cohesive component that allows to describe the bi-linearity of the failure surface, p'_{tr} is a threshold mean effective stress, and r_{dev} is the bounding surface deviatoric radius. The threshold mean effective stress represents the value of the mean effective stress at which the change in slope of the failure envelope occurs:

$$p'_{tr} = \frac{c_{pq}}{\left(M_2 - M_1\right)} \tag{7.12}$$

The failure surface is therefore defined by the parameter M_2 in the lower mean effective stress range, while both M_1 and c_{pq} are to be defined for the higher mean effective stress range. The parameter M_1 and M_2, and the cohesive component c_{pq} are expressed as follows:

$$M_1 = \frac{6\sin\phi'_1}{3-\sin\phi'_1} \tag{7.13}$$

$$c_{pq} = \frac{c'\cdot M_1}{\tan\phi'_1} \tag{7.14}$$

$$M_2 = \frac{6\sin\phi'_2}{3-\sin\phi'_2} \tag{7.15}$$

where ϕ'_1 is the friction angle for the domain $p' \geq p'_{tr}$ and c' is the cohesion for the same domain, while ϕ'_2 is the friction angle for the domain $p' < p'_{tr}$.

The deviatoric radius r_{dev} allows to have plasticity before reaching the failure conditions, thanks to the evolution of the bounding surface with the deviatoric plastic strain. The deviatoric radius r_{dev} evolves from its initial value r_{dev}^{el}, up to 1, and it is expressed as follows:

$$r_{dev} = r_{dev}^{el} + \frac{\varepsilon_{dev}^{p}}{a+\varepsilon_{dev}^{p}} \tag{7.16}$$

Moreover:

$$\partial r_{dev} = \frac{\left(1-r_{dev}+r_{dev}^{el}\right)^2}{a}\partial\varepsilon_{dev}^{p} \tag{7.17}$$

where a is a material parameter and ε_{dev}^{p} is the deviatoric plastic strain.

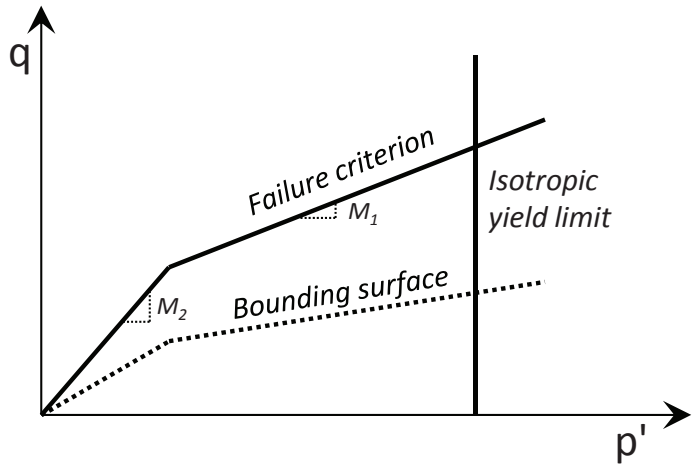

Figure 7-3: The isotropic yield limit, the bounding surface, and the failure surface for Opalinus Clay.

As introduced in Section 7.2, several experimental investigations on Opalinus Clay have highlighted the dependency of the strength on the loading orientation with respect to the bedding planes. Different approaches have been presented in the literature to reproduce the anisotropic strength behaviour as reported by Duveau et al. (1998). Among the available approaches, the empirical approach proposed by McLamore and Gray (1967) is considered in this work, where variable cohesion and friction angle are adopted as a function of the angle θ' between the loading orientation and the anisotropic planes. McLamore and Gray (1967) proposed the following relationships:

$$c'(\theta') = c'_a - c'_b \cdot \left[\cos 2\left(\theta'_{c'\min} - \theta'\right)\right]^{m_c} \tag{7.18}$$

$$\tan\phi'(\theta') = \tan\phi'_a - \tan\phi'_b \cdot \left[\cos 2\left(\theta'_{\phi'\min} - \theta'\right)\right]^{m_\phi} \tag{7.19}$$

where $\theta'_{c'\min}$ and $\theta'_{\phi'\min}$ are the angle between the loading direction and the anisotropic plane at which c' and $\tan\phi'$ have the minimum values, respectively, and $c'_a, c'_b, m_c, \phi'_a, \phi'_b, m_\phi$ are parameters of the model. The shape of Eq. (7.18) and (7.19) is shown in Figure 7-4, where $\theta'_{c'\min}$ and $\theta'_{\phi'\min}$ are taken equal to 30° and 45° respectively. The dependency of the cohesion and friction angle on the load orientation with respect to the anisotropic plane allows to capture the loss of strength that is encountered in layered materials, such as shales, when the failure surface approaches the orientation of the bedding planes.

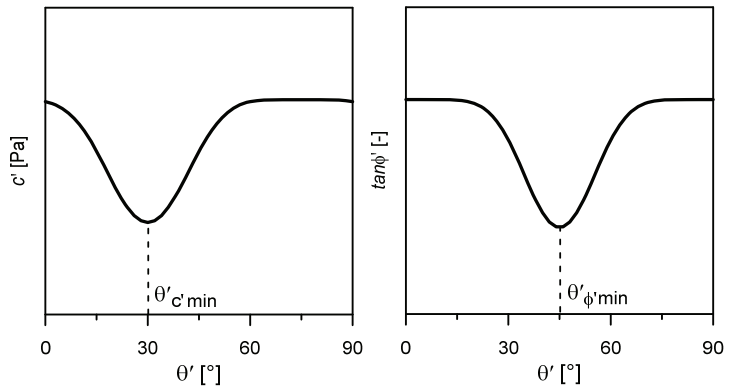

Figure 7-4: Functions describing variable cohesion and friction angle as a function of loading orientation.

The model flow rule is associated for the isotropic mechanism, therefore $f_{iso} = g_{iso}$; while non-associated flow rule is considered for the deviatoric part. In this last case the shape of the plastic potential is taken after the work of Nova and Wood (1979) and modified as follows:

$$g_{dev} = q - M_1\left(p' + \frac{c_{pq}}{M_1}\right)\left(1 - \ln\frac{2\left(p' + \frac{c_{pq}}{M_1}\right)}{p'_c}\right) = 0 \tag{7.20}$$

Therefore the plastic flows are expressed as follows:

$$d\varepsilon_v^p = \lambda_{iso}^p \frac{\partial g_{iso}}{\partial p'} + \lambda_{dev}^p \frac{\partial g_{dev}}{\partial p'} \tag{7.21}$$

$$d\varepsilon_{dev}^p = \lambda_{dev}^p \frac{\partial g_{dev}}{\partial q} \tag{7.22}$$

where λ_{iso}^p and λ_{dev}^p are the plastic multipliers, which are defined through the respect of the consistency conditions:

$$\partial f_{iso} = \frac{\partial f_{iso}}{\partial p'} \partial p' + \frac{\partial f_{iso}}{\partial p'_c} \frac{\partial p'_c}{\partial \varepsilon_v^p} \partial \varepsilon_v^p = 0 \tag{7.23}$$

$$\partial f_{MC} = \frac{\partial f_{MC}}{\partial q} \partial q + \frac{\partial f_{MC}}{\partial p'} \partial p' + \frac{\partial f_{MC}}{\partial r_{dev}} \frac{\partial r_{dev}}{\partial \varepsilon_{dev}^p} \partial \varepsilon_{dev}^p = 0 \tag{7.24}$$

The resolution of the consistency equations allows obtaining the plastic multipliers and thus the magnitude of the plastic strains.

7.4. The Disturbed State Concept (DSC)

Opalinus Clay manifests quasi-brittle failure response, with a softening behaviour which marks the transition from the peak to the ultimate state condition. In order to take this feature into account, the disturbed state concept (DSC) is introduced.

7.4.1. The concept

The disturbed state concept (DSC), proposed by Prof. Desai (Desai and Toth, 1996; Desai, 2000), is based on the idea that a mixture's response can be expressed in terms of the responses of its interacting components. In the case of the same material, the components are considered to be material parts: the relatively intact (RI) state and the fully adjusted (FA) state. As loading progresses, the material transforms progressively from the RI state to the FA state through a process of internal self-adjustment of its microstructure. The RI and FA parts are interacting mechanisms and they both contribute to the observed response of the material. So the deviation of the observed response of the material from the response of the reference – relative intact state, is due to the disturbance (D) which couples the two RI and FA parts of the same material (Figure 7-5). The observed or average response is then expressed in terms of the RI response and of the FA response by using the disturbance function, D, as an interpolation and coupling mechanism.

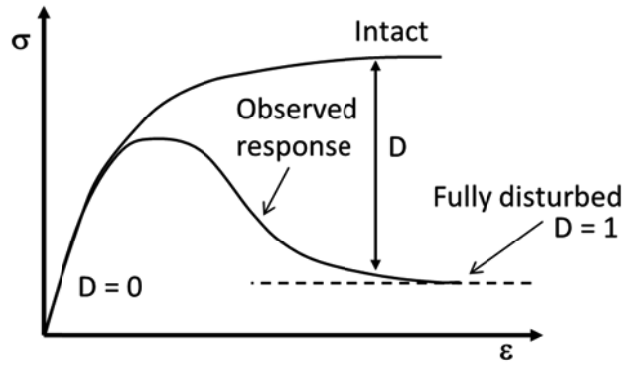

Figure 7-5: Disturbed State Concept, modified from Desai (2000).

7.4.2. The DSC formulation

The DSC model formulation is described in this section. The observed stress is divided into two stress components acting on the intact part (RI) and on the fully adjusted (FA) part, respectively. Therefore, the response of the material is due to the coupled interaction between the RI and FA parts through the disturbance function *D*, as follows:

$$\sigma_{ij}^{ob} = (1-D)\sigma_{ij}^{i} + D\sigma_{ij}^{d} \tag{7.25}$$

where σ_{ij}^{ob} is the observed stress tensor, σ_{ij}^{i} is the stress tensor for the intact part, σ_{ij}^{d} is the stress tensor for the fully adjusted part and *D* is the disturbance function. The previous expression can be written in incremental form, thus obtaining:

$$d\sigma_{ij}^{ob} = (1-D)\,\mathrm{d}\,\sigma_{ij}^{i} + Dd\sigma_{ij}^{d} + dD(\sigma_{ij}^{d} - \sigma_{ij}^{i}) \tag{7.26}$$

This formulation is then rewritten, isolating the isotropic part and the deviatoric one. The stress tensor can be written as the sum of an isotropic component and a deviatoric one as follows:

$$\sigma_{ij}^{ob} = \frac{1}{3}\sigma_{kk}\delta_{ij} + S_{ij} \tag{7.27}$$

where σ_{kk} is the trace of the isotropic stress tensor, S_{ij} is the deviatoric stress tensor and δ_{ij} is the Kronecker delta. The mean stress *p* is defined as follows:

$$p = \frac{\sigma_{kk}}{3} \tag{7.28}$$

Equation (7.25) can be rewritten as:

$$p^{ob}\delta_{ij} + S_{ij}^{\ ob} = (1-D)\left(p^{i}\delta_{ij} + S_{ij}^{\ i}\right) + D\left(p^{d}\delta_{ij} + S_{ij}^{\ d}\right) \tag{7.29}$$

Or:

$$p^{ob}\delta_{ij} + S_{ij}^{\ ob} = (1-D)p^{i}\delta_{ij} + (1-D)S_{ij}^{\ i} + Dp^{d}\delta_{ij} + DS_{ij}^{\ d} \tag{7.30}$$

Focusing only on the isotropic part, the following can be written:

$$p^{ob}\delta_{ij} = (1-D)p^{i}\delta_{ij} + Dp^{d}\delta_{ij} \tag{7.31}$$

The second invariant of the deviatoric stress tensor is defined as:

$$J_{2D} = \frac{1}{2}S_{ij}S_{ij} \tag{7.32}$$

The deviatoric stress q is defined as:

$$q = \sqrt{3J_{2D}} \tag{7.33}$$

The following relationship can be written (Katti, 1991):

$$\sqrt{J_{2D}^{\ ob}} = (1-D)\sqrt{J_{2D}^{\ i}} + D\sqrt{J_{2D}^{\ d}} \tag{7.34}$$

Writing Eq. (7.34) in terms of deviatoric stress q, the following is obtained:

$$q^{ob} = (1-D)q^{i} + Dq^{d} \tag{7.35}$$

Writing equations (7.31) and (7.35) in terms of increments, the followings are obtained:

$$dp^{ob} = (1-D)\,\mathrm{d}\,p^{i} + Ddp^{d} + dD(p^{d} - p^{i}) \tag{7.36}$$

$$dq^{ob} = (1-D)\,\mathrm{d}\,q^{i} + Ddq^{d} + dD(q^{d} - q^{i}) \tag{7.37}$$

7.4.3. The disturbance function *D*

The disturbance function, which couples the RI and the FA states, can be represented in different ways (Desai, 2000), and it is generally determined through laboratory tests. In this work it is defined as follows:

$$D = \frac{\sqrt{J_{2Di}} - \sqrt{J_{2Dob}}}{\sqrt{J_{2Di}} - \sqrt{J_{2Dd}}} \tag{7.38}$$

Or, alternatively:

$$D = \frac{q_{i} - q_{ob}}{q_{i} - q_{d}} \tag{7.39}$$

In general, the disturbance function D can be expressed in terms of internal variables α_i (such as time, temperature, chemistry, etc...):

$$D = D\left[\xi(t, T, \alpha_i)\right] \tag{7.40}$$

The original functional form of the disturbance function D as proposed by Desai (2000) is function of the deviatoric plastic strains as follows:

$$D = D_u\left(1 - e^{-A_d\left(\varepsilon_{dev}^p\right)^Z}\right) \tag{7.41}$$

where D_u, A_d and Z are the model parameters. The analysis of the experimental results on Opalinus Clay presented in Chapter 6 highlight that the softening behaviour of Opalinus Clay, and therefore the development of disturbance, depends on the mean effective stress: the greater the mean effective stress, the later the development of the disturbance occurs due to greater confinement of the material. Moreover, the mechanism of disturbance development appears to be anisotropic: when the material is loaded parallel to the bedding the material displays a higher stiffness and the softening occurs fast, at low deviatoric strain. On the other hand, when the material is loaded perpendicular to the bedding orientation, the material is more compliant and the disturbance manifests later, at higher deviatoric strain. For these reasons the original formulation reported in Eq. (7.41) is modified in order to introduce a dependency of the disturbance function D on the mean effective stress as well as on the orientation of the loading with respect to the bedding planes direction:

$$D = D_u\left[1 - e^{-\alpha}\right] \tag{7.42}$$

with:

$$\alpha = \frac{A_d\left(\varepsilon_{dev}^p\right)^{Z(\theta')}}{\left(p'\right)^{n_d}} \tag{7.43}$$

where n^d is a model parameter, and θ' is the angle between the loading direction and the bedding planes. Based on the experimental evidences reported in Chapter 6 on P- and S- samples, the following expression for $Z(\theta')$ is adopted:

$$Z = Z_S\left(1 - \frac{\cos\theta'}{3}\right) \tag{7.44}$$

where Z_S is the value of Z when the loading is perpendicular to the bedding planes $(\theta' = 90°)$. The proposed relationship should be validated or improved by considering different loading orientations with respect to the bedding planes, since in this work only the results of two loading orientations

(parallel and perpendicular to the bedding) were considered. The shape of the disturbance function is depicted in Figure 7-6 for different mean effective stress values and different values of θ'.

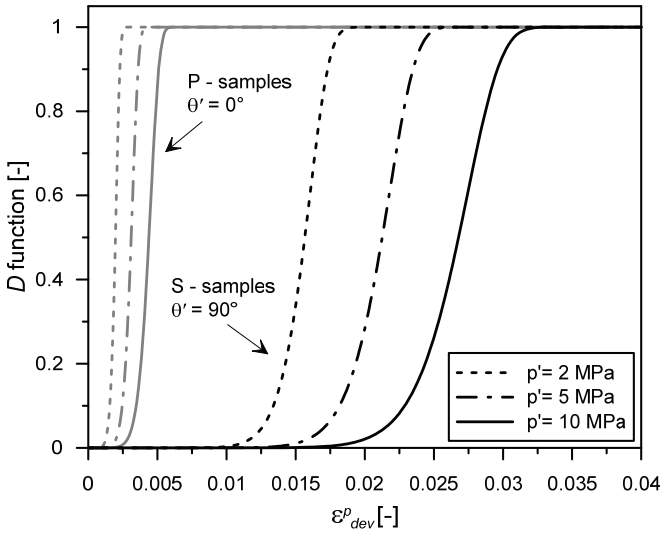

Figure 7-6: Shape of *D* function for different mean effective stress values and different values of θ'.

7.5. Numerical simulations

The RI and FA states of the material as described in Section 7.4.1, are consider here as representing the behaviour of the material before the peak and at the ultimate state, respectively. Such behaviours are reproduced using the proposed constitutive framework. The observed stress response is given by the combined action of the intact and disturbed parts according to the formulation described in Section 7.4.2. In the following section the calibration of the model parameters, as well as the results of the numerical simulations of the triaxial tests are reported.

7.5.1. Parameters calibration

The determination of the elastic parameters is described first. The results of the triaxial testing campaign reported in Chapter 6 allow to assume a reference Young modulus $E_{2,\mathrm{ref}}$ and a Poisson's ratio ν_2 for the S-samples equal to about 1000 MPa and 0.32, respectively. Moreover, the experimental evidences presented in Chapter 6 as well as the data collection reported in Bock (2009) suggest that the average anisotropy factor for the Young Modulus (E_1/E_2) can be assumed as between 2 and 2.5. An anisotropy factor of 2.2 is considered in order to determine the reference Young modulus $E_{1,\mathrm{ref}}$ for the P-samples. Moreover, a Poisson ratio ν_1 equal to 0.30 is considered taking into account both the experimental evidences presented in Chapter 6, as well as the data collection reported in Bock (2009). The shear modulus $G_{2,ref}$ is computed as follows (Wittke, 1984):

$$G_{2,ref} = \frac{E_{2,ref}}{2(1+\nu_2)} \tag{7.45}$$

Finally, an overage value for the elastic exponent n_{el} equal to 0.5 is estimated from the results presented in Figure 6.20. The adopted anisotropic elastic parameters are reported in Table 7-1, and they are attributed to the intact state of the material. The elastic properties of the fully disturbed material are not investigated in this work; however, their values do not affect the observed response of the material in the considered cases, since when the disturbance manifests, the material is already in the post-peak domain.

The model parameters related to the shear strength behaviour (ϕ'_1, ϕ'_2 and c') are estimated based on the results of the triaxial testing campaign presented in Chapter 6 and on their comparison with data from the literature, as depicted in Figure 6.19. For the intact material (RI) a value of ϕ'_2 equal to 45° has been assumed for the low mean effective stress range ($p' < p'_{tr}$), while values of 22° and 2.6 MPa have been assumed for the friction angle and cohesion, respectively, in the higher mean effective stress range ($p' \geq p'_{tr}$). For the fully disturbed material (FA) a value of ϕ'_2 equal to 45° has been assumed for the low mean effective stress range ($p' < p'_{tr}$), while values of 18° and 0.8 MPa have been assumed for the friction angle and cohesion, respectively, in the higher mean effective stress range ($p' \geq p'_{tr}$).

The analysis of the elasto-plastic behaviour of Opalinus Clay conducted in Chapter 3, as well as in Chapters 4 and 5, allows to estimate a value for the mean effective yield stress between 9 and 16 MPa. This is done by converting the vertical effective yield stress estimated using Casagrande (1936) method, into mean effective yield stress, by considering the K_0 coefficient, which is computed according to Jaky (1948):

$$K_0 = 1 - \sin\phi' \tag{7.46}$$

and

$$p'_c = \frac{\sigma'_c\left(1+2K_0\right)}{3} \tag{7.47}$$

The initial mean effective stress p'_{c0} is taken equal to 12 MPa. The remaining parameters (β, r_{dev}^{el} and a) are calibrated by curve fitting and the adopted values are reported in Table 7-1. In particular, the parameter r_{dev}^{el} dictates the amount of plasticity that is experienced through the activation of the bounding surface. From this point of view, an anisotropic behaviour is experimentally observed, where more plasticity is manifested by the S-samples with respect to the P-samples. Therefore, the value of r_{dev}^{el} must be related to the angle θ' between the loading direction and the bedding planes. The following expression for r_{dev}^{el} is adopted:

$$r_{dev}^{el} = r_{dev,S}^{el}\left(1+5\cos\theta'\right) \tag{7.48}$$

where $r_{dev,S}^{el}$ is the value of r_{dev}^{el} for the S- samples, when the loading is perpendicular to the bedding planes $(\theta' = 90°)$. Eq. (7.48) is determined based on the results of two loading orientations (parallel and perpendicular to the bedding planes); therefore, the proposed relationship should be validated or improved by considering different loading orientations with respect to the bedding planes direction.

Table 7-1: Mechanical model parameters.

Parameter	Unit	Intact State	Fully Disturbed State
$E_{1\,ref}$	[MPa]	2330	-
$E_{2\,ref}$	[MPa]	1060	-
ν_1	[-]	0.30	-
ν_2	[-]	0.32	-
$G_{2\,ref}$	[MPa]	400	-
n_{el}	[-]	0.5	-
β	[-]	60	-
ϕ'_2	[°]	45	45
ϕ'_1	[°]	22	18
c'	[MPa]	2.6	0.8
$r_{dev,S}^{el}$	[-]	0.1	-
a	[-]	0.003	-
p'_{c0}	[MPa]	12	-

The rheological behaviour of the Opalinus Clay specimens after peak, which is reported in Chapter 6 was considered in order to determine the DSC model parameters. The adopted values are reported in Table 7-2.

Table 7-2: DSC model parameters.

Parameter	Unit	Value
D_u	[-]	1
A_d	[-]	5.1×10^{22}
Z_S	[-]	12
n_d	[-]	4

7.5.2. Results of the model performance

The results of the simulations of the triaxial tests presented in Chapter 6 are reported in this section. Figure 7-7 presents the $q - \varepsilon_a$ diagrams for both P- and S-samples tested at three levels of radial effective stress as reported in Figure 7-7. The anisotropic behaviour is well-captured by the model, where a more compliant response is observed in the simulation of the S-samples with respect to P-samples. The elasto-plastic features of the material are successfully taken into account by the model,

since accumulation of plastic deformations is observed when unloading-reloading cycles are modelled. The softening behaviour after peak is also well-reproduced, where a faster transition from peak to ultimate state is observed for the P- samples, while a smoother transition is obtained for the S-samples.

The results of the model concerning the prediction of the volumetric behaviour of the material are reported in Figure 7-8 for the S-samples and in Figure 7-9 for the P-samples. Positive strain increments correspond to compression, while negative strain increments describe expensive behaviour. The volumetric behaviour of the material tested in the perpendicular direction (S-samples) at 5 MPa and 12 MPa of radial effective stress is well reproduced by the model, however higher compressive volumetric strain is predicted by the model at 2 MPa of radial effective stress. The volumetric behaviour of the material tested parallel to the bedding planes (P-samples) is also quite well reproduced by the model.

The experimental and model results for all the tested S-samples are presented in Figure 7-10 in the $p'-q$ and $q-\varepsilon_a$ diagrams, while the same diagrams are presented for all the tested P-sample in Figure 7-11. The results of the simulations show that the strength and stiffness dependency on the mean effective stress level are well taken into account. Moreover, the dependency of the onset of disturbance development on the mean effective stress is also well reproduced thanks to the modification of the disturbance function *D* as detailed in Section 7.4.3.

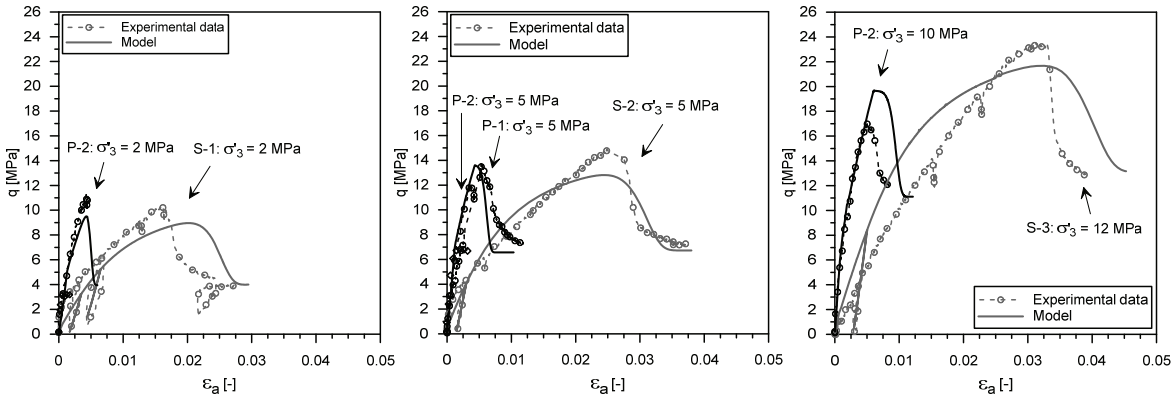

Figure 7-7: Deviatoric stress versus axial strain behaviour for P- and S-samples: experimental results and numerical simulations.

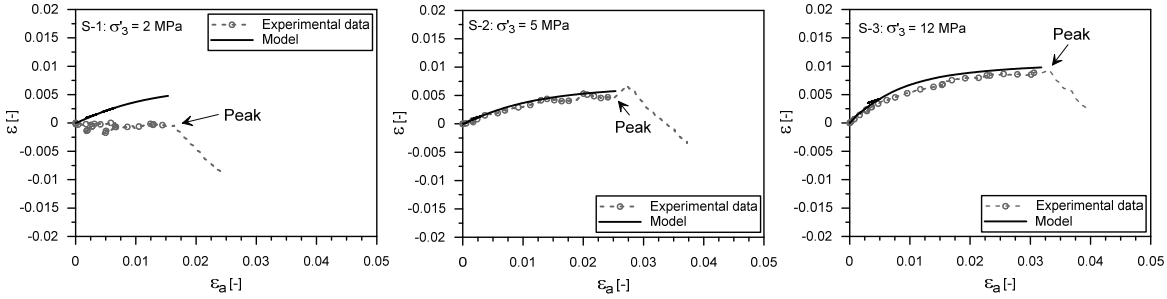

Figure 7-8: Volumetric behaviour of S-samples upon triaxial compression: experimental results and numerical simulations.

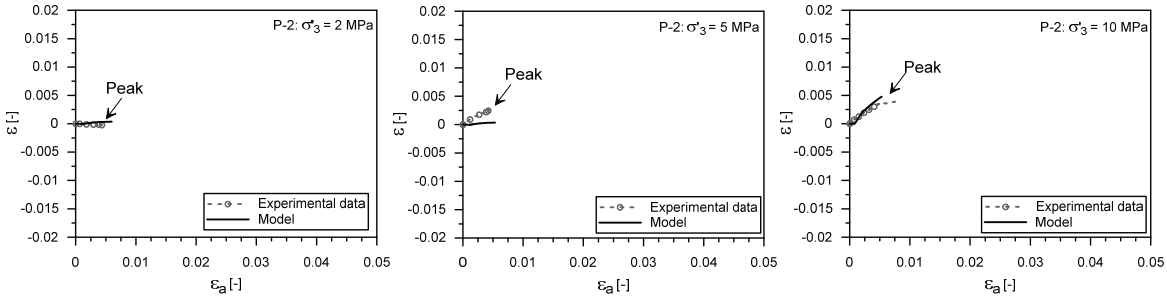

Figure 7-9: Volumetric behaviour of P-samples upon triaxial compression: experimental results and numerical simulations.

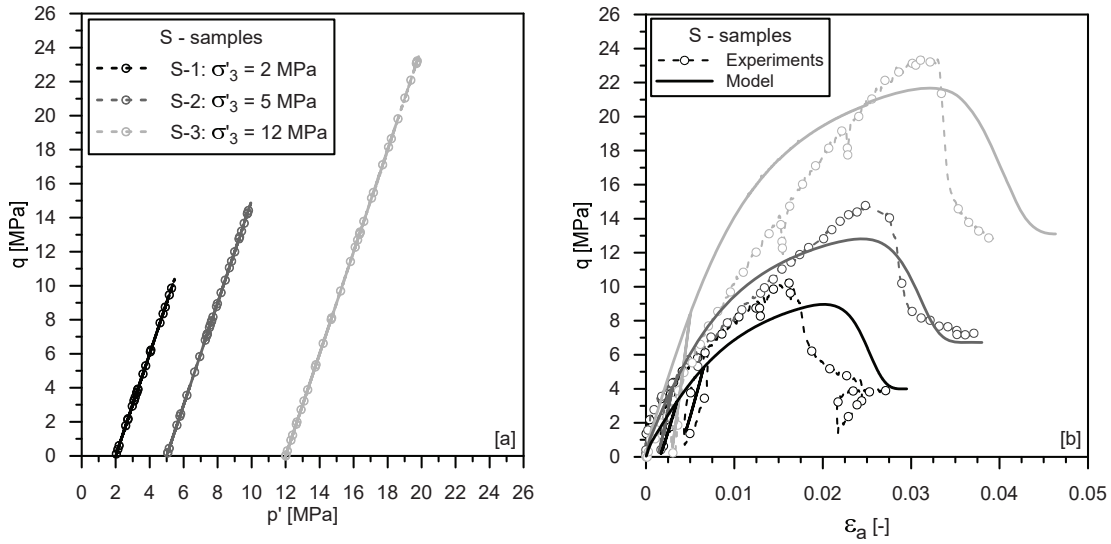

Figure 7-10: Experimental and model results for the tested S-samples: stress paths in the *p'- q* plane [a] and deviatoric stress versus axial strain [b].

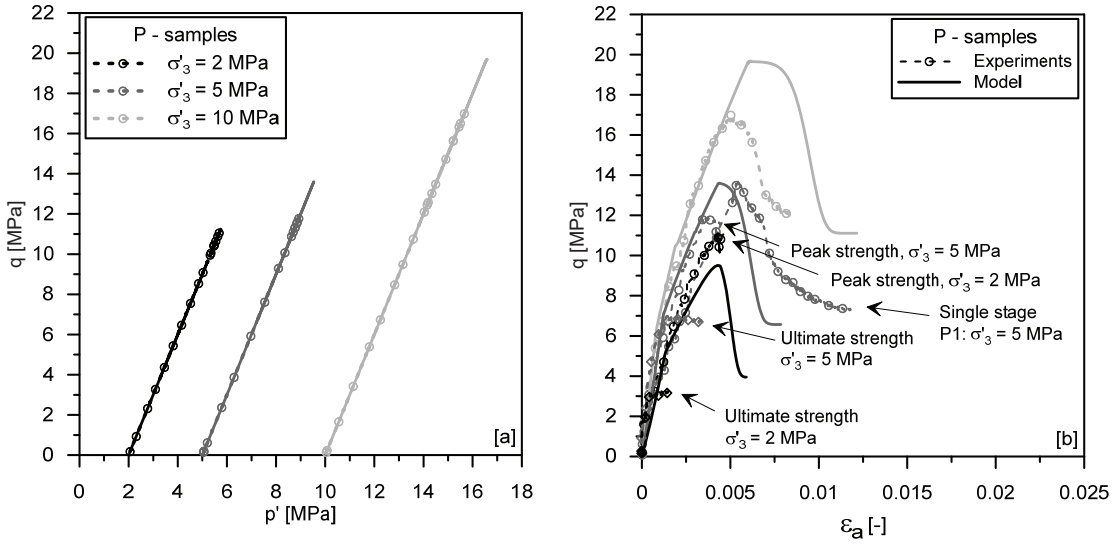

Figure 7-11: Experimental and model results for the tested P-samples: stress paths in the *p'*- *q* plane [a] and deviatoric stress versus axial strain [b].

7.6. Concluding remarks

In this chapter a constitutive framework was developed with the aim to reproduce and predict the mechanical response of Opalinus Clay. The rheological characteristics of the shale were studied in the previous chapters of the Thesis and were carefully taken into account in order to formulate the constitutive equations. The transversely isotropic elasticity equations have been considered in order to reproduce the transversely isotropic elastic response of the material. Moreover, the five independent elastic parameters, which constitute the transversely isotropic elastic stiffness matrix, are defined in order to manifest stress dependency of the elastic moduli and of the shear moduli. The possibility to consider an anisotropic strength response has also been included in the model.

Finally, the proposed constitutive approach includes the introduction of the disturbed state concept (DSC) in order to reproduce the softening behaviour of the material. The disturbance function has been formulated in order to consider the stress dependency of the onset of disturbance development. Moreover, a dependency of the disturbance function on the loading orientation with respect to the bedding planes has been introduced in order to reproduce the anisotropic response in the mechanism of disturbance development. However, the law describing such dependency should be further validated based on experimental results, which consider different loading orientations with respect to the bedding planes direction.

The numerical simulations of the triaxial tests presented in Chapter 6 highlighted the capability of the constitutive framework to take into account the main rheological features of the mechanical behaviour of Opalinus Clay. The elasto-plastic features of the material are successfully taken into account, while the introduction and re-elaboration of the DSC provide an alternative and simple formulation to model the softening after peak and thus the transition from the peak (failure) condition, to the ultimate state condition.

The proposed constitutive framework benefits of a relatively moderate number of parameters, which can be easily determined through conventional laboratory tests such as triaxial tests. Therefore, it can be readily applied to any shale or similar geomaterial, whose behaviour has been experimentally studied through a few series of triaxial tests. Moreover the model allows to predict the stress-strain response of the material under different type of loading, as shown in Chapter 5, where the oedometric loading response of Opalinus Clay has been successfully reproduced.

The proposed model presents also the advantage to be flexible: the framework can be further developed in order to take into account the multiphysical behaviour of the involved material. This fact has been demonstrated in Chapter 5, where the effects of the osmotic suction have been taken into account through the introduction of a new independent variable inside the proposed mechanical framework. Therefore, the chemo-mechanical behaviour of Opalinus Clay could be successfully reproduced.

7.7. References

Bock, H. RA Experiment: Updated Review of the Rock Mechanics Properties of the Opalinus Clay of the Mont Terri URL based on Laboratory and Field Testing. TECHNICAL REPORT 2008-04 (2009).

Casagrande, A. The determination of the pre-consolidation load and its practical significance. Proceedings of the international conference on soil mechanics and foundation engineering, Harvard University Cambridge, (1936). 60-64.

Corkum, A.G. and Martin, C.D. The mechanical behaviour of weak mudstone (Opalinus Clay) at low stresses. International Journal of Rock Mechanics and Mining Sciences (2007) 44(2): 196-209.

Dafalias, Y. and Popov, E. A model of nonlinearly hardening materials for complex loading. Acta mechanica (1975) 21(3): 173-192.

Dafalias, Y.F. and Popov, E.P. Cyclic loading for materials with a vanishing elastic region. Nuclear Engineering and Design (1977) 41(2): 293-302.

Desai, C.S. Mechanics of materials and interfaces: The disturbed state concept, CRC press, (2000).

Desai, C.S. and Toth, J. Disturbed state constitutive modeling based on stress-strain and nondestructive behavior. International Journal of Solids and Structures (1996) 33(11): 1619-1650.

Duveau, G., Shao, J. and Henry, J. Assessment of some failure criteria for strongly anisotropic geomaterials. Mechanics of Cohesive-frictional Materials (1998) 3(1): 1-26.

François, B. and Laloui, L. ACMEG-TS: A constitutive model for unsaturated soils under non-isothermal conditions. International Journal for Numerical and Analytical Methods in Geomechanics (2008) 32(16): 1955-1988.

Gräsle, W. Multistep triaxial strength tests: Investigating strength parameters and pore pressure effects on Opalinus Clay. Physics and Chemistry of the Earth, Parts A/B/C (2011) 36(17): 1898-1904.

Hsu, S.-C. and Nelson, P.P. Characterization of eagle ford shale. Engineering Geology (2002) 67(1): 169-183.

Islam, M.A. and Skalle, P. An experimental investigation of shale mechanical properties through drained and undrained test mechanisms. Rock mechanics and rock engineering (2013) 46(6): 1391-1413.

Jahns, E. Geomechanical laboratory tests on Opalinus Clay cores from the bore hole Schlattingen SLA-1. Nagra Work Report NAB (2013): 13-18.

Jaky, J. Pressure in soils. Proceedings of the 2nd international conference on soil mechanics and foundation engineering, (1948). 103-107.

Katti, D.R. Modelling including associated testing of cohesive soil using disturbed state concept. (1991).

Krieg, R. A practical two surface plasticity theory. Journal of applied mechanics (1975) 42(3): 641-646.

McLamore, R. and Gray, K. The mechanical behavior of anisotropic sedimentary rocks. Journal of Manufacturing Science and Engineering (1967) 89(1): 62-73.

Naumann, M., Hunsche, U. and Schulze, O. Experimental investigations on anisotropy in dilatancy, failure and creep of Opalinus Clay. Physics and Chemistry of the Earth, Parts A/B/C (2007) 32(8): 889-895.

Niandou, H., Shao, J., Henry, J. and Fourmaintraux, D. Laboratory investigation of the mechanical behaviour of Tournemire shale. International Journal of Rock Mechanics and Mining Sciences (1997) 34(1): 3-16.

Nova, R. and Wood, D.M. A constitutive model for sand in triaxial compression. International Journal for Numerical and Analytical Methods in Geomechanics (1979) 3(3): 255-278.

Popp, T. and Salzer, K. Anisotropy of seismic and mechanical properties of Opalinus clay during triaxial deformation in a multi-anvil apparatus. Physics and Chemistry of the Earth, Parts A/B/C (2007) 32(8): 879-888.

Siegesmund, S., Popp, T., Kaufhold, A., Dohrmann, R., Gräsle, W., Hinkes, R. and Schulte-Kortnack, D. Seismic and mechanical properties of Opalinus Clay: comparison between sandy and shaly facies from Mont Terri (Switzerland). Environmental earth sciences (2014) 71(8): 3737-3749.

Wild, K., Amann, F., Martin, C., Wassermann, J., David, C. and Barla, M. Dilatancy of clay shales and its impact on pore pressure evolution and effective stress for different triaxial stress paths. 49th US Rock Mechanics/Geomechanics Symposium, American Rock Mechanics Association, (2015).

Wittke, W. Rock mechanics based on an anisotropic jointed rock model (AJRM), John Wiley & Sons, (2014).

Wittke, W. Felsmechanik, Springer-Verlag, Berlin, (1984).

Wong, R. Swelling and softening behaviour of La Biche shale. Canadian geotechnical journal (1998) 35(2): 206-221.

Conclusions

1. Summary of the achieved results

The research conducted in this Thesis has contributed to the expansion of the available experimental database on the multiphysical behaviour of shales, taking into account the thermo-hydro-chemo-mechanical conditions encountered in geo-energy applications and in particular in the nuclear waste geological disposal. The obtained experimental results have provided a better understanding of the behaviour of the selected host formation for the construction of a nuclear waste repository in Switzerland. The constitutive analysis has allowed the development of a framework to model and predict the behaviour of shales. A focus on the main achievements is reported in the following sections.

1.1. Results on the water retention behaviour

An advanced testing methodology was developed, in order to overcome the great challenge of testing the retention properties of materials with very low porosity and pore size. The proposed technique has been capable of capturing important features of the retention behaviour of shales. In particular the following results are highlighted:

- The hysteresis domain for the studied shales has been identified, scanning paths occur within this domain when the shale is initially rewetted from its after-extraction state. This fact must be taken into account when hydraulic properties of the material, such as relative permeability, are sought;
- The air entry value of Opalinus Clay is found to increase with the decrease in void ratio of the material; an exponential function is proposed in order to capture the observed trend;
- The minimum relative humidity threshold at which the studied shales can be exposed without experiencing desaturation has been identified for a selected reference temperature; moreover, this threshold is a function of the void ratio of the material;
- The mineralogical composition and the dominant entrance pore size are found to impact the retention behaviour of the material, where higher quartz content and a greater dominant entrance pore size reduce the retention capabilities of the material.

The obtained results are of great importance, since the retention capacity is a characteristic that plays a fundamental role during the ventilation (drying) and resaturation (wetting) phases of the nuclear waste repository.

1.2. Results on the compression and consolidation behaviour of intact and remoulded shales

An advanced high-pressure oedometric cell and a new comprehensive technique for investigating the one-dimensional volumetric behaviour and consolidation of shales have been developed. An analytical solution was rigorously derived to enable the analysis of the time-dependent settlement curves of the tested shales. The developed method allows for the interpretation of the experimental

results in light of the deformation of the testing device and of the secondary consolidation phenomenon. Thanks to the proposed experimental procedure and analytical technique, fundamental hydro-mechanical features of Swiss shales, at intact and remoulded states, retrieved from different depths and different sites, were successfully investigated:

- The values of the oedometric modulus and consolidation coefficient, and their dependency on the stress level and stress path were successfully defined for all the tested shales. Deeper shales manifest greater stiffness than shallower shales when tested at the same effective stress level, in response to relevant diagenetic processes;
- The insight into the swelling behaviour of Opalinus Clay highlights that the swelling pressure values are related to the initial void ratio of the material. Moreover, the results reveal that the development of the swelling pressure is a complex mechanism which involves the mineralogical composition and the geologic history (diagenesis) of the shale formation. In general, a lower swelling sensitivity is registered for the deeper shales, as results of diagenetic effects; while greater swelling tendency is manifested when the material is disturbed or remoulded;
- Significant information regarding the poroelastic behaviour of the tested material was derived, extending the available knowledge concerning the poroelastic parameters of Opalinus Clay;
- The values of the secondary compression coefficient were investigated as a function of the vertical effective stress. Diagenetic effects are found to cause a reduction of the creep deformations experienced by the material;
- The peculiar permeability-void ratio relationship was analysed for the tested shales. Diagenesis is found to have little impact on the permeability of the tested shales;
- Diagenetic effects in Opalinus Clay are found to cause an important reduction in porosity, as the void ratio of the intact material cannot be reached simply by mechanical compaction of the remoulded one.

Porosity variations due to consolidation processes, creep effects and diagenetic phenomena are of major concern in all applications involving shales. These results can provide guidance regarding consolidation and settlements evolution during tunnel excavation, swelling phenomena during resaturation, displacements related to delayed convergence due to creep effects, and porosity variations due to possible diagenetic processes in a long-term perspective.

1.3. Results on the thermo-mechanical volume change behaviour

The results presented in this Thesis widen the scientific knowledge on the thermal response of shales under different stress conditions, and on the effects of temperature on their hydro-mechanical properties. The major outcomes are the following:

- The volumetric behaviour of Opalinus Clay during heating is found to be dependent on the OCR: thermal expansion is observed when the material is heated at high OCR values, whereas thermal

compaction and porosity reduction are observed when the material is subjected to heating at a vertical effective stress that is close to the vertical effective yield stress (low OCR);

- The volumetric behaviour of Opalinus Clay when subjected to heating/cooling cycles was analysed: first heating cycles caused irreversible compaction or irreversible expansion, depending on the value of the OCR. Additional heating/cooling cycles revealed a reversible behaviour;
- The negligible effects of temperature on the oedometric modulus and on the secondary compression coefficient suggest that the overall mechanical performance of the shale formation is not affected in a significant way when heated within the specified temperature range;
- Consolidation processes are improved upon heating: a faster dissipation of the induced excess pore water pressures is found, thanks to the decrease in pore fluid viscosity with the increase in temperature;
- A decrease in the yield threshold is observed upon compression at high temperature (80°C), with respect to the yield threshold found at ambient temperature.

Among the outcomes listed above, particular attention must be addressed to the decrease in the yield stress with increasing temperature, since the thermal load induced by the emplacement of a heat source in the considered shale formation may result in the development of plastic settlements when the in-situ stress is sufficiently close to the yield stress. While, when heating is conducted at an in-situ stress that is sufficiently low with respect to the yield stress, thermal expansion is expected together with an increase in the material void ratio under constant effective stress conditions.

1.4. Results on the chemo-mechanical coupled processes

The results of the testing campaign, which was carried out with the aim of characterizing the chemo-osmotic processes in Opalinus Clay and their impact on the hydro-mechanical behaviour of the shale, allow to draw the following conclusions:

- The swelling potential of the material decreases if the osmotic suction of the pore fluid is increased; therefore, the self-sealing properties of the material are reduced at high osmotic suction values;
- The increase in osmotic suction at constant effective stress conditions leads to irreversible chemical settlements development; the magnitude of these settlements is related to the stress conditions and stress history of the material;
- No relevant impact of the osmotic suction on the stiffness and consolidation coefficient of Opalinus Clay is observed for the investigated range of osmotic suction values (1 – 15 MPa); therefore, the hydro-mechanical performance of the shale is not affected in a significant way;

- The effective diffusion coefficient for the shale is derived from the analysis of the chemical consolidation behaviour; the information is useful in order to estimate the time for ions diffusion processes to take place;

- The combined analysis of the chemical consolidation mechanism, of the MIP tests results and of the knowledge concerning chemo-osmotic effects in clays, allows to discuss possible microstructural changes during osmotic suction variations: irreversible chemical settlements are likely to generate from the collapse of bigger pores where the contact forces among particles are lower; whereas the reversible reduction in the dominant entrance pore size is likely due to reversible double layer effects which take place in the clay matrix of the shale.

The presented experimental evidences widen the knowledge on the coupled chemo-mechanical behaviour of shales, providing a base for a better understanding of the material performance under multiphysical conditions, and allowing the development of a constitutive framework to reproduce and predict the coupled chemo-mechanical behaviour of shales. The chemo-mechanical elasto-plastic framework includes the dependency of the osmotic stiffness on the maximum stress level reached, as well as the possibility to reproduce irreversible chemical settlements. The framework has been calibrated and successfully applied in order to back analyse the results of the chemo-mechanical testing campaign on Opalinus Clay.

1.5. Results on the experimental and constitutive analysis of the anisotropic mechanical behaviour of Opalinus Clay

Triaxial tests on Opalinus Clay in carefully saturated and drained conditions were carried out in order to study the anisotropic mechanical behaviour of the material. The results on P- and S-samples of Opalinus Clay retrieved at the Mont Terri URL allow to draw the following conclusions:

- Opalinus Clay P- and S-samples manifest similar properties in terms of both peak and ultimate shear strength, regardless the direction of loading with respect to the bedding orientation;

- The comparison of the results with additional recent data available in the literature shows that the failure behaviour of Opalinus Clay, in the investigated range, can be well reproduced through a bilinear Mohr-Coulomb failure criterion;

- A marked anisotropic elastic behaviour is observed for the tested shale, where S-samples present a more compliant response than P-samples. Moreover, the Young moduli are found to increase with the increase in mean effective stress.

The triaxial tests results have been analysed in order to derive relevant rheological characteristics of the shale. Subsequently, a suitable constitutive framework was developed in order to model and predict the hydro-mechanical response of the material. The model features the following:

- Transversely isotropic elasticity equations are considered in order to reproduce the transversely isotropic elastic response of the material;

- The five independent elastic parameters constituting the transversely isotropic elastic matrix are defined in order to manifest stress dependency of the Young moduli and of the shear moduli;
- The possibility to consider anisotropic strength response is included in the model through the definition of variable cohesion and friction angle as a function of the loading orientation with respect to the anisotropy planes;
- The disturbed state concept (DSC) is introduced in order to reproduce the softening behaviour of the material. The disturbance function is formulated in order to consider the stress dependency of the disturbance development process. Moreover, a dependency of the disturbance function on the loading orientation with respect to the bedding planes has been introduced in order to reproduce the anisotropic response in the disturbance development process.

The numerical simulations of the triaxial tests results presented in this Thesis highlighted the capability of the constitutive framework to take into account the main rheological features of Opalinus Clay.

2. Future perspectives

In this conclusive section some perspectives for future work and possible further developments are suggested. The research presented in this Thesis has investigated the multiphysical phenomena occurring in shales and their impact on the mechanical response of the involved material. The study has been conducted by considering one additional physical variable (temperature, osmotic suction and total suction) at a time, in order to better identify its impact on the behaviour of the material. However, in real geo-energy applications, such physical variables are likely to act simultaneously. For instance, the rewetting front coming from the host-formation after the closure of the nuclear waste repository may advance together with the propagation of the heating front from the canister containing the radioactive waste; variations in depth of the repository may induce both a variation in temperature as well as in the pore fluid osmotic suction. Therefore, the study of the material response under the combined action of different physical variables remains to be investigated.

The research conducted in this Thesis provides significant evidences on the impact of temperature on elasto-plastic properties of the material; however other thermo-mechanical aspects in shales remain to be better investigated, such as:

- The impact of temperature on the retention properties of shales;
- The effect of temperature on the mechanical response of shales in unsaturated conditions;
- The impact of temperature on the shear strength of shales;
- The impact of temperature on the long-term creep response.

Further insights into the anisotropic mechanical response of shales are also recommended as future perspectives. The shear strength behaviour of Opalinus Clay has been investigated on specimens tested parallel (P-samples) and perpendicular (S-samples) to the bedding planes. The study of the

mechanical behaviour of shale specimens tested at an angle of 45° (Z-samples) or 30° (X-samples) with respect to the bedding plane orientation is suggested. In fact, no tests results obtained from sounded experimental procedures and carried out in saturated conditions are available on this type of specimens. Therefore, the performance of such tests is considered fundamental in order to better investigate the anisotropic mechanical behaviour of the material. In fact, the results of these tests would allow to better analyse the failure mode of shales, as well as the impact of the bedding orientation on the peak and ultimate shear strength. Moreover, a more comprehensive database is of utmost importance to further develop the constitutive framework formulated in this Thesis.

The mechanical behaviour of shales in controlled unsaturated conditions remains to be studied. Detailed analyses are needed in order to better characterize the impact of suction on the strength, stiffness and hydraulic properties of the material. Moreover, one of the major limits encountered in the evaluation of the hydro-mechanical behaviour of shales is the lack of knowledge concerning the effective stress definition in unsaturated conditions. In fact, the contribution of suction to the effective stress for shales is currently unknown, and therefore, remains to be investigated. Further research and experimental evidences addressing this thematic would provide significant advances in the understanding of the multiphysical response of shales. Moreover, they would allow the development of constitutive and numerical models capable of reproducing the hydro-mechanical response of shales in unsaturated conditions.

The nuclear waste geological disposal in shale formations foresees long-term storage conditions (thousands of years). Therefore, the study of the long-term creep behaviour of the involved material should be also considered, in order to better characterize the long-term performance of the repository. In particular, the creep behaviour at different temperatures and considering different pore fluids would be of interest, given the considered multiphysical context. These analyses would also be of great interest in other geo-energy applications involving shale formations for long-term storage or exploitation, such as the CO_2 capture and storage technology and the deep geothermal energy recovery.

Appendix A
Summary table of all tests performed and shale cores used

The complete list of tests performed in the PhD thesis is reported in Table 1. The table reports the tests described in Chapters 2, 3, 4, 5 and 6. The tests are listed in order of appearance in the thesis. Details about the cores used, their location and depth are also provided.

Table 1: Summary table of all tests performed, the shale tested (OPA= Opalinus Clay, BD= Brown Dogger), and the cores used together with their location and depth.

Test	*Shale*	*Location*	*Core*	*Depth* (m)
Chapter 2				
Water retention behaviour	Intact OPA	Mont Terri	BHG-D1	~300 m
Water retention behaviour	Intact BD	Schlattingen	BD-6	766.67 - 767.00
Water retention behaviour	Intact OPA	Schlattingen	OPA-3	837.44 - 837.66
Water retention behaviour	Intact OPA	Schlattingen	OPA-18	891.00 - 891.25
Water retention behaviour	Intact OPA	Schlattingen	OPA-20	854.60 - 854.82
Water retention behaviour	Intact OPA	Schlattingen	OPA-6	882.20 - 882.50
Water retention behaviour	Intact BD	Schlattingen	BD-7	781.18 - 781.48
Water retention behaviour	Intact BD	Schlattingen	BD-18	774.95 - 775.16
Water retention behaviour	Intact BD	Schlattingen	BD-30	807.14 - 807.44
Chapter 3				
High pressure 1D compression	Intact OPA	Mont Terri	BOP-A5	~300 m
High pressure 1D compression	Intact OPA	Mont Terri	BHG-D1	~300 m
High pressure 1D compression	Intact OPA	Schlattingen	OPA-18	891.00 - 891.25
High pressure 1D compression	Intact OPA	Schlattingen	OPA-20	854.60 - 854.82
Low pressure 1D compression	Remoulded OPA	Mont Terri	BHG-D1	~300 m
High pressure 1D compression	Remoulded OPA	Mont Terri	BHG-D1	~300 m
High pressure 1D compression	Remoulded OPA	Mont Terri	BHG-D1	~300 m
High pressure 1D compression	Remoulded OPA	Schlattingen	OPA-6	882.20 - 882.50
Low pressure 1D compression	Remoulded OPA	Schlattingen	OPA-6	882.20 - 882.50
Permeability tests	Remoulded OPA	Mont Terri	BHG-D1	~300 m
High pressure 1D compression	Intact OPA	Schlattingen	OPA-2	837.98 - 838.25
High pressure 1D compression	Intact OPA	Schlattingen	OPA-6	882.20 - 882.50
High pressure 1D compression	Intact OPA	Schlattingen	OPA-6	882.20 - 882.50
High pressure 1D compression	Intact BD	Schlattingen	BD-6	766.67 - 767.00
High pressure 1D compression	Intact BD	Schlattingen	BD-16	769.55 - 769.85
High pressure 1D compression	Intact BD	Schlattingen	BD-12	778.30 - 778.52
High pressure 1D compression	Intact BD	Schlattingen	BD-7	781.18 - 781.48

Table 2: Summary table of all tests performed, the shale tested (OPA= Opalinus Clay, BD= Brown Dogger), and the cores used together with their location and depth (continued).

Test	*Shale*	*Location*	*Core*	*Depth* (m)
Chapter 4				
High pressure/ high temperature 1D compression	Intact OPA	Mont Terri	BHG-D1	~300 m
High pressure/ high temperature 1D compression	Intact OPA	Mont Terri	BHG-D1	~300 m
High pressure/ high temperature 1D compression	Intact OPA	Mont Terri	BHG-D1	~300 m
Thermal behaviour	Intact OPA	Mont Terri	BHG-D1	~300 m
Thermal behaviour	Intact OPA	Mont Terri	BHG-D1	~300 m
Thermal behaviour	Intact OPA	Mont Terri	BHG-D1	~300 m
Chapter 5				
Wetting tests – impact of osmotic suction	Intact OPA	Mont Terri	BHG-D1	~300 m
Chemo-mechanical 1D compression	Intact OPA	Mont Terri	BOP-A5	~300 m
Chemo-mechanical 1D compression	Intact OPA	Mont Terri	BHG-D1	~300 m
Chemo-mechanical 1D compression	Intact OPA	Mont Terri	BHG-D1	~300 m
Chemo-mechanical 1D compression	Intact OPA	Mont Terri	BHG-D1	~300 m
Chemo-mechanical 1D compression	Intact OPA	Mont Terri	BHG-D1	~300 m
MIP tests – impact of osmotic suction	Intact OPA	Mont Terri	BHG-D1	~300 m
Chapter 6				
CD triaxial test	Intact OPA	Mont Terri	BFE-B019	~300 m
CD multistage triaxial test	Intact OPA	Mont Terri	BFE-B022	~300 m
CD triaxial test	Intact OPA	Mont Terri	BDR-B7	~300 m
CD triaxial test	Intact OPA	Mont Terri	BDR-B7	~300 m
CD triaxial test	Intact OPA	Mont Terri	BDR-B7	~300 m

Appendix B
Derivation of the Biot coefficient in oedometric conditions for a transversely isotropic geomaterial

The Biot coefficient under oedometric conditions is defined in Chapter 3 in accordance with the definition expressed in Eq. (3.13). Here, this coefficient is derived as a function of the elastic properties for a transversely isotropic geomaterial. Shales generally manifest transversely isotropic elastic response, and their mechanical behaviour can be described by means of the stress-strain relationship:

$$\delta\varepsilon_{ij} = D_{ijkl}\delta\sigma'_{kl} \tag{1}$$

where D_{ijkl} is the transversely isotropic elastic matrix. The effective stress is defined as follows:

$$\delta\sigma'_{kl} = \delta\sigma_{kl} - \alpha_{kl}\delta u \tag{2}$$

where σ'_{kl} is the effective stress tensor, σ_{kl} is the total stress tensor, u is the pore water pressure and ε_{ij} is the strain tensor:

$$\delta\varepsilon_{ij} = \left[\delta\varepsilon_x \;\delta\varepsilon_y \;\delta\varepsilon_z \;\delta\gamma_{xy} \;\delta\gamma_{xz} \;\delta\gamma_{yz}\right]^T \tag{3}$$

$$\delta\sigma_{kl} = \left[\delta\sigma_x \;\delta\sigma_y \;\delta\sigma_z \;\delta\tau_{xy} \;\delta\tau_{xz} \;\delta\tau_{yz}\right]^T \tag{4}$$

Moreover, the Biot coefficient α_{kl} is defined as follows for anisotropic materials (Cheng, 1997):

$$\alpha_{kl} = \left[\alpha_x \;\alpha_y \;\alpha_z \;0\;0\;0\right]^T \tag{5}$$

with $\alpha_x = \alpha_y = \alpha_1$ and $\alpha_z = \alpha_3$ for the case of transverse isotropy.

The elastic matrix D_{ijkl} for a transversely isotropic material is defined as follows:

$$D_{ijkl} = \begin{bmatrix} \frac{1}{E_x} & -\frac{\nu_{xy}}{E_x} & -\frac{\nu_{zx}}{E_z} & 0 & 0 & 0 \\ -\frac{\nu_{xy}}{E_x} & \frac{1}{E_x} & -\frac{\nu_{zx}}{E_z} & 0 & 0 & 0 \\ -\frac{\nu_{zx}}{E_z} & -\frac{\nu_{zx}}{E_z} & \frac{1}{E_z} & 0 & 0 & 0 \\ 0 & 0 & 0 & \frac{2(1+\nu_{xy})}{E_x} & 0 & 0 \\ 0 & 0 & 0 & 0 & \frac{1}{G_z} & 0 \\ 0 & 0 & 0 & 0 & 0 & \frac{1}{G_z} \end{bmatrix} \tag{6}$$

where E_x and ν_{xy} are the elastic modulus and Poisson's ratio in the direction parallel to the bedding, E_z and ν_{zx} are the elastic modulus and Poisson's ratio in the direction perpendicular to the bedding, and G_z is the shear modulus related to shearing along the bedding plane.

In the oedometric case, the following conditions hold:

$$\delta\varepsilon_x = \delta\varepsilon_y = 0 \tag{7}$$

$$\delta\sigma_x = \delta\sigma_y = \delta\sigma_r \tag{8}$$

The following relationships are thus obtained:

$$\delta\varepsilon_z = -\frac{2\delta\sigma_r\nu_{zx}}{E_z} + \frac{\delta\sigma_z}{E_z} - \delta u\left(-\frac{2\alpha_1\nu_{zx}}{E_z} + \frac{\alpha_3}{E_z}\right) = \frac{1}{E_z}\left(\delta\sigma_z - \alpha_3\delta u\right) - \frac{2\nu_{zx}}{E_z}\left(\delta\sigma_r - \alpha_1\delta u\right) \tag{9}$$

$$\delta\varepsilon_r = \left(\frac{1-\nu_{xy}}{E_x}\right)\left(\delta\sigma_r - \alpha_1\delta u\right) - \frac{\nu_{zx}}{E_z}\left(\delta\sigma_z - \alpha_3\delta u\right) = 0 \tag{10}$$

Eq. (10) yields the following:

$$\left(\delta\sigma_r - \alpha_1\delta u\right) = \frac{\nu_{zx}}{E_z}\left(\delta\sigma_z - \alpha_3\delta u\right)\frac{E_x}{1-\nu_{xy}} \tag{11}$$

or:

$$\delta\sigma'_r = \delta\sigma'_z\,\frac{\nu_{zx}E_x}{E_z(1-\nu_{xy})} \tag{12}$$

By inserting Eq. (11) into Eq. (10), the following expression is obtained:

$$\delta\varepsilon_z = \left(\delta\sigma_z - \alpha_3\delta u\right)\frac{1}{E_z}\left[1 - \frac{2\nu_{zx}{}^2E_x}{E_z(1-\nu_{xy})}\right] = \delta\sigma'_z\,\frac{1}{E_{oed}} \tag{13}$$

Under oedometric conditions, the mean effective stress can be written as follows:

$$\delta p' = \frac{\delta\sigma'_z + 2\delta\sigma'_r}{3} = \frac{\delta\sigma'_z}{3}\left[1 + \frac{2\nu_{zx}E_x}{E_z(1-\nu_{xy})}\right] \tag{14}$$

The Biot coefficient can thus be rewritten following his definition:

$$\alpha_{oed} = \frac{\delta V_w}{\delta V} = \frac{\delta V - \delta V_s}{\delta V} = 1 - \frac{\delta p'}{K_s}\frac{E_{oed}}{\delta\sigma'_z} = 1 - \frac{E_{oed}}{3K_s}\left[1 + \frac{2\nu_{zx}E_x}{E_z(1-\nu_{xy})}\right] \tag{15}$$

Under the assumption of isotropic conditions:

$$E_x = E_z = E \tag{16}$$

$$\nu_{xy} = \nu_{zx} = \nu \tag{17}$$

Consequently:

$$\alpha_{oed} = \alpha = 1 - \frac{K}{K_s} \tag{18}$$

References

Cheng, A.-D. Material coefficients of anisotropic poroelasticity. International Journal of Rock Mechanics and Mining Sciences (1997) 34(2): 199-205.

Appendix C
Analytical Solution for 1D chemo-mechanical consolidation

C.1 Hypotheses

The derivation of the governing equations describing the chemo-mechanical consolidation process is based on the following hypotheses:

- One-dimensional process
- Elastic behaviour
- Small strains
- Presence of one ion type only
- No sorption
- Validity of Van't Hoff equation
- Saturated conditions
- Incompressibility of solid grains and fluid

C.2 Diffusion equation

Three components are needed in order to derive the diffusion equation: (i) the mass conservation equation, (ii) the fluid flow equation, and (iii) the constitutive law.

Mass conservation equation

Considering the condition of mass conservation for fluid and for solids, the equation describing the coupling between fluid pressure (u) and vertical strain (ε_z) is obtained:

$$\left[\frac{n}{K_f}+\frac{(1-n)}{K_s}\right]\frac{\partial u}{\partial t}+\frac{\partial v_{rf}}{\partial z}+\frac{\partial \varepsilon_z}{\partial t}=0 \tag{1}$$

where n is the porosity, K_f and K_s are the fluid and grains stiffness moduli, respectively, z is the space coordinate, t is the time and $v_{rf}=n\,(v_f-v_s)$ is the relative velocity of the fluid with respect to the solid part. For incompressible solid and fluid parts equation (1) can be written as follows:

$$\frac{\partial v_{rf}}{\partial z}+\frac{\partial \varepsilon_z}{\partial t}=0 \tag{2}$$

Fluid flow equation

The fluid flow is expressed by a Darcy's law type equation, where the flow of fluid is driven by both an imposed hydraulic gradient and an osmotic potential gradient:

$$v_{rf}=-k\frac{\partial h}{\partial z}+\omega k\frac{\partial \pi_h}{\partial z}=-\frac{k}{\rho_w g}\frac{\partial u}{\partial z}+\omega k\frac{RT}{\rho_w g}\frac{\partial c}{\partial z} \tag{3}$$

where k is the hydraulic conductivity, ω is the osmotic membrane efficiency, ρ_w is the density of water, g is the specific gravity, h is the hydraulic pressure head, c is the chemical concentration, and π_h is the osmotic pressure head which is expressed as follows:

$$\pi_h = \frac{\pi}{\rho_w g} = \frac{\upsilon RTc}{\rho_w g} \tag{4}$$

where π is the osmotic suction [MPa], R is the universal gas constant equal to 8.314 [J/mol/K], T is the absolute temperature [K] and υ is the number of constituents ions (equal to one according to the hypotheses). Inserting Eq.(3) in (2), the following relationship is derived:

$$\frac{\partial \varepsilon_z}{\partial t} = k\frac{\partial^2 h}{\partial z^2} - \omega k\frac{\partial^2 \pi_h}{\partial z^2} = \frac{k}{\rho_w g}\frac{\partial^2 u}{\partial z^2} - \omega k\frac{RT}{\rho_w g}\frac{\partial^2 c}{\partial z^2} \tag{5}$$

Constitutive law

A change in osmotic pressure is directly related to a change in volume, similarly to the case of a change in vertical effective stress; the constitutive relationship describing the volume changes is thus expressed as follows under the hypothesis of elastic behaviour (Fredlund and Barbour 1989, Peters and Smith 2004, Sarout and Detournay 2011):

$$d\varepsilon_z = -\frac{\partial \varepsilon_z}{\partial \sigma'_z}\partial \sigma'_z - \frac{\partial \varepsilon_z}{\partial \pi}\partial \pi \tag{6}$$

which is re-written as:

$$d\varepsilon_z = -m_v \partial \sigma'_z - m_\pi \partial \pi \tag{7}$$

where m_v is the coefficient of volume change and m_π is the osmotic coefficient of volume change. If the vertical total stress is applied and held constant, the magnitude of the change in effective stress is equal to the magnitude of the change in fluid pressure and Eq.(7) can be rewritten as follows:

$$d\varepsilon_z = m_v \partial u - m_\pi \partial \pi \tag{8}$$

And:

$$\frac{\partial \varepsilon_z}{\partial t} = m_v \frac{\partial u}{\partial t} - m_\pi \frac{\partial \pi}{\partial t} = m_v \frac{\partial u}{\partial t} - m_\pi RT\frac{\partial c}{\partial t} \tag{9}$$

Inserting (9) into (5) the following equation is obtained:

$$\frac{\partial u}{\partial t} = \frac{k}{m_v \rho_w g}\frac{\partial^2 u}{\partial z^2} - \frac{\omega k}{m_v}\frac{RT}{\rho_w g}\frac{\partial^2 c}{\partial z^2} + \frac{m_\pi}{m_v}RT\frac{\partial c}{\partial t} \tag{10}$$

The first term on the right side of Eq.(10) describes the change in fluid pressure due to a hydraulic gradient and it is of relevance when mechanical consolidation is acting. The second term describes the change in fluid pressure due to an osmotic potential gradient and it is of relevance when the material is capable of sustaining an osmotic potential gradient, behaving as a semi-permeable osmotic membrane. An osmotic potential gradient would generate negative pore water pressures inducing an increase in effective stress. In the case of low osmotic membrane efficiency (as typically the case for shales), this terms have a negligible impact. The third term describes the change in fluid pressure through the coupling with the porosity variation induced by chemical consolidation: this contribution would consist in the generation of positive pore water pressures in the specimen. In this last case, the entity of the phenomenon is related to the ratio between the osmotic and the mechanical compressibility. If the osmotic compressibility is very low with respect to the mechanical one, as often the case for clays and shales, this term has a negligible impact. Kaczmarek and Hueckel (1998) carried out numerical simulations in order to understand the contribution of this term in a clayey medium and found that very small positive pore water pressures (less than 1 kPa) were generated under a chemical load of 4M of NaCl (about 20 MPa). As a consequence the contribution of the term to the development of excess pore water pressure is very small. The analysis highlights the fact that chemo-osmotic consolidation has a very negligible impact on the fluid pressure generation under the condition of low osmotic membrane efficiency and high osmotic stiffness.

C.3 Ions transport equation

The mass conservation equation, flow equation and constitutive law are rewritten for the ionic component in order to derive the governing equation for ion transport.

Ions mass conservation

The conservation of the ions mass in a fluid saturated porous medium is expressed through the following equation (Hassanizadeh, 1986; Kaczmarek and Hueckel, 1998):

$$\frac{\partial(cn)}{\partial t} + div(cnv_c) = 0 \tag{11}$$

where c is the chemical concentration, n is the porosity and v_c is the velocity of the ions. Developing equation (11) the following is obtained:

$$n\frac{\partial c}{\partial t} + c\frac{\partial n}{\partial t} + div(cnv_c) = 0 \tag{12}$$

From the mass conservation for the solid part the following relationship is obtained:

$$\frac{\partial n}{\partial t} = (1-n)div(v_s) \tag{13}$$

Substituting equation (13) in (12) the following equation is obtained:

$$n\frac{\partial c}{\partial t}+cdiv(v_s)+cndiv(v_c-v_s)=0 \tag{14}$$

Since:

$$div(v_s)=\frac{\partial \varepsilon_v}{\partial t} \tag{15}$$

And:

$$n(v_c-v_s)=v_{c\,rel\,s} \tag{16}$$

where $v_{c\,rel\,s}$ is the relative velocity of the ions with respect to the solid phase. Eq.(14) becomes:

$$n\frac{\partial c}{\partial t}+c\frac{\partial \varepsilon_v}{\partial t}+div(cv_{c\,rel\,s})=0 \tag{17}$$

where the term $cv_{c\,rel\,s}$ contains the contributions to the flow of ions related to the fluid advection as well as the non-advective flow; therefore, it is the total ions flux *J*.

$$n\frac{\partial c}{\partial t}+c\frac{\partial \varepsilon_v}{\partial t}+div(J)=0 \tag{18}$$

Ions flow equation

The flow of ions is driven by several direct and indirect phenomena. Assuming isothermal conditions (no temperature gradient is present), the total flow of ions writes (Soler, 2001):

$$J=-D_e\frac{\partial c}{\partial z}-ck\frac{\partial h}{\partial z}+c\omega k\frac{\partial \pi_h}{\partial z}+c\omega k\frac{\partial h}{\partial z} \tag{19}$$

where the first term is the contribution to the flow due to diffusion (direct mechanism), the second term is the transport due to advection, the third term is the transport due to the osmotically driven flow of fluid, finally the last term is the contribution to transport due to ultrafiltration (i.e. the flow of ions due to a water flow generated by an hydraulic gradient induced by the presence of an osmotic potential). Inserting (19) into (18) the following equation is obtained:

$$n\frac{\partial c}{\partial t}+c\frac{\partial \varepsilon_v}{\partial t}-D_e\frac{\partial^2 c}{\partial z^2}+\frac{\partial}{\partial z}\left(-ck\frac{\partial h}{\partial z}+c\omega k\frac{\partial \pi_h}{\partial z}+c\omega k\frac{\partial h}{\partial z}\right)=0 \tag{20}$$

where D_e is the effective diffusion coefficient. The constitutive law was introduced in Eq.(6). Inserting Eq.(9) into (20) the following relationship is obtained:

$$n\frac{\partial c}{\partial t}+cm_v\frac{\partial u}{\partial t}-cm_\pi RT\frac{\partial c}{\partial t}-D_e\frac{\partial^2 c}{\partial z^2}+\frac{\partial}{\partial z}\left(-ck\frac{\partial h}{\partial z}+c\omega k\frac{\partial \pi_h}{\partial z}+c\omega k\frac{\partial h}{\partial z}\right)=0 \tag{21}$$

Inserting equation (10) into (21) we obtain the following expression:

$$\begin{aligned}&n\frac{\partial c}{\partial t}+ck\frac{\partial^2 h}{\partial z^2}-c\omega k\frac{RT}{\rho_w g}\frac{\partial^2 c}{\partial z^2}+cm_\pi RT\frac{\partial c}{\partial t}-cm_\pi RT\frac{\partial c}{\partial t}-D_e\frac{\partial^2 c}{\partial z^2}+\\&+\frac{\partial}{\partial z}\left(-ck\frac{\partial h}{\partial z}+c\omega k\frac{\partial \pi_h}{\partial z}+c\omega k\frac{\partial h}{\partial z}\right)=0\end{aligned} \tag{22}$$

$$\begin{aligned}&n\frac{\partial c}{\partial t}+ck\frac{\partial^2 h}{\partial z^2}-c\omega k\frac{RT}{\rho_w g}\frac{\partial^2 c}{\partial z^2}+cm_\pi RT\frac{\partial c}{\partial t}-cm_\pi RT\frac{\partial c}{\partial t}-D_e\frac{\partial^2 c}{\partial z^2}-ck\frac{\partial^2 h}{\partial z^2}+c\omega k\frac{RT}{\rho_w g}\frac{\partial^2 c}{\partial z^2}+\\&+c\omega k\frac{\partial^2 h}{\partial z^2}+\frac{\partial c}{\partial z}\left(-k\frac{\partial h}{\partial z}+\omega k\frac{\partial \pi_h}{\partial z}+\omega k\frac{\partial h}{\partial z}\right)=0\end{aligned} \tag{23}$$

$$D_e\frac{\partial^2 c}{\partial z^2}=n\frac{\partial c}{\partial t}+c\omega k\frac{\partial^2 h}{\partial z^2}+\frac{\partial c}{\partial z}\left(-k\frac{\partial h}{\partial z}+\omega k\frac{\partial \pi_h}{\partial z}+\omega k\frac{\partial h}{\partial z}\right) \tag{24}$$

The coupling terms inside the brackets on the right side of Eq. (24) are respectively the contribution to ions transport due to advection, chemical-osmosis and ultrafiltration; the second term on the right side is also expressing ultrafiltration. Advection is usually disregarded due to the different time scale involved with respect to the diffusive process (Kaczmarek and Hueckel, 1998; Peters and Smith, 2004; AL-Bazali, 2011), ultrafiltration can also be neglected as well as the contribution to the transport due to chemo-osmosis since very low osmotic membrane efficiency values are involved. The variation in ions concentration in therefore described by the following equation:

$$n\frac{\partial c}{\partial t}-D_e\frac{\partial^2 c}{\partial z^2}=0 \tag{25}$$

Which is rewritten in the form of the second Fick's law as follows:

$$D\frac{\partial^2 c}{\partial z^2}=\frac{\partial c}{\partial t} \tag{26}$$

Or

$$D\frac{\partial^2 \pi}{\partial z^2}=\frac{\partial \pi}{\partial t} \tag{27}$$

where D is the apparent diffusion coefficient defined as:

$$D = \frac{D_e}{n} \tag{28}$$

D_e is the effective diffusion coefficient which is different from the well-known Fick's diffusion coefficient D_0 due to the microstructural geometry of the porous material:

$$D_e = n\frac{\chi}{\tau^2}D_0 \tag{29}$$

where χ is the constrictivity, which takes into account the pore narrowing, and τ is the tortuosity, which takes into account the path lengthening (Horseman et al., 1996). The solution of Eq. (27) under the initial condition (t=0) of constant osmotic suction π_0 along z-direction, and under the boundary condition of null osmotic suction at the top and bottom bases of the specimen for t>0, is the following:

$$\pi(z,t) = \sum_{m=0}^{\infty}\frac{2\pi_0}{M}\left(\sin\frac{Mz}{H}\right)e^{-M^2\frac{Dt}{H^2}} \tag{30}$$

where π_0 is the imposed increment in osmotic suction, H is the diffusion path length (half of the height of the specimen) and $M = 0.5\pi(2m+1)$, with m being an integer. The variation in osmotic suction inside the material is therefore expressed as follows:

$$\Delta\pi(z,t) = \pi_0 - \pi(z,t) \tag{31}$$

An increase in osmotic suction induces a decrease in volume according to the following constitutive relationship (volumetric strains are considered positive when compressive):

$$-\frac{\Delta V}{V}(z,t) = \varepsilon_v(z,t) = m_\pi\Delta\pi(z,t) = m_\pi\left[\pi_0 - \pi(z,t)\right] \tag{32}$$

The settlement induced by the increase in osmotic suction is therefore expressed as follows:

$$\delta(\mathrm{t}) = \int_0^{2H}\varepsilon_v(t,z)dz = \int_0^{2H}m_\pi\Delta\pi(t,z)dz = m_\pi\int_0^{2H}\left[\pi_0 - \pi(z,t)\right]dz \tag{33}$$

$$\delta(\mathrm{t}) = m_\pi\int_0^{2H}\left[\pi_0 - \sum_{m=0}^{\infty}\frac{2\pi_0}{M}\left(\sin\frac{Mz}{H}\right)e^{-M^2\frac{Dt}{H^2}}\right]dz \tag{34}$$

$$\delta(\mathrm{t}) = m_\pi\pi_0\int_0^{2H}\left[1 - \sum_{m=0}^{\infty}\frac{2}{M}\left(\sin\frac{Mz}{H}\right)e^{-M^2\frac{Dt}{H^2}}\right]dz \tag{35}$$

$$\delta(\mathrm{t}) = 2Hm_{\pi}\pi_0\left[1+\sum_{m=0}^{\infty}\frac{1}{M^2}e^{-M^2\frac{Dt}{H^2}}(\cos 2M-1)\right] \tag{36}$$

$$\delta(\mathrm{t}) = 2Hm_{\pi}\pi_0\left[1-\sum_{m=0}^{\infty}\frac{2}{M^2}e^{-M^2\frac{Dt}{H^2}}\right] \tag{37}$$

C.4 Poroelasticity

If poroelastic conditions are considered and, therefore, the hypothesis of incompressibility of the solid grains and of the pore fluid is removed, Eq. (5) becomes as follows:

$$\frac{\partial\varepsilon_z}{\partial t} = \frac{k}{\rho_w g}\frac{\partial^2 u}{\partial z^2} - \omega k\frac{RT}{\rho_w g}\frac{\partial^2 c}{\partial z^2} - \left[\frac{n}{K_f}+\frac{(1-n)}{K_s}\right]\frac{\partial u}{\partial t} \tag{38}$$

when the vertical total stress is applied and held constant, the change in effective stress is proportional to the change in fluid pressure trough the poroelastic coefficient *C*, that is the coefficient defining the ratio of the increment in the pore water pressure to the increment in the vertical total stress under one-dimensional and undrained conditions as defined in Chapter 3:

$$\partial\sigma'_z = \frac{\partial u}{C} \tag{39}$$

Equation (9) is therefore written as follows:

$$\frac{\partial\varepsilon_z}{\partial t} = \frac{m_v}{C}\frac{\partial u}{\partial t} - m_{\pi}RT\frac{\partial c}{\partial t} \tag{40}$$

Inserting (40) into (38) the following equation is obtained:

$$\left[\frac{m_v}{C}+\frac{n}{K_f}+\frac{(1-n)}{K_s}\right]\frac{\partial u}{\partial t} = m_{\pi}RT\frac{\partial c}{\partial t}+\frac{k}{\rho_w g}\frac{\partial^2 u}{\partial z^2}-\omega k\frac{RT}{\rho_w g}\frac{\partial^2 c}{\partial z^2} \tag{41}$$

Eq. (41) is rewritten as follows:

$$\frac{m_v}{C}A\frac{\partial u}{\partial t} = m_{\pi}RT\frac{\partial c}{\partial t}+\frac{k}{\rho_w g}\frac{\partial^2 u}{\partial z^2}-\omega k\frac{RT}{\rho_w g}\frac{\partial^2 c}{\partial z^2} \tag{42}$$

where *A* is defined as follows:

$$A = 1+\frac{nC}{m_v K_f}+\frac{(1-n)C}{m_v K_s} \tag{43}$$

Inserting Eq. (40) into (20), the following is obtained:

$$n\frac{\partial c}{\partial t}+c\frac{m_v}{C}\frac{\partial u}{\partial t}-cm_\pi RT\frac{\partial c}{\partial t}-D_e\frac{\partial^2 c}{\partial z^2}+\frac{\partial}{\partial z}\left(-ck\frac{\partial h}{\partial z}+c\omega k\frac{\partial \pi_h}{\partial z}+c\omega k\frac{\partial h}{\partial z}\right)=0 \tag{44}$$

Inserting Eq. (42) into (44) and considering the above discussion about the osmotic membrane efficiency for shales and the relevance of the coupling terms in Eq.(24), in the case of a poroelastic material Eq.(25) becomes the following:

$$D_e\frac{\partial^2 c}{\partial z^2}=n\frac{\partial c}{\partial t}+\left(\frac{1-A}{A}\right)cm_\pi RT\frac{\partial c}{\partial t}+\left(\frac{1-A}{A}\right)c\frac{k}{\rho_w g}\frac{\partial^2 u}{\partial z^2} \tag{45}$$

The consideration of the poroelastic constants brings relevant complexity to the problem; the significance of term A is therefore estimated for Opalinus Clay. Porosity is about 16% for Opalinus Clay shaly facies, K_f is taken equal to the bulk modulus of water (2.2 GPa), the parameter C, K_s and m_v have been estimated in Chapter 3 and they are taken equal to 0.9, 14 GPa and 1.0 GPa^{-1}, respectively. The resulting value of A is equal to 1.1, which suggest that the last two terms in Eq. (45) can be considered negligible. Therefore, the solution of Eq.(25) is considered for the analysis of the experimental results presented in Chapter 5.

C.5 References

Kaczmarek, M. and Hueckel, T. Chemo-mechanical consolidation of clays: analytical solutions for a linearized one-dimensional problem. Transport in Porous Media (1998) 32(1): 49-74.

Hassanizadeh, S.M. Derivation of basic equations of mass transport in porous media, Part 1. Macroscopic balance laws. Advances in water resources (1986) 9(4): 196-206.

Soler, J.M. The effect of coupled transport phenomena in the Opalinus Clay and implications for radionuclide transport. Journal of Contaminant Hydrology (2001) 53(1): 63-84.

Peters, G.P. and Smith, D.W. The influence of advective transport on coupled chemical and mechanical consolidation of clays. Mechanics of Materials (2004) 36(5): 467-486.

AL-Bazali, T.M. The consequences of using concentrated salt solutions for mitigating wellbore instability in shales. Journal of Petroleum Science and Engineering (2011) 80(1): 94-101.

Horseman, S., Higgo, J., Alexander, J. and Harrington, J. Water, gas and solute movement through argillaceous media. Nuclear Energy Agency Rep. CC-96/1. OECD, Paris (1996).

Appendix D
Triaxial testing of Opalinus Clay

D.1 Pore water pressure evolution during B-check tests

This section reports the results from B-check tests in terms of mean total stress and pore water pressure evolution in time for all the tested specimens and for all the performed steps of mean total stress increment. The pore water pressure diffusion mechanism is further analysed through the development of an analytical solution, which takes into account the presence of a water reservoir for the measurement of the pore water pressure increment.

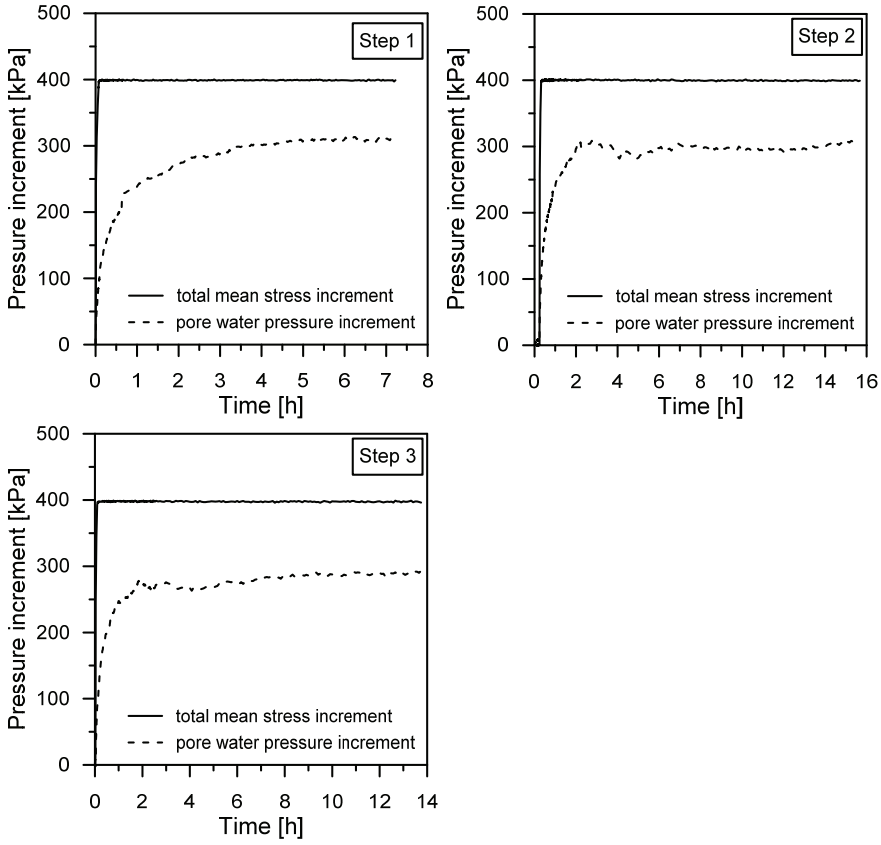

Figure 1: B-check test results for specimen P-2.

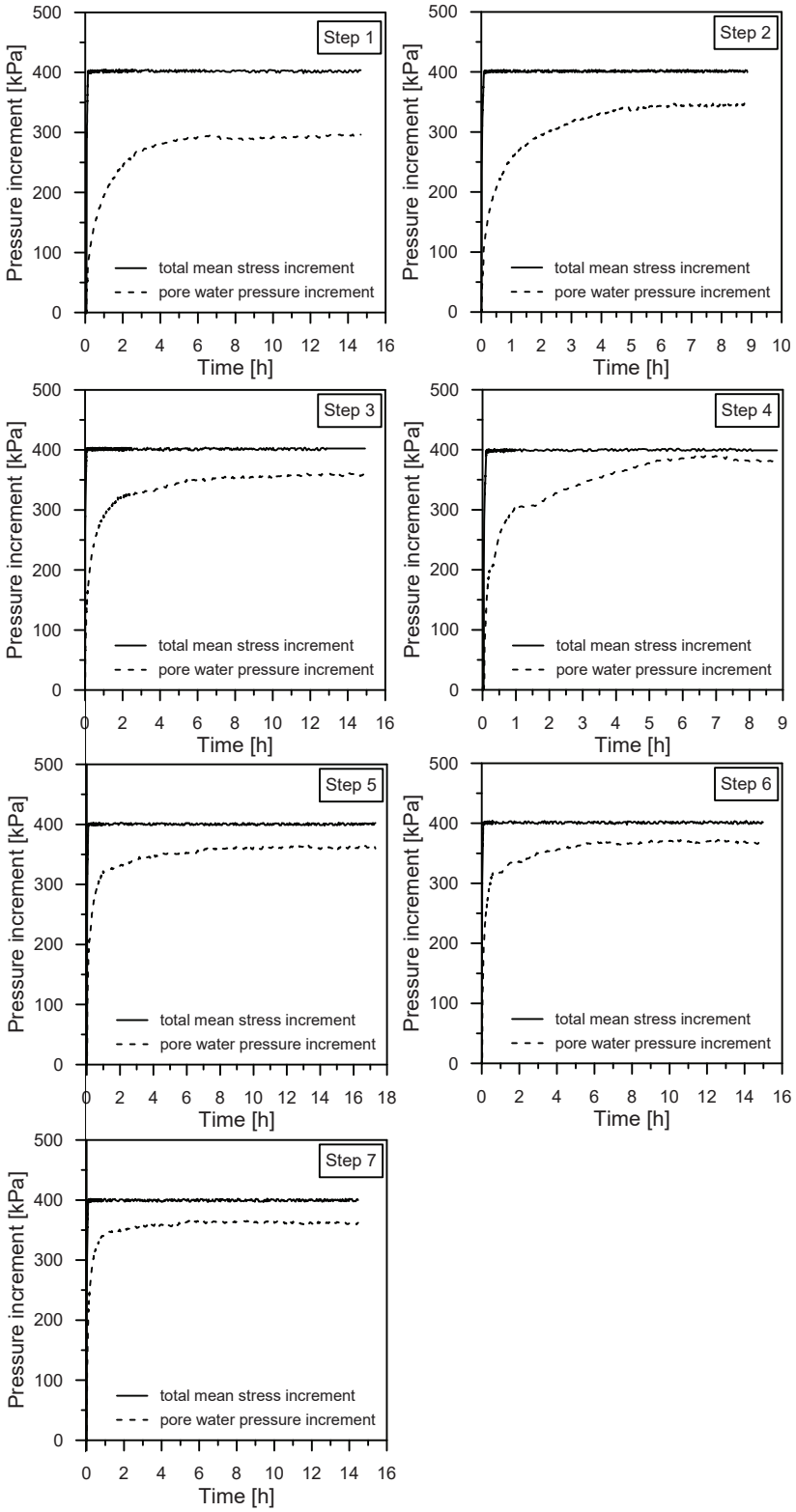

Figure 2: B-check test results for specimen P-1.

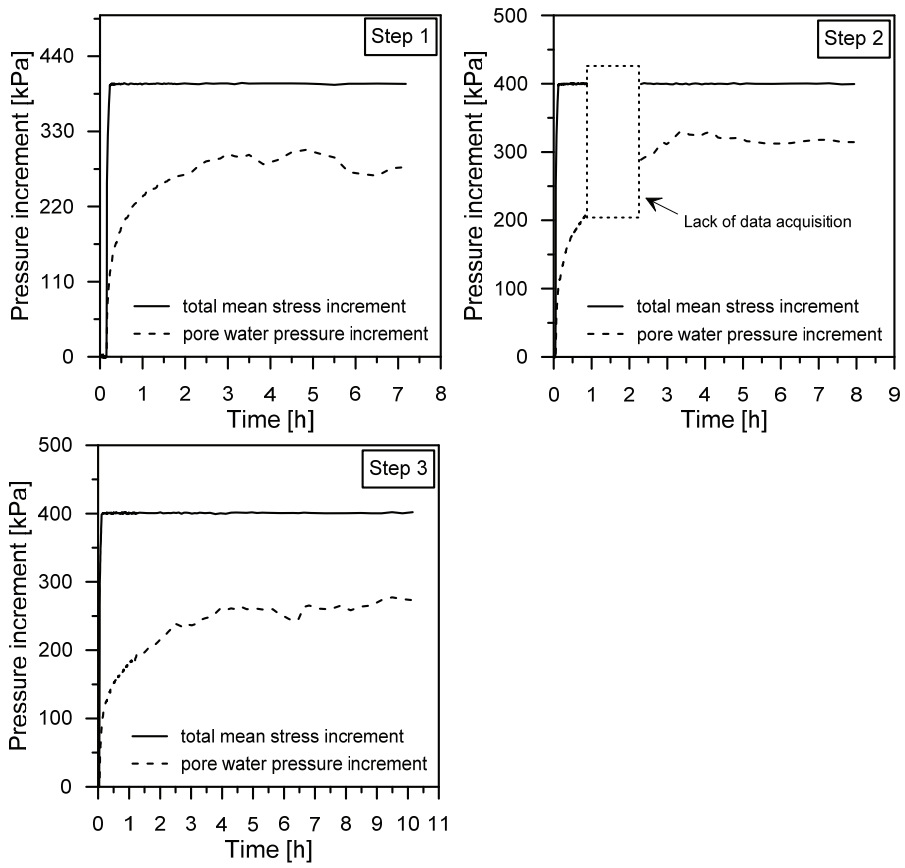

Figure 3: B-check test results for specimen S-1.

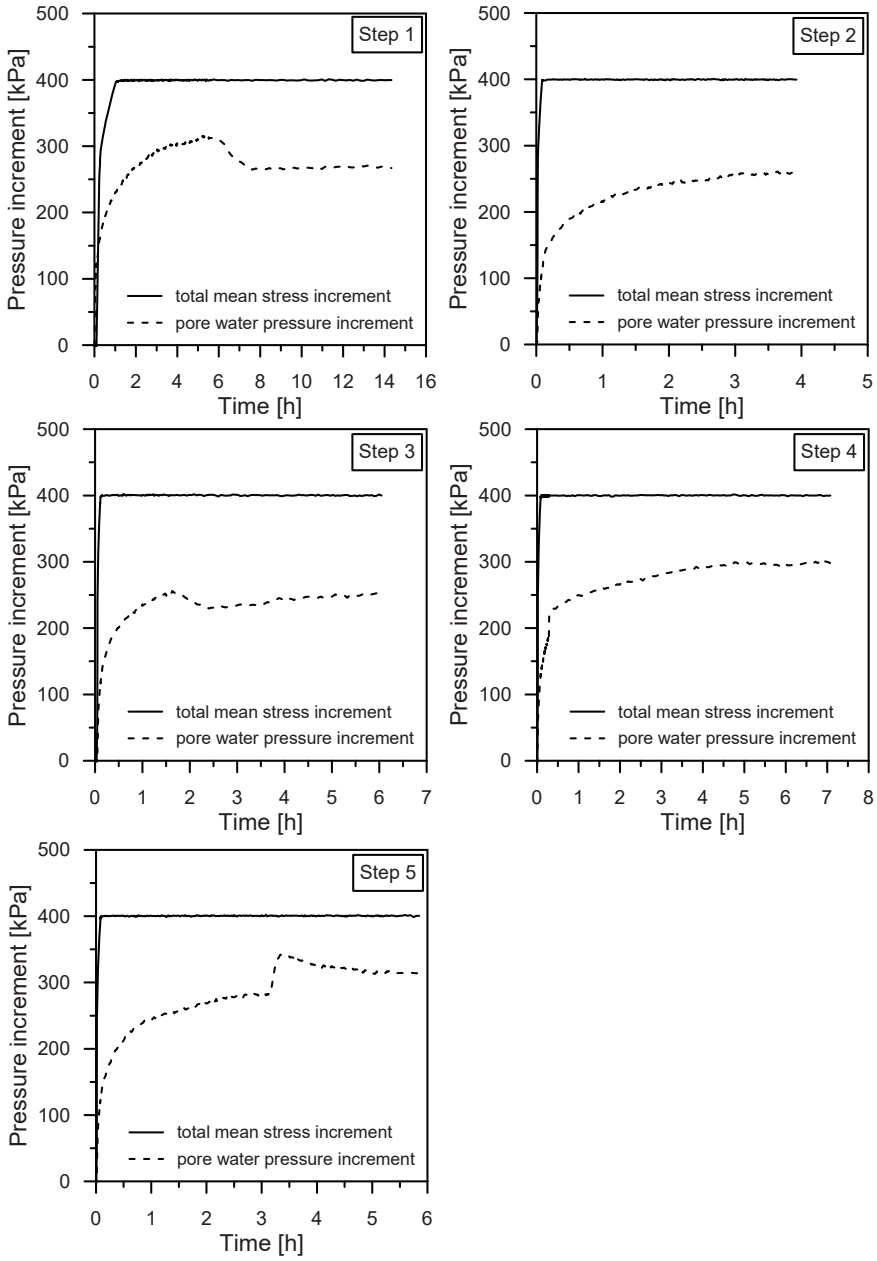

Figure 4: B-check test results for specimen S-2.

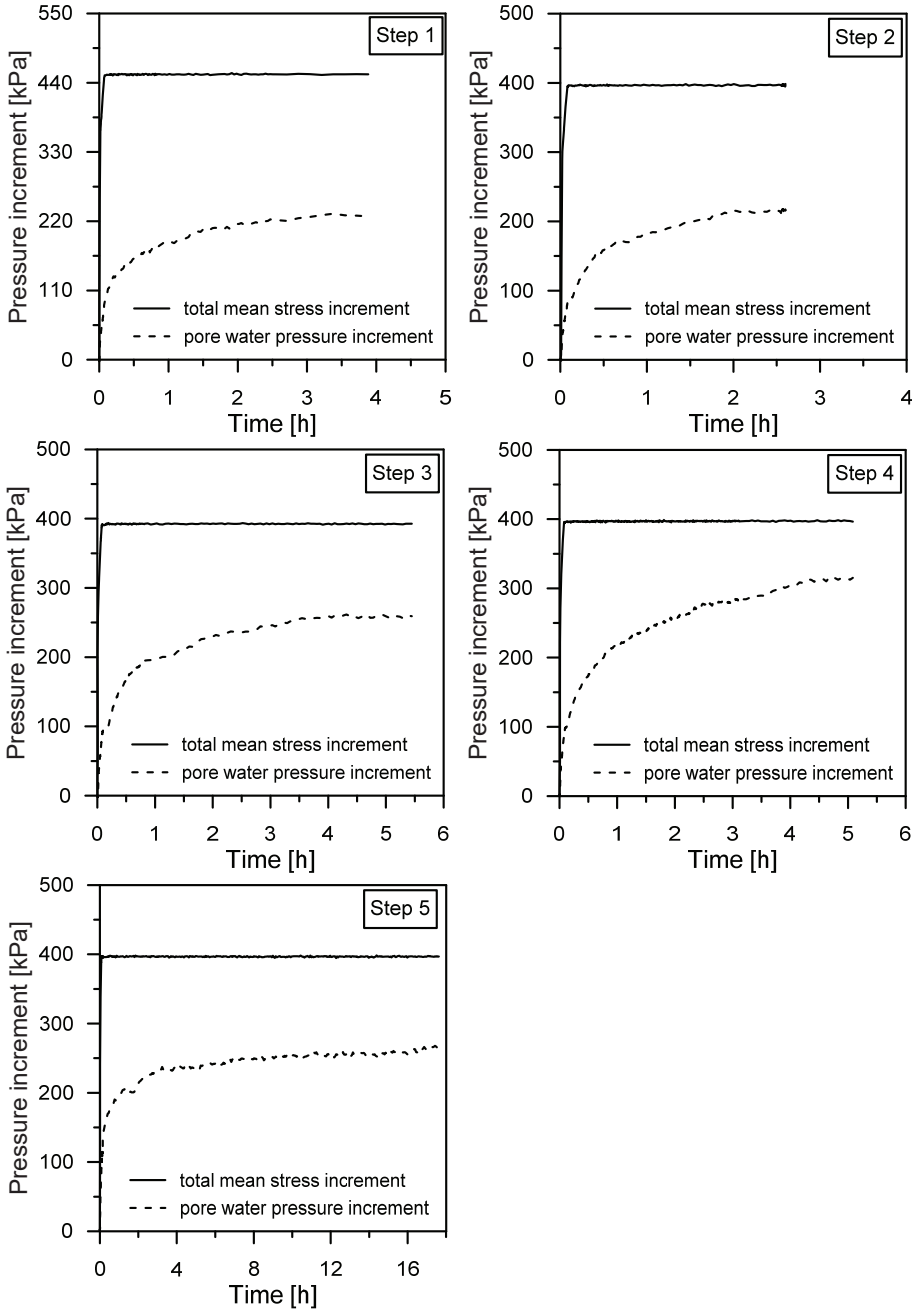

Figure 5: B-check test results for specimen S-3.

Figures from 1 to 5 highlight the fact that some hours are necessary for the pore pressure to stabilize and reach the final value. The delay in the pore pressure transmission may be due to several factors among which:

- The low permeability of the tested material, which implies that some time is needed for internal pore pressure equilibration;
- The presence of a water reservoir at the top and bottom bases of the specimen, which is constituted by the internal drainage lines and by the water pressure sensor.

The latter phenomenon can be analysed considering the fluid mass balance in the water reservoir, where the variation in the mass of water within the reservoir must be equal to the water mass going out from the specimen and entering in the reservoir, since undrained conditions are imposed.

The fluid mass variation in time per unit volume, within the specimen, can be written as follows:

$$\frac{\partial(n\rho_f)}{\partial t} + div(n\rho_f v_f) = 0 \tag{1}$$

where n is the porosity, ρ_f is the fluid density and v_f is the fluid velocity. Assuming constant porosity during the pore water pressure diffusion process, Eq.(1) can be written as follows:

$$\frac{\partial M}{V\,\partial t} + n\rho_f div(v_f) = 0 \tag{2}$$

where M is the fluid mass and V is the volume. Assuming that flow is occurring only in z direction and readjusting, the following is obtained:

$$\partial M = -\rho_f V \frac{\partial v_{rf}}{\partial z}\partial t \tag{3}$$

where v_{rf} is the relative velocity of the fluid. After integration, the following is obtained:

$$M_e = -A\rho_f v_{rf}\partial t \tag{4}$$

where M_e is the fluid mass entering in the reservoir and exiting from the specimen, and A is the area of the specimen. Introducing Darcy's law in order to express the fluid velocity, Eq.(4) becomes as follows:

$$M_e = \rho_f A \frac{k}{\gamma_w}\frac{\partial P_f}{\partial z}\partial t \tag{5}$$

where k is the coefficient of permeability, P_f is the fluid pressure and γ_w is the specific weight of water. The fluid mass going out from the specimen must be equal to the fluid mass variation within the reservoir (M_{res}) since undrained conditions are imposed:

$$\frac{\partial M_{res}}{\partial t}\partial t = \frac{V_{res}\partial \rho_f}{\partial t}\partial t = \rho_f A \frac{k}{\gamma_w}\frac{\partial P_f}{\partial z}\partial t \tag{6}$$

where V_{res} is the volume of the reservoir, which is constant. Readjusting Eq.(6) the following is obtained:

$$\frac{1}{\rho_f}\frac{\partial \rho_f}{\partial P_f}\frac{\partial P_f}{\partial t} = \frac{Ak}{V_{res}\gamma_w}\frac{\partial P_f}{\partial z} \tag{7}$$

And therefore:

$$\frac{\partial P_f}{\partial t} = \frac{Ak}{\beta_f V_{res}\gamma_w}\frac{\partial P_f}{\partial z} \tag{8}$$

where β_f is the compressibility of the fluid. Eq.(8) is solved assuming the following boundary conditions: the fluid pressure within the specimen P_1 has to be transmitted to the reservoirs at the two ends of the specimen, where undrained conditions are imposed and the volume of the reservoirs is constant. Axial symmetric conditions can be assumed, therefore, the middle-height H of the specimen is considered as the maximum path length encountered. P_1 is the fluid pressure inside the specimen, which is considered constant in time, while P_2 is defined as the fluid pressure inside the reservoir, which varies in time, therefore the following can be written:

$$\frac{\partial P_1}{\partial t} - \frac{\partial P_2}{\partial t} = -\frac{Ak}{\beta_f V_{res}\gamma_w}\frac{(P_1 - P_2)}{H} \tag{9}$$

And:

$$\frac{\partial (P_1 - P_2)}{(P_1 - P_2)} = -\frac{Ak}{\beta_f V_{res}\gamma_w H}\partial t \tag{10}$$

After integration, the following is obtained:

$$\ln(P_1 - P_2) = -\frac{Ak}{\beta_f V_{res}\gamma_w H}t + C \tag{11}$$

The constant C is determined for the case where $t = 0$ and $(P_1 - P_2) = \Delta P_0$, therefore:

$$\ln \Delta P = -\alpha t + \ln \Delta P_0 \tag{12}$$

where:

$$\alpha = \frac{Ak}{\beta_f V_{res}\gamma_w H} \tag{13}$$

Therefore:

$$\Delta P(t) = \Delta P_0 e^{-\alpha t} \tag{14}$$

The solution of Eq. (14) is used to analyse the pore fluid pressure diffusion behaviour during B-check tests. The area of the specimen A is equal to 19.6 cm^2, the volume of the reservoir is equal to 9.5 cm^3, H is equal to 50 mm, fluid compressibility is taken as equal to 0.45 GPa^{-1}, finally the values of the coefficient of permeability are optimised in order to obtained the best fitting of the model with respect to the experimental results. The results of the last B-check step for all the performed tests are presented in Figure 6 and in Figure 7, in terms of both experimental results and model prediction. Permeability values between 4 x 10^{-13} and 5 x 10^{-13} m/s are obtained for S-samples, while values between 6 x 10^{-13} and 8 x 10^{-13} m/s are obtained for P-samples. The model captures quite well the pore water pressure diffusion response; some discrepancies with respect to the observed behaviour are present and they may be related to the following aspects:

- The initial water pressure increase predicted by the model is in general slower than the experimental results. This is due to the fact that the pore water pressure increase does not occur only at the middle-height of the specimen (as imposed in the boundary conditions), but it is distributed within the whole height of the specimen. As a consequence, the initial water pressure transmission from the specimen to the reservoir is faster than predicted.

- In the final part of the curves, the water pressure equilibrates more slowly than predicted by the model. This fact may be due to some internal pore water pressure equilibration, which takes some time due to the low porosity and low permeability of the material, so that the pressure inside the specimen is not initially constant. This aspect could thus introduce some delay in the pore pressure transmission mechanism.

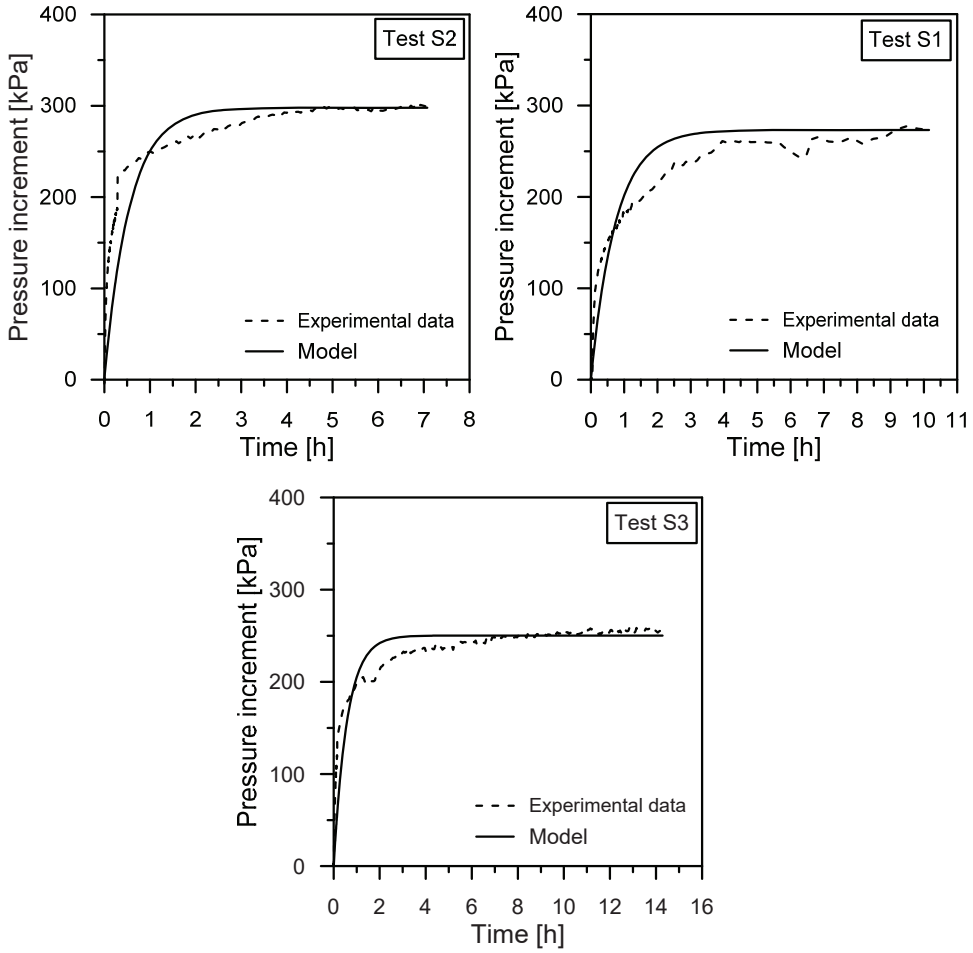

Figure 6: Water pressure transmission during a B-check test for S-specimens.

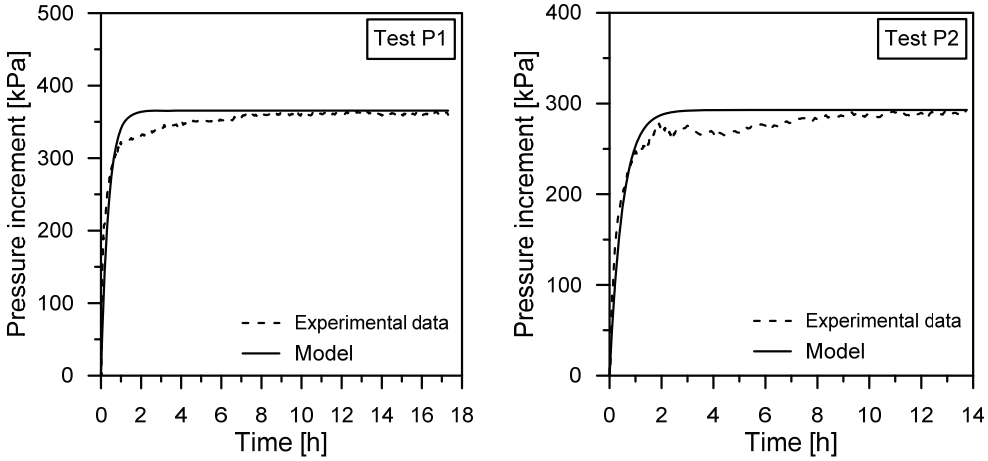

Figure 7: Water pressure transmission during a B-check test for P-specimens.

D.2 Tested specimens

In this section the photos of the tested specimens after testing are reported.

Figure 8: Specimen P-1.

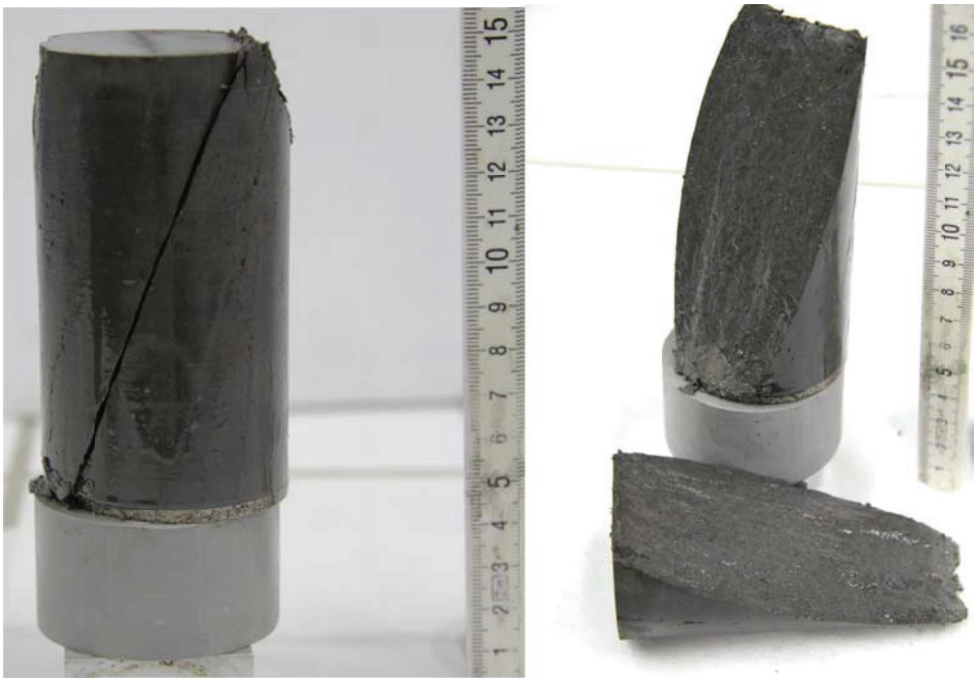

Figure 9: Specimen P-2.

Figure 10: Specimen S-1.

Figure 11: Specimen S-2.

Figure 12: Specimen S-3.

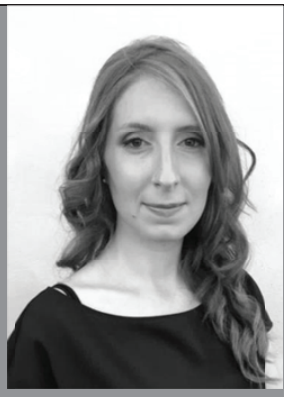

VALENTINA FAVERO

CIVIL ENGINEER

31 January 1987
Italian nationality
Permit B
Driving licence B

Rue du Maupas, 10
1004 Lausanne
valentina.favero@epfl.ch
076 704 30 63

EDUCATIONN

05.2012 – 01.2017 PhD IN GEOMECHANICS
École Polytechnique Fédérale de Lausanne, EPFL
PhD Thesis : « Multiphysical behaviour of shales from Northern Switzerland»

09.2009 – 12.2011 MASTER IN CIVIL ENGINEERING / GEOTECHNICAL ENGINEERING
Università degli Studi di Padova

09.2009 – 06.2010 ERASMUS PROGRAM
University of Southampton (UK), faculty of Civil Engineering and the Environment

09.2006 – 07.2009 BACHELOR IN CIVIL ENGINEERING
Università degli Studi di Padova

WORK EXPERIENCES

01.2017 – Present EPFL POST-DOCTORAL RESEARCHER
École Polytechnique Fédérale de Lausanne
Post-doctoral research assistant on geomechanical aspects of the CO_2 storage technology

05.2012 – 01.2017 DOCTORAL ASSISTANT, TEACHING ASSISTANT
École Polytechnique Fédérale de Lausanne EPFL

- Scientific research
- Teaching assistant (Soil mechanics, Analysis II, Slope stability)
- Supervision of bachelor and master students
- Organization of workshops
- Management of the laboratory library

01.09.2008 – 01.10.2008 SERVIZI GEOLOGICI SAS, Curtarolo (PD) Italy
Internship

GENERAL

- Very good organization skill and respect of the delays
- Very good communication skills with different interlocutors
- Problem solving skills
- Teaching skills
- Good capacity of speaking in public
- Very good team-spirit
- Project management

TECHNICAL

- Performance and analysis of laboratory tests concerning soil and rock mechanics.
- Writing of technical reports and scientific papers
- Organization of conferences and workshops

INFORMATICS

- Good knowledge of Office: Word, PowerPoint and Excel
- Grapher, Surfer
- Autocad
- Geoslope
- Plaxis
- Zsoil
- Good capability of learning new software

LANGUAGES

ITALIAN Mother tongue
ENGLISH Very good level (both oral and written) (C1)
FRENCH Good level (B2)
GERMAN Basic level (A2)

SCIENTIFIC PUBBLICATIONS

Journal papers

- Favero, V., Ferrari, A. and Laloui, L. (2016). Thermo-mechanical volume change behaviour of Opalinus Clay. International Journal of Rock Mechanics and Mining Sciences, 90, 15-25.
- Ferrari, A., Favero, V. and Laloui, L. (2016). One-dimensional Compression and Consolidation of Shales. International Journal of Rock Mechanics and Mining Sciences, 88, 286-300.
- Favero, V., Ferrari, A., & Laloui, L. (2016). On the hydro-mechanical behaviour of remoulded and natural Opalinus Clay shale. Engineering Geology, 208: 128–135.
- Ferrari, A., Favero, V., Marschall, P., & Laloui, L. (2014). Experimental analysis of the water retention behaviour of shales. International Journal of Rock Mechanics and Mining Sciences, 72: 61-70.

Conference papers

- Ferrari, A., Favero, V., & Laloui, L. (2014). On the water retention behaviour of shales. In *48th US Rock Mechanics/Geomechanics Symposium*. American Rock Mechanics Association.
- Ferrari, A., Favero, V., Manca, D., & Laloui, L. (2013). Volumetric behaviour and consolidation of shales at high confining stresses. In *47th US Rock Mechanics/Geomechanics Symposium*. American Rock Mechanics Association.

Scientifics reports

- Favero, V., Ferrari, A. & Laloui, L. (2016): Consolidated-drained triaxial testing of Opalinus Clay. Nagra Int. Ber.
- Favero, V., Ferrari, A. and Laloui, L. 2013. Diagnostic analyses of the geomechanical database from cores of the Borehole Schlattingen SLA-1. Nagra Arbeitsbericht NAB 13-45. Nagra, Wettingen.
- Ferrari, A., Favero, V., Manca, D. and Laloui, L. 2012. Geotechnical characterization of core samples from the geothermal well Schlattingen LSA-1 by LMS/EPFL. Nagra Arbeitsbericht NAB 12-50. Nagra, Wettingen.

TALKS AT INTERNATIONAL CONFERENCES

- 2017: ATMSS International Workshop. Villars-sur-Ollon (Switzerland).
- 2016: Fifth EAGE Shale Workshop: Quantifying Risk and Potential. Catania (Italy).
- 2015: Second EAGE International Workshop on Geomechanics and Energy: the Ground as Energy Source and Storage. Celle (Germany).
- 2015: Sixth international conference on "Clays in natural and engineered barriers for radioactive waste confinement". Brussels (Belgium).
- 2014: Fourth EAGE Shale Workshop. Porto (Portugal).
- 2014: Swiss Geoscience Meeting. Fribourg (Switzerland).
- 2014: 48th US Rock Mechanics/Geomechanics Symposium. Minneapolis (USA).
- 2013: EAGE International Workshop on Geomechanics and Energy. Lausanne (Switzerland).
- 2013: Swiss Geoscience Meeting. Lausanne (Switzerland), 2013.
- 2013: XVI French-Polish Colloquium of Soil and Rock Mechanics. Montpellier (France).
- 2013: 47th US Rock Mechanics/Geomechanics Symposium. San Francisco (USA).

ORGANIZED WORKSHOPS

- 2012: AMTSS Workshop - Advances in Multiphysical Testing of Soils and Shales. EPFL, Lausanne, Switzerland.
- 2017: ATMSS Workshop - Advances in Laboratory Testing and Modelling of Soils and Shales. Villars-sur-Ollons, Switzerland.